

DISS. ETH No. 13176

**CONTRIBUTIONS TOWARD  
UNCERTAINTY ASSESSMENTS AND  
ERROR MINIMIZATION OF FDTD  
SIMULATIONS INVOLVING COMPLEX  
DIELECTRIC BODIES**

A dissertation submitted to the  
SWISS FEDERAL INSTITUTE OF TECHNOLOGY  
ZURICH

for the degree of  
Doctor of Technical Sciences

presented by  
MICHAEL ROGER BURKHARDT  
dipl. El.-Ing. TH Darmstadt  
born March 31, 1969  
citizen of Germany

accepted on the recommendation of  
Prof. Dr. N. Kuster, examiner  
Prof. Dr. W. Fichtner, Prof. Dr. M. Taki, co-examiners

1999

# Contents

Summary	v
Zusammenfassung	vii
List of Acronyms	xiii
Acknowledgments	xv
<b>I Introduction</b>	<b>1</b>
<b>1 Background and Objectives</b>	<b>3</b>
<b>2 Review of Exposure Assessment for Mobile Communications De-</b>	<b>7</b>
<b>vices</b>	
2.1 Introduction . . . . .	7
2.2 Safety Standards & Requirements for Exposure Assessment . . . . .	8
2.3 Methods for Dosimetric Evaluation . . . . .	10
2.3.1 Numerical Methods . . . . .	10
2.3.2 Experimental Methods . . . . .	14
2.3.3 Temperature Probes and Radiation Thermometry . . . . .	14
2.3.4 Dosimetric Field Probes . . . . .	15
2.3.5 Free-Space Field Probes . . . . .	16
2.3.6 Automated Near-Field and Dosimetric Scanners . . . . .	16
2.4 Review of Basic Studies on Absorption in the Near-Field of MTE . .	17
2.4.1 Introduction . . . . .	17
2.4.2 General Absorption Mechanism in the Near-Field . . . . .	18
2.4.3 Tissue Parameters . . . . .	18
2.4.4 Modeling of the Human Head . . . . .	19
2.4.5 Effect of the Hand . . . . .	21
2.4.6 Metallic Accessories & Environmental Effects . . . . .	21
2.4.7 Handset Position . . . . .	22
2.4.8 Handset Modeling . . . . .	22
2.5 Review of Compliance Evaluations . . . . .	23
2.5.1 Introduction . . . . .	23
2.5.2 Generic Phones . . . . .	23
2.5.3 Commercially Available Cellular Phones . . . . .	25
2.6 Review of Antenna Studies for Optimized Radiation Performance with	
Reduced User Exposure . . . . .	26

2.6.1	Introduction . . . . .	26
2.6.2	Basic Studies . . . . .	27
2.6.3	Wire Antenna Configurations . . . . .	27
2.6.4	Planar Configurations . . . . .	28
2.6.5	Other Configurations . . . . .	29
2.7	Conclusions and Outlook . . . . .	29
<b>II Uncertainty Analysis and Error Minimization in FDTD Simulations</b>		<b>47</b>
<b>3</b>	<b>Finite-Difference Time-Domain (FDTD) Technique</b>	<b>49</b>
3.1	Introduction . . . . .	49
3.2	The Finite-Difference Time-Domain Formulation . . . . .	49
3.3	Gridding and Material Treatment . . . . .	51
3.4	Boundary Conditions . . . . .	52
3.5	Source Implementation . . . . .	52
3.5.1	Plane Wave Source . . . . .	52
3.5.2	Waveguide Source . . . . .	52
3.5.3	Lumped Sources . . . . .	53
3.6	Stability . . . . .	53
3.7	Implementation . . . . .	53
<b>4</b>	<b>FDTD Intrinsic Uncertainties</b>	<b>59</b>
4.1	Classification of Numerical Errors in FDTD . . . . .	59
4.2	Dispersion . . . . .	60
4.3	Reflections from Boundaries . . . . .	61
4.4	Source Modeling . . . . .	62
4.5	Discussion . . . . .	63
<b>5</b>	<b>Estimation of Artifacts Caused by FDTD-Staircasing in RF Simulation Involving Lossy Dielectric Objects</b>	<b>67</b>
5.1	Introduction . . . . .	67
5.2	Staircasing . . . . .	68
5.3	Methods for Conformal Modeling . . . . .	68
5.4	Methods . . . . .	69
5.4.1	Numerical Techniques . . . . .	69
5.4.2	Basic Modeling . . . . .	70
5.4.3	Material Boundary Treatment . . . . .	70
5.4.4	Partially Filled Cell . . . . .	70
5.5	Local Errors in Absorption due to Single Steps . . . . .	72
5.5.1	Model . . . . .	72
5.5.2	Results . . . . .	72
5.6	Global Errors in Absorption due to Staircasing . . . . .	76
5.6.1	Model . . . . .	76
5.6.2	Results . . . . .	76
5.7	Performance of Partially Filled Cells to Reduce Staircasing Effects at Dielectric Material Boundaries . . . . .	79
5.7.1	Model . . . . .	79

5.7.2	Results . . . . .	79
5.8	Modeling of a Step . . . . .	81
5.9	Conclusion . . . . .	81
<b>III</b>	<b>Benchmarks and Applications</b>	<b>89</b>
<b>6</b>	<b>Study on the FDTD Performance for Transmitters in Complex Environments</b>	<b>91</b>
6.1	Introduction . . . . .	91
6.2	Generic Setup . . . . .	92
6.3	Methods . . . . .	94
6.3.1	Simulation . . . . .	94
6.3.2	Far Field Measurement . . . . .	94
6.3.3	Near Field Measurement . . . . .	95
6.4	Results . . . . .	96
6.4.1	Free Space Evaluation . . . . .	96
6.4.2	Near Field Evaluation with a Flat Absorbing Phantom . . . . .	96
6.5	Conclusion . . . . .	98
<b>7</b>	<b>Numerical and Experimental Dosimetry of Petri Dish Exposure Setups</b>	<b>101</b>
7.1	Introduction . . . . .	101
7.2	Problem Description . . . . .	102
7.3	Applied Numerical Techniques . . . . .	103
7.3.1	MAFIA Code . . . . .	103
7.3.2	3D MMP Code . . . . .	104
7.4	Experimental Setup . . . . .	105
7.4.1	Temperature Probes . . . . .	105
7.5	Results . . . . .	106
7.6	Validation . . . . .	107
7.6.1	Validation of modeling . . . . .	108
7.6.2	Validation of Simplifications . . . . .	111
7.6.3	Analytical Approximation . . . . .	112
7.7	Conclusions . . . . .	115
<b>8</b>	<b>Exposure Setup to Test CNS Effects of Wireless Communications Systems</b>	<b>119</b>
8.1	Introduction . . . . .	119
8.2	Exposure Setup . . . . .	120
8.3	Experimental Dosimetry . . . . .	122
8.3.1	Setup . . . . .	122
8.3.2	Discussion of Uncertainties . . . . .	123
8.3.3	Results . . . . .	124
8.4	Numerical Dosimetry . . . . .	125
8.4.1	Method . . . . .	125
8.4.2	Modeling . . . . .	125
8.4.3	Dependence of the SAR Distribution on the Rat Modeling . . . . .	126
8.4.4	Results . . . . .	130



8.5	Effects of Movements and Different Sizes . . . . .	132
8.5.1	Effects of Movements . . . . .	132
8.5.2	Sensitivity to Size . . . . .	132
8.6	Exposure Efficiency . . . . .	133
8.7	Whole Body Temperature rise . . . . .	134
8.8	Conclusion . . . . .	134
<b>9</b>	<b>Appropriate Modeling of the Ear for Compliance Testing of Hand-held MTE with SAR Safety Limits at 900/1800 MHz</b>	<b>137</b>
9.1	Introduction . . . . .	137
9.2	Head Modeling and Transmitter Representation . . . . .	138
9.3	Methods . . . . .	140
9.4	Validation of the New Head Model . . . . .	141
9.5	Results at 900 MHz . . . . .	142
9.5.1	Dipole Configurations . . . . .	142
9.5.2	Generic Phone Configuration in Simplified Positions . . . . .	146
9.5.3	Intended Use Position . . . . .	148
9.6	Results at 1800 MHz . . . . .	149
9.7	Discussion and Conclusions . . . . .	150
	<b>Epilogue</b>	<b>155</b>

# Summary

The spectacular growth of mobile communications equipment (MTE) in the last decades has strongly risen the demand for precise and reliable methods for electromagnetic field prediction involving complex dielectric environments. This thesis addresses the reliability and uncertainty aspects of using a numerical technique such as the Finite-Difference Time-Domain (FDTD) technique for antenna configurations in complex dielectric environments. The developed techniques were not only tested and benchmarked on the bases of generic problems but also on real-world problems which addressed needs in other research areas.

The objective of the studies performed within this thesis was to add contributions toward closing the scientific gap in uncertainty assessment for the described class of problems. Error sources have been identified and modeling errors of complex dielectric bodies for RF simulations with FDTD have been studied in particular. Within this thesis, special emphasis was put on benchmarking the FDTD technique in near-field situations.

A considerable amount of work has also been attributed to the implementation of algorithms within the development of the FDTD kernel of the MINAST EMSIM project. Since FDTD had been chosen as the main technique not only to cover the simulation needs of BIOEM/EMC but also for becoming the basis of two commercial software packages developed in collaboration with ETH spin-off companies, know-how about uncertainty assessments and improved algorithm and modeling support to enhance precision were key elements for the success of this project.

In the first part of the thesis, the most important numerical and experimental methods used for electromagnetic analysis of antennas embedded in complex dielectric environments, the most significant compliance evaluations for handheld devices and antennas for optimized radiation performance with reduced user exposure are reviewed. The information on uncertainty assessment performed for other methods in this context was invaluable when evaluating the performance, in particular precision prediction, of FDTD.

In the second part, uncertainties in electromagnetic field simulation with FDTD are analyzed and separated in uncertainties arising from the numerical scheme itself and modeling errors of complex dielectric environments. From these studies it was concluded that the errors inherent in the FDTD technique itself contribute only little when the technique is appropriately used. Since modeling uncertainties can contribute significantly to the overall error, they are investigated in greater detail. Various techniques to minimize staircasing effects have been explored and will already be utilized in the first version of the CAD-tool for antenna design to be commercially released in a few months. Large errors in local field values inside complex dielectric materials arise from results related to coarse discretizations, whereas significant global errors in field distributions inside complex dielectric materials can

arise from resonant or focusing effects.

In the third part, FDTD is benchmarked for well defined antenna configurations and applied to electromagnetic field prediction of a variety of antenna near-field configurations. Within the first study, potential difficulties from simulating transmitters in the closest proximity of lossy scatterers were investigated. For this purpose a geometrically and electrically well-defined generic phone was developed and analyzed in free space and close to a lossy phantom in the far- and near-field. The results showed that FDTD is highly suitable with high accuracy for well defined antenna configurations in the close proximity of lossy scatterers.

In a second study, a specific Crawford TEM cell exposure setup was analyzed that had already been utilized for bio-experiments but could not previously be characterized with respect to the exposure. The results of this study not only had significant impact on the interpretation of these bio-experiments but also on a series of other experiments which were scheduled to be conducted in TEM cells. It was discovered that the exposure homogeneity as well as the efficiency were much lower than originally anticipated. This was the starting point for the proposal and analysis of a variety of other exposure setups better suited for *in vitro* bio-experiments.

In a third study, a carousel exposure setup used for *in vivo* bio-experiments was analyzed and optimized with respect to its efficiency. For the first time, the performance of an *in vivo* exposure setup was analyzed in great detail using high resolution MRI data of animals, including experimentally validated SAR distributions in the animal brains.

Thanks to this initial experience and the unique combination of the availability of both the most advanced numerical and experimental tools, the group currently evaluates, optimizes and develops *in vitro* and *in vivo* exposure setups for various laboratories throughout the world.

The last study documented in this thesis is an application of FDTD for an issue which was also driven by an urgent request from outside, namely by the US Federal Communications Commission (FCC). It addresses the question of ear exposure during usage of a mobile phone. This issue was brought up in a legal conflict since it is related to the question of correct ear modeling for testing compliance with safety guidelines for electromagnetic exposure. The study was an excellent test for the developed code since it required the use of a phantom with better resolution than had ever been used before and with arbitrarily oriented phone positions.

All applications have been thoroughly validated with either an independent numerical technique, experimental investigations or using both approaches.

# Zusammenfassung

Das dynamische Wachstum mobiler Kommunikationsgeräte für den privaten und beruflichen Gebrauch in den letzten Jahrzehnten verstärkte den Druck auf Forschungsinstitutionen und Industrie, zuverlässige, hochpräzise Methoden zur Nahfeldbestimmung von Antennen in komplexer dielektrischer Umgebung zu entwickeln. Die vorliegende Dissertation befasst sich mit der Zuverlässigkeitsabschätzung und Fehleranalyse einer numerischen Methode, der Finiten-Differenzen Methode im Zeitbereich, zur Feldbestimmung von Antennenanordnungen in komplexer, inhomogener Umgebung. Die entwickelten Algorithmen wurden sowohl an wohldefinierten Benchmarkanordnungen als auch an realitätsnahen, komplizierten Anordnungen die sich unmittelbar aus den universitären und industriellen Forschungsprojekten der Gruppe BIOEM/EMC ergaben, getestet und evaluiert.

Zielsetzung der vorliegenden Untersuchungen war es, einen Beitrag zur Schliessung der Wissenslücke bezüglich Unsicherheitsanalyse elektromagnetischer Feldsimulationen mit FDTD für den beschriebenen Anwendungsbereich zu leisten. Fehlerquellen bei Hochfrequenz FDTD Simulationen wurden identifiziert und analysiert. Einen besonderen Schwerpunkt bildeten die Untersuchungen von aufgrund von Modellierungsunsicherheiten komplexer dielektrischer Körper entstandenen Fehlern. Sehr grosser Wert wurde dabei auf das *benchmarking* der Methode für Antennen-Nahfeldsituationen gelegt.

Einen wesentlichen Teil der Dissertation nahm auch die Implementierung von Algorithmen im Rahmen der FDTD Kernelentwicklung des Projektes MINAST EM-SIM in Zusammenarbeit mit dem *Institut für Integrierte Systeme* der ETH Zürich und vier Industriepartnern in Anspruch, die nicht weiter in der vorliegenden Arbeit dokumentiert sind. Da die FDTD Methode die Simulationsbedürfnisse eines grossen Anwendungsspektrums der Gruppe BIOEM/EMC am besten befriedigte und auch als Basis zweier in Zusammenarbeit mit ETH spin-off Firmen entwickelten CAD-Simulationsprogrammen gewählt wurde, stellten eine fundierte Unsicherheitsanalyse und genauigkeitssteigernde Algorithmen und Modellierungsrichtlinien wesentliche Faktoren für den weiteren Erfolg der Gruppenaktivitäten dar.

Der erste Teil dieser Arbeit besteht aus einer umfangreichen Literaturrecherche im Bereich numerischer und experimenteller Methoden zur elektromagnetischen Feldbestimmung von komplexen Antennenanordnungen im extremen Nahfeld und den wichtigsten Untersuchungen zu Typenprüfverfahren mobiler Kommunikationsgeräte bezüglich Sicherheitsnormen sowie strahlungsoptimierter Antennenanordnungen mit minimaler elektromagnetischer Belastung des Benutzers. Unsicherheitsanalysen anderer Methoden waren hier für vergleichende Untersuchungen zur Leistungsfähigkeit von FDTD von besonderem Interesse.

Der zweite Teil dieser Arbeit behandelt FDTD typische Fehlerquellen bei der elektromagnetischen Feldsimulation. Grob eingeteilt wurden die Fehlerquellen in Fehler

aufgrund der numerischen Methode, wie Dispersion und Randbedingungen, sowie Fehler aufgrund von Modellierungsungenauigkeiten komplexer dielektrischer Strukturen im kartesischen FDTD Gitter. Dabei stellte sich heraus, dass FDTD spezifische Fehlerquellen der ersten Art nur einen kleinen Teil zu Fehlern im Nahfeld beitragen, im Gegensatz zu Fehlern aufgrund von Modellierungsungenauigkeiten dielektrischer Strukturen. Fehler der zweiten Art sowie Algorithmen zu deren Minimierung waren Gegenstand weiterführender Studien im Rahmen dieser Arbeit. Die Ergebnisse dieser Studien führen zur Implementierung der entsprechenden Techniken in eines der erwähnten CAD-Programme für Antennendesign und Optimierung, dessen Kommerzialisierung Ende 1999 vorgesehen ist. Signifikant grosse Fehler in lokalen Feldwerten innerhalb komplexer dielektrischer Strukturen ergeben sich aufgrund des *Staircasing Effektes*, relevante globale Fehler in den Feldverteilungen innerhalb der Materialien für Resonanz- und Fokussierungseffekte.

Im dritten Teil der Arbeit wurde die Leistungsfähigkeit von FDTD zur elektromagnetischen Feldbestimmung wohldefinierter Antennenanordnungen getestet.

Mögliche Probleme grundlegender Art bei der Simulation des Nah- und Fernfeldes hochfrequenter Sender in stark inhomogener dielektrischer Umgebung wurden in einer ersten Studie untersucht. Dazu wurde ein wohldefiniertes, repräsentatives und künstliches Telefon im Fernfeld als auch im Nahfeld allein und in komplexer Umgebung experimentell und numerisch analysiert. Die Studie belegte die Leistungsfähigkeit, hohe Präzision und Robustheit von FDTD für die beschriebene Art von wohldefinierten Antennenkonfigurationen.

In einer zweiten Studie wurde die Feldverteilung in Petrischalen, plazierte in Crawford TEM-Zellen, analysiert, die in der Vergangenheit zur Exposition von Zellkulturen in biologischen Experimenten über mögliche Effekte hochfrequenter Strahlung verwendet wurden. Aufgrund fehlender Möglichkeiten zur detaillierten Expositionsbestimmung konnten zuvor nur grobe Abschätzungen vorgenommen werden. Die in dieser Studie erzielten Erkenntnisse hatten einerseits einen erheblichen Einfluss auf die Interpretation der biologischen Ergebnisse als auch auf die bereits in Planung befindlichen weiteren biologischen Studien. Die Expositionsanalyse zeigte, dass sich für die vorgeschlagene Art von Experimenten nur eine weitaus schlechtere Homogenität und Effizienz mit Crawford TEM Zellen Einrichtungen erzielen lässt als zuvor angenommen. Dies war der Ausgangspunkt für Design, Analyse und Optimierung von geeigneteren Expositionseinrichtungen für biologische *in vitro* Experimente.

In einer dritten Studie wurde die Leistungsfähigkeit von FDTD für die Analyse und Optimierung von *in vivo* Expositionseinrichtungen untersucht. Erstmals wurde detailliert die Effizienz einer solchen Einrichtung mit Hilfe eines numerischen Modells, generiert aus hochauflösenden Magnetresonanz-Aufnahmen (MRI) Daten eines Versuchstieres bestimmt, einschliesslich der experimentell validierten Feldverteilung im Gehirn.

Aufgrund der geschilderten ursprünglichen Ergebnisse und der Verfügbarkeit fortgeschrittenster experimenteller und numerischer Werkzeuge entwickelt, analysiert und optimiert die Fachgruppe BIOEM/EMC Expositionseinrichtungen für eine Reihe biologischer Gruppen auf der ganzen Welt.

Die letzte in dieser Arbeit dokumentierte Studie betrifft die Anwendung von FDTD auf eine Anordnung, die aufgrund einer dringenden Anfrage seitens der amerikanischen Behörde *Federal Communications Commission* untersucht wurde: die elektromagnetische Exposition im Ohrbereich bei der Benutzung eines drahtlosen, mo-

bilen Kommunikationsgerätes. Hervorgegangen ist diese Problemstellung aus der juristischen Fragestellung zur korrekten Modellierung des Ohres bei der Typenprüfung drahtloser, mobiler Kommunikationsgeräte bezüglich der Sicherheitsstandards. Für das im Rahmen von MINAST entwickelte CAD Simulationstool bot sich mit dieser Studie ein hervorragender Testfall, da die Modellierung eine noch nicht erreichte detaillierte Darstellung des menschlichen Kopfes und Flexibilität bezüglich der Antennenposition erforderte.

Alle in dieser Arbeit beschriebenen Anwendungen wurden detailliert unter Verwendung einer unabhängigen numerischen Methode, experimenteller Techniken oder beiden validiert.

## Papers Included in the Thesis

- [1] M. Burkhardt and N. Kuster, "Review of exposure assessment for mobile communications devices," *Review of Radio Science 1996-1999*, 1999. in press.
- [2] M. Burkhardt and N. Kuster, "Estimation of artifacts caused by FDTD-staircasing in RF simulation involving dielectric objects," *Electromagnetics and Guided Waves*, 1999. submitted.
- [3] M. Burkhardt, N. Chavannes, K. Poković, T. Schmid, and N. Kuster, "Study on the FDTD performance for transmitters in complex environments," in *Proceedings, 14th International Conference on Applied Electromagnetics and Communications*, (Dubrovnik, Croatia), pp. 83–86, June 1997.
- [4] M. Burkhardt and N. Kuster, "Appropriate modeling of the ear for compliance testing of handheld MTE with SAR safety limits at 900/1800 MHz," *IEEE Transactions on Electromagnetic Compatibility*, 1999. submitted.
- [5] M. Burkhardt, K. Poković, M. Gnos, T. Schmid, and N. Kuster, "Numerical and experimental dosimetry of petri dish exposure setups," *Journal of the Bioelectromagnetics Society*, vol. 17, no. 6, pp. 483–493, 1996.
- [6] M. Burkhardt, Y. Spinelli, and N. Kuster, "Exposure setup to test CNS effects of wireless communications systems," *Health Physics*, vol. 73, pp. 770–778, Nov. 1997.

## Other Publications

- [7] K. Meier, M. Burkhardt, T. Schmid, and N. Kuster, "Broad band calibration of E-field-probes in lossy media," *IEEE Transactions on Microwave Theory and Techniques*, vol. 44, pp. 1954–1962, Oct. 1996.
- [8] V. Hombach, K. Meier, M. Burkhardt, E. Kuehn, and N. Kuster, "The dependence of EM energy absorption upon human head modeling at 900 MHz," *IEEE Transactions on Microwave Theory and Techniques*, vol. 44, pp. 1865–1873, Oct. 1996.
- [9] F. Schönborn, M. Burkhardt, and N. Kuster, "Differences in energy absorption between heads of adults and children in the near field of sources," *Health Physics*, vol. 74, pp. 160–168, Feb. 1998.
- [10] M. Burkhardt and N. Kuster, "Dosimetric analysis of a near field exposure system used for RF animal studies," in *Latsis Symposium*, (Zürich), Sept. 1995.
- [11] K. Poković, M. Burkhardt, and N. Kuster, "Evaluation of in vitro exposure systems for wireless communications," in *Third international Congress of the European Bio Electromagnetics Association (EBEA)*, (Nancy, France), 1996.

- [12] K. Poković, M. Burkhardt, M. Gnos, T. Schmid, and N. Kuster, "Suitability of tem cells for in vitro experiments at wireless communications frequencies," in *BEMS, Eightteenth Annual Meeting*, (Victoria, Canada), 1996.
- [13] M. Burkhardt, Y. Spinelli, and N. Kuster, "Exposure setup to test CNS effects of wireless communications systems," in *BEMS, Eightteenth Annual Meeting*, (Victoria, Canada), 1996.
- [14] K. Meier, R. Kästle, M. Burkhardt, T. Schmid, and N. Kuster, "Dependence of human head modeling on the spatial peak SAR values," in *BEMS, Eightteenth Annual Meeting*, (Victoria, Canada), 1996.
- [15] M. Burkhardt, L. Bombholt, and N. Kuster, "Hybrid electromagnetic simulation approach for dosimetric assessments," in *URSI*, (Lille, France), 1996.
- [16] M. Burkhardt, Y. Spinelli, and N. Kuster, "Exposure setup to test CNS effects of wireless communications systems," in *URSI*, (Lille, France), 1996.
- [17] F. Schönborn, M. Burkhardt, and N. Kuster, "Experimental requirements for RF laboratory experiments," in *World Congress on Medical Physical and Biomedical Engineering*, (Nice, France), p. 31, Sept. 1997.
- [18] O. Voles, K. Poković, M. Burkhardt, and N. Kuster, "Limitations of precise simulations of handheld mobile phones with FDTD," in *North American Radio Science Meeting*, (Montreal, Canada), p. 134, July 1997.
- [19] M. Burkhardt, F. Schönborn, and N. Kuster, "EM-energy absorption in human heads depending on age, size and shape," in *North American Radio Science Meeting*, (Montreal, Canada), p. 671, July 1997.
- [20] F. Schönborn, M. Burkhardt, and N. Kuster, "Variations in energy absorption between heads of children and adults at 900 MHz," in *Second World Congress for Electricity and Magnetism in Biology and Medicine*, (Bologna, Italy), p. 165, June 1997.
- [21] M. Burkhardt, K. Poković, F. Schönborn, and N. Kuster, "Evaluation and design of an optimized *in vitro* exposure setup for the mobile frequency range of 1.5-1.9 GHz," in *Second World Congress for Electricity and Magnetism in Biology and Medicine*, (Bologna, Italy), p. 166, June 1997.
- [22] F. Schönborn, R. Jones, M. Burkhardt, W. R. Adey, and N. Kuster, "Numerical and experimental characterization of the carousel setup for the exposure of rats at 1.62 GHz," in *Twentieth Annual Meeting of the Bioelectromagnetics Society*, (St. Pete Beach, Florida, USA), p. 67, June 1998.
- [23] M. Burkhardt and N. Kuster, "Appropriate modeling of the ear for compliance testing of handheld MTE with SAR safety limits," in *Twentieth Annual Meeting of the Bioelectromagnetics Society*, (St. Pete Beach, Florida, USA), p. 79, June 1998.
- [24] F. Schönborn, R. Jones, M. Burkhardt, K. Poković, W. R. Adey, and N. Kuster, "Waveguide setup optimized for the exposure of petri dishes in the mobile frequency range of 1.6-1.8 GHz," in *Twentieth Annual Meeting of the Bioelectromagnetics Society*, (St. Pete Beach, Florida, USA), p. 201, June 1998.



- [25] M. Burkhardt and N. Kuster, "Artifacts at material boundaries in exposure assessment with FDTD," in *Twentieth Annual Meeting of the Bioelectromagnetics Society*, (St. Pete Beach, Florida, USA), p. 263, June 1998.
- [26] N. Chavannes, M. Burkhardt, and N. Kuster, "Simulation of wire antennas non-conformally oriented to the FDTD grid," in *USNC/URSI National Radio Science Meeting*, (Atlanta, Georgia, USA), p. 73, June 1998.
- [27] M. Burkhardt and N. Kuster, "Artifacts at material boundaries of lossy dielectric bodies in FDTD simulations," in *USNC/URSI National Radio Science Meeting*, (Atlanta, Georgia, USA), p. 72, June 1998.
- [28] A. Christ, K. Poković, M. Burkhardt, and N. Kuster, "Sensitivity analysis of a planar antenna with respect to FDTD modeling," in *USNC/URSI National Radio Science Meeting*, (Atlanta, Georgia, USA), p. 274, June 1998.
- [29] N. Kuster, M. Burkhardt, and F. Schönborn, "Dosimetry and optimization of exposure setups for *in vitro* and *in vivo* studies of microwave effects," in *Technical Report of the IEICE, EMCJ98-40*, pp. 1–5, Aug. 1998.
- [30] M. Burkhardt, T. Samaras, and N. Kuster, "SAR absorption in the ear region induced by mobile communications equipment," in *Proceedings of the 4th Ebea Congress*, (Zagreb, Croatia), p. 88, Nov. 1998.
- [31] M. Burkhardt, K. Poković, T. Schmid, and N. Kuster, "Experimental and numerical near-field evaluation of rf transmitters," in *NATO Advanced Research Workshop, Radio Frequency Radiation Dosimetry and its Relationship to the Biological Effects of Electromagnetic Fields*, (Gozd Martuljek, Slovenia), Oct. 1998.
- [32] F. Schönborn, K. Poković, and M. Burkhardt, "In vitro exposure setups for HF," in *COST244bis Workshop: Biomedical Effects of Electromagnetic Fields*, (Zurich, Switzerland), pp. 12–23, Feb. 1999.
- [33] M. Burkhardt, F. Schönborn, K. Poković, and N. Kuster, "Setups for partial-body exposure," in *COST244bis Workshop: Biomedical Effects of Electromagnetic Fields*, (Zurich, Switzerland), pp. 49–54, Feb. 1999.
- [34] N. Kuster, M. Burkhardt, P. Regli, and W. Fichtner, "A CAD tool for rigorous electromagnetic simulations of microsystems," in *Swiss Physical Society, Jahrestagung in Bern*, (Bern, Switzerland), p. 73, Feb. 1999.
- [35] M. Burkhardt, H.-U. Gerber, T. Samaras, and N. Kuster, "EM exposure of the auditory system dependent on phone position," in *Twenty-first Annual Meeting of the Bioelectromagnetics Society*, (Long Beach, California, USA), June 1999.
- [36] M. Burkhardt, H.-U. Gerber, T. Samaras, and N. Kuster, "Dependence of EM energy absorption in the ear on handheld phone position," in *XXVIth General Assembly of the International Union of Radio Science*, (Toronto, Ontario, Canada), Aug. 1999.

# List of Acronyms

ABC	Absorbing Boundary Condition
ANSI	American National Standard Institute
ARIB	Association of Radio Industries and Businesses
CAD	Computer Aided Design
CENELEC	European Committee for Electrotechnical Standardization
CNS	Central Nervous System
COST	Cooperation in the Field of Scientific and Technical Research
CP	Contour-Path
CT	Computer Tomography
DASY	Dosimetric Assessment System
DCS	Digital Communications System
DTX	Discontinuous Transmission Mode
EBCM	Extended Boundary Condition Method
EFIE	Electric Field Integral Equation
EM	Electromagnetic
EMSIM	Electromagnetic Simulation Platform
ETH	Eidgenössische Technische Hochschule
FCC	Federal Communications Commission
FDTD	Finite-Difference Time-Domain
FE	Finite-Element
FEM	Finite-Element Method
FI	Finite-Integration
FIT	Finite-Integration Technique
FM	Frequency Modulation
FS-PIFA	Full Short Circuit Planar Inverted “F”-Antenna
FVTD	Finite-Volume Time-Domain
GHz	Gigahertz
GMT	Generalized Multipole Technique
GSM	Global System for Mobile
ICNIRP	International Commission in Non-Ionizing Radiation Protection
IEBCM	Iterative Extended Boundary Condition Method
IEEE	Institute of Electrical and Electronics Engineers
IFA	Inverted “F”-Antenna
IFH	Institut für Feldtheorie und Höchstfrequenztechnik
IIS	Institut für Integrierte Systeme
ISE	Integrated Systems Engineering AG
MHz	Megahertz
MINAST	Micro & Nano System Technology

MMP	Multiple Multipole Technique
MoM	Method of Moments
MPI	Max-Planck Institut
MRI	Magnetic Resonance Images
MTE	Mobile Telecommunications Equipment
NCRP	National Council on Radiation Protection and Measurement
NIST	National Institute of Standards and Technology
NMT	Nordic Mobile Telephone
PIFA	Planar Inverted "F"-Antenna
PML	Perfectly Matched Layer
RCDLA	Radiation Coupled Dual-L Antenna
RCR	Research and Development Center for Radio Systems
RF	Radiofrequency
SAR	Specific Absorption Rate
SEMCAD	Simulator for Electromagnetic Compatibility, Antennas and Dosimetry
SPEAG	Schmid & Partner Engineering AG
SPP	Swiss Priority Program
TEM	Transverse Electromagnetic
TDMA	Time Division Multiple Access

# Acknowledgments

Back in 1995 when I joined the BIOEM/EMC group at the EMF and Microwave Electronics Laboratory (IFH) at ETH Zurich, the group was only two years old and was - at that time - mainly concentrated on the development of near-field measurement technology. However, the prevailing intention was to reactivate its second complementary research arm, namely the field of numerical electrodynamics, which had previously been restricted to the Generalized Multipole Technique (GMT). Various techniques and hybrid approaches were being evaluated, whereby the group took advantage of my previous experience in the Finite-Integration Technique (FIT) from my work at the Technical University of Darmstadt. I was assigned the task of evaluating and benchmarking FDTD against the results of other techniques. The initial scepticism against purely numerical methods faded quickly and FDTD was chosen as the core technique for the kernel to be implemented as part of the EMSIM project. This project began in 1996 and was part of the Swiss Priority Program for Micro and Nano System Technology (MINAST) with the objective of developing a simulation platform for micro and wireless systems. This became the basis of my PhD work and was realized jointly with the Integrated Systems Laboratory (IIS) and four Swiss companies. In addition to this implementation work, I was continuously called upon by the group to perform numerical evaluations which were needed for progress in other projects. This resulted in my becoming involved in a broad range of projects with the concomitant long working nights and weekends at the institute. Some of these activities have also been documented in this thesis.

This thesis would not have been possible without the advice and help of many who have been involved in the development of the simulation platform and related projects. Firstly I would like to express my deep gratitude to the BIOEM/EMC group, where I was able to experience the synergy effects that can arise from outstanding team work. Thomas Schmid, the engineering brain of the group, was able to argue with me for hours on the comparative advantages of any experimental approach vis-a-vis numerical simulations; Klaus Meier, who introduced me to the work at the laboratory and his passion for aviation piloting; Katja Poković for providing the experimental data for many projects we have been jointly involved in throughout my stay; Frank Schönborn, who took over a burgeoning range of activities in optimizing exposure setups for *in vivo* and *in vitro* bio-experiments; Andreas Christ for his valuable help within the EMSIM project; and Nicolas Chavannes, who despite working together with me for his semester and diploma theses did go on to become a fellow PhD student. I also would like to thank for all the technical support I obtained: Thomas Schwitter for relying exclusively on Mac platforms and Ray Ballisti for his day and night UNIX support, traditionally acknowledged in any thesis performed at the laboratory. Computer support was also provided by Hans-Uli Gerber, minimizing complex 3D visualization problems to 3 line code fragments, and Oliver Egger,

who integrated programming support with the cultural exploration of Zurich; both of whom are from Schmid & Partner Engineering AG (SPEAG), Zurich. My sincere gratitude goes to the team leader Prof. Niels Kuster, for introducing me to the exciting research field of BIOEM/EMC and guiding me through this work. Although I still am at odds with him as to his notion of what constitutes regular working hours, particularly with respect to weekends, I greatly appreciate being able to have had all the benefits of his outstanding scientific competence and his finely-tuned political sense in the cagey matter of dealing with critical issues that touch both industry interests and consumer safety.

I also would like to express my appreciation to Prof. Wolfgang Fichtner of IIS for enabling my close collaboration with his electromagnetics research group and for co-examining this work; Peter Regli, the EMSIM project leader and his crew at IIS as well as Lars Bomholt from Integrated Systems Engineering AG (ISE), Zurich for our smooth collaboration and their continuous support throughout the years.

I benefited greatly from various discussions at our annual conference meetings with Prof. Masao Taki, Tokyo Metropolitan University, Japan, for whose co-examination of this work I am very grateful. I also greatly appreciate the advice of Dr. So-ichi Watanabe, Communications Research Laboratory, Tokyo, Japan, for letting me share his expertise in FDTD for electromagnetic dosimetry at various meetings of the Bioelectromagnetics Society.

The close collaboration with T-Mobil, Deutsche Telekom and Swisscom, providing advice and support through Dr. Eduard Kühn, Dr. Fritz Lauer and Bernhard Eicher, was extremely fruitful right from the onset of this work.

I must specially emphasise my thanks to Dr. Quirino Balzano and his group for providing valuable advice and support for this thesis.

Our close cooperation with Ericsson Radio Systems AB and our fruitful discussions on FDTD issues with Martin Siegbahn at various meetings was a valuable contribution to this work.

I would also like to express my gratitude for the support from the Swiss Priority Program MINAST and Motorola Inc., which enabled me to become a PhD-student and which provided me with excellent infrastructure.

Finally, I would like to thank Michelle Stubbs and Benedict de Silva for proof-reading this manuscript and all the reports and papers during the last few years. Most of all, I should not forget the support and motivation I received from Marie Fevrier-Vincent, often over a distance of 600 km and yet showing me that there is more to life than work alone.

**Part I**

**Introduction**

Seite Leer /  
Blank leaf

# Chapter 1

## Background and Objectives

The BIOEM/EMC group, founded in 1993 with Niels Kuster's appointment as assistant Professor at ETH, initially focused its activities exclusively on the development of near-field measurement technology. This was due to the limited resources (a single PhD student) available at the time. However, the early successes in this area enabled a continuous expansion of the scope of their activities. The inception of the MINAST Swiss Priority Program in 1995 opened up an opportunity to resume earlier research in numerical electrodynamics. The objectives envisaged at the time were to complement measurement technology with a flexible, robust and user-friendly simulation platform for the simulation of antennas embedded in complex environments. Furthermore, it should enable the prediction of the solution accuracy. The latter was of particular importance to Prof. Kuster since he, together with Ed Miller, is one of the pioneer researchers in this field. The aspect of precision prediction had long been overlooked by the electromagnetics community.

Different approaches were initially considered. Lars Bomholt, supported by BIOEM/EMC, evaluated a hybrid approach by combining GMT with MoM and FE during his stay at MIT. He completed the implementation of the kernel called GMT++ during his first period at IIS. Another technique being evaluated was FDTD. Whereas the GMT approach was evaluated on the basis of real-world applications by Roger Tay, I was assigned to evaluate FDTD. FDTD was finally chosen as the basic technique for the simulation platform to be developed within the MINAST program. The advantages with respect to robustness and facility of modeling strongly inhomogeneous problems, as well as the implementation of a user-friendly GUI, clearly outweighed any shortcomings with respect to precision prediction arising from the explicit scheme. Our initial benchmark tests also gave us confidence that the maximum uncertainties could be controlled by enhanced implementations and adhering to a suite of basic modeling guidelines. The disconcerting variations found during the course of a benchmark comparison (see Figure 1.1) can be attributed rather more to a lack of problem awareness within the scientific community regarding assessment and minimization of uncertainties than to problems inherent to FDTD. However, this clearly demonstrated the existence of substantial gaps in the scientific knowledge in this area. Since the suitability of numerical simulations directly depends on the capability of precision prediction, a single major topic of my thesis was devoted to this issue.



The objectives of the studies performed during the course of my thesis term can be summarized as follows:

- Review of the most important numerical and experimental methods used for antennas embedded in complex dielectric environments.
- Evaluation of commercial FDTD software packages when used for real-world problems and scientific studies. Comparison of results with those of other techniques.
- Participation in the implementation of the FDTD kernel EMSIM within the framework of the SPP MINAST. Only the availability of a world class source code can enable the study of possible measures to minimize the uncertainty of simulations and implement improvements. The contribution to the implementation, which consumed a major part of the PhD work, is not documented in this thesis.
- Analysis of the uncertainties inherent in the FDTD technique and development and testing of strategies for the minimization of these uncertainties.
- Extensive application of FDTD to various benchmark problems and real-world studies in order to assess its feasibility and inclusion of uncertainty assessments for electromagnetic exposure studies involving antenna structures operating within a complex dielectric environment.

At the end of my thesis those aspects of my study which could not be resolved within the scope of this thesis are outlined and suggestions on how these issues should be addressed in the future are discussed.

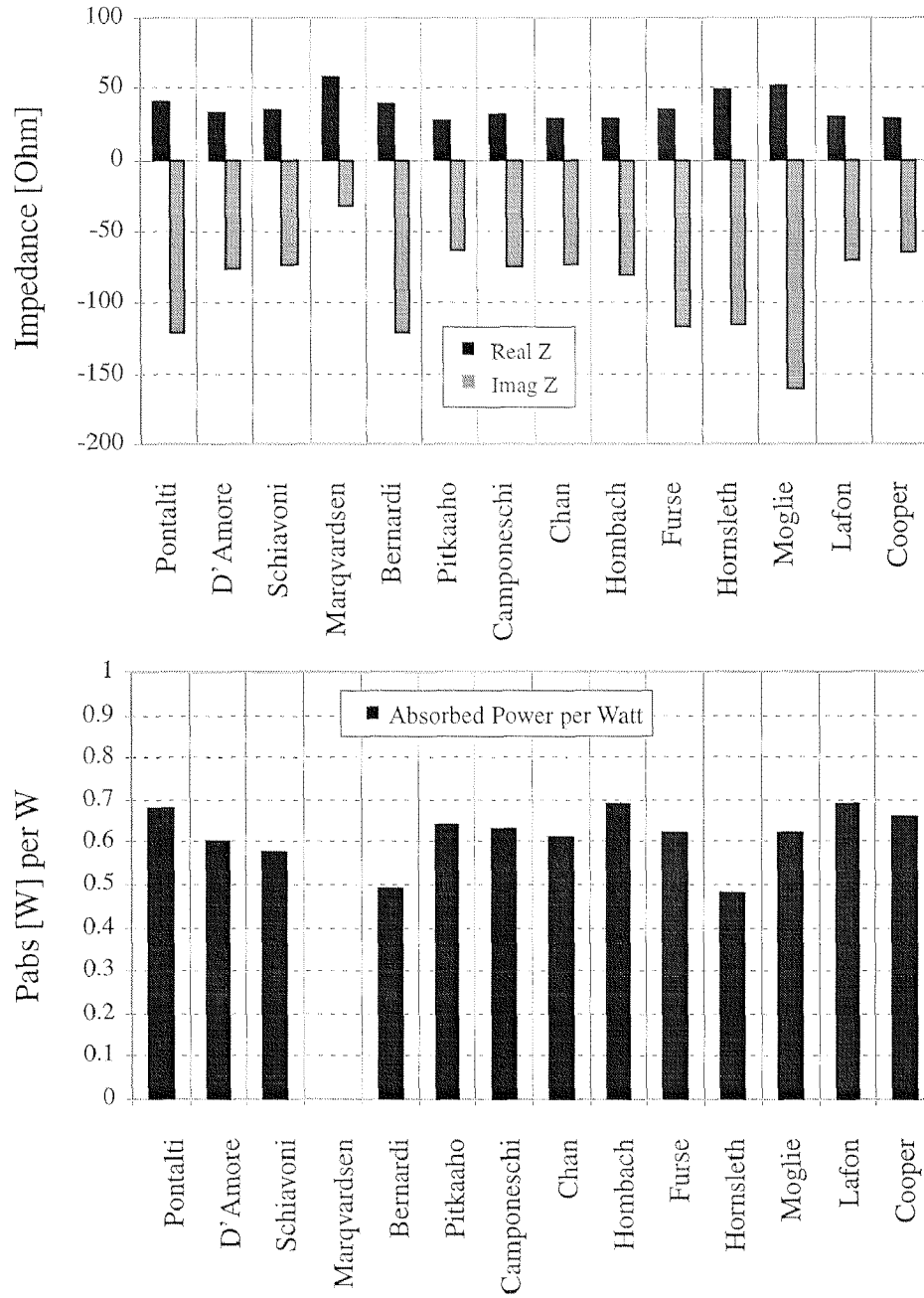


Figure 1.1: Comparison of the FDTD results provided by 14 different groups for the COST244 benchmark. Shown is the comparison of the feedpoint impedance and absorbed power per Watt antenna input power. The benchmark consists of a homogeneous sphere ( $\epsilon=43$ ,  $\sigma=0.83$  mho/m, diameter=200mm) exposed to a dipole antenna (thickness=2.5mm, length=0.4 $\lambda$ , feeding gap=2.5mm, distance antenna axis-sphere=15mm) at 900 MHz. Most of the researchers used a 2.5mm grid, 2nd order Mur or comparable boundaries and a voltage source (Pontalti et al., "Cost244bis canonical cases for mobile communications equipment", in 4th EBEA Congress Zagreb, Croatia, Nov. 1998).

Seite Leer /  
Blank leaf

## Chapter 2

# Review of Exposure Assessment for Mobile Communications Devices

### 2.1 Introduction

In response to consumer demand for ever smaller and lighter handheld mobile telecommunications equipment (MTE), the industry has succeeded in producing major technological advances in rapid cycles. The size of the chip set as well as its power consumption has been dramatically reduced. At the same time major breakthroughs in battery technology have also been made. However, little to no attention has been paid to antenna efficiency, even though the amount of antenna input power absorbed by the head can largely vary between 10% - 70% depending on design factors. Consequently, most currently employed antennas are still of the classical helical and dipole antenna designs.

Nevertheless, numerical and experimental techniques to assess the power deposition in the heads of users have significantly advanced during the last few years. This development has been driven less by a need for tools enabling antenna optimization and more by statutory requirements imposed by regulatory bodies to demonstrate compliance with safety limits. Regulatory action has been partially the result of growing public interest in the possible adverse health effects of wireless communications. This issue has received much worldwide publicity in 1993 with the first lawsuit claiming that handheld phones cause brain tumors [1]. Since then discussion about this matter has become more rational, although the issue is still sporadically exaggerated in the media.

In the following Section safety limits and requirements are discussed as they have developed in recent years. In Section 2.3 experimental and numerical techniques developed for and applied in dosimetric evaluations are reviewed.

Section 2.4 summarizes the studies designed to evaluate the most important exposure defining parameters. This includes studies on the principal energy absorption mechanism in the close near-field of sources, anatomic variations, the effects of the hand, device position with respect to the head, effects of the environment as well as device modeling. In Section 2.5 the dosimetric evaluations conducted for various handset devices are compared.

In the final Section 2.6 the publications which compare various MTE antenna

design concepts with respect to efficiency and user exposure are reviewed.

## 2.2 Safety Standards & Requirements for Exposure Assessment

In the frequency range of mobile communications, the physical unit used to define the safety limits of the major international and national safety standards around the world (e.g., [2], [3]) is the Specific Absorption Rate (SAR). SAR can be expressed in terms of the induced electric field strength or the temperature rise in tissue by:

$$SAR = \frac{dP}{dm} = \frac{\sigma}{\rho} E^2 = c \frac{dT}{dt} \quad (2.1)$$

where  $E$  is the root-mean-square value of the induced electric field strength,  $dT/dt$  the temperature rise,  $\rho$  the tissue density,  $\sigma$  the dielectric conductivity and  $c$  the specific heat capacity.

SAR limits are defined for whole-body averaged as well as for local absorption. In the case of local absorption the so-called spatial peak SAR limit is averaged over a given volume in order to distinguish between non-hazardous strong local heating of the skin (e.g., RF burns) and possible hazards caused by the exposure of greater volumes of tissue. For example, [3] defines a spatial peak SAR value of 1.6 mW/g and an averaging volume of 1 g cube-shaped tissue mass, whereas [2] defines a limit of 2 mW/g and an averaging volume of 10 g of tissue mass of any shape. [4] and [5] require spatial averaging over 10 g of cube-shaped tissue mass. Because of the strong attenuation due to the skin effect at higher frequencies, the size and shape of the averaging volume is of great importance. For example, using an averaging cube of 10 g instead of 1 g tissue mass can reduce the spatial averaged SAR value by a factor of about two at higher frequencies. The defined SAR limits are not only volume averaged but also time averaged values. The time averaging introduces the relationship between absorbed power and induced heat. The various regulatory bodies employ differing time and volume averaging schemes for their guidelines and standards. Although all the standards/guidelines are based on the same scientific foundation, each regulatory body employs its own schemes, the choice of which has substantial implications on compliance requirements, which indicates that the various commissions follow differing scientific rationales and interpretations.

Assessment of the basic limits requires considerable technical resources and can in actual practise only be conducted in a laboratory environment. To enable on-the-spot compliance checks, exposure limits that are expressed in terms of incident field strengths have been defined. These can be measured using standard field probes. The rationale for employing these derived or secondary limits is that they are conservative: if the secondary limits have been met then it is certain that the basic limits cannot have been exceeded (worst case scenario). In the case of quasi far-field conditions (i.e., field impedance  $\approx 377$  Ohms), it is sufficient to evaluate either the electric, magnetic or poynting field strength to demonstrate compliance. However, in the near-field of transmitters compliance with basic limits can only be demonstrated by employing incident field strength measurements if both the electric and magnetic field strength limits have been met. Poynting field measurements are not of much use for characterizing the absorption in the near-field since there can be wide deviations from

	FCC [6]	CENELEC [4]	ARIB STD-T56 [5]
based on	NCRP <sup>1</sup> /ANSI <sup>2</sup>	ENV <sup>3</sup>	RCR STD-38 <sup>4</sup>
group	uncontrolled env.	general public	condition G
whole-body av. SAR	0.08 mW/g	0.08 mW/g	0.08 mW/g
spatial peak SAR	1.6 W/kg	2 W/kg	2 W/kg
averaging time	30 min.	6 min.	6 min.
averaging mass	1 g	10 g	10 g
volume shape	cube	cube	cube
phantom requir.	not defined	reasonable cross-section of users	several proposed phantoms
device position	standard	4 positions	normal

Table 2.1: Basic compliance test requirements proposed in the USA [6], Europe [4] and Japan [5]. <sup>1</sup>[7], <sup>2</sup>[3], <sup>3</sup>[8], <sup>4</sup>[9].

the field impedance of 377 Ohms, and each particular situation determines whether the dominant coupling mechanism is electric or magnetic.

In the very close proximity of transmitters, the values of field strengths often greatly exceed those of derived limits, so that compliance can only be demonstrated by directly assessing the basic limits. In many cases, the limits for whole-body average SAR are met in any case, since the average output power is less than 1 W and it is reasonable to assume that users weigh more than 12 kg. For the spatial peak SAR, such worst-case considerations can not be applied to cellular phones, whose typically greatest antenna input power is not more than a few mW, so that compliance can only be demonstrated by means of experimental or numerical evaluations.

In the last few years various organizations have begun developing standardized procedures for compliance testing of handheld RF transmitters. The current status of the most important documents is summarized in Table 2.1.

Some of the more progressive health agencies require that for a device to pass the compliance test it must be unlikely that any user will be exposed to levels exceeding the safety limits provided the device is properly used, i.e., in the way it was designed and marketed for. On the other hand, the test procedure should not be too restrictive and thereby unnecessarily inhibit the advancement of promising technologies. Although these criteria appear quite obvious and straightforward, their implementation is everything but trivial. The reason is due to the complexity of the task and the fact that most modern devices are within very small margins of the safety limits [10]. Near-field evaluations involve various procedures with a multitude of parameters to be considered and therefore require considerable engineering skills to keep the total uncertainty reasonably low. The various uncertainty components can be grouped into three main uncertainty classes:

- The assessment uncertainty (measurement uncertainty or simulation uncertainty): This is the uncertainty for assessment of the spatial peak SAR value in a given SAR distribution using a given setup (e.g., head phantom). The uncertainty must be determined in a manner that it is valid for all evaluations.
- The phantom uncertainty: This is the deviation of the technical setup (head phantom) with respect to definitions in the standard. Such definitions could be the description of a standard phantom or the requirement that a given minimum percentage of the total user group be covered. Assessing this uncertainty requires insights into the dependence of absorption on anatomical variations as well as the effect of accessories such as optical glasses and jewelry. The uncertainty due to the phantom needs only be assessed once, so that it is valid for all RF transmitters operating in the near-field.
- The source uncertainty: This is the uncertainty for the assessed spatial peak SAR of a particular phone or numerical representation thereof, taking into consideration the variations possible in the mass production of that model (output power, frequency response, modulation, amplifier, matching network, antenna, manufacturer's tolerances, etc.). The uncertainty of the position with respect to the phantom can also be considered to be part of the source uncertainty. The source uncertainty is especially crucial, since it involves the object under test and is therefore dependent upon it. The easiest way to handle this problem is by assessing the spatial peak SAR values of different samples from mass production and using appropriate statistics to assess the source uncertainty.

In addition to labor and investment overheads, the ability to perform dosimetric evaluations with a small degree of uncertainty will be the deciding criteria in the selection of a standardized evaluation technique for testing of RF transmitters for compliance with safety standards.

## 2.3 Methods for Dosimetric Evaluation

### 2.3.1 Numerical Methods

This section gives an overview of the numerical methods used for dosimetric evaluation of exposure from MTE, as well as a detailed review of the latest developments. For more complete information on early exposure assessment from non-ionizing radiation, the reader is referred to [11, 12, 13].

#### Analytically Based Methods

Early dosimetric data on whole-body and local specific absorption rates inside biological bodies was based on plane wave exposure of homogeneous or layered spheres and prolate spheroids, such as using the *Mie scattering* technique [14, 15, 16, 17]. Early dosimetric studies for near-field exposure of humans at frequencies below a few hundred MHz were performed using analytical expansion methods such as *long-wavelength analysis* [18, 19], the *Extended Boundary Condition Method* (EBCM) [20] [21] and the *Iterative Extended Boundary Condition Method* (IEBCM) [22, 23]. These techniques were not only limited to the lower frequency band, basic antenna structures and geometrically simple bodies such as prolate spheroids, but also with respect

to the maximum proximity of the source from the body, i.e., to the farer near-field. Subsequent interest in these techniques has long since declined due to their rigid limitations.

Recently, R. W. King has published analytical expressions for layered biological structures exposed to the near-field of dipoles [24]. Comparison of his results with data given in [25] shows good agreement. However, comparisons with data from other studies has been reported to be rather difficult, due to a lack of information, such as an incomplete description of the setup, feedpoint impedances, etc..

### Method of Moments (MoM)

The *Method of Moments* (MoM) was originally presented in a very general formulation for the solution of partial differential equations represented by a system of linear equations [26]. In electromagnetics the term MoM is commonly referred to those techniques where charge and current distributions described by an integral equation are discretized. This method allowed more realistic models of humans exposed to plane waves to be developed, initially based on the electric-field integral equation (EFIE). MoM was applied to arbitrarily shaped biological bodies in [27] and for a block model of a human in [28], leading to a dense matrix system.

Early dosimetric information for a biological body in the near-field of a source other than an aperture source was presented in [29] for a rectangularly shaped body close to a dipole antenna operating at 50 MHz. The solution obtained by a MoM approach expressed the sensitivity of absorbed power and antenna parameters, such as the feedpoint impedance on the antenna-body location. It was concluded that input power levels as small as 20 W for certain dipole locations may result in potentially hazardous fields. Comparison with measurements for a prolate spheroid close to a dipole antenna from 27-90 MHz using a Moment Method (MoM) was presented in [30].

Restrictions of this method when using delta functions as test functions with respect to a limited number of cells, constant field behavior within one cell, insufficient satisfaction of the boundary conditions between the cells and instabilities [31, 32] can be partially overcome by using a number of modifications and improvements [33, 34, 35]. A block model of a human exposed to a dipole antenna and simulated with MoM was presented in [36] but with major limitations.

A MoM implementation with some potential for exposure assessment and compliance testing is surface-discretization MoM, which allows the modeling of arbitrary dielectric and lossy domains. This technique has been successfully applied to antennas in the vicinity of lossy bodies in [37, 38, 39]. The restriction to largely homogeneous bodies does not constitute a disadvantage for compliance testing since homogeneous phantoms are accepted by regulatory bodies. Limitations with respect to modeling the various lossy dielectric materials of the phone may be a greater handicap when compared to other techniques.

### Generalized Multipole Technique (GMT)

During the eighties, several groups worked on methods similar to the Mie scattering method. These methods, unified under the name *Generalized Multipole Technique* (GMT) [40, 41], approximated the unknown field in homogeneous domains using sets of basic functions. The expansions, most commonly but not necessarily multipole



expansions, are matched on discrete points on the boundaries of the domains. The resulting overdetermined system of equations is solved in a least square sense. Information on the mismatching of the fields can be used with some restrictions to assess the worst-case uncertainty of the solution. However, GMT is limited to homogeneous linear domains which are not very complicated in shape [42, 43]. Although the thin wire approximation as well as line multipoles have been introduced, the modeling of complicated antenna structures is limited in practise [44, 45]. Nevertheless, GMT has proven to be a very efficient method for general studies investigating the dependence of the exposure on various parameters, due to its ability to assess the uncertainty of the solution; for example, the study on the absorption mechanism in the near-field of dipole antennas above 300 MHz in [25], antenna efficiency studies of different dipole configurations near lossy objects [46, 47], etc. The method is also routinely applied to achieve reference solutions [48, 49, 50, 51]. In addition, it has also been applied for compliance tests for devices which can be well represented by a simple dipole structure [52].

### Finite Element (FE) Method

The Finite-Element (FE) method was popularized in electromagnetics by Silvester and Ferrari [53]. Within FE the whole computational space is discretized, allocating the unknown field values originally in the nodes of the finite-element mesh. Linear or polynomial expansion functions are associated within each element. A variational method or a method of weighted residuals is used to obtain a system of equations with a sparse matrix. Original problems with spurious modes and open domains encouraged work related to hybrid schemes paired with boundary element methods and edge-element techniques [54]. Recently work has been done to adopt Berenger-style boundary conditions [55]. Early work on human tissue interaction with electromagnetic energy using the Finite Element method was reported in [56] for microwave absorption by a cranial structure and for hyperthermia treatment in [57, 58, 59]. The thermal response of a coarse block model of a human in the near-zone of a resonant thin-wire antenna from 45-200 MHz using MoM and Finite Element Method (FEM) was calculated in [60]. More recently, the technique has been applied to study absorption during MRI diagnostics [61].

Although FE allows the modeling of more arbitrarily shaped bodies, it has not been as extensively used for MTE related absorption studies as FDTD. This is due to the fact that its implementation is not as straightforward, and reliable automated discretizations of complex 3D structures such as human heads is still not possible. An absorption study related to MTE using a FE technique was recently reported for a box model of biological tissue close to a dipole antenna operating at 900 MHz in [62].

### Finite-Difference Time-Domain (FDTD) Technique

The *Finite-Difference Time-Domain* (FDTD) technique is currently the clearly leading technique for exposure assessments. It was initially introduced by Yee [63]. The whole computational space is discretized in voxels of homogeneous material. Originally proposed on a staggered cubical grid, the electric field components are allocated tangentially at the middle of the edges between adjacent nodes, the magnetic field components respectively on a dual grid. With initial field conditions, the elec-

Electromagnetic fields are calculated in the time-domain following an explicit leap-frog algorithm. Initial problems with open domain boundaries were the subject of extensive research in the eighties. A boundary condition, which has recently gained much popularity is Berenger's *Perfectly Matched Layer* (PML) [64], offering an increased dynamic range for numerical computations. The finite-integration (FI) technique in the time domain [65] is conceptually slightly different from FDTD, but leads to the same numerical scheme. Disadvantages of modeling restrictions related to rectilinear grids have been partly overcome by means of a variety of approaches such as *Contour-Path* modeling [66] and *Finite-Volume* formulations [67]. Today, standard features for complex modeling include graded grids [68], partially filled cells [69], subgridding [70] and importing CAD data [71].

In the context of dosimetric applications, FDTD was first applied to assess the absorption in a human eye exposed to an incident plane wave at 750 MHz and 1.5 GHz [72]. Later, FDTD was used for a variety of dosimetric problems, e.g., for human far-field exposure [73, 74], working place exposure [75] and hyperthermia research [76]. More recently it has been applied to mobile phone related issues in [77, 78, 79, 80, 81, 82, 83, 84, 85, 86, 49, 87, 88, 89, 90, 50, 91, 92, 93, 94, 71]. Many of these studies were based on human head models developed from clinical MRI data. Due to the possible straightforward implementation of the algorithm, simple modeling of complexly shaped structures and the availability of computational power, FDTD has become the first choice for MTE related exposure assessments. However, limitations are still seen, due to the rather difficult departure from the commonly used rectilinear grid and cell size limitations regarding very detailed structures of a handset which might be essential for reliable compliance testing. Some major advantages are the straightforward modeling within rectilinear grids and the robustness of the technique, enabling the implementation of easy-to-use tools.

## Hybrid Methods

Since each method has its particular strengths and limitations, it is tempting to combine different methods in hybrid approaches, in such a way as to combine the advantages of the individual methods. A very simple hybrid approach is an unidirectional or explicit scheme, whereby the solution of one method is taken as the excitation in a second method. Original limitations of FE techniques to deal with open space have been partially overcome by employing implicit hybrid techniques, coupling FE with boundary element methods [95]. However, improvements in boundary conditions for FE techniques have made many of those hybrid approaches obsolete.

A hybridization of the eigenfunction expansion method and MoM has been used in [96] to assess absorption in thin skin layers using a spherical head model at high frequencies (30 GHz). Minimization of exposure was achieved through use of directional antennas, since the human head is already in the far-field at these frequencies.

A combination of GMT and FE has been presented in [97] and was subsequently generalized into a combination of MoM, GMT and FE [98]. The applied iterative hybrid scheme has the advantage that the different codes do not have to be changed, i.e., generation of a complex combined matrix, which usually eliminates the advantages of a combination, can be avoided. A similar approach has been proposed by [99] combining MoM and GMT. It has been applied to a generic handset in the close vicinity of a lossy sphere. The handset was simulated by MoM and the sphere by GMT.

A problem inherent in hybrid approaches is the difficulty of achieving an implementation in which modeling of realistic setups is straightforward and robust and which does not require the user to have much knowledge of the hybrid coupling and the various techniques employed.

### 2.3.2 Experimental Methods

#### 2.3.3 Temperature Probes and Radiation Thermometry

A very straightforward and nevertheless elegant design of a *temperature probe* for measurements in RF electromagnetic environments was presented by Bowman [100] in the mid seventies. It is based on a high-resistance thermistor as sensor which is connected to four resistive leads (approx. 160 kOhms/cm) whereby the current is induced in two of these and the voltage monitored across the other two. This ensures that the probe becomes highly RF transparent but not completely insensitive to RF exposures and temperature changes in the leads. Nevertheless, precise temperature rise measurements can be conducted when the necessary precautions for a well designed setup are followed.

[101] suggested the use of a standard voltmeter module to drive the sensor and evaluate the signal. Lately, it has been shown that the sensitivity can be increased up to  $\pm 0.15$  mK/s (10 s evaluation time) by using specialized electrometer grade amplifiers and software for filtering [51].

During the eighties optical temperature sensors were developed and commercialized for applications such as temperature control in high voltage transformers, industrial microwave heating, hyperthermia, etc.. The optical effects employed were temperature dependent fluorescent decay of phosphorescent layers or interferometric microshift of cavity resonators. Since the sensors are driven and monitored by optical fibers, they provide a high degree of immunity to RF exposure. However, a lack of sensitivity makes these probes unsuitable for SAR evaluation in the range of the safety limits.

Thermistor probes were already used in the late seventies for exposure assessments of handheld communications devices inside human phantoms [102, 103]. However, the minimum measurement time per point and the need to reach thermal equilibrium prior to each measurement, usually involving several hundred measurement points, make thermistor probes unsuitable for standardized dosimetric evaluations. Currently, temperature probes are applied in dosimetry for temperature transfer calibrations of E-field probes as well as for specialized dosimetric tasks [51, 25, 104].

*Radiation thermometry*, which dates back to the early seventies, is a more time efficient method which assesses the temperature rise caused by the absorption of electromagnetic energy [105]. The technique can be easily applied without any interference and provides valuable information on the temperature distribution on surfaces. More recently, this method has also been employed to study human exposure from mobile phones using dry ceramic phantoms [106, 107] and dry phantoms composed of resin and graphite [108]. For utilization during standardized compliance testing the technique has severe limitations with respect to sensitivity and requirements for ambient control [109], especially since volume scans are practically impossible due to the restrictions to certain cross-sections.

### 2.3.4 Dosimetric Field Probes

Miniaturized, isotropic three-dimensional diode loaded E-field probes were first presented in [110]. Since then, they have been used for various dosimetric studies [111, 112]. The probes consist of three small orthogonally positioned dipoles, which are directly loaded with Schottky diodes. The theory of this approach has been described in detail in [113].

Originally, transmission lines of relatively low resistance ( $< 50 \text{ k}\Omega$ ) have been used for E-Field probes, resulting in secondary modes of reception which appear particularly at lower frequencies. More recently, improved performance over a broader frequency range (10 MHz-3 GHz) has been achieved by employing high-ohmic lines and distributed filters placed immediately behind the sensor [114]. Performance evaluations of several probe designs have revealed that probes with orthogonally positioned sensors have an isotropic response with spherical deviations of between  $\pm 0.6$  and  $\pm 3.5$  dB. These major deviations are caused by diffraction inside the dielectric material of the probe, whose permittivity differs greatly from that of the surrounding media. Significantly improved performance was achieved by adjusting the alignment of the sensor dipoles so that their receiving pattern becomes orthogonal to the incident field [115]. Probes whose deviation from spherical isotropy is better than  $\pm 0.3$  dB in tissue simulating material have been developed [116]. More recently, miniaturized E-field probes have been developed for special tasks such as the characterization of larger probes (e.g., boundary effects, spatial resolution, etc.), dosimetric measurements inside small structures (e.g., small animals, in vitro dishes, etc.) and special physical phenomena. One such single-sensor probe described in [117] has an outer tip diameter of only 1 mm. The orientation of the dipole sensor of 0.8 mm length inside the tip has been optimized to ensure isotropy (deviation  $< \pm 0.2$  dB) by rotating the probe around its axis and taking three sequential measurements in  $120^\circ$  steps. Precise and repeatable on-the-spot rotation ( $< \pm 0.1$  mm) can be realized by using a high precision robot in combination with a light beam probe alignment device. The probe provides about the same spatial resolution as temperature probes but with a significantly higher sensitivity ( $< 0.05 \text{ mW/g}$ ) and independence from actual temperature fluctuations.

Several groups are currently working on developing fiberoptical E-field sensors for various kinds of EMC applications. These sensors utilize electro-optical effects such as the Pockel's effect [118]. The advantages of this technique are the non-metallic construction, broad-band applicability and foremost the ability to measure in the time domain. However, the sensitivity and spatial dimensions of the suggested implementations do not meet current requirements for dosimetric evaluations.

The classic calibration technique for E-field probes in lossy media is transfer calibration using temperature probes [25, 104]. As an alternative, a waveguiding technique has also been suggested in [119]. A new approach also based on waveguides has recently been introduced providing better precision and improved traceability of the procedure to power measurements, as well as better robustness and efficiency [120]. The standard uncertainty of this technique was assessed to be better than  $\pm 3.5\%$  but requires several waveguide setups to cover the frequency range between 800 MHz - 2.5 GHz. Due to the increasing size of waveguides with larger wavelengths, at lower frequencies calibration is best performed with transfer calibration using temperature probes. Another proposed technique is based on computer simulation. This method requires a detailed model of the probe and provides poorer precision

than in experimental calibration techniques [104].

In addition to calibration techniques, procedures have also been developed to fully characterize the performance of probes in tissue simulating liquids. These include assessment of the uncertainties due to field disturbances, deviation from spherical isotropy, spatial resolution, boundary effects and secondary modes of reception [117].

### 2.3.5 Free-Space Field Probes

Free-space scans of the electric and magnetic near-field of RF transmitters provide important information about the quality of the RF design of antenna and device. For example, poor design of handheld wireless communication devices may result in significantly impaired radiation performance due to large increases of power loss inside the device and through absorption if operated in the closest vicinity of lossy structures. It is even possible that malfunctions might occur in certain near-field environments. Hence, free-space near-field evaluations can constitute a powerful design tool.

In special cases, magnetic and electric near-field scans can also be used to demonstrate compliance with safety limits, such as for indoor base stations or other indoor antennas.

For the above applications, near-field probes optimized for measurement in air have been developed [114]. In order to obtain a maximum of information, it is often advantageous to align the three sensors with a specific coordinate system with respect to the antenna. This is facilitated by the fact that one of the isotropic electric field probe's sensors is aligned along the probe axis with the other two normal to it. Equivalent to the optimization procedure employed in the design of the dosimetric probes described in [114], the spatial orientation of the sensors has been adjusted in order to compensate for the field distortion inside the probe caused by the core, substrate and protective shell. The spherical isotropy achieved hereby is better than  $\pm 0.4$  dB.

An isotropic near-field H-field probe optimized for the mobile frequency range has been described in [116]. This new probe consists of three orthogonally and concentrically arranged loops. The 3.8 mm loops with resistively loaded detectors were designed to achieve optimal sensitivity at the desired frequency range of 300 MHz to 2.5 GHz (deviation from isotropy:  $< 0.2$  dB). In free space, probes are usually calibrated in the far-field, e.g., [121]. Due to the small dimensions of these near-field probes and their RF transparency, calibration in waveguides has been proposed for the frequency range between 800 MHz - 2.5 GHz and TEM-cells for below 1 GHz [104], providing a precision of better than  $\pm 5\%$ .

### 2.3.6 Automated Near-Field and Dosimetric Scanners

The experimental assessment of the three-dimensional SAR distribution within a phantom easily involves several hundred measurement points. Especially at higher frequencies, the locations of these points with respect to the phantom must be known with the greatest precision in order to obtain repeatable measurements in the presence of rapid spatial attenuation and field variations. High precision is especially required to accurately evaluate the SAR close to the surface, since the physical dimensions and boundary effects prevent measurement directly at the surface, such that the values at the surface must be obtained by careful extrapolations with ap-

propriate functions. Due to the considerably large number of measurement points and extensive data processing required, it is obvious that the measurement process must be highly automated if such measurements must be performed routinely.

Several automated scanning systems based on E-field probes have been implemented. Systems developed in the 80s range from one-dimensional positioners [122] to three-axis scanners [123] and on to six-axis robots [124]. The first version of the latter goes back to the early 80s and has been continually improved and extended since then.

Systems explicitly designed for evaluation of handheld or body mounted transmitters are described in [114], [124] and [125].

The scanner described in [114] incorporates a high precision robot (working range greater than 0.9 m and a position repeatability of better than  $\pm 0.02$  mm), advanced dosimetric E-field probes (see previous sections), an optical proximity sensor for automated positioning of the probe with respect to the phantom surface (precision better than  $\pm 0.2$  mm) and sophisticated software for data processing and measurement control. The generic twin phantom (enables testing of left-hand, right-hand and body mounted devices without requiring a change of phantoms) was developed with the objective of covering the maximum exposure occurring in over 80% of the entire user population [125]. A test procedure based on a calibrated dipole has been integrated which enables verification of whether the system is operating within its specifications. This check also ensures that all laboratories working with the above system will assess the same SAR values within  $\pm 12\%$  ( $k=2$ ).

The analysis of the uncertainty budget performed in compliance with the NIS81 [126] and the NIST1297 [127] documents has shown that a precision for spatial peak SAR evaluation of better than  $\pm 12\%$  ( $k=1$ ) is achieved, which is excellent when compared to the common uncertainty of far-field measurements. The uncertainty for the 95% confidence level ( $k=2$ ) of  $< \pm 24\%$  is acceptable for compliance testing.

In addition to the spatial peak SAR limit, the same instrumentation also enables determination of the total energy absorbed in the user, which is another important measure for device performance.

Several other systems based on similar concepts have been developed at various universities [128, 129] or commercialized [130, 131].

## 2.4 Review of Basic Studies on Absorption in the Near-Field of MTE

### 2.4.1 Introduction

The availability of reliable instrumentation or simulation techniques for precise assessment of SAR distribution inside tissue simulating materials is an essential prerequisite for the implementation of compliance testing standards. However, in order to enable generalization of dosimetric evaluations conducted with a particular setup to the exposure occurring in a specific cross-section of the user population, extensive information about the dependence of the absorption mechanism on various parameters is necessary. This includes:

- the dominant absorption mechanisms, in order to derive the parameters that most affect absorption;

- the effects of anatomical variability, such as head shape, tissue distribution and tissue parameters, etc.;
- the effect of the hand;
- the effects of accessories such as the metallic frames of optical glasses, jewellery, medical implants, etc.;
- the effect of the variability of the position of the phone with respect to the head;
- the requirements for handset modeling, in case the instrumentation or procedure does not allow testing of the actual physical device.

Answers to these questions are particularly important so that a dosimetric evaluation performed using a particular setup (phantom, phone position, etc.) can be generalized with respect to the exposure of the entire user population. The latter is especially important in view of standardized compliance testing with safety limits. Significant insights into these topics have been gained during recent years, the publications of which are reviewed in this Section.

#### 2.4.2 General Absorption Mechanism in the Near-Field

The energy absorption mechanism in the close near-field of dipole antennas operating above 300 MHz was investigated in [25]. The dependence of the absorption on the frequency, electrical dipole length, distance between dipole and tissue, and shape of the lossy structures was investigated. The results revealed that the dominant interaction mechanism for all configurations is inductive coupling, i.e., surface/eddy currents induced by the incident magnetic field. The strong dominance of inductive coupling over capacitive coupling enabled the proposition of an approximation formula, the precision of which was assessed to be better than  $\pm 3$  dB independent of frequency, distance, tissue parameters, antenna length, etc. These findings were essentially confirmed by [24]. In [43], it was further shown that this approximation also results in very accurate results for helical antennas. In order to allow for estimations of the spatial peak SAR, the scope of the approximation was extended in [132].

The main conclusion of these findings is that the absorption as well as the spatial peak SAR values are proportional to the square of the magnitude of the current and not to the input power. This means that an antenna with a feedpoint impedance of 10 Ohms can potentially induce five times the absorption compared to a 50 Ohm antenna for the same radiated power. In addition, the study revealed that the 7 Watt exclusion clause of the ANSI standard [133] for low-power communication devices was in direct contradiction with the basic peak SAR limits.

#### 2.4.3 Tissue Parameters

The dielectric properties of tissue simulating materials at a specific frequency should accurately correspond with the dielectric properties of living tissues. Since the SAR is defined as the time rate of energy absorption per unit weight, only the macroscopic simulation of the tissue's permittivity  $\epsilon$ , permeability  $\mu$  and conductivity  $\rho$  are required. Generally, dielectric properties have been collected from animal tissues, for which large variations can be found in the open literature. This is due to the

difficulties encountered when handling living or freshly excised tissues during data collection and due to the natural variations of tissues. Data collected directly from human corpse has large uncertainties, since right after death the dielectric properties might change drastically, in particular changes in water content in brain tissues [134]. The most recent dielectric data from living tissue can be found in [135] and in [136] which, however, differ considerably in both permittivity and conductivity. An overview of dielectric data found by different researchers can be found in [137].

Since the absorbed energy depends strongly on the tissue parameters  $\epsilon$  and  $\rho$ , it is desirable to know them with highest accuracy. Unfortunately, little research has been conducted to perform a thorough uncertainty analysis for available dielectric data for human tissues. However, since the natural variability of these parameters within the MTE user group and in time might be considerably, the chosen dielectric parameters for a compliance procedure must be chosen in a worst-case approach rather than representing a specific person at a specific time.

#### 2.4.4 Modeling of the Human Head

Many different phantoms have been used in the past to assess RF transmitter related exposure, ranging from simply shaped bodies such as spheres, boxes and cylinders to more realistic complex phantoms including MRI and CT derived models with resolutions down to  $0.125 \text{ mm}^3$ .

Whereas early numerical assessments were largely limited to simply shaped bodies due to computational restrictions, i.e., spheres [138, 139], prolate spheroids [20, 21], multilayered slabs [140] or brick phantoms [29, 30], complex experimental phantoms were used from very early on. Anatomically shaped homogeneous phantoms filled with tissue simulating liquids or gels were used in [103, 112, 141] as well as dry ceramic phantoms [106, 107, 108, 142]. In addition, studies have been performed using multi-tissue phantoms [48, 122] and phantoms based on real human skulls packed with various types of tissue [102, 122]. A realistic phantom of the whole body of a man including simulated bone, brain, muscle and lungs was used in [143]. Most recently a 5-tissue head phantom consisting of skin, muscle, bone, eye and brain tissue has been constructed and made commercially available [144, 48].

The increasing availability of powerful computers with adequate processing and memory resources from the early 90s onwards has enabled the simulation of realistic MRI, CT, etc. based head phantoms using FDTD [145, 146, 147, 148, 149, 77, 150, 151, 152, 79, 153, 154, 155, 83, 82, 84, 156, 90, 86, 157, 158, 49, 87, 88, 85, 159, 160, 50, 92, 94, 71]. Today, resolutions of  $0.125 \text{ mm}^3$  for parts of the head are state-of-the-art on high-end workstations [161].

Only the availability of such phantoms which can be straightforwardly discretized for FDTD based on CT or MRI scans has made systematic parameter studies with respect to the internal anatomy possible. The authors of [85] compared non-homogeneous with homogeneous modeling, whereby the tissues were replaced by brain simulating tissues. The authors reported an overestimation of about 40% for the 1 g spatial peak SAR values. Other studies found a consistent but low overestimation for the spatial peak SAR values, e.g., the authors of [87] reported no significant change of the maximum SAR value in the brain for a variation in the conductivity of skin. For ordinary use of the MTE, the heterogeneity of the head was reported to have little effect on the maximum SAR values.

The absorption in several high-resolution phantoms derived from MRI data of



various persons was compared at 900 MHz for exactly the same exposure conditions including the source in [49]. The overestimation reported was 25% for the 1 g and 10% for the 10 g spatial peak values for a tissue composition with slightly higher dielectric parameters than the average values between white and gray brain tissues. A similar study was performed by the same authors at 1800 MHz [50]. The results were similar with an overestimation of about 20% for the 1 g and 5% for the 10 g spatial peak values using a tissue-simulating liquid whose conductivity ( $\epsilon_r = 41.0$ ,  $\sigma = 1.65$  mho/m) was considerably larger than that of brain-average equivalent tissue ( $\epsilon_r = 42.3$ ,  $\sigma = 1.2$  mho/m). The authors of these two studies concluded that the variability of the tissue structure could be best covered by replacing the non-homogeneous structure by a homogeneous phantom of appropriate shape and dielectric material. For very high frequencies the absorption in a spherical head model has been investigated by [96] in the Ka-band (e.g., 30 GHz), reporting high absorption in the skin layer due to the small penetration depth.

An early study investigating possible differences in absorption between children and adults by scaling the numerical model by 0.7 to the head size of a 1 year old infant found comparable or lower values for the smaller head model [79]. Another study on possible differences in absorption between children and adults was reported in [85] by scaling the phantom used in [84] to the size of children according to body size and weight. Significantly higher 1 g averaged SAR at 835 MHz and a greater penetration depth was found in the case of the children's heads. These findings could not be confirmed by [94] using head models of MRI data of 3 and 7 year old children as well as variously scaled heads. No significant increase in averaged SAR values or penetration depth was found when the dipole source was kept at the same distance from the head. The spatial SAR values for children were within the variations found between various adults, suggesting that the maximum exposure occurring in the user group including adults and children can be assessed by using a single phantom of appropriate shape and composition. An explanation for part of the differences found in [84] might be the closer proximity of the source for the scaled heads as compared to adult heads.

In [86] realistic head models derived from CT and MRI data were compared with canonically shaped bodies (boxes and spheres), based on which the author concluded that the box overestimates the exposure to a great extent, whereas the sphere could be used for a worst case SAR approximation. Weak dependence of the feedpoint impedance of a generic phone for spherical or realistic head modeling, but significant dependence for radiation characteristics was reported in [82]. Higher SAR values were found for the inhomogeneous head compared to the spherical head model.

The authors in [88] reported a significant effect of the modeling of the auricle on the maximum 1 g spatial SAR values assessed with FDTD using a  $15.6 \text{ mm}^3$  resolution and a non-pressed ear. In [161] a pressed ear as occurring in a real world MTE situation and based on MRI data was modeled with  $0.125 \text{ mm}^3$  resolution and simulated with FDTD. Although high local one-voxel SAR were found in the ear auricle, spatial averaged SAR values were not significantly higher compared to a homogeneous model without ear and an appropriate spacing between phone and head.

Although the head shape does not significantly alter absorption, it is nevertheless of great importance, since it defines the distance between the source of the magnetic field and the tissue for a given position of the RF transmitter with respect to the

head. The compliance testing requirement to cover the highest absorption occurring in real life can be satisfied if the distance between the phantom and phone parts in the test setup is not larger than the minimum distance occurring within the user group between the phone and the skin. In order to develop a phantom satisfying this requirement, data of the head shape in the ear region was measured for a total of 52 adult volunteers (male and female) from which a generic phantom head was derived [125]. It was constructed in such a way that the distance between the phone structure and phantom surface is always smaller than for 90% of the investigated people. The thickness of the compressed ear was also evaluated, resulting in an average thickness of about 6 mm and a 10%-percentile thickness of 4 mm. So far, no investigations on the thicknesses of the compressed ears of children have been conducted.

#### 2.4.5 Effect of the Hand

In [82] numerical research was focused on the effect of the head and hand on the performance parameters of monopole and PIFA antennas mounted on a simplified radio. It was reported that the antenna impedance in the case of the monopole was largely unaffected by both: the presence of the hand at the investigated distance, and the complexity of head modeling. However, radiation patterns were affected to a greater extent.

Authors in [87] reported that the varying hand positions scarcely affect maximum spatial SAR values as long as the hand does not shade the antenna. [86] and [79] reported that modeling a hand around the device results in lower spatial peak SAR values in the head compared to the same configuration without the hand at 900 MHz. At 1800 MHz the opposite result was found in [79].

In the case of a sleeved dipole antenna the maximum spatial SAR values were unaffected [90] at 900 MHz whereas decreased values in the range of 30% were found for a whip antenna at the same frequency.

The problem inherent in many of these numerical studies is that the hand was simulated using simple block models which can only poorly represent the complex anatomy of a real hand. Due to the difficulties of modeling a realistic hand grasping the phone in various positions, the effect of the hand was experimentally studied in [125] using a real hand. The studies were performed using commercially available cellular phones. The frequency bands investigated were 450, 900 and 1800 MHz. Each phone was grasped in three different ways. The highest spatial peak SAR values of these three ways of grasping the phone resulted in no or only a slight reduction of SAR values as compared to the values assessed in the absence of the hand. This suggests that the upper exposure range occurring under real-life conditions is best described by neglecting the effect of the hand.

#### 2.4.6 Metallic Accessories & Environmental Effects

The effects of metallic accessories, such as spectacle frames and jewellery, have been investigated in [48] and summarized in [125] based on worst-case scenarios. The authors concluded that it is unlikely that metallic accessories significantly increase absorption.

Possible enhancement in SAR due to medical implants was investigated in [162], simulating resonant wire and disc structures inside and outside a tissue-simulating spherical body. The excitation was a  $0.45\lambda$  dipole. Enhancement of up to a factor of

about 40 were found for the local peak SAR and a factor of 1.6 for the spatial peak SAR value averaged over 1 g. Similar results were reported in [48] for various tissue types in which enhancement factors of several hundred times were reported. Such discrepancies are not surprising since the local peak SAR strongly depends on the sharpness of the metallic structures.

The dependence of energy absorption due to use of a MTE in partially closed environments was investigated in [90]. The simulations were performed using a realistic head model derived from CT data (125 mm<sup>3</sup> voxel size) exposed to a generic phone either equipped with a sleeved dipole antenna or a whip antenna inductively loaded with a helical coil. Nearby metallic walls spread the SAR distribution and decreased the maximum spatial 1 g SAR value by more than 30% in certain configurations and increased the spatial peak SAR values by more than 110% in others. These results seem to contradict the absorption mechanism and warrant further investigation.

A large body of literature is available on RF interference of medical devices by mobile communications transmitters. For a summary on this subject the reader is referred to [163].

#### 2.4.7 Handset Position

Since the absorption mechanism suggests that the SAR is approximately proportional to the square of the incident magnetic field strengths at the skin surface of the user, the dominant parameter for the exposure is the current distribution on the phone and its position with respect to the head. The strong dependence on the current distribution and position was demonstrated experimentally by the spatial peak SAR values assessed for different phones and positions in [132, 10]. The effect of position can be larger than a factor of three. This strong dependence underlines the importance of the shape of the phantom as well as the need for test positions to be very precisely defined in order to achieve reproducible results between different laboratories. Some of the rather large differences of the spatial peak SAR values reported in the literature can be attributed to the different positions of the phone. For example, many of the FDTD analyses were performed with the phone oriented vertically or horizontally to the head [149, 151, 152, 79, 154, 155, 83, 156, 90, 86, 164] whereas most of the experimental assessments were measured in more natural operational positions. Lately, tilted head phantoms have been used so that the ear piece and microphone is positioned on an imaginary line between the ear and mouth but still 90° with respect to the line connecting both auditory channels [82, 84, 88, 87, 165]. Some studies have used more realistically tilted numerical head models [85, 159, 71] for absorption studies of MTE, although a touch position as defined in [4] has been difficult to realize.

#### 2.4.8 Handset Modeling

As important as a well defined position is the exact magnitude and distribution of the current on the phone. A study comparing numerical and experimental procedures [93] showed that for the same field magnitude but slightly different current distributions, the spatial peak SAR differed by more than 50% for some phone positions. The magnitude may differ by more than 30% from phone to phone [10] even though the output power at the adapter terminal remains within  $\pm 0.1$  dB. On the other hand, excellent agreement was found between simulation and measurement even though

different phantoms and positions were compared in [149, 166, 128]. Authors in [156] compared a real MTE to a generic phone of analogous shape finding a fair agreement in the results, concluding that more accurate modeling of the phone is needed for satisfactory validation. Subsequently improved detailed modeling of the phone resulted in the same range of differences between measurements and simulations as for the generic phone [167]. The exposure due to a CAD model of a handheld phone was numerically investigated using FDTD in [71].

For studies in which position and phone, e.g., a well defined generic phone, were precisely described, a generally good agreement between measurements and computations was found [168, 165, 169].

## 2.5 Review of Compliance Evaluations

### 2.5.1 Introduction

Dosimetric evaluations were not a requirement for handheld devices until a few years ago. An exclusion clause for low power devices introduced by ANSI in 1982 [133] and subsequently adopted by most international and national standards excluded any transmitter having an antenna input power of less than 7 Watts from test requirements by assuming that they intrinsically comply with the basic safety limits. Only a few studies on the exposure of handheld or body mounted devices were published before the early 90s. These included studies on dipole antennas in the proximity of geometrically simple tissue-simulating bodies [29, 60, 139, 170] and detailed experimental human phantoms [171, 172] as well as evaluations of commercially available handheld dispatch radios operated in front of the face or torso [103, 102, 112, 141, 30, 171, 172, 122, 52]. The results of these studies were controversial with respect to the validity of the exclusion clause. Clarification was brought about by the study on the absorption mechanism [25] whose results implied that the exclusionary clause strongly contradicted the basic limits. According to this study, antennas with an input power of 1 W at 1.5 GHz have the potential of inducing spatial peak SAR values of 5.7 mW/g (1g averaged) at a 25 mm distance when the feedpoint current is increased to 350 mA due to changes in the feedpoint impedance. Even much higher values can be predicted for closer proximity to the body. Consequently, the exclusion clause was dropped during revisions of the standards and authorities began to request compliance testing of handheld devices [132], in particular for cellular phones.

A considerable body of literature dealing with compliance testing of cellular phones with safety limits has been published during the last four years. In order to simplify comparison of the reviewed studies, the results are either normalized to the actual or nominal (for commercial devices) antenna input power of 1 W. This Section is divided into more basic evaluations using generic phones and evaluations performed for commercially available phones. Evaluations performed in the context of exploring novel antennas for handsets providing minimum energy loss in the user and improved radiation performance are reviewed in the following Section.

### 2.5.2 Generic Phones

In [77], the exposure of a dipole in the proximity of the face of a heterogeneous human head model based on MRI scans was numerically evaluated at 900/1900 MHz. It was

concluded that an exposure of less than 10 W/kg/W averaged over the eye is obtained at a distance greater than 6 mm from the dipole to the eye at 900 MHz and at least 17 mm at 1900 MHz.

A dipole next to a simply shaped head was numerically investigated in [80] at 835 MHz. It was concluded that the spatial peak SAR (1g averaged) for a cellular phone operating at 0.6 W when placed further away than 2 cm is below the 1.6 W/kg (i.e., 2.7 W/kg/W) given by the ANSI standard.

Studies [49, 50, 94] conducted with  $0.45\lambda$  dipoles (900 and 1800 MHz) at a distance of 15 mm next to various heterogeneous and homogeneous head phantoms (vertical position) have resulted in 2.6 - 4.7 W/kg (1g averaged) and 2.1 - 3.2 W/kg (10g averaged) for a feedpoint current of 100 mA. Assuming a feedpoint impedance of 50 Ohms, this is equivalent to 5.2 - 9.4 and 4.2 - 6.4 W/kg/W respectively. At 1800 MHz the corresponding values were 14.2 - 20.6 W/kg/W (1g averaged) and 9.0 - 10.6 W/kg/W (10g averaged).

The first detailed numerical study of a more realistic phone model (generic phone equipped with a monopole antenna) in the closest proximity of a detailed heterogeneous human head phantom was published by [79]. The head phantom was derived from a MRI data set and numerically represented with a voxel size of  $2 \times 2 \times 2 \text{ mm}^3$ . The horizontal and vertical positions at the ear (ear not compressed) were compared for the operation frequencies of 900 and 1800 MHz, as well as a position in front of the eye. The maximum exposure was achieved in the front position to be 4.7 W/kg/W (1g averaged) and 3.1 W/kg/W (10g averaged) at 900 MHz. At 1800 MHz the maximum exposure was 7.7 W/kg/W (1g averaged) and 4.6 W/kg/W (10g averaged), also in the front position but with a hand grasping the device.

The exposure of a homogeneous simply-shaped human model to a generic phone with monopole antenna operating at 144/450/900 MHz was numerically investigated in [38]. The maximum SAR for a distance of 5 cm antenna/head at 900 MHz was assessed to be 0.53 W/kg/W.

A generic phone equipped with a monopole and a half-wave dipole was evaluated using FDTD with a MRI based head phantom at 900 MHz in [173]. For a vertical phone position and a distance of 15 mm between antenna (top) and head, the spatial peak SAR values were 9.8 W/kg/W (1g averaged in skin) and 4.5 W/kg/W (10g averaged in skin) in the case of the monopole antenna and 4.1 (1g averaged) and 2.9 W/kg/W (10g averaged) for the dipole antenna.

Very similar results were also reported in [86] for a generic phone equipped with a monopole antenna (915 MHz) in the vertical position and 15 mm distance between the phone and head, i.e., the exposure ranging from 2.6 to 8.6 W/kg/W and 1.8 to 4.8 W/kg/W averaged over 1 g and 10 g respectively.

A generic phone equipped with a sleeved dipole or a whip antenna in a partially closed environment at 900 MHz was evaluated next to a heterogeneous head model in a vertical position in [90] using FDTD. The exposure was assessed to be nearly always below 1.6 W/kg averaged over 1 g of tissue and an output power of 0.6 W, except for the case with a whip antenna in a partially closed environment.

A generic handset with a monopole antenna operating at 900 and 1500 MHz in a vertical position was evaluated using FDTD for a heterogeneous head model in [87] and [88]. The 1 g peak SAR value for an antenna-head distance of 3.75 cm (phone touches ear) was assessed to be below 3.4 W/kg/W and 7.4 W/kg/W at 900 and 1500 MHz respectively.

The exposure of a generic handset equipped with  $\lambda/4$  and  $3/8\lambda$  antennas was evaluated with FDTD at 835 and 1900 MHz for a vertical and tilted standard positions in [85] and [159]. At 835 MHz the 1g-averaged spatial peak SAR value ranged from 2.7 W/kg/W - 4.9 W/kg/W and at 1900 MHz from 5.5 - 9.6 W/kg/W for an adult head and the most recent available set of human tissue parameters.

Only a few studies have been made for transmitters in the near-field above 2 GHz. In [84] a generic handset with different antennas operating at 6 GHz was evaluated with FDTD for a heterogeneous head model in a tilted standard position. Two of the antenna configurations were in compliance with the standard for a 0.6 W transmitter, resulting in 1 g averaged spatial peak SAR values between 0.8 and 1.7 W/kg/W. A third configuration was above the ANSI limit with 1 g averaged spatial peak values of 3.4 W/kg/W.

The exposure in the Ka-band at 30 GHz due to a nearby dipole (2 cm distance) was assessed for a layered sphere using a hybrid approach of the eigenfunction expansion method and MoM in [96]. For an undirected antenna configuration 1 g averaged spatial peak SAR values of 10 W/kg/W and for a directing configuration 0.1 W/kg/W were assessed.

### 2.5.3 Commercially Available Cellular Phones

The dosimetric evaluation of seven different commercially available NMT devices (Nordic Mobile Telephone Standard: 890-915 MHz, maximum power 1 W), conducted with an automated E-field scanner and a homogeneous shell phantom, was reported in [174]. The spatial peak SAR for the intended use position ranged between 0.2 - 2.8 W/kg/W (1g averaged) and 0.1 - 1.8 W/kg/W (10 g averaged).

[175] reported the results of an experimental evaluation of a mobile phone operating at 890 MHz. The assessed exposure levels for an intended use position were 3.5 W/kg/W (1g averaged) and 3.2 W/kg/W (10 g averaged).

The exposure of ten different MTE devices operating at 835 MHz (0.6 W) was evaluated using FDTD in a tilted standard position with a heterogeneous MRI based head phantom as well as experimentally in [149]. The spatial peak SAR values ranged from 0.3 - 1.2 W/kg/W (1g averaged).

FDTD and a MoM approach together with a generic shaped head phantom were applied in [81] to assess the absorption of an analog cellular phone operating at 450 MHz (0.75 W). The exposure for the *Pocky* antenna (15 mm distance antenna-head) was assessed to be below 0.3 and 0.5 W/kg/W averaged over 1 and 10 g respectively.

Authors in [176] tested a TACS phone and GSM phone at 900 MHz using numerical and experimental worst-case considerations. They concluded that the exposure limited by current standards was not exceeded.

Two mobile phones operating at 824-849 MHz, were experimentally evaluated using a homogeneous torso phantom and an automated near-field scanner in [124]. The maximum spatial 1 g peak SAR was reported to be in the range of 0.1-1.6 W/kg for the "classic" design with a sleeved dipole antenna and the so-called "flip" phone with a dual antenna system operating in various modes (FMCW 0.6 W, GSM 2 W peak, NADC 0.6 W).

Three different AMPS phones operating at 825-845 MHz (0.6 W) were tested with a heterogeneous human head model based on a plastic skull packed with jellies using

electric field probes in [177]. The maximum peak SAR was 1.4 W/kg/W in brain tissue and 0.35 W/kg/W in eye tissue.

The evaluation of six GSM phones with extended and retracted antennas (average power of 250 mW) was published in [178]. The phones were tested in two different positions with the near-field scanner described in [114]. In the standard position of [4] the spatial peak SAR values ranged between 0.6 - 4.0 W/kg/W (1 g averaged) and 0.4 - 2.8 W/kg/W (10 g averaged). In the worst-case position, the values ranged from 0.8 - 8.4 W/kg/W (1 g averaged) and 0.4 - 4.8 W/kg/W (10 g averaged).

The exposure from two GSM (900 MHz; 250 mW) and two DCS (1800 MHz; 0.125 mW) devices was reported in [125] using a homogeneous shell phantom designed to cover the maximum exposure in 80% of the MTE user group. At 900 MHz the exposure was below 4 W/kg/W (1g averaged), respectively 2.4 W/kg/W (10 g averaged). At 1800 MHz (125 mW) it was below 13.0 W/kg/W (1 g averaged) and 6.4 W/kg/W (10 g averaged) for all positions tested.

In [179] two handheld phones at 835 MHz and two at 1900 MHz were numerically investigated with FDTD and a MRI based head phantom. The maximum 1 g averaged peak SAR values were assessed to be 4.9 W/kg/W and 8.9 W/kg/W at 835 and 1900 MHz respectively for a vertical phone position.

The CAD data of actual MTE devices was used as the basis for the FDTD models in [71] and evaluated in a tilted position at a human head model based on MRI data. The spatial peak SAR value averaged over 1 g was assessed to be below 3.6 W/kg/W and 11.6 W/kg/W at 835 and 1900 MHz respectively.

Eighteen different european digital phones (250 mW) were measured with the dosimetric scanner as described in [125] and reported in [10]. Each phone was tested in up to 16 different configurations as specified by [4]. The maximum assessed exposure ranged from 1.1 - 6.2 W/kg/W averaged over 10 g.

## 2.6 Review of Antenna Studies for Optimized Radiation Performance with Reduced User Exposure

### 2.6.1 Introduction

Antennas for mobile communications equipment must not only be inexpensive to produce, small, and light; they must also provide high radiation efficiency in order to conserve battery energy and ensure communications under bad radiation conditions. In addition, the antennas must withstand the mechanical and environmental demands of daily usage (bending, dropping, etc.). Classical simple whip and helical antennas mounted on the top of handsets are therefore still the dominant antenna type for current cellular phones. However, their omnidirectional free-space pattern with cylindrical symmetry is degraded when operated in close proximity to the user's body due to absorption and reflections at the head. In general, the smaller the antenna and the closer to the head it is operated, the more directional its radiation pattern becomes and the greater the amount of energy lost through absorption by the user. Since the resulting far-field pattern is similar to that of directional radiators, more sophisticated antennas with minimum energy loss in the user's head could substantially increase radiation performance. An additional motivation for improved antennas is that the user's exposure could become a factor for a consumer's choice.

Therefore, several groups have begun investigating different antenna concepts

providing high radiation efficiency and low user exposure. In the following, the most recent studies, which explore antenna concepts for mobile phones aimed at optimizing radiation performance and minimizing user exposure are reviewed.

### 2.6.2 Basic Studies

Directional antenna configurations have been suggested and studied to minimize human exposure. In [180] arrays of small dipoles of different directivity in the proximity of a lossy sphere have been analytically investigated. The authors concluded that directional antennas substantially reduce the energy loss whereby the disadvantage of the enhanced front-to-back ratio is marginal.

A study aimed at deriving the basic design criteria for antenna structures with reduced energy loss in the user's tissue and improving radiation efficiency was conducted by [47]. This study was performed on the basis of dipole structures ( $\lambda/2$  dipole combined with a directive or reflective element). The results showed that certain directional half-wave dipole configurations result in lower absorption ( $>4$  dB), higher efficiency ( $>70\%$ ) and a feedpoint impedance less affected by varying distances from the head as compared to the standard dipole, whereas other directional configurations caused a contrary effect, i.e., degenerated radiation performance. A closer analysis revealed that the magnitude of the H-field strengths at the skin was reduced for those configurations providing improved efficiency and vice versa. The authors concluded that the primary design criterion to improve the radiation efficiency is not directivity, but the reduction of the maximum incident magnetic field strength in the exposed skin area of the user's head. This finding is also consistent with [25].

### 2.6.3 Wire Antenna Configurations

A flat inductance loaded open sleeve antenna has been presented by [181]. This antenna, which has been commercialized, results in a minimum of currents on the phone case and maximum current at the top of the antenna. Since the distance between the head and the upper part of the antenna is usually rather large for normal phone positions, this design would minimize absorption losses in the user. Wire and printed folded loop antennas for mobile phone applications were investigated in [182]. Their feedpoint impedances were reported to be less sensitive to the effect of a hand holding the device than when Planar Inverted F-Antenna (PIFA) elements are employed. A disadvantage is the high driving point impedance which poses a challenge for the matching network.

A normal mode helical antenna with a parasitically coupled monopole antenna and L-shaped parasitic elements for Inverted-F Antennas (IFA) was investigated for dual frequency applications in [183]. The increased bandwidth and the low profile meet the requirements for wireless applications. Combined helical and monopole configurations for dual frequency use at 900/1800 MHz were proposed in [184]. None of these studies provided data on the magnetic near-field or the energy loss when operated in the vicinity of the users.

The effects of human proximity on the circular polarization from a generic axial model helical antenna mounted on a phone case was investigated in [185], and significant sensitivity of the axial ratio was reported. However, the antenna and handset were rather decoupled from the nearby head, resulting in a stable feedpoint impedance. This effect was attributed to the greater distances and the dimensions



of the helical model.

The use of lossy ferrite shields on a rectangular phone model with a  $\lambda/4$  monopole antenna for lower absorption in a human head phantom was investigated with FDTD in [92]. Configurations with 13% lower 1 g SAR values were found, whereas gain and radiation patterns were minimally affected. Performance relevant for a real phone would however be the behavior of the feedpoint impedance due to the presence of a ferrite sheet.

#### 2.6.4 Planar Configurations

In order to meet requirements for compactness and minimal absorption by the user, a variety of planar antenna configurations, mostly mounted on the backside of the device, have been proposed.

In [186] a Full Short circuit Planar Inverted-F Antenna (FS-PIFA) was analyzed. In order to achieve low exposure of the operator and to achieve performance that is independent of the handling of the handset, the current must be concentrated near the antenna and suppressed on the handset. In order to prevent covering the antenna with the hand, adjustment of the design of the handset was proposed. In addition, a small antenna size, its location on the handset and the feeding location would contribute to make the performance less dependent on handling. Absorption measurements with a head phantom revealed spatial SAR values up to ten times less than ANSI standard requirements. Gain measurements for three different common user environments showed that the proposed antenna had approximately 2 dB less effective gain than a half-wave dipole. Gain degradation effects due to operator proximity have been experimentally investigated for various PIFA configurations in [187].

A Radiation Coupled Dual-L Antenna (RCDLA) was analyzed in [188] and compared to the above mentioned FS-PIFA configurations. It was stated that the RCDLA outperforms the FS-PIFA, since the currents were not only suppressed on the housing, but a concentration of currents at any point on the antenna was avoided as well. This leads to a more uniform overall current distribution. The performance of a RCDLA mounted on a box model of a phone was numerically assessed in [89] using a spherical human head model (diameter of 9 cm) and compared to that of a monopole antenna. Efficiency in the range of 80 % compared to 56 % in case of the monopole antenna was reported. However, the phone models were of completely different dimensions and located differently with respect to the head.

A variety of planar antennas varying in shape, loading, feeding and mounting characteristics were investigated in [189] and [190] and compared to monopole and loop antennas. Combinations of different antenna configurations were numerically investigated to realize diversity schemes. A Dual Inverted-L antenna and a Diode-Tunable PIFA were studied and compared to normal PIFA configurations in [191] providing enhanced bandwidth characteristics. A Dual-Frequency Planar Inverted-F Antenna was recently investigated in [192] for use at both 900 MHz and 1800 MHz with an acceptable bandwidth if the antenna is optimized together with the casing. No results on its performance near the head were provided. [193] presented the numerical comparison of the energy absorption between a planar backside mounted microstrip double patch antenna and a conventional monopole antenna at 1800 MHz.

Acceptable bandwidth and reduced resonance length was achieved for a PIFA configuration using capacitive loading in [194] and for dual frequency applications

in [195]. No data on the performance at the head were given. The performance of a Double-T slot antenna was investigated in [196] operated near a simplified head and hand model. Excellent efficiency of better than 90% was reported. However, the assessment has been made on a spherical head phantom, which generally underestimates the energy loss.

### 2.6.5 Other Configurations

Many new antenna types for mobile communications devices have been and are still being currently investigated as to whether they meet the above mentioned requirements. However, there are only a few basic antenna structures and most antenna types can be considered to be derivatives. Improvements have been attempted by modifying dipole, loop, slot, planar and printed antenna configurations.

The N-type antenna, similar to inverted-F antenna configurations [197] has been recently proposed for mobile communications systems in [198]. Sufficient bandwidth is ensured by a double resonant construction; a quarter-wave choke ensures low currents on the device. The spatial peak SAR and radiation efficiency as a function of the distance between a spherical and block model of tissue have been compared to those of a monopole antenna mounted on the same generic phone. The significantly improved performance was attributed to smaller near-fields at the side facing the operator and a larger distance between antenna and head. This also had a positive effect on the stability of the feedpoint impedance.

A novel design has been developed using an electromagnetically coupled microstrip antenna with a rotatable patch [199]. The objective was to reduce the polarization mismatching between the portable phone and base station caused by inclination of the device at the head. In a manner similar to the design proposed in [186] it has a low profile and can be integrated on the backside of the case. Although the low profile generally increases durability, the constant mechanical stresses of the antenna might increase the chance of breakage. The effects of human proximity were not investigated in the paper.

A new backfire fed, bifilar helix antenna type, a miniature dielectric-loaded antenna structure, was proposed in [200] and optimized to minimize the SAR in a human operator at 900/1800 MHz. The exposure for the antenna mounted on a generic phone was tested with the near-field measurement system described in [114]. Due to the concentration of currents on the upper end of the antenna, significant reduction of currents on the casing and cancellation of magnetic near-fields, the exposure resulted in low SAR values of approximately 0.96 mW/g/W for a 900 MHz GSM phone (250 mW) in the intended use position.

## 2.7 Conclusions and Outlook

Significant progress in the area of exposure assessments of MTE devices has been achieved during the last few years. In particular the precision and flexibility of experimental and numerical techniques have been greatly improved. These new techniques have been applied to investigate the effect of various parameters on absorption in the user's body. This information has enabled the establishment of a scientific basis for the development of setups for compliance testing. Several of these experimental setups have been made commercially available, so that dosimetric evaluations of

cellular phones have become routine. The availability of near-field scanners in combination with improved numerical tools enables the study of new antenna concepts for improved radiation efficiency and reduced user exposure.

The coming years will see further significant improvements in both experimental and numerical techniques. The greatest potential for improvements is seen to lie in the optimization of antennas, which must efficiently operate in complex environments. The future will also see the development of an area of research closely related to exposure assessment, namely, the study of electromagnetic interference and compatibility problems with wireless life support systems.

## References

- [1] Mark Fischetti, "The cellular phone scare", *IEEE Spectrum*, , no. 6, pp. 43–47, June 1993.
- [2] ICNIRP, *CLC/TC211: Human Exposure to Electromagnetic Fields*, Mar. 1998.
- [3] ANSI/IEEE, *C95. 1-1992, IEEE Standard for Safety Levels with Respect to Human Exposure to Radio Frequency Electromagnetic Fields, 3 kHz to 300 GHz*, New York, NY 10017, 1992.
- [4] CENELEC, *prES 59005, CLC/TC211 (SEC) 17, Considerations for evaluation of human exposure to Electromagnetic Fields (EMFs) from Mobile Telecommunication Equipment (MTE) in the frequency range 30 MHz - 6 GHz*, Brussels, Mar. 1998.
- [5] ARIB, *STD-T56, Specific Absorption Rate (SAR) Estimation for Cellular Phone*, Jan. 1998.
- [6] FCC, "Evaluating compliance with FCC guidelines for human exposure to radiofrequency electromagnetic fields", Tech. Rep. OET Bulletin 65, Federal Communications Commission, Washington, D.C. 20554, 1997.
- [7] NCRP, "Biological effects and exposure criteria for radiofrequency electromagnetic fields", Tech. Rep., National Council on Radiation Protection and Measurement , Report No. 86, 1986.
- [8] CENELEC CLC/TC111B, *European Prestandard (prENV 50166-2), Human Exposure to Electromagnetic Fields High-Frequency : 10 kHz - 300 GHz*, CENELEC, Brussels, Jan. 1995.
- [9] ARIB, *Radiofrequency Exposure Protection Standard*, Association of Radio Industries and Businesses, 1993.
- [10] Niels Kuster, "Radiation performance and evaluation of human exposure from mobile handsets using near-field measurements", in *International Symposium on Electromagnetic Compatibility*, Tokyo, Japan, May 1999.
- [11] Carl H. Durney, "Electromagnetic dosimetry for models of humans and animals: A review of theoretical and numerical techniques", *Proceedings of the IEEE*, vol. 68, no. 1, pp. 33–39, Jan. 1980.
- [12] Ronald J. Spiegel, "A review of numerical models for predicting the energy deposition and resultant thermal response of humans exposed to electromagnetic fields", *IEEE Transactions on Microwave Theory and Techniques*, vol. 32, no. 8, pp. 730–746, Aug. 1984.
- [13] C. H. Durney, H. Massoudi, and M. F. Iskander, *Radiofrequency Radiation Dosimetry Handbook, 4th edition*, USAFSAM-TR-85-73, 1986.
- [14] A. R. Shapiro, R. F. Lutomirski, and H. T. Yura, "Induced fields and heating within a cranial structures irradiated by an electromagnetic plane wave", *IEEE Transactions on Microwave Theory and Techniques*, vol. 19, no. 2, pp. 187–196, Feb. 1971.

- [15] H. N. Kritikos and H. P. Schwan, "Hot spots generated in conducting spheres by electromagnetic waves and biological implications", *IEEE Transactions on Bio-Medical Engineering*, vol. 19, no. 1, pp. 53–58, Jan. 1972.
- [16] H. N. Kritikos and H. P. Schwan, "The distribution of heating potential inside lossy spheres", *IEEE Transactions on Biomedical Engineering*, vol. 22, no. 6, pp. 457–463, Nov. 1975.
- [17] C. M. Weil, "Absorption characteristics of multilayered sphere models exposed to UHF/microwave radiation", *IEEE Transactions on Biomedical Engineering*, vol. 22, no. 6, pp. 468–476, Nov. 1975.
- [18] Carl H. Durney, Curtis C. Johnson, and Habib Massoudi, "Long-wavelength analysis of plane wave irradiation of a prolate spheroid model of man", *IEEE Transactions on Microwave Theory and Techniques*, vol. 23, no. 2, pp. 246–253, Feb. 1975.
- [19] Habib Massoudi, Carl H. Durney, and Curtis C. Johnson, "Long-wavelength electromagnetic power absorption in ellipsoidal models of man and animals", *IEEE Transactions on Microwave Theory and Techniques*, vol. 25, no. 1, pp. 47–52, Jan. 1977.
- [20] Magdy F. Iskander, Peter W. Barber, Carl H. Durney, and Habib Massoudi, "Irradiation of prolate spheroidal models of humans in the near-field of a short electric dipole", *IEEE Transactions on Microwave Theory and Techniques*, vol. 28, no. 7, pp. 801–807, July 1980.
- [21] Akhlesh Lakhtakia, Magdy F. Iskander, Carl H. Durney, and Habib Massoudi, "Near-field absorption in prolate spheroidal models of human exposed to a small loop antenna of arbitrary orientation", *IEEE Transactions on Microwave Theory and Techniques*, vol. 29, no. 6, pp. 588–594, June 1981.
- [22] Magdy F. Iskander, Akhlesh Lakhtakia, and Carl H. Durney, "A new procedure for improving the solution stability and extending the frequency range of the EBCM", *IEEE Transactions on Antennas and Propagation*, vol. 31, no. 2, pp. 317–324, Mar. 1983.
- [23] Magdy F. Iskander, Steven C. Olson, and J. F. Mc Calmont, "Near-field absorption characteristics of biological models in the resonance frequency range", *IEEE Transactions on Microwave Theory and Techniques, Short Papers*, vol. 35, no. 8, pp. 776–781, Aug. 1987.
- [24] R. W. P. King, "Electromagnetic field generated in model of human head by simplified telephone transceiver", *Radio Science*, vol. 30, no. 1, pp. 267–281, Jan. 1995.
- [25] N. Kuster and Q. Balzano, "Energy absorption mechanism by biological bodies in the near field of dipole antennas above 300 MHz", *IEEE Transactions on Vehicular Technology*, vol. 41, no. 1, pp. 17–23, Feb. 1992.
- [26] R. F. Harrington, *Field Computation by Moment Methods*, New York, Macmillan, 1968.

- [27] Donald E. Livesay and Kun-Mu Chen, "Electromagnetic fields induced inside arbitrarily shaped biological bodies", *IEEE Transactions on Microwave Theory and Techniques*, vol. 22, no. 12, pp. 1273–1280, Dec. 1974.
- [28] Mark J. Hagmann, Om P. Gandhi, and Carl H. Durney, "Numerical calculation of electromagnetic energy deposition for a realistic model of man", *IEEE Transactions on Microwave Theory and Techniques*, vol. 27, no. 9, pp. 804–809, Sept. 1979.
- [29] D. P. Nyquist, K. M. Chen, and B. S. Guru, "Coupling between small thin-wire antennas and a biological body", *IEEE Transactions on Antennas and Propagation*, vol. 25, no. 6, pp. 863–866, Nov. 1977.
- [30] K. Karimullah, K. M. Chen, and D. P. Nyquist, "Electromagnetic coupling between a thin-wire antenna and a neighboring biological body: Theory and experiment", *IEEE Transactions on Microwave Theory and Techniques*, vol. 28, no. 11, pp. 1218–1225, Nov. 1980.
- [31] Habib Massoudi, Carl H. Durney, and Magdy F. Iskander, "Limitations of the cubical block model of man in calculating SAR distributions", *IEEE Transactions on Microwave Theory and Techniques*, vol. 32, no. 8, pp. 746–752, Aug. 1984.
- [32] Mark J. Hagmann and Ronald L. Levin, "Accuracy of block models for evaluation of the deposition of energy by electromagnetic fields", *IEEE Transactions on Microwave Theory and Techniques*, vol. 34, no. 6, pp. 653–659, June 1986.
- [33] Chi-Taou Tsai, Habib Massoudi, Carl H. Durney, and Magdy F. Iskander, "A procedure for calculating fields inside arbitrarily shaped, inhomogeneous dielectric bodies using linear basis functions with the moment method", *IEEE Transactions on Microwave Theory and Techniques*, vol. 34, no. 11, pp. 1131–1139, Nov. 1986.
- [34] David T. Borup and Om P. Gandhi, "Fast-fourier-transform method for calculation of SAR distributions in finely discretized inhomogeneous models of biological bodies", *IEEE Transactions on Microwave Theory and Techniques*, vol. 32, no. 4, pp. 355–359, Apr. 1984.
- [35] Tapan K. Sarkar, Ercument Arvas, and Sadasiva M. Rao, "Application of FFT and the conjugate gradient method for the solution of electromagnetic radiation from electrically large and small conducting bodies", *IEEE Transactions on Antennas and Propagation*, vol. 34, no. 5, pp. 635–640, May 1986.
- [36] Maria A. Stuchly, Ronald J. Spiegel, Stanislaw S. Stuchly, and Andrzej Kraszewski, "Exposure of man in the near-field of a resonant dipole: Comparison between theory and measurements", *IEEE Transactions on Microwave Theory and Techniques*, vol. 34, no. 1, pp. 26–31, Jan. 1986.
- [37] H. D. Brüns, H. Singer, and T. Mader, "Field distributions of a hand-held transmitter due to the influence of the human body", in *International Symposium on EMC*, Zürich, 1993.

- [38] H. Singer, H. D. Brüns, and T. Mader, "Berechnung der Feldeinkopplung eines Handsprechfunkgeräts in den menschlichen Körper", *Kleinheubacher Berichte*, vol. 37, pp. 599–608, 1994.
- [39] H. O. Ruoss, U. Jakobus, and F. M. Landstorfer, "Efficient EM analysis of hand-held mobile telephones close to human head using modified method of moments", *Electronics Letters*, vol. 31, no. 12, pp. 947–948, June 1995.
- [40] A. Ludwig, "A new technique for numerical electromagnetics", *IEEE AP-S Newsletter*, vol. 31, pp. 40–41, 1989.
- [41] Christian Hafner, *The Generalized Multipole Technique for Computational Electromagnetics*, Artech House, 1990.
- [42] N. Kuster and R. Ballisti, "MMP-method simulation of antennae with scattering objects in the closer nearfield", *IEEE Transactions on Magnetism*, vol. 25, no. 4, pp. 2881–2883, Apr. 1989.
- [43] N. Kuster, "Multiple multipole method for simulating EM problems involving biological bodies", *IEEE Transactions on Biomedical Engineering*, vol. 40, no. 7, pp. 611–620, July 1993.
- [44] Roger Yew Tay and Niels Kuster, "Performance of the generalized multipole technique (GMT/MMP) for antenna design and optimization", *Applied Computational Electromagnetics (ACES) journal*, vol. 9, no. 3, pp. 79–89, Dec. 1994.
- [45] Roger Tay and Niels Kuster, "Modeling of thick wire antennas using curved line multipole expansions", in *Proceedings of the International Conference on Electromagnetics in Advanced Applications (ICEAA 95)*, 1995.
- [46] Roger Yew-Siow Tay, Quirino Balzano, and Niels Kuster, "Optimization of dipole antenna for effective radiation efficiency in the presence of a spherical head phantom", *Transactions on Antennas and Propagation*, vol. 20, no. 5, pp. 1–12, 1997.
- [47] Roger Yew-Siow Tay, Quirino Balzano, and Niels Kuster, "Dipole configurations with strongly improved radiation efficiency for hand-held transceivers", *IEEE Transactions on Antennas and Propagation*, vol. 46, no. 6, pp. 798–806, 1998.
- [48] Klaus Meier, *Scientific Bases for Dosimetric Assessments in Compliance Tests*, PhD thesis, Diss. ETH Nr. 11722, Zurich, 1996.
- [49] Volker Hombach, Klaus Meier, Michael Burkhardt, Eberhard Kühn, and Niels Kuster, "The dependence of EM energy absorption upon human head modeling at 900 MHz", *IEEE Transactions on Microwave Theory and Techniques*, vol. 44, no. 10, pp. 1855–1863, Oct. 1996.
- [50] K. Meier, V. Hombach, R. Kästle, R. Y-S. Tay, and N. Kuster, "The dependence of electromagnetic energy absorption upon human-head modeling at 1800 MHz", *IEEE Transactions on Microwave Theory and Techniques*, vol. 45, no. 11, pp. 2058–2062, Nov. 1997.

- [51] M. Burkhardt, K. Pokovic, M. Gnos, T. Schmid, and N. Kuster, "Numerical and experimental dosimetry of petri dish exposure setups", *Bioelectromagnetics*, vol. 17, pp. 483–493, 1996.
- [52] Niels Kuster, "Multiple multipole method applied to an exposure safety study", in *ACES Special Issue on Bioelectromagnetic Computations*, A.H.J. Fleming and K.H. Joyner, Eds., vol. 7, pp. 43–60. Applied Computational Electromagnetics Society, No. 2, 1992.
- [53] Peter P. Silvester and Ronald F. Ferrari, *Finite Elements for Electrical Engineers*, Cambridge University Press, Cambridge UK, 1983.
- [54] A. Bossavit, "A rationale for edge elements in 3-D fields computations", *IEEE Transactions on Magnetics*, vol. 24, pp. 74–79, 1988.
- [55] U. Pekel and R. Mittra, "A finite-element-method frequency domain application of the perfectly matched layer (PML) concept", *Microwave and Optical Technology Letters*, vol. 9, pp. 117–122, June 1995.
- [56] Michael A. Morgan, "Finite element calculation of microwave absorption by the cranial structure", *IEEE Transactions on Biomedical Engineering*, vol. 28, no. 10, pp. 687–695, Oct. 1981.
- [57] R. B. Roemer, T. C. Cetas, J. R. Oleson, S. Halac, and A. Y. Matloubieh, "Comparative evaluation of hyperthermia heating modalities", *Radiation Research*, vol. 100, pp. 450–472, 1984.
- [58] J. W. Strohbehn and R. B. Roemer, "A survey of computer simulations of hyperthermia treatments", *IEEE Transactions on Biomedical Engineering*, vol. 31, pp. 136–149, 1984.
- [59] Daniel R. Lynch, Keith D. Paulsen, and John W. Strohbehn, "Finite element solution of Maxwell's equations for hyperthermia treatment planning", *Journal of Computational Physics*, vol. 58, pp. 246–269, 1985.
- [60] R. J. Spiegel, "The thermal response of a human in the near-zone of a resonant thin-wire antenna", *IEEE Transactions on Microwave Theory and Techniques*, vol. 30, no. 2, pp. 177–185, Feb. 1982.
- [61] Dina Šimunić, Paul Wach, Werner Renhart, and Rudolf Stollberger, "Spatial distribution of high-frequency electromagnetic energy in human head during MRI: Numerical results and measurements", *IEEE Transactions on Biomedical Engineering*, vol. 43, no. 1, pp. 88–94, Jan. 1996.
- [62] W. Renhart, W. Rucker, and O. Biro, "Calculation of antenna near field reactions on low conducting materials using the finite element method", *IEEE Transactions on Magnetics*, vol. 32, no. 3, pp. 862–865, May 1996.
- [63] Kane S. Yee, "Numerical solution of initial boundary value problems involving Maxwell's equations in isotropic media", *IEEE Transactions on Antennas and Propagation*, vol. 14, no. 3, pp. 302–307, May 1966.
- [64] J. Berenger, "A perfectly matched layer for the absorption of electromagnetic waves", *Journal of Computational Physics*, vol. 114, pp. 185–200, 1994.



- [65] T. Weiland, "Maxwell's grid equations", *Frequenz*, vol. 44, no. 1, pp. 9–16, 1990.
- [66] Thomas Jurgens, Allen Taflove, Korada Umashankar, and Thomas G. Moore, "Finite-difference time-domain modeling of curved surfaces", *IEEE Transactions on Antennas and Propagation*, vol. 40, no. 4, pp. 357–365, Apr. 1992.
- [67] Vijaya Shankar and Alireza H. Mohammadian, "A time-domain, finite-volume treatment for the Maxwell equations", *Electromagnetics*, vol. 10, pp. 127–145, 1990.
- [68] Z. M. Liu, A. S. Mohan, and T. A. Aubrey, "EM scattering using nonuniform mesh FDTD, PML and Mur's ABC", *Electromagnetics*, vol. 16, no. 4, pp. 341–358, July 1996.
- [69] Thomas Weiland, "Verlustbehaftete Wellenleiter mit beliebiger Randkontur und Materialbelegung", *Electronics and Communication*, vol. 33, no. 4, pp. 170–174, 1979.
- [70] S. S. Zivanovic, K. S. Yee, and K. K. Mei, "A subgridding method for the time-domain finite-difference method to solve Maxwell's equations", *IEEE Transactions on Microwave Theory and Techniques*, vol. 39, no. 3, pp. 471–479, Mar. 1991.
- [71] A. D. Tinniswood, C. M. Furse, and O. P. Gandhi, "Computations of SAR distributions for two anatomically based models of the human head using CAD files of commercial telephones and the parallelized FDTD code", *Transactions on Antennas Propagation*, vol. 46, no. 6, pp. 829–833, 1998.
- [72] Allen Taflove and Morris E. Brodwin, "Computation of the electromagnetic fields and induced temperatures within a model of the microwave-irradiated human eye", *IEEE Transactions on Microwave Theory and Techniques*, vol. 23, no. 11, pp. 888–896, Nov. 1975.
- [73] R. J. Spiegel, M. B. E. Fatmi, and K. S. Kunz, "Application of a finite-difference technique to the human radiofrequency dosimetry problem", *Journal on Microwave Power*, vol. 20, pp. 241–254, 1985.
- [74] Dennis M. Sullivan, OM P. Gandhi, and Allen Taflove, "Use of the finite-difference time-domain method for calculating EM absorption in man models", *IEEE Transactions on Biomedical Engineering*, vol. 35, no. 3, pp. 179–186, Mar. 1988.
- [75] Jin-Yuan Chen and Om P. Gandhi, "Electromagnetic deposition in an anatomically based model of man for leakage fields of a parallel-plate dielectric heater", *IEEE Transactions on Microwave Theory and Techniques*, vol. 37, no. 1, pp. 174–180, Jan. 1989.
- [76] Dennis Sullivan, "Three-dimensional computer simulation in deep regional hyperthermia using the finite-difference time-domain method", *IEEE Transactions on Microwave Theory and Techniques*, vol. 38, no. 2, pp. 204–211, Feb. 1990.

- [77] P. J. Dimbylow, "FDTD calculations of the SAR for a dipole closely coupled to the head at 900 MHz and 1.9 GHz", *Physics in Medicine and Biology*, vol. 38, pp. 361–368, 1993.
- [78] Jorn Toftgard, Sten N. Hornsleth, and Jorgen Bach Andersen, "Effects on portable antennas of the presence of a person", *IEEE Transactions on Antennas and Propagation*, vol. 41, no. 6, pp. 739–746, June 1993.
- [79] P. J. Dimbylow and S. M. Mann, "SAR calculations in an anatomically realistic model of the head for mobile communication transceivers at 900 MHz and 1.8 GHz", *Physics in Medicine and Biology*, vol. 39, pp. 1537–1553, 1994.
- [80] Hsing-Yi Chen and Hou-Hwa Wang, "Current and SAR induced in a human head model by the electromagnetic fields irradiated from a cellular phone", *IEEE Transactions on Microwave Theory and Techniques*, vol. 42, no. 12, pp. 2249–2254, Dec. 1994.
- [81] V. Hombach, H. Thielen, and W. Feiss, "Einfluss der Antennenform eines Handfunkgeraetes auf das Antennendiagramm und die Exposition des Nutzers", *ITG Fachberichte*, vol. 124, pp. 315–320, 1994.
- [82] Michael A. Jensen and Yahya Rahmat-Samii, "EM interaction of handset antennas and a human in personal communications", in *Proceedings of the IEEE*, 1995, vol. 83, pp. 7–17.
- [83] L. Martens, J. De Moerloose, and D. De Zutter, "Calculation of the electromagnetic fields induced in the head of an operator of a cordless telephone", *Radio Science*, vol. 30, no. 1, pp. 283–290, Feb. 1995.
- [84] Om P. Gandhi and Jin Yuan Chen, "Electromagnetic absorption in the human head from experimental 6-GHz handheld transceivers", *IEEE Transactions on Electromagnetic Compatibility*, vol. 37, pp. 547–558, 1995.
- [85] Om P. Gandhi, Gianluca Lazzi, and Cynthia M. Furse, "Electromagnetic absorption in the human head and neck for mobile telephones at 835 and 1900 MHz", *IEEE Transactions on Microwave Theory and Techniques*, vol. 44, no. 10, pp. 1884–1897, Oct. 1996.
- [86] Michal Okoniewski and Maria A. Stuchly, "A study of the handset antennas and human body interaction", *IEEE Transactions on Microwave Theory and Techniques*, vol. 44, no. 10, pp. 1855–1863, Oct. 1996.
- [87] Soichi Watanabe, Masao Taki, Toshio Nojima, and Osamu Fujiwara, "Characteristics of the SAR distributions in a head exposed to electromagnetic fields radiated by hand-held portable radio", *IEEE Transactions on Microwave Theory and Techniques*, vol. 44, no. 10, pp. 1874–1883, Oct. 1996.
- [88] Masao Taki, Soichi Watanabe, and Toshio Nojima, "FDTD analysis of electromagnetic interaction between portable telephone and human head", *IEEE Transactions on Electronics*, vol. 79, no. 10, pp. 1300–1307, Oct. 1996.
- [89] I. Shtrikman and H. Fruechting, "Comparative numerical study of antennas for hand held mobile telephones", *Frequenz*, vol. 50, no. 1, pp. 35–40, 1996.

- [90] Paolo Bernardi, Marta Cavagnaro, and Stefano Pisa, "Evaluation of the SAR distribution in the human head for cellular phones used in a partially closed environment", *IEEE Transactions on Electromagnetic Compatibility*, vol. 38, no. 3, pp. 357–366, Aug. 1996.
- [91] Yew Siow Tay, *Contributions Towards the Optimization of Hand-Held Mobile Telecommunication Equipment by Computational Electromagnetics*, PhD thesis, Diss. ETH Nr. 12311, Zurich, 1997.
- [92] Jianqing Wang and Osamu Fujiwara, "Reduction of electromagnetic absorption in the human head for portable telephones by a ferrite sheet attachment", *IEICE Transactions on Communications*, vol. 80, no. 12, pp. 1810–1815, Dec. 1997.
- [93] Achim Bahr, Sheng Gen Pan, Thomas Beck, Ralf Kästle, Thomas Schmid, and Niels Kuster, "Comparison between numerical and experimental near-field evaluation of a DCS1800 mobile telephone", *Radio Science*, vol. 33, no. 6, pp. 1553–1563, Nov. 1998.
- [94] F. Schoenborn, M. Burkhardt, and N. Kuster, "Differences in energy absorption between heads of adults and children in the near field of sources", *Health Physics*, 1998.
- [95] C. R. I. Emson, "Methods for the solution of open-boundary electromagnetic-field problems", *IEE Proceedings, Reviews*, vol. 135, no. 3, Mar. 1988.
- [96] K. W. Kim and Y. Rahmat-Samii, "Handset antennas and humans at Ka-band: The importance of directional antennas", *Transactions on Antennas Propagation*, vol. 46, no. 6, pp. 949–950, 1998.
- [97] Lars H. Bomholt, "Coupling of the generalized multipole technique and the Finite Element method", *ACES*, vol. 9, no. 3, pp. 63–68, 1994.
- [98] L. Bomholt, "Coupling of the generalized multipole technique with the finite element method", in *ANTEM '94, Symposium on Antenna Technology and Applied Electromagnetics*, Ottawa, Canada, Aug. 1994.
- [99] H. O. Ruoss, U. Jakobus, and F. M. Landsdorfer, "Iterative coupling of MoM and MMP for the analysis of metallic structures radiating in the presence of dielectric bodies", *Applied Computational Electromagnetics Society*, 1998.
- [100] R.R. Bowman, "A probe for measuring temperature in radio-frequency-heated material", *IEEE Transactions on Microwave Theory and Techniques*, vol. 24, no. 1, pp. 43–45, Jan. 1976.
- [101] R. G. Olsen and R. R. Bowman, "Simple nonperturbing temperature probe for microwave/radio frequency dosimetry", *Bioelectromagnetics*, vol. 10, pp. 209–213, 1989.
- [102] Q. Balzano, O. Garay, and F. R. Steel, "Energy deposition in simulated human operators of 800-MHz portable transmitters", *IEEE Transactions on Vehicular Technology*, vol. 27, no. 2, pp. 174–181, Nov. 1978.

- [103] Q. Balzano, O. Garay, and F. R. Steel, "Heating of biological tissue in the induction field of VHF portable radio transmitters", *IEEE Transactions on Vehicular Technology*, vol. 27, no. 2, pp. 51–56, May 1978.
- [104] K. Meier, M. Burkhardt, T. Schmid, and N. Kuster, "Broadband calibration of E-field probes in lossy media", *IEEE Transactions on Microwave Theory and Techniques*, vol. 44, no. 10, pp. 1954–1962, Oct. 1996.
- [105] A. W. Guy, "Analyse of electromagnetic fields induced in biological tissues by thermographic studies on equivalent phantom models", *IEEE Transactions on Microwave Theory and Techniques*, vol. 19, no. 2, pp. 205–215, Feb. 1971.
- [106] T. Kobayashi, T. Nojima, K. Yamada, and S. Uebayashi, "Dry phantom composed of ceramics and its application to SAR estimation", *IEEE Transactions on Microwave Theory and Techniques*, vol. 41, no. 1, pp. 136–140, 41 1993.
- [107] T. Nojima, S. Nishiki, and T. Kobayashi, "An experimental SAR estimation of human head exposure to UHF near fields using dry-phantom models and a thermograph", *IEICE Transactions on Communications*, vol. 77, no. 6, pp. 708–713, June 1994.
- [108] A. Antolini and A. Leoni, "Thermographic method for the determination of SAR caused by cellular phones", *CSELT*, vol. 25, no. 1, pp. 131–137, Feb. 1997.
- [109] T. C. Cetas, "Practical thermometry with a thermographic camera – calibration, and emittance measurements", *Rev. Sci. Instrum.*, vol. 49, no. 2, pp. 245–254, 1978.
- [110] H. I. Bassen, M. Swicord, and J. Abita, "A miniature broad-band electric field probe", *Annals New York Academy of Science*, vol. 20, no. 5, pp. 481–493, 1975.
- [111] G. H. Wong, S. S. Stuchly, A. Kraszewski, and M. A. Stuchly, "Probing electromagnetic fields in lossy spheres and cylinders", *IEEE Transactions on Microwave Theory and Techniques*, vol. 32, no. 8, pp. 824–828, Aug. 1984.
- [112] Indira Chatterjee, Yong-Gong Gu, and Om P. Gandhi, "Quantification of electromagnetic absorption in humans from body-mounted communication transceivers", *Transactions on Vehicular Technology*, vol. 34, no. 2, pp. 55–63, May 1985.
- [113] H. I. Bassen and G. S. Smith, "Electric field probes - a review", *IEEE Transactions on Microwave Theory and Techniques*, vol. 31, no. 5, pp. 710–718, May 1983.
- [114] T. Schmid, O. Egger, and N. Kuster, "Automated E-field scanning system for dosimetric assessments", *IEEE Transactions on Microwave Theory and Techniques*, vol. 44, no. 1, pp. 105–113, Jan. 1996.
- [115] K. Pokovic, T. Schmid, and N. Kuster, "E-field probe with improved isotropy in brain simulating liquids", in *ELMAR'96*, Zadar Croatia, June 1996, pp. 172–175.

- [116] Katja Pokovic, Thomas Schmid, Oliver Egger, and Niels Kuster, "High precision near-field scanner for analysis of handheld transmitters", in *USNC/URSI National Radio Science Meeting*, Atlanta, USA, June 1997, p. 196.
- [117] Thomas Schmid, Katja Poković, and Niels Kuster, "Novel E-field probe optimized for in vivo applications", in *4th EBEA Congress*, Zagreb, Croatia, Nov. 1998, pp. 71–72.
- [118] M. Schwerdt, J. Berger, B. Schueppert, and K. Petermann, "Integrated optical E-field sensors with a balanced detection scheme", *IEEE Transactions on Electromagnetic Compatibility*, vol. 39, no. 4, pp. 386–390, Nov. 1997.
- [119] D. Hill, "Waveguide technique for the calibration of miniature implantable electric-field probes for use in microwave-bioeffects studies", *IEEE Transactions on Microwave Theory and Techniques*, vol. 30, pp. 92–99, 1982.
- [120] Katja Poković, Thomas Schmid, and Niels Kuster, "Robust setup for precise calibration of E-field probes in tissue simulating liquids at mobile communications frequencies", in *ICECOM'97*, Dubrovnik, Croatia, October 15–17, 1997, pp. 120–124.
- [121] N. S. Nahman, M. Kanda, E. B. Larsen, and M. L. Crawford, "Methodology for standard electromagnetic field measurements", *IEEE Transactions on Instrumentation and Measurement*, vol. 34, no. 4, pp. 490–503, Dec. 1985.
- [122] Robert F. Cleveland, Jr., and T. Whit Athey, "Specific absorption rate (SAR) in models of the human head exposed to hand-held UHF portable radios", *Bioelectromagnetics*, vol. 10, pp. 173–186, 1989.
- [123] S. S. Stuchly, M. Barski, and B. Tam, "Computer-based scanning system for electromagnetic scanning", *Review on Scientific Instrumentation*, vol. 54, no. 11, pp. 1547–1550, 1983.
- [124] Quirino Balzano, Oscar Garay, and Thomas J. Manning, "Electromagnetic energy exposure of simulated users of portable cellular telephones", *IEEE Transactions on Vehicular Technology*, vol. 44, no. 3, pp. 390–403, Aug. 1995.
- [125] N. Kuster, R. Kästle, and T. Schmid, "Dosimetric evaluation of handheld mobile communications equipment with known precision", *IEICE Transactions on Communications*, vol. 80, no. 5, pp. 645–652, May 1997.
- [126] NIS81 NAMAS, "The treatment of uncertainty in EMC measurement", *Tech. Rep.*, NAMAS Executive, 1994.
- [127] Barry N. Taylor and Christ E. Kuyatt, "Guidelines for evaluating and expressing the uncertainty of NIST measurement results", *Tech. Rep.*, 1994.
- [128] Q. Yu, M. Aronsson, D. Wu, and O. P. Gandhi, "Automated SAR measurements for compliance testing of cellular telephones", in *IEEE Antennas and Propagation Symposium*, Atlanta, USA, June 1997, pp. 1980–1983.
- [129] K. Haelvoet, S. Criel, F. Dobbelaere, and L. Martens, "Near-field scanner for the accurate characterization of electromagnetic fields in the close vicinity

- of electronic devices and systems", *IEEE Instrumentation and Measurement Technology Conference*, pp. 1119–1123, June 1996.
- [130] IDX, "Near field measurement systems", Tech. Rep., IDX Systems Inc., 20 NE Granger Ave Bldg. B. , Coryallis OR 97330, USA, 1996.
  - [131] Ilsan, "3D near field scanner", Tech. Rep., Ilsan America Inc., 1997.
  - [132] N. Kuster, Q. Balzano, and J. C. Lin, *Mobile Communications Safety*, Chapman & Hall, London, 1997.
  - [133] ANSI/IEEE, *C95. 1-1982, American National Standard Safety Levels with Respect to Human Exposure to Radio Frequency Electromagnetic Fields, 300 kHz to 100 GHz*, New York, NY 10017, 1982.
  - [134] R. Porter, W. R. Adey, and R. T. Kado, "Measurement of electrical impedance in the human brain", *Neurology*, vol. 14, no. 11, pp. 1002–1012, Nov. 1964.
  - [135] S. Gabriel, R. W. Lau, and C. Gabriel, "The dielectric properties of biological tissues: II. measurements in the frequency range 10 hz to 20 GHz", *Phys. Med. Biol.*, vol. 41, pp. 2251–2269, 1996.
  - [136] C. C. Davis, G. A. Katona, L. S. Taylor, and E. C. Elson, "Dielectric measurement of tissues in the mammalian head at cellular telephone frequencies", in *Eighteenth Annual Meeting of the Bioelectromagnetics Society*, Victoria, Canada, June 1996, pp. 46–47.
  - [137] C. Gabriel, S. Gabriel, and E. Corthout, "The dielectric properties of biological tissues: I. literature survey", *Phys. Med. Biol.*, vol. 41, pp. 2231–2249, 1996.
  - [138] A. Hizal and Y. K. Baykal, "Heat potential distribution in an inhomogeneous spherical model of a cranial structure exposed to microwaves due to loop or dipole antennas", *IEEE Transactions on Microwave Theory and Techniques*, vol. 26, no. 8, pp. 607–558, Aug. 1978.
  - [139] Y. Amemiya and S. Uebayashi, "Distribution of absorbed power inside a sphere simulating the human head in the near field of a  $\lambda/2$  dipole antenna", *Electronics and Communications in Japan*, vol. 66, no. 9, pp. 64–72, Sept. 1983.
  - [140] I. Chatterjee, M. J. Hagmann, and O. P. Gandhi, "Electromagnetic absorption in a multilayered slab model of tissue under near-field exposure conditions", *Bioelectromagnetics*, vol. 1, pp. 379–388, 1980.
  - [141] Arthur W. Guy and Chung-Kwang Chou, "Specific absorption rates of energy in man models exposed to cellular UHF mobile-antenna fields", *IEEE Transactions on Microwave Theory and Techniques*, vol. 34, no. 6, pp. 671–680, June 1986.
  - [142] H. Tamura, Y. Ishikawa, T. Kobayashi, and T. Nojima, "A dry phantom material composed of ceramic and graphite powder", *IEEE Transactions on Electromagnetic Compatibility*, vol. 39, no. 2, pp. 132–137, May 1997.

- [143] Maria A. Stuchly, Andrzej Kraszewski, Stanislaw S. Stuchly, George W. Harts-grove, and Ronald J. Spiegel, "RF energy deposition in a heterogeneous model of man: Near-field exposures", *IEEE Transactions on Biomedical Engineering*, vol. 34, no. 12, pp. 944-949, Dec. 1987.
- [144] Camelia Gabriel, "Phantom models for antenna design and exposure assess-ment", in *IEE Colloquium on Design of Mobile Antennas for Optimal Perfor-mance in the Presence of Biological Tissue*, Jan. 1997.
- [145] Ronald J. Spiegel, M. B. A. Fatmi, Stanislaw S. Stuchly, and Maria A. Stuchly, "Comparison of finite-difference time-domain SAR calculations with measure-ments in a heterogenous model of man", *IEEE Transactions on Biomedical Engineering*, vol. 36, no. 8, pp. 849-855, Aug. 1989.
- [146] P. J. Dimbylow and O. P. Gandhi, "Finite-difference time-domain calculations of SAR in a realistic heterogeneous model of the head for plane-wave exposure from 600 MHz to 3 GHz", *Physics in Medicine and Biology*, vol. 36, no. 8, pp. 1075-1089, 1991.
- [147] Akira Kato and Osamu Fujiwara, "Specific absorption rate deposited in realis-tic three-dimensional model of human-head for microwave exposure", *Technical Report of IEICE, EMCJ92-48, MW92-88*, , no. 10, pp. 45-49, 1992.
- [148] Akira Kato and Osamu Fujiwara, "Numerical determination of local specific absorption rate in realistic three-dimensional model of human-head for mi-crowave exposure", *Technical Report of IEICE, EMCJ92-67*, , no. 12, pp. 1-5, 1992.
- [149] O. P. Gandhi, J. Y. Chen, and D. Wu, "Electromagnetic absorption in the head and neck for cellular telephones at 835 MHz", in *Cost 244: Biomedical Effects of Electromagnetic Fields*, Dina Simunic, Ed., 1993, pp. 14-22.
- [150] Osamu Fujiwara and Michihiko Nomura, "Correlation between spatial dis-tributions of surface-SAR and magnetic near-field in realistic head model for microwave exposure", *IEICE Transactions on Communications*, vol. 76, no. 7, pp. 765-767, July 1993.
- [151] Luc Martens, "Electromagnetic field calculations for wireless telephones", *The Radio Science Bulletin*, pp. 9-11, Dec. 1994.
- [152] M. Dohlus, S. Gutschling, P. Thoma, and T. Weiland, "Berechnung elektro-magnetischer Felder in komplexen Modellen des menschlichen Koerpers", *Klein Heubacher Berichte*, pp. 609-618, 1994.
- [153] O. Fujiwara and A. Kato, "Computation of SAR inside eyeball for 1. 5-GHz mirowave exposure using finite-difference time-domain technique", *IEICE Transactions on Communications*, vol. 77, no. 6, pp. 732-737, June 1994.
- [154] Yahya Rahmat-Samii and Michael A. Jensen, "FDTD investigation of the antenna-tissue interaction for cellular and satellite systems", in *11th Annual Review of Progress in Applied Computational Electromagnetics*, Monterey, CA USA, 1995, pp. 732-739.

- [155] P. J. Dimbylow, "Dosimetry in a voxel model of the head", in *11th Annual Review of Progress in Applied Computational Electromagnetics*, Monterey, CA USA, 1995, pp. 240–244.
- [156] P. Bielli, A. Leoni, P. Massaglia, A. Schiavoni, S. Dionisi, F. Grimaldi, and P. Parente, "Numerical and experimental characterization of the electromagnetic field radiated by a hand-held telephone", *CSELT, Technical Reports*, vol. 23, no. 4, pp. 499–506, Aug. 1995.
- [157] O. P. Gandhi and J. Y. Chen, "Millimeter-resolution dosimetry for EM fields from mobile telephones and power lines", in *Biological Effects of Magnetic and Electromagnetic Fields*. 1996, pp. 765–767, Plenum Press.
- [158] Yilong Lu, Jianling Ying, Tat-Kee Tan, and K. Arichandran, "Electromagnetic and thermal simulations of 3-D human head model under RF radiation by using the FDTD and FD approaches", *IEEE Transactions on Magnetism*, vol. 32, no. 3, pp. 1653–1656, May 1996.
- [159] Gianluca Lazzi and Om P. Gandhi, "Realistically tilted and truncated anatomically based models of the human head for dosimetry of mobile telephones", *IEEE Transactions on Electromagnetic Compatibility*, vol. 39, no. 1, pp. 55–61, Feb. 1997.
- [160] P. J. Dimbylow, "FDTD calculations of the whole-body averaged SAR in an anatomically realistic voxel model of the human body from 1 MHz to 1 GHz", *Physics in Medicine and Biology*, vol. 42, pp. 479–490, 1997.
- [161] Michael Burkhardt and Niels Kuster, "Appropriate modeling of the ear for compliance testing of handheld MTE with safety limits", in *Twentieth Annual Meeting of the Bioelectromagnetics Society*, St. Pete Beach, Florida, USA, June 1998, p. 79.
- [162] J. Cooper and V. Hombach, "Increase in specific absorption rate in human heads arising from implantations", *Electronics Letters*, vol. 32, no. 24, pp. 2217–2219, 1996.
- [163] H. Bassen, "RF interference (RFI) of medical devices by mobile communications transmitters", in *N. Kuster and Q. Balzano and J. C. Lin, Mobile Communications Safety*. 1997, pp. 65–94, Chapman & Hall, London.
- [164] K. Sato, K. Nishikawa, N. Suzuki, and A. Ogawa, "Design of portable telephone antenna", *Technical Report of IEICE*, vol. 84, no. 2, pp. 19–24, Feb. 1996, in Japanese.
- [165] M. Siegbahn, S. Mazur, and C. Törnevik, "Comparisons of measurements and FDTD calculations of mobile phone electromagnetic far-fields and near-fields", in *IEEE Antennas and Propagation Symposium*, Montreal, Canada, July 1997, pp. 978–981.
- [166] Gianluca Lazzi and Om P. Gandhi, "Comparison of calculated and measured near-fields, radiation patterns, and SAR distributions for model of the human head for some typical cellular telephone antennas", in *IEEE Antennas and Propagation Symposium*, Montreal, Canada, July 1997, p. 659.



- [167] A. Schiavoni, G. Richiardi, and P. Bielli, "SAR calculation and measurement into a human head phantom generated by cellular phones", in *Eighteenth Annual Meeting of the Bioelectromagnetics Society*, Victoria, Canada, June 1996, p. 111.
- [168] S. Mazur, D. Martensson, and C. Toernevik, "Comparisons of measurements and FDTD calculations of electromagnetic near-fields and SAR distributions", in *Eighteenth Annual Meeting of the Bioelectromagnetics Society*, Victoria, Canada, June 1996, p. 123.
- [169] M. Burkhardt, N. Chavannes, K. Pokovic, T. Schmid, and N. Kuster, "Study on the FDTD performance for transmitters in complex environments", in *ICECOM'97*, Dubrovnik, Croatia, Oct. 1997, pp. 83–86.
- [170] O. Fujiwara, H. Higashihama, and T. Azakami, "Calculation of face-SAR due to portable transmitter", in *International Wroclaw Symposium, June 26-29th*, Wroclaw, 1990, pp. 169–172.
- [171] S. S. Stuchly, A. Kraszewski, M. A. Stuchly, G. Hartsgrrove, and D. Adamski, "Energy deposition in a model of man in the near field", *Bioelectromagnetics*, vol. 6, pp. 115–129, 1985.
- [172] Stanislaw Stuchly, Maria A. Stuchly, Andrzej Kraszewski, and George Hartsgrrove, "Energy deposition in a model of man: Frequency effects", *IEEE Transactions on Biomedical Engineering*, vol. 33, no. 7, pp. 702–711, July 1986.
- [173] J. Wiart and R. Mittra, "Power deposited in biological tissues from a hand-held mobile antenna", in *IEEE Antennas and Propagation Symposium*, July 1996, pp. 1104–1107.
- [174] Niels Kuster, Thomas Schmid, and Klaus Meier, "Untersuchungen der Absorption im extremen Nahfeld von Sendern", in *VDE-Fachbericht 45: Biologische Wirkungen elektromagnetischer Felder*, pp. 135–143. Verband Deutscher Elektrotechniker (VDE), Nov. 1993.
- [175] G. A. Lovisolo, L. Raganella, S. Nocentini, F. Bardati, A. Gerardino, and P. Tognolatti, "Hand-held portable telephones: Electromagnetic radiation absorption studies", in *Biomedical Effects of Electromagnetic Fields, COST244*, 1993.
- [176] Von Heinrich Garn, Harald Kremser, Roland Kremser, and Georg Neubauer, "Beurteilung der Strahlungsexposition bei D-Netz-Hand-Mobilfunktelefonen", *Frequenz*, vol. 48, no. 7, pp. 153–162, July 1994.
- [177] V. Anderson and K. H. Joyner, "Specific absorption rate levels measured in a phantom head exposed to radio frequency transmissions from analog hand-held phones", *Bioelectromagnetics*, vol. 16, pp. 60–69, 1995.
- [178] Klaus Meier and Niels Kuster, "Dosimetric measurements on various GSM-mobile telephones", in *Proc. of the 17th Annual Meeting of the Bioelectromagnetics Society*, Boston, USA, June 18–22, 1995, p. 30.

- [179] C. M. Furse, Gianluca Lazzi, and O. P. Gandhi, "FDTD computation of power deposition in the head for cellular telephones", *Antennas and Propagation Symposium 1996*, pp. 1794–1797, 1996.
- [180] K. Noguchi, M. Ando, N. H. Goto, M. N. Hirose, T. Uno, and Y. T. Kaminmura, "Directional antennas for portable telephones", *IEICE Transactions on Communications*, vol. 79, no. 9, pp. 1234–1241, Sept. 1996.
- [181] K. Tsunekawa, "High performance portable telephone antenna employing a flat-type open sleeve", *IEICE Transactions on Electronics*, vol. 79, no. 5, pp. 693–698, May 1996.
- [182] Konstantinos D. Katsibas, Constantine A. Balanis, Panayiotis A. Tirkas, and Craig R. Birtcher, "Folded loop antenna for mobile hand-held units", *IEEE Transactions on Antennas and Propagation*, vol. 46, no. 2, pp. 260–266, 1998.
- [183] H. Nakano, N Ikeda, Y. Wu, R. Suzuki, H. Mimaki, and J. Yamauchi, "Realization of dual-frequency and wide-band VSWR performances using normal-mode helical and inverted-F antennas", *IEEE Transactions on Antennas and Propagation*, vol. 46, no. 6, pp. 788–793, 1998.
- [184] P. Erätuuli, P. Haapala, and P. Vainikainen, "Dual frequency wire antennas", *Electronics Letters*, vol. 32, no. 12, pp. 1051–1052, June 1996.
- [185] J. S. Colburn and Y. Rahmat-Samii, "Human proximity effects on circular polarized handset antennas in personal satellite communications", *IEEE Transactions on Antennas and Propagation*, vol. 46, no. 6, pp. 813–820, June 1998.
- [186] Gert Frølund Pedersen and Jørgen Bach Andersen, "Integrated antennas for hand-held telephones with low absorption", in *IEEE 44th Vehicular Technology Conference Proceedings*, June 1994, vol. 3, pp. 1537–1541.
- [187] Tokio Taga and Kouichi Tsunekawa, "Performance analysis of a built-in planar inverted F antenna for 800 MHz band portable radio units", *IEEE Journal on Selected Areas in Communications*, vol. 5, no. 5, pp. 921–929, June 1987.
- [188] Josef Fuhl, Paul Nowak, and Ernst Bonek, "Improved internal antenna for hand-held terminals", *Electronics Letters*, vol. 30, no. 22, pp. 1816–1818, Oct. 1994.
- [189] Y. Rahmat-Samii and M. A. Jensen, "Characterization of antennas for personal wireless communications applications", *International Journal of Wireless Information Networks*, vol. 1, no. 3, pp. 165–176, 1994.
- [190] M. A. Jensen and Y. Rahmat-Samii, "Performance analysis of antennas for hand-held transceivers using FDTD", *IEEE Transactions on Antennas and Propagation*, vol. 42, no. 8, pp. 1106–1113, Aug. 1994.
- [191] K. L. Virga and Y. Rahamat-Samii, "Low-profile enhanced-bandwidth PIFA antennas for wireless communications packaging", *IEEE Transactions on Microwaves Theory and Techniques*, vol. 45, no. 10, pp. 1879–1888, Oct. 1997.

- [192] Z. D. Liu, P. S. Hall, and D. Wake, "Dual-frequency planar inverted-F antenna", *IEEE Transactions on Antennas and Propagation*, vol. 45, no. 10, pp. 1451–1457, Oct. 1997.
- [193] Richard Dlouhy, "Analysis of hand-held phones using the finite integration algorithm", *Radioengineering*, vol. 5, no. 4, pp. 10–14, Dec. 1996.
- [194] C. R. Rowell and R. D. Murch, "A capacitively loaded PIFA for compact mobile telephone handsets", *IEEE Transactions on Antennas and Propagation*, vol. 45, no. 5, pp. 837–842, May 1997.
- [195] Corbett R. Rowell and R. D. Murch, "A compact PIFA suitable for dual-frequency 900/1800-MHz operation", *IEEE Transactions on Antennas and Propagation*, vol. 46, no. 4, pp. 596–598, 1998.
- [196] H. O. Ruoss and F. M. Landstorfer, "Slot antenna for hand held mobile telephones showing significantly reduced interaction with the human body", *Electronics Letters*, vol. 32, no. 6, pp. 513–514, Mar. 1996.
- [197] K. Fujimoto and J. R. James, *Mobile Antenna Systems Handbook*, Artech House, Boston-London, 1994.
- [198] S. G. Pan, T. Becks, A. Bahrwas, and I. Wolff, "N antennas and their applications in portable handsets", *IEEE Transactions on Antennas and Propagation*, vol. 45, no. 10, pp. 1475–1483, Oct. 1997.
- [199] A. Ando, Y. Honma, and K. Kagoshima, "A novel electromagnetically coupled microstrip antenna with a rotatable patch for personal handy-phone system units", *IEEE Transactions on Antennas and Propagation*, vol. 46, no. 6, pp. 794–797, 1998.
- [200] O. Leisten, Y. Vardaxoglou, T. Schmid, B. Rosenberger, E. Agboraw, N. Kuster, and G. Nicolaidis, "Miniature dielectric-loaded personal telephone antennas with low user exposure", *Electronics Letters*, vol. 34, no. 17, pp. 1628–1629, 1998.

## Part II

# Uncertainty Analysis and Error Minimization in FDTD Simulations

Seite Leer /  
Blank leaf

## Chapter 3

# Finite-Difference Time-Domain (FDTD) Technique

*Abstract* - The basics of the Finite-Difference Time-Domain (FDTD) technique are outlined. The appropriate references are given whenever possible and when extensive formulations are not essential.

### 3.1 Introduction

As outlined in Part I, FDTD is currently the clearly dominant technique for near-field scattering problems in complex environments. Although it was originally proposed by Yee [1] in 1966, it only gained significant popularity in the late seventies. Initial problems with open domain boundaries were the subject of extensive research in the seventies and eighties. The simple, explicit formulation, the possible straight forward implementation of the governing equations and the recently available computational power and memory resources have enabled the success story of FDTD. Today a variety of text books on the technique and its applications have been published [2], [3], [4] and commercial codes based on FDTD have been made available [5], [6], [7], [8], [9].

### 3.2 The Finite-Difference Time-Domain Formulation

The conventional Finite-Difference Time-Domain method is a direct solution of the time dependent Maxwell's curl equations. The electric and magnetic field components are allocated in space on a staggered grid of a cartesian coordinate system (Fig. 3.1) and are solved alternatively in time in a leap frog manner (Fig. 3.2). The transient fields can be calculated when the initial field, boundary and source conditions are known.

Yee originally discretized Maxwell's curl equations using 2nd order both in space and time on a homogeneous grid, resulting in second order accuracy. The first partial space and the time derivative lead to

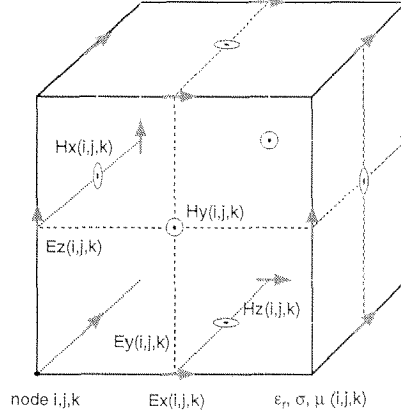


Figure 3.1: Allocation of the field components in the Yee scheme in space. Each node  $i, j, k$  of the lattice refers to one volume element (voxel), three electric and three magnetic field components.

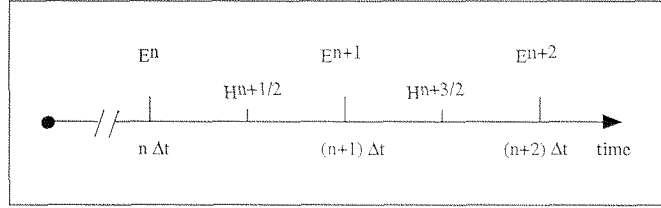


Figure 3.2: Allocation of the field components in time in the leap-frog scheme. E- and H-field components are separated by half a time step.

$$\frac{\partial F(i, j, k, n)}{\partial x} = \frac{F^n(i + 1/2, j, k) - F^n(i - 1/2, j, k)}{\Delta x} + O[(\Delta x)^2] \quad (3.1)$$

$$\frac{\partial F(i, j, k, n)}{\partial t} = \frac{F^{n+1/2}(i, j, k) - F^{n-1/2}(i, j, k)}{\Delta t} + O[(\Delta t)^2] \quad (3.2)$$

where  $F^n$  represents the electric ( $E$ ) or magnetic ( $H$ ) field at time  $n\Delta t$ ;  $i, j, k$  are indices in the spatial lattice and  $O[(\Delta x)^2]$ ,  $O[(\Delta t)^2]$  are the error terms.

Applying central differences to Maxwell's curl equation

$$\frac{\partial \vec{E}}{\partial t} = \frac{1}{\epsilon} \nabla \times \vec{H} - \frac{\sigma}{\epsilon} \vec{E} \quad (3.3)$$

for the proposed allocation of the fields in space and time, we obtain for example for the electric field component  $E_x$ :

$$\frac{E_x|_{i,j,k}^{n+1} - E_x|_{i,j,k}^n}{\Delta t} = \frac{1}{\epsilon_{i,j,k}} \left( \frac{H_z|_{i,j+1/2,k}^{n+1/2} - H_z|_{i,j-1/2,k}^{n+1/2}}{\Delta y} - \frac{H_y|_{i,j,k+1/2}^{n+1/2} - H_y|_{i,j,k-1/2}^{n+1/2}}{\Delta z} - \sigma_{i,j,k} E_x|_{i,j,k}^{n+1/2} \right) \quad (3.4)$$

If we assume the semi-implicit approximation:

$$E_x|_{i,j,k}^{n+1/2} = \frac{E_x|_{i,j,k}^{n+1} + E_x|_{i,j,k}^n}{2} \quad (3.5)$$

equation 3.4 can be reduced to the unknown  $E_x^{n+1}$  of the new timestep:

$$E_x|_{i,j,k}^{n+1} = \left( \frac{1 - \frac{\Delta t \sigma_{i,j,k}}{2\epsilon_{i,j,k}}}{1 + \frac{\Delta t \sigma_{i,j,k}}{2\epsilon_{i,j,k}}} \right) E_x|_{i,j,k}^n + \left( \frac{\frac{\Delta t}{\epsilon_{i,j,k}}}{1 + \frac{\Delta t \sigma_{i,j,k}}{2\epsilon_{i,j,k}}} \right) \left( \frac{H_z|_{i,j+1/2,k}^{n+1/2} - H_z|_{i,j-1/2,k}^{n+1/2}}{\Delta y} - \frac{H_y|_{i,j,k+1/2}^{n+1/2} - H_y|_{i,j,k-1/2}^{n+1/2}}{\Delta z} \right) \quad (3.6)$$

$$(3.7)$$

Following this procedure, Maxwell's curl equations can be discretized and reformulated to explicit expressions for all six field components [3].

For the proposed central differences the numerical solution approaches the continuous one with the square of the discretization step. If the mesh is non-uniform, thus the general rectilinear case, the local truncation error is first order, since in this case equations 3.1 and 3.2 are not centered finite difference equations. However, it has been shown in [10], that the method is still globally 2nd order convergent.

The Finite-Integration (FI) formulation [11] is based on the discretization of Ampere's and Faraday's law, thus Maxwell's equations in integral form. In the time domain it leads to the same numerical scheme, with the same stability and dispersion properties, as the FDTD scheme [3], [12].

### 3.3 Gridding and Material Treatment

Most FDTD formulations are based on a uniform or graded rectilinear grid, although different grids on which the field components are located have been proposed, e.g., non-orthogonal coordinates but regular grids [13], [14], irregular nonorthogonal grids [15], [16] and Finite-Volume Time-Domain (FVTD) formulations [17], [18]. However, a loss in robustness and stability is the cost for many of these techniques providing increased modeling flexibility. This is one of the reasons that almost all commercially available codes are based on the conventional rectilinear gridding, which can also be easily automated.

Metal structures can simply be modeled by explicitly forcing the tangential E-field components to zero in each time step. This implies that the modeled structure must be conformally oriented to the grid. For unique details, such as thin wires, corners and edges, field approximations can be used to individually model the field behavior close to the structure of interest. The contour-path formulation has been proposed in [19], [20] to enhance the modeling of thin wires, thin slots, etc. In [21], [22], [23] the contour-path formulation was used to model grid non-conformal structures, e.g., curved surfaces.

Dielectric materials can be straightforwardly modeled for grid conformal structures. The conventional FDTD modeling assigns each voxel a dielectric material



which is assumed to be homogeneously distributed within the voxel. If grid non-conformal structures are modeled in this manner, the typical staircasing effect will occur. Before evaluating the explicit expression (3.7), the permittivity  $\epsilon_{i,j,k}$  and the conductivity  $\sigma_{i,j,k}$  must, however, be averaged, taking into account the size and material parameters of the neighboring cells by following the procedure in [24]. If the FI formulation is used instead of FDTD, the necessary averaging of material parameters is implicitly given [11]. Errors in absorption assessment due to staircasing effects and improved treatment of material parameters are discussed extensively in chapter 5.

### 3.4 Boundary Conditions

Due to computational limitations, the discretized space must be finite and therefore be truncated by boundary conditions which properly represent the radiation outside the domain of investigation. A very early radiation boundary operator for FDTD has been proposed in [25].

Basically, the radiation boundary operators can be classified into mode annihilating and one-way wave equation approximations. A general operator of the first kind that annihilates an arbitrary number of modes has been derived and described in [26]. Boundary operators of the second class permit wave propagation only in certain directions [27]. The application of such a boundary operator to FDTD has been presented in [28]. The design of boundary conditions for plane waves incident at arbitrary angles has been reported in [29].

In [30], a new class of absorbing boundaries, the perfectly matched layer (PML), was proposed. This approach is based on splitting the electric and magnetic field components in additional layers in the absorbing boundary region and assigning individual losses to the split field components. It has been extended to evanescent waves and to terminate lossy media in [31]. With the PML technique it is now possible to obtain broadband reflection coefficients as low as -80 dB [3].

Very recently, new research on absorbing boundary conditions has been reported, e.g. on concurrent complementary operators [32], transparent absorbing boundary conditions [33] and exact nonreflecting explicit boundary conditions [34].

### 3.5 Source Implementation

#### 3.5.1 Plane Wave Source

Plane wave source conditions are easily introduced into FDTD through the total field/scattered field formulation. In the inner total field region, the FDTD update equations apply to the total field, thus the incident plane wave plus the scattered field, whereas in the outer scattered field region as well as at the lattice truncation the FDTD update equations apply only to the scattered field. The incident plane wave is introduced at the boundary between the total field and scattered field region [3].

#### 3.5.2 Waveguide Source

Waveguide source conditions pose a greater challenge than simple plane wave excitation. Waveguide ports can be excited with the propagating modes if their field distribution at the location of the port is known. If the propagation constants are

known, the total field at the waveguide port can be expressed as the sum of all modes. Within FIT [35], the frequency domain formulation enables the direct determination of the modes for the same grid as used during time stepping.

### 3.5.3 Lumped Sources

Lumped sources can be dipole radiators, voltage or current sources, etc. For antenna excitation, common sources are the hard (voltage) and added (current) source [36]. Voltage sources with an internal resistance or with a non-linear load have also been implemented for FDTD simulations [37]. Modeling a voltage source in FDTD is straightforward, since the electric field appears explicitly in the update equations. At each time step, it must be set at the grid edge of interest according to a time varying function. A current source can be modeled by adding it to the current density in the discretized form of Maxwell's equation [36]. An improved FDTD model for the feeding gap of a thin-wire antenna has been proposed in [38].

## 3.6 Stability

Since transient field information can move only one grid step away within one time step, it is obvious that there must be an upper bound for the choice of the time step within the leap-frog scheme. The correct stability criterion was first derived in [39] by evaluating the eigenvalues of all possible spatial numerical modes. The derived Courant-Friedrich Criterion limits the maximum possible time steps for simulation within three dimensions by:

$$\Delta t \leq \frac{1}{c \sqrt{\frac{1}{(\Delta x)^2} + \frac{1}{(\Delta y)^2} + \frac{1}{(\Delta z)^2}}} \quad (3.8)$$

where  $\Delta x$ ,  $\Delta y$  and  $\Delta z$  are the mesh steps of a cartesian coordinate system and  $c$  the speed of light within the material of a cell. This criterion must be fulfilled for any mesh cell.

Even stronger restrictions on the maximum allowable time step might be necessary, if additional field approximations or interface conditions (e.g., subgrids) are introduced.

## 3.7 Implementation

Within the Swiss Priority Program MINAST 4.03 EMSIM, a Finite-Difference Time-Domain kernel has been implemented in collaboration with the Integrated Systems Laboratory (ETH) and several industry partners. The implemented kernel includes various simulation modes (2D/3D transient simulation, 2D/3D harmonic simulation and 2D static simulation), various sources (hard and added sources, voltage source with internal resistance, TEM excitation, excitation via total field/scattered field interface, etc.), various boundary conditions (1st and 2nd order Mur, Higdon operator up to 4th order, Perfectly Matched Layer (PML), periodic boundary conditions) and postprocessing features such as voltage, current, impedance and energy calculation, spectrum extraction, far-field computation, etc. The simulations can be performed with uniform and graded meshes. Graded meshes can be generated automatically. A CAD tool developed by Schmid & Partner Engineering AG (SPEAG, Zurich,

Switzerland) serves as a modeling front end and CAD data input interface. This CAD interface enables generation of basic solid structures, import of common CAD data, transformation such as rotation of the CAD data and automatic discretization.

## References

- [1] Kane S. Yee, "Numerical solution of initial boundary value problems involving Maxwell's equations in isotropic media", *IEEE Transactions on Antennas and Propagation*, vol. 14, no. 3, pp. 302–307, May 1966.
- [2] Karl S. Kunz and Raymond J. Luebbers, *The finite difference time domain method for electromagnetics*, CRC Press, 1993.
- [3] Allen Taflove, *Computational Electromagnetics: The Finite-Difference Time-Domain Method*, Artech House Publishers, 1995.
- [4] Allen Taflove, Ed., *Advances in Computational Electromagnetics: The Finite Difference Time-Domain Method*, Artech House, 1998.
- [5] CST, *The MAFIA collaboration, Mafia Version 3. x, User's Guide*, CST GmbH, Lautenschlägerstr. 38, D-64289 Darmstadt, 1994.
- [6] XFDTD, *XFDTD*, Remcom Inc., Calder Square, P.O. Box 10023, State College, PA 16805-0023, USA.
- [7] IMST, *EMPIRE*, Institut für Mobil- und Satellitenfunktechnik, Carl-Friedrich Gauss-Str. 2, D-47475 Kamp Lintfort, Germany.
- [8] ISE, *EMLAB*, Integrated Systems Engineering, ISE AG, Technoparkstr. 1, CH-8005 Zurich, Switzerland.
- [9] SPEAG, *Simulator for Electromagnetic Compatibility, Antennas and Dosimetry (SEMCAD)*, Schmid & Partner Engineering AG, SPEAG, Staffelstr. 8, CH-8045 Zurich, Switzerland.
- [10] Peter Monk and Endre Sli, "Error estimates for Yee's method on non-uniform grids", *IEEE Transactions on Magnetics*, vol. 30, no. 5, pp. 3200–3203, Sept. 1994.
- [11] T. Weiland, "Maxwell's grid equations", *Frequenz*, vol. 44, no. 1, pp. 9–16, 1990.
- [12] P. Thoma and T. Weiland, "A consistent subgridding scheme for the finite difference time domain method", *International Journal of Numerical Modelling: Electronic Networks, Devices and Fields*, vol. 8, pp. 359–374, 1996.
- [13] Richard Holland, "Finite-difference solution of Maxwell's equations in generalized nonorthogonal coordinates", *IEEE Transactions on Nuclear Science*, vol. 30, no. 6, pp. 4589–4591, Dec. 1983.
- [14] K. K. Mei, A. Cangellaris, and D. J. Angelakos, "Conformal time domain finite difference method", *Radio Science*, vol. 19, no. 5, pp. 1145–1147, Sept. 1984.
- [15] Mario A. Fusco, Mary V. Smith, and Lawrence W. Gordon, "A three-dimensional FDTD algorithm in curvilinear coordinates", *IEEE Transactions on Antennas and Propagation*, vol. 39, no. 10, pp. 1463–1471, Oct. 1991.

- [16] J. F. Lee, R. Palandech, and R. Mittra, "Modeling three-dimensional discontinuities in waveguides using nonorthogonal FDTD algorithm", *IEEE Transactions on Microwave Theory and Techniques*, vol. 40, no. 2, pp. 346–352, Feb. 1992.
- [17] Vijaya Shankar and Alireza H. Mohammadian, "A time-domain, finite-volume treatment for the Maxwell equations", *Electromagnetics*, vol. 10, pp. 127–145, 1990.
- [18] Kane S. Yee and Jei S. Chen, "Conformal hybrid finite difference time domain and finite volume time domain", *IEEE Transactions on Antennas and Propagation*, vol. 42, no. 10, pp. 1450–1458, Oct. 1994.
- [19] Korada R. Umashankar, Allen Taflove, and Benjamin Beker, "Calculation and experimental validation of induced currents on coupled wires in an arbitrary shaped cavity", *IEEE Transactions on Antennas and Propagation*, vol. 35, no. 11, pp. 1248–1257, Nov. 1987.
- [20] Allen Taflove, Korada Umashankar, Benjamin Beker, Fady Harfoush, and Kane S. Yee, "Detailed FD-TD analysis of electromagnetic fields penetrating narrow slots and lapped joints in thick conducting screens", *IEEE Transactions on Antennas and Propagation*, vol. 36, no. 2, pp. 247–257, Feb. 1988.
- [21] Thomas Jurgens, Allen Taflove, Korada Umashankar, and Thomas G. Moore, "Finite-difference time-domain modeling of curved surfaces", *IEEE Transactions on Antennas and Propagation*, vol. 40, no. 4, pp. 357–365, Apr. 1992.
- [22] C. J. Railton, "An algorithm for the treatment of curved metallic laminas in the finite difference time domain method", *IEEE Transactions on Microwave Theory and Techniques*, vol. 41, no. 8, pp. 1429–1438, Aug. 1993.
- [23] Nicolas Chavannes, Michael Burkhardt, and Niels Kuster, "Simulation of Wire Antennas Non-Conformally Oriented to the FDTD Grid", in *USNC/URSI National Radio Science Meeting*, Atlanta, Georgia, USA June 1998.
- [24] J. Fang, *Time Domain Finite Difference Computation for Maxwell's Equations*, University of California at Berkeley, 1989.
- [25] David E. Merewether, "Transient currents induced on a metallic body of revolution by a n electromagnetic pulse", *IEEE Transactions on Electromagnetic Compatibility*, vol. 13, no. 2, pp. 41–44, May 1971.
- [26] Alvin Bayliss and Eli Turkel, "Radiation boundary conditions for wave-like equations", *Communications on Pure and Applied Mathematics*, vol. 33, pp. 707–725, 1980.
- [27] Bjorn Engquist and Andrew Majda, "Radiation boundary conditions for acoustic and elastic wave calculations", *Communications on Pure and Applied Mathematics*, vol. 32, pp. 313–375, 1979.
- [28] Gerrit Mur, "Absorbing boundary conditions for the finite-difference approximation of the time-domain electromagnetic-field equations", *IEEE Transactions on Electromagnetic Compatibility*, vol. 23, no. 4, pp. 377–382, Nov. 1981.

- [29] Robert L. Higdon, "Absorbing boundary conditions for difference approximations to the multi-dimensional wave equation", *Mathematics of Computation*, vol. 47, no. 176, pp. 437–459, Oct. 1986.
- [30] J. Berenger, "A perfectly matched layer for the absorption of electromagnetic waves", *Journal of Computational Physics*, vol. 114, pp. 185–200, 1994.
- [31] Jiayuan Fang and Zhonghua Wu, "Generalized perfectly matched layer—an extension of Berenger's perfectly matched layer boundary condition", *IEEE Microwave and Guided Wave Letters*, vol. 5, no. 12, pp. 451–453, Dec. 1995.
- [32] Omar M. Ramahi, "The concurrent complementary operators method for fdtd mesh truncation", *IEEE Transactions on Antennas and Propagation*, vol. 46, no. 10, pp. 1475–1482, Oct. 1998.
- [33] Jian Peng and Constantine A. Balanis, "A generalized reflection-free domain-truncation method: Transparent absorbing boundary", *IEEE Transactions on Antennas and Propagation*, vol. 46, no. 7, pp. 1015–1022, July 1998.
- [34] Marcus J. Grote and Joseph B. Keller, "Nonreflecting boundary conditions for maxwell's equation", *Computational Physics*, vol. 139, no. 2, pp. 327–342, Jan. 1998.
- [35] T. Weiland, "Time domain electromagnetic field computation with finite difference methods", *International Journal of Numerical Modelling: Electronic Networks, Devices and Fields*, vol. 9, pp. 295–319, 1996.
- [36] Dale N. Buechler, Daniel H. Roper, Carl H. Durney, and Douglas A. Christensen, "Modeling sources in the FDTD formulation and their use in quantifying source and boundary condition errors", *IEEE Transactions on Microwave Theory and Techniques*, vol. 43, no. 4, pp. 810–813, Apr. 1995.
- [37] Raymond Luebbers, John Beggs, and Kent Chamberlin, "Finite Difference Time-Domain Calculation of Transients in Antennas with Nonlinear Loads", *IEEE Transactions on Antennas and Propagation*, vol. 41, no. 5, pp. 566–573, Sept. 1993.
- [38] S. Watanabe and M. Taki, "An improved FDTD model for the feeding gap of a thin-wire antenna", *IEEE Microwave and Guided Wave Letters*, vol. 8, no. 4, pp. 152–154, Apr. 1998.
- [39] Allen Taflov and Morris E. Brodwin, "Numerical solution of steady-state electromagnetic scattering problems using the time-dependent Maxwell's equations", *IEEE Transactions on Microwave Theory and Techniques*, vol. 23, no. 8, pp. 623–630, Aug. 1975.

Seite Leer /  
Blank leaf

## Chapter 4

# FDTD Intrinsic Uncertainties

*Abstract-* Within this section, error sources when using FDTD for exposure assessment are classified. Uncertainties in FDTD simulations arising from error sources of the numerical scheme itself are outlined in the context of near-field absorption studies. The dispersion relation is analyzed in detail.

### 4.1 Classification of Numerical Errors in FDTD

Basically, errors in FDTD simulations can be attributed to three classes, as represented in Fig. 4.1. Errors of the first class are introduced due to the uncertainty in the description of the physical model of any object that is part of the domain of investigation (scatterer, antenna, etc.). This includes the correct description of the geometry as well as the material parameters.

The second class of errors is related to the discretization of the physical model within a finite grid with finite mesh spacing and are based on the differences between the physical and numerical model. Modeling uncertainties arising from these errors are discussed in detail for lossy dielectric scatterers in the next section.

In the particular case of compliance evaluations of mobile telecommunications equipment (MTE), errors of the first class comprise the deviation from the human head phantom description to a specifically defined phantom in the standard and the deviation of the MTE description (e.g., from a CAD file) to the real physical handheld phone. Studies as reported in [1], [2] have shown that modeling of realistic MTE appropriately representing the relevant current distribution is a tedious task and can easily introduce significant errors in exposure assessment.

This section will discuss errors of the third class, which are related to the numerical scheme itself that is used to solve the governing equations on the chosen grid, in our case Maxwell's equations. Also belonging to this class of errors are those introduced by reflections at the boundary of the computation domain and the modeling of the source, e.g., the excitation in the feeding gap of an antenna. Many studies have been performed for these kind of errors, and methods have been developed to improve the accuracy of the method itself, e.g., in [3], [4], [5], [6].

Underlying all of these classes are errors introduced due to the numerical representation (e.g., roundoff errors) of the material parameters and geometry, as well



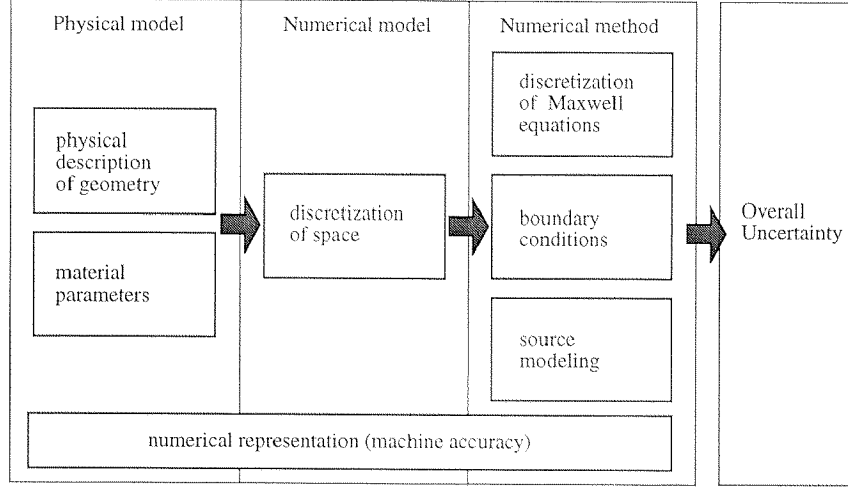


Figure 4.1: Classification of error sources within FDTD. The computational uncertainty is determined by errors in the numerical model, the numerical method and the numerical representation.

as calculated values within the numerical scheme. Compared to modeling errors, uncertainties arising from finite numerical representation are in general negligible for near-field absorption assessment. In situations of low-precision representation or when these errors can accumulate, their significance may increase.

## 4.2 Dispersion

Regarding an infinite empty space, the accuracy of the conventional non-dissipative FDTD scheme can be fully described by its numerical dispersion relation [3].

Let  $F(i, j, k)$  represent the exact solution of the differential equation at any grid point,  $\bar{F}(i, j, k)$  the exact solution of the FDTD difference equation and  $\tilde{F}(i, j, k)$  the obtained solution with the FDTD algorithm with a finite number of decimal places. Then the error introduced using finite differences will approach the roundoff error defined by  $F(i, j, k) - \tilde{F}(i, j, k)$  as the mesh step tends to zero. The rate of convergence, in our case 2nd order, characterizes the accuracy of the method. The resulting errors at a certain grid point can be an error in amplitude or in phase of the wave, however, staggered mesh schemes using central differences such as the Yee scheme show excellent amplitude characteristics [7]. The dispersion relation describes the actual phase velocity of a plane wave propagating in the numerical grid. For the three dimensional Yee algorithm with uniform mesh steps  $\Delta x$ ,  $\Delta y$  and  $\Delta z$  the dispersion relation is:

$$\sin^2\left(\frac{\omega\Delta t}{2}\right) = (c\Delta t)^2 \left[ \frac{1}{(\Delta x)^2} \sin^2\left(\frac{k_{nx}\Delta x}{2}\right) + \frac{1}{(\Delta y)^2} \sin^2\left(\frac{k_{ny}\Delta y}{2}\right) + \frac{1}{(\Delta z)^2} \sin^2\left(\frac{k_{nz}\Delta z}{2}\right) \right]$$

$$\left. \frac{1}{(\Delta z)^2} \sin^2 \left( \frac{k_{ny} \Delta z}{2} \right) \right] \quad (4.1)$$

where  $k_{nx}$ ,  $k_{ny}$  and  $k_{nz}$  are the numerical wavenumbers in the three coordinate directions and  $w$  is the angular frequency of the propagating wave. Besides the dependency on the time and space increments ( $\Delta t$ ,  $\Delta x$ ,  $\Delta y$ ,  $\Delta z$ ) and thus on the Courant stability factor  $s = c\Delta t/\Delta$  ( $\Delta \in \{\Delta x, \Delta y, \Delta z\}$ ), the dispersion error is dependent on the angle of propagation of the plane wave. The numerical wavelength  $\lambda_n$  is related to the numerical wave numbers  $k_{nx}$ ,  $k_{ny}$  and  $k_{nz}$  by:

$$\begin{aligned} k_{nx} &= \frac{2\pi}{\lambda_n} \cos\phi \sin\theta \\ k_{ny} &= \frac{2\pi}{\lambda_n} \sin\phi \sin\theta \\ k_{nz} &= \frac{2\pi}{\lambda_n} \cos\theta \end{aligned} \quad (4.2)$$

where  $\phi$  and  $\theta$  are spherical coordinates. The grid dispersion per wavelength can be defined as described in [4]:

$$\psi_{err} = 360^\circ \left( \frac{\lambda}{\lambda_n} - 1 \right) \quad (4.3)$$

The ratio of the numerical wavelength and the physical wavelength is illustrated for the two-dimensional case as a polar plot in the xy-plane in Fig. 4.2 for two different stability factors and different discretizations. Fig. 4.3 and 4.4 show the grid dispersion per wavelength for the two dimensional case and different stability factors. From Fig. 4.3 it can be clearly seen that for a stability factor chosen at the Courant limit, the dispersion is zero for a plane wave traveling along the diagonal and largest for a plane wave traveling parallel to the grid lines. For a stability factor chosen not to be at the Courant limit, the dispersion is no longer zero but still smallest along the diagonal.

Additional dispersion is added for non uniform gridding. The dispersion error can be minimized by choosing the appropriate discretization, higher order schemes [4] or dispersion optimized schemes [3], [8], [9], [10], [11].

### 4.3 Reflections from Boundaries

Errors resulting from artificial reflections at the lattice truncation have been analyzed in great detail for various boundary conditions in the literature [4], [6], [12]. Using one of the most sophisticated boundaries, the *Perfectly Matched Layer* (PML) [13], broadband reflection coefficients can be kept as low as -80 dB. However, absorbing boundary conditions developed in the 80's such as the Mur absorbing boundaries seem appropriate for near-field absorption studies, where a high dynamic range of the scattered field is not of interest and contributes only little to the final uncertainty. Studies such as reported in [14] and [15] on the comparison of PML boundaries to retarded time boundary conditions, which are similarly effective as Mur boundary conditions, confirm this assumption for MTE related near-field exposure problems.

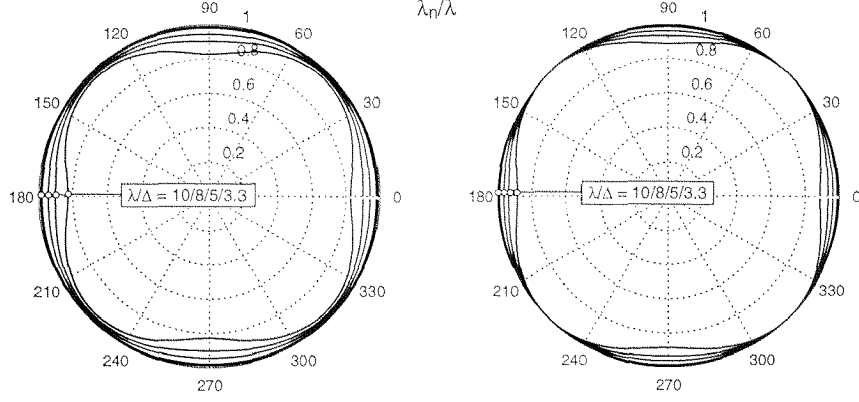


Figure 4.2: The ratio of numerical to physical wavelength, whereby in the left picture a stability factor of 0.5 and in the right picture a stability factor of  $1/\sqrt{2}$  were chosen.  $\lambda/\Delta$  is the number of cells per wavelength.

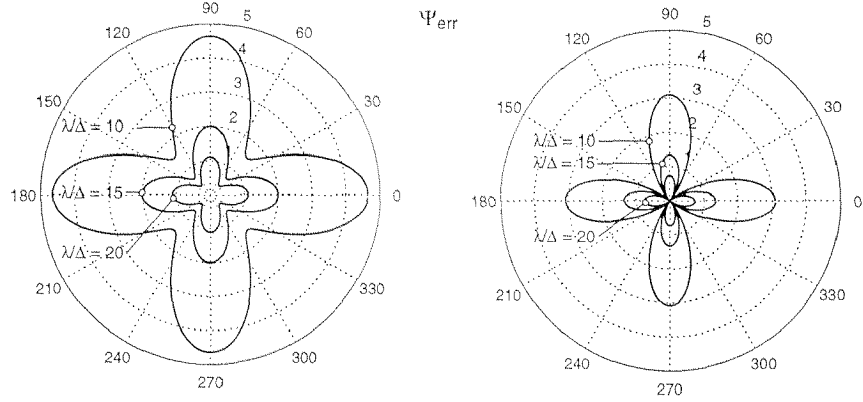


Figure 4.3: The grid dispersion per wavelength as defined in 4.3, whereby in the left picture a stability factor of 0.5 and in the right picture a stability factor of  $1/\sqrt{2}$  was chosen.  $\lambda/\Delta$  is the number of cells per wavelength.

#### 4.4 Source Modeling

Source modeling errors in particular for added and hard sources in the feeding point of antennas have been studied in [5] and [16]. In [16] an improved transparent source model has been proposed. Although benchmark sources can be simulated with known accuracy, quantifying the source modeling error for certain realistic objects such as a MTE is a tedious task. Correct modeling of the source of such an object would also require correct modeling of the matching network.

Significant differences in well defined benchmark problems, e.g., as presented in [17] (Figure 1.1), can be caused by differences in gap modeling, using hard or added sources and modeling the antenna as a filament, a solid wire or with the thin wire approximation. As can be seen from Figure 1.1, the variations in the feedpoint impedance are significant, leading to large variations in the absorbed power. An

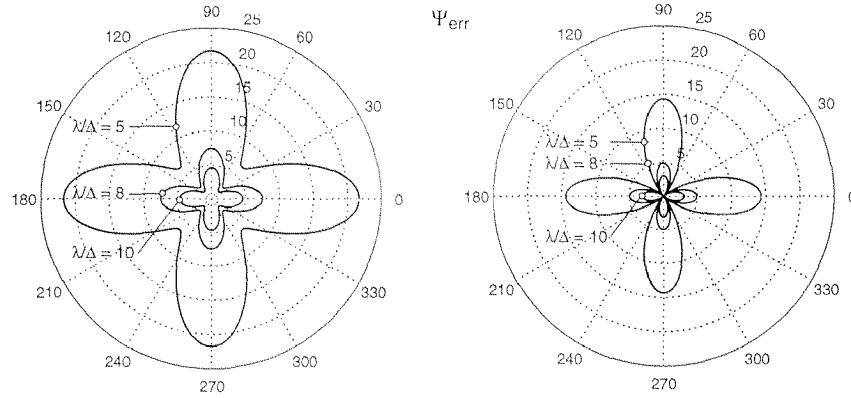


Figure 4.4: The grid dispersion per wavelength as defined in 4.3, whereby in the left picture a stability factor of 0.5 and in the right picture a stability factor of  $1/\sqrt{2}$  was chosen.  $\lambda/\Delta$  is the number of cells per wavelength.

improved gap model for dipole antennas has been presented in [18]. In the context of near-field exposure assessment, the use of an added source is advantageous, since the SAR is directly proportional to the square of the feedpoint current [19]. This eliminates the uncertainty of the sensitive feedpoint impedance.

## 4.5 Discussion

The errors inherent in the numerical scheme of FDTD can be well described with respect to dispersion, reflection from boundaries and well defined source modeling. Appropriate techniques have been developed to minimize these kinds of errors. Whereas errors of the numerical scheme can be kept small (well below a few percent), large uncertainties may arise from modeling errors of the objects in the domain of investigation. In the context of near-field absorption studies and compliance testing of MTE with safety standards, modeling uncertainties of the MTE are dominant compared to uncertainties due to the numerical scheme itself, as will be outlined in the next chapter.

## References

- [1] Achim Bahr, Sheng Gen Pan, Thomas Beck, Ralf Kästle, Thomas Schmid, and Niels Kuster, "Comparison between numerical and experimental near-field evaluation of a DCS1800 mobile telephone", *Radio Science*, vol. 33, no. 6, pp. 1553–1563, Nov. 1998.
- [2] M. Burkhardt, N. Chavannes, K. Pokovic, T. Schmid, and N. Kuster, "Study on the FDTD performance for transmitters in complex environments", in *ICE-COM'97*, Dubrovnik, Croatia, Oct. 1997, pp. 83–86.
- [3] Allen Taflove, *Computational Electromagnetics: The Finite-Difference Time-Domain Method*, Artech House Publishers, 1995.
- [4] J. Fang, *Time Domain Finite Difference Computation for Maxwell's Equations*, University of California at Berkeley, 1989.
- [5] Dale N. Buechler, Daniel H. Roper, Carl H. Durney, and Douglas A. Christensen, "Modeling sources in the FDTD formulation and their use in quantifying source and boundary condition errors", *IEEE Transactions on Microwave Theory and Techniques*, vol. 43, no. 4, pp. 810–813, Apr. 1995.
- [6] Deane T. Prescott and Nicholas V. Shuley, "Reflection analysis of FDTD boundary conditions-part I: Time-space absorbing boundaries", *IEEE Transactions on Microwave Theory and Techniques*, vol. 45, no. 8, pp. 1162–1170, Aug. 1997.
- [7] Kane S. Yee, "Numerical solution of initial boundary value problems involving Maxwell's equations in isotropic media", *IEEE Transactions on Antennas and Propagation*, vol. 14, no. 3, pp. 302–307, May 1966.
- [8] S. Castillo and S. Omick, "Suppression of dispersion in fdtd solutions of maxwell's equations", *Journal of Electromagnetic Waves and Applications*, vol. 8, no. 9, pp. 1193–1221, 1994.
- [9] Kurt L. Shlager, James G. Maloney, Scott L. Ray, and Andrew F. Peterson, "Relative accuracy of several finite-difference time-domain methods in two and three dimensions", *IEEE Transactions on Antennas and Propagation*, vol. 41, no. 12, pp. 1732–1737, Dec. 1993.
- [10] John W. Nehrbass, Jovan O. Jevtic, and Robert Lee, "Reducing the phase error for Finite-Difference methods without increasing the order", *IEEE Transactions on Antennas and Propagation*, vol. 46, no. 8, pp. 1194–1201, Aug. 1998.
- [11] Andreas Christ, and Niels Kuster, "Correction of Numerical Phase Speed Errors in Graded FDTD Meshes", in *USNC/URSI National Radio Science Meeting*, Orlando, Florida, July 1999.
- [12] Thomas G. Moore, Jeffrey G. Blaschak, Allen Taflove, and Gregory A. Kriegsmann, "Theory and application of radiation boundary operators", *IEEE Transactions on Antennas and Propagation*, vol. 36, no. 12, pp. 1797–1811, Dec. 1988.
- [13] J. Berenger, "A perfectly matched layer for the absorption of electromagnetic waves", *Journal of Computational Physics*, vol. 114, pp. 185–200, 1994.

- [14] M. Rayner, A. D. Olver, and A. D. Monk, "Proximity effects of absorbing boundary conditions on antenna radiation patterns", *Radio Science*, vol. 31, no. 6, pp. 1845–1852, Nov. 1996.
- [15] C. Furse, Y. Cui, G. Lazzi, and O. Gandhi, "Use of PML boundary conditions for wireless telephone simulations", *Microwave and Optical Technology letters*, vol. 15, no. 2, pp. 95–98, June 1997.
- [16] John B. Schneider, Christopher L. Wagner, and Omar M. Ramahi, "Implementation of transparent sources in fdtd simulations", *IEEE Transactions on Antennas and Propagation*, vol. 46, no. 8, pp. 1159–1167, Aug. 1998.
- [17] R. Pontalti, "Cost 244bis canonical cases for mobile communications equipment", in *4th EBEA Congress*, Zagreb, Croatia, Nov. 1998.
- [18] S. Watanabe and M. Taki, "An improved FDTD model for the feeding gap of a thin-wire antenna", *IEEE Microwave and Guided Wave Letters*, vol. 8, no. 4, pp. 152–154, Apr. 1998.
- [19] N. Kuster and Q. Balzano, "Energy absorption mechanism by biological bodies in the near field of dipole antennas above 300 MHz", *IEEE Transactions on Vehicular Technology*, vol. 41, no. 1, pp. 17–23, Feb. 1992.

Seite Leer /  
Blank leaf

## Chapter 5

# Estimation of Artifacts Caused by FDTD-Staircasing in RF Simulation Involving Lossy Dielectric Objects

*Abstract* - While many publications have dealt with artifacts on the scattered field arising from staircased FDTD modeling of the scatterer, little is known about such artifacts on the induced fields inside lossy dielectric structures. On the other hand reliable uncertainty assessments, even for local field strengths, would be a necessity in many applications, e.g., in compliance evaluations of mobile phones with safety standards, in the analysis of *in vivo* and *in vitro* exposure setups, etc. Usually, modeling of complex structures within a rectilinear finite-difference time-domain (FDTD) grid is performed in a straightforward manner, assigning material parameters to entire voxels. This not only leads to modeling uncertainties but might also result in numerical artifacts. Within the context of this paper, error sources due to modeling uncertainties, in particular staircasing effects for biological materials, were quantified and compared with other error sources in FDTD simulations. Various techniques for more appropriate material boundary treatment are discussed. A technique to avoid staircasing based on effective material parameters was applied to dielectric materials and analyzed in the context of exposure assessment.

### 5.1 Introduction

The finite-difference time-domain (FDTD) technique [1], [2], [3] which has become one of the most popular techniques in electrodynamics, has been applied for assessing the exposure of complex shaped biological bodies from very early on [4]. This includes far-field evaluations [5], compliance considerations for mobile phones with safety standards [6]-[14], exposure in working environments [15], design and analysis of *in vivo* [16] and *in vitro* [17], [18] exposure setups for biological studies and hy-



perthermia investigations [19], [20], etc. The popularity of FDTD for this class of problems is based on its ability to model highly complex dielectric structures in a straightforward manner and on its robustness and numerical stability in the case of such structures. However, the conversion or discretization of a non-rectilinear body into a rectilinear grid results in differences between the geometry of the physical and numerical model. Since the results obtained for the numerical model will differ from those of the original one, the uncertainty must be quantified. Obviously, significant errors may occur for resonant structures. Techniques involving varying degrees of computational expense to avoid staircasing problems have been the subject of many investigations and will be discussed in the following. Possible artifacts on induced fields for staircased boundaries may be of particular importance if results are related to a very small region in space, e.g., spatial peak SAR values averaged over a small number of voxels.

## 5.2 Staircasing

Staircasing within rectilinear FDTD grids related to metallic structures in particular has been investigated, e.g., in [21]. The authors presented a rigorous dispersion analysis due to the presence of a staircased scatterer additional to the numerical dispersion of the Yee scheme. However, for discretization schemes such as the FDTD method, the main source of error in the presence of a dielectric body is related to the material boundary representation rather than to dispersion effects [22]. Reduced accuracy at dielectric material boundaries including edges and corners has been investigated in [23] for plane waves, proposing corrected FDTD coefficients for better representation of various material boundary configurations. Instead of errors caused by dispersion and artificial reflections, our concern is related to possible artifacts at material boundaries of biological objects due to staircasing effects for an originally smoothly shaped body.

## 5.3 Methods for Conformal Modeling

Motivation for conformal modeling within rectilinear grids has mainly been driven by problems involving the staircasing of metallic structures, e.g., more accurate simulation of waveguide modes [24], [25] and more accurate RCS calculation with a wider dynamic range for metallic scatterers [26], [27], but also more accurate characterization in the near- and far-fields, e.g., of horn antennas [26], [28].

Many different approaches have been proposed to improve the modeling drawbacks of rectilinear grids. In the context of finite difference frequency domain formulations, diagonal cells for polygonal contour modeling were proposed in [24] and [29] for more accurate waveguide mode computation. For simulation in the time domain locally conformal grids applying contour-path FDTD modeling [30], [31] were proposed. Attempts to overcome time instabilities arising in some contour path formulations from the borrowing of field components from neighboring cells are presented in [32], [33]. FDTD formulations using non-orthogonal coordinates, but regular grids, for specially shaped objects have been proposed in [34], [35]. Irregular nonorthogonal grids were the subject of investigation in [36], [37]. More arbitrarily shaped objects have been modeled within the Finite-Volume Time-Domain (FVTD) formulation [38] or hybrid FVTD/FDTD formulations [39], facing in certain cases the

problem of dissipative grid properties. Locally enhanced resolution through subgridding has also been extensively investigated, e.g., in [40], [41]. Although rectilinear subgridding cannot eliminate staircasing effects, it can decrease them in certain situations. Overlapping of different coordinate systems for better conformal modeling has been studied in [27], [42], faced with interpolation problems between the different coordinates.

However, especially for irregular meshes and coupled different coordinate systems, implementation is a rather cumbersome task. Although not equally applicable for truly arbitrarily shaped 3D objects as for irregular nonorthogonal grids, contour-path modeling [30] or very similar formulations including diagonal cells, as proposed in [29], represent an alternative approach with low additional computational cost.

Whereas many of the approaches mentioned for conformal modeling are applicable and have also been proposed for dielectric objects, in particular contour-path modeling and diagonal cells, they have not been used as extensively for dielectric objects as for metallic structures. It has even been stated that the rationale for conformal FDTD modeling of biological structures relative to EM wave interactions is not justified [43]. Staircase approximation was cited as sufficiently predicting the penetration of fields in the dielectric object, thus the penetrating fields were much less sensitive to the surface approximation of the structure than the scattered field. However, if the result is related to a small region in space, e.g., the spatial peak SAR value averaged over a small number of voxels and located close to a material boundary with a staircase approximation, the accuracy might be questionable. Moreover, even globally significant errors can be obtained in certain configurations, as will be shown in the following.

## 5.4 Methods

### 5.4.1 Numerical Techniques

Three different methods have been applied to conduct this study. The effects depending on the geometry were investigated with the commercial code MAFIA [44] which is based on the Finite-Integration Technique (FIT) [45]. This formulation in the time domain is based on the discretization of Maxwell's equations in integral form. It has also been generalized in the form of matrix equations for use in the frequency domain [45]. In the time domain it leads to the same numerical scheme, with the same stability and dispersion properties as the FDTD scheme. In the absence of dielectric materials it is identical to the contour-path formulation [30] and thus to the FDTD scheme [3] and in the case of the treatment of material boundaries in FDTD as described in [46] as well as in the presence of dielectric materials. However, since subcell geometric details such as non-conformal boundaries can be effectively treated with the contour-path formulation, the implementation is more straightforward within FIT, since it is already based on the integral form.

For the investigations on material boundary treatment, an inhouse Yee-grid based FDTD code which has recently been completed, was used. It enables plane wave, TEM, hard, added and voltage source excitation. The computation domain can be truncated with Mur 1st & 2nd order, Higdon operators, PML or periodic boundaries. The graphical user interface enables modeling of simple solid structures as well as the import of CAD data and optimized, automated graded mesh generation [47].

The third method applied was the Generalized Multipole Technique (GMT) [48], with which the reference solution for the spherical body was obtained.

#### 5.4.2 Basic Modeling

For most computations reported the computation domain was truncated by 2nd order Mur boundary conditions approximately a wavelength away from the object of interest. Although better boundary conditions have been developed [49], Mur absorbing boundaries seem appropriate for our absorption studies, where a high dynamic range of the scattered field is not of interest. Studies such as reported in [50] on the comparison of PML boundaries to retarded time boundary conditions, which are similar in effect to Mur boundary conditions, confirm this assumption for our type of bioelectromagnetic applications. The time step was chosen according to the Courant stability condition [3]. SAR values were calculated by interpolating the 12 electric field components on the edges of a voxel into the center following the equation:

$$SAR = \frac{\sigma}{\rho} |E|^2 \quad (5.1)$$

whereby  $\sigma$  is the conductivity and  $\rho$  the specific density assigned to the voxel.

#### 5.4.3 Material Boundary Treatment

At the material boundaries of dielectric objects where step changes in material parameters occur, special treatment within the FDTD formulation is necessary for proper boundary representation [46]. We will consider only the case where the material boundary is located on the primary grid of the Yee scheme (Fig. 5.1) and  $\mu = \mu_0$ . In this case only E-field components tangential to material boundaries occur; thus the continuity of the tangential E-field can be ensured and the effective permittivity for this component must be chosen as the average of the two neighboring cells (Fig. 5.1):  $\epsilon_{eff} = (\epsilon_{r1} + \epsilon_{r2})/2$ . For our assumption of  $\mu = \mu_0$ , no special treatment or storage is necessary for the normal H-field components at the material boundary.

#### 5.4.4 Partially Filled Cell

Within FIT the derivation of the effective permittivity is more obvious, since evaluating the electric flux within the integral form of Ampere's law for cells at a material boundary yields exactly the same result. For a partially filled cell ( $\mu = \mu_0$ ,  $\sigma = 0$ ), as illustrated in Fig. 5.2 for the particular case of a diagonal cell [29] which does not vary its geometry in the z-direction, the left side of Ampere's law

$$\frac{\partial}{\partial t} \iint \vec{D} d\vec{A} = \oint \vec{H} d\vec{l} \quad (5.2)$$

yields:

$$\begin{aligned} \frac{\partial}{\partial t} \iint \vec{D} d\vec{A} = \\ \frac{\partial}{\partial t} \left( \iint \epsilon_0 \epsilon_{r1} \vec{E}_z d\vec{A}_1 + \iint \epsilon_0 \epsilon_{r2} \vec{E}_z d\vec{A}_2 \right) = \end{aligned}$$

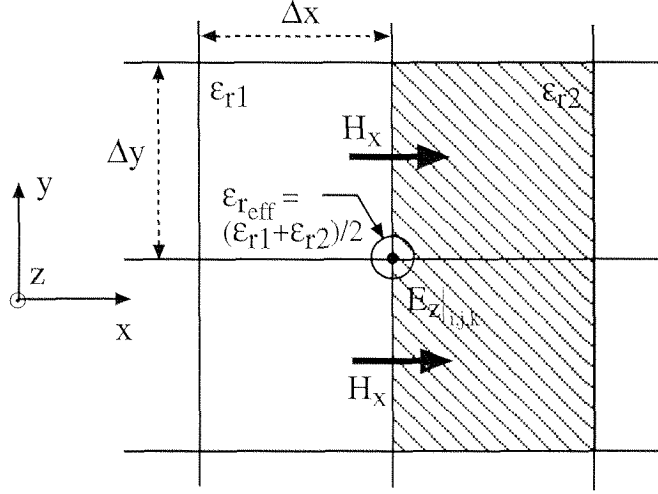


Figure 5.1: Treatment of a dielectric material boundary with an effective permittivity within FDTD.

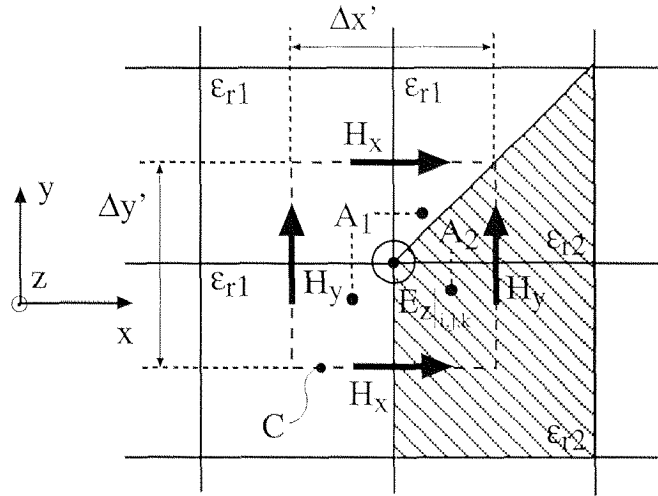


Figure 5.2: Derivation of an effective permittivity for a partially filled cell following the procedure described in [29]. Areas 1 and 2 are the combined areas for two materials within the integration loop  $C$ .

$$\frac{\partial}{\partial t} \iint \epsilon_{eff} \vec{E}_z d\vec{A} \quad (5.3)$$

whereas

$$\epsilon_{eff} = \frac{\epsilon_0}{\Delta x' \Delta y'} (\epsilon_{r1} A_1 + \epsilon_{r2} A_2). \quad (5.4)$$

and  $\vec{E}_z$  is assumed to be constant within the area described by the integration path  $C$ . This effective permittivity can be used straightforwardly within the finite difference formulation of Ampere's law (5.2) at timepoint  $n + 1$  and node location  $i, j, k$ :

$$\begin{aligned}
\epsilon_{eff} \left( \frac{E_z|_{i,j,k}^{n+1} - E_z|_{i,j,k}^n}{\Delta t} \right) \Delta x \Delta y = \\
(H_x|_{i,j-1/2,k}^{n+1/2} - H_x|_{i,j+1/2,k}^{n+1/2}) \Delta x \\
-(H_y|_{i+1/2,j,k}^{n+1/2} - H_y|_{i-1/2,j,k}^{n+1/2}) \Delta y
\end{aligned} \tag{5.5}$$

The equations including electric losses can be derived analogously. For cells in a rectilinear grid filled truly arbitrarily (also in the z-direction) with dielectric material, this contour path formulation has been successfully extended in [51] by introducing an averaged electric-flux density leading as well to an effective permittivity. The great advantage of looking at flux field values and deriving effective permittivities as compared to other conformal grid techniques is that no additional computational cost is needed during time stepping. Effective permittivities can be completely calculated during preprocessing.

## 5.5 Local Errors in Absorption due to Single Steps

### 5.5.1 Model

It is desirable to automatically discretize complex 3-dimensional bodies. Hence, straightforward modeling of smoothly shaped biological bodies will result in stair-cased material boundaries by simply assigning materials to whole voxels of the rectilinear FDTD grid and treating material parameters as described in section 5.4.3. This may result in steps, single voxels, holes, rough surfaces or surfaces with holes and even local disappearance of structures (Fig. 5.3). Locally the surface may shift forward or backward by up to half of the voxel size.

The absorption at the material boundary of a single homogeneous tissue layer has been studied for a single step, as represented in Fig. 5.3a) in 2D for different dielectric parameters, polarizations, frequencies and discretizations. For this trivial kind of 2-D problem, the computation domain was truncated in the  $\pm x$  direction by 1st order Mur absorbing boundary conditions and by perfectly electric conducting material in the  $\pm z$  direction for polarization a) and perfectly magnetic conducting material in the case of polarization b) (Fig. 5.4 - 5.5). To avoid any influence from these boundaries, the computation domain was rather large in the  $\pm z$  direction.

### 5.5.2 Results

The SAR distribution in the first line of voxels for the model with a step relative to the SAR distribution in the absence of the step is represented in Figures 5.4 and 5.5 for two different plane wave polarizations and three different discretizations at 900 MHz. At the location of the step, an enhancement in SAR of approximately 50% was found at the inner edge and a decrease of approximately 50% at the outer edge for polarization a). This effect was found to be rather discretization independent. In the case of polarization b), enhancements were less than for polarization a); they were located at the outer edge (Fig. 5.5) and tended to be lower for decreasing meshsteps. The behavior of both polarizations did not change significantly for permittivities between 5 and 80 (Fig. 5.6), conductivities between 0.85 and 2 (Fig. 5.7) and other frequencies (Fig. 5.8) between 900-1800 MHz.

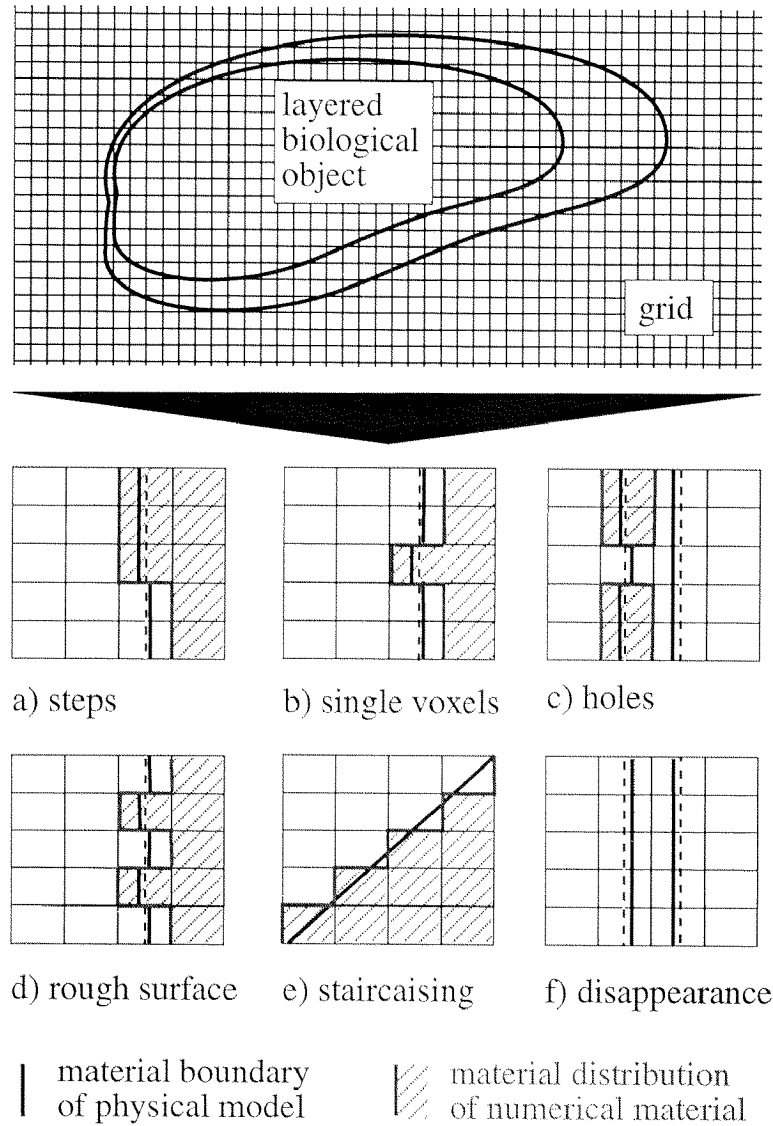


Figure 5.3: Straightforward modeling of arbitrarily shaped objects in the conventional staggered FDTD scheme leads to staircasing effects such as pixels, ripples or disappearance of thin layers. The dashed line represents the middle of a meshstep.

The conclusion from these investigations is that field values derived from voxels located at material boundaries are subject to great uncertainties. Nevertheless, spatial averaged values can be obtained with great accuracy if the volume contains significantly more non-boundary voxels than boundary voxels. For example, the influence on spatial peak SAR values averaged over 1 g of tissue were less than 5% for the coarsest discretization in the above example. Modeling strongly complex tissue compositions, where layers have about the same resolution as the voxel size, may result in large uncertainties and should therefore be avoided. For example, the discretization of the skull of a small animal may result in various holes at some lo-

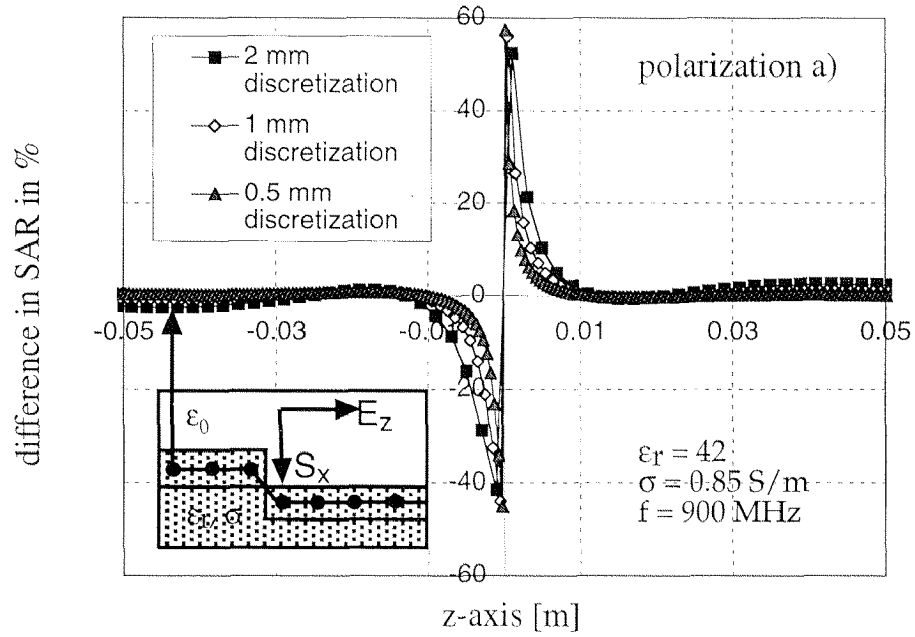


Figure 5.4: Difference in SAR distribution in the first row of voxels relative to a plane tissue layer depending on the discretization. The E-field vector is perpendicular to the edge of the step.

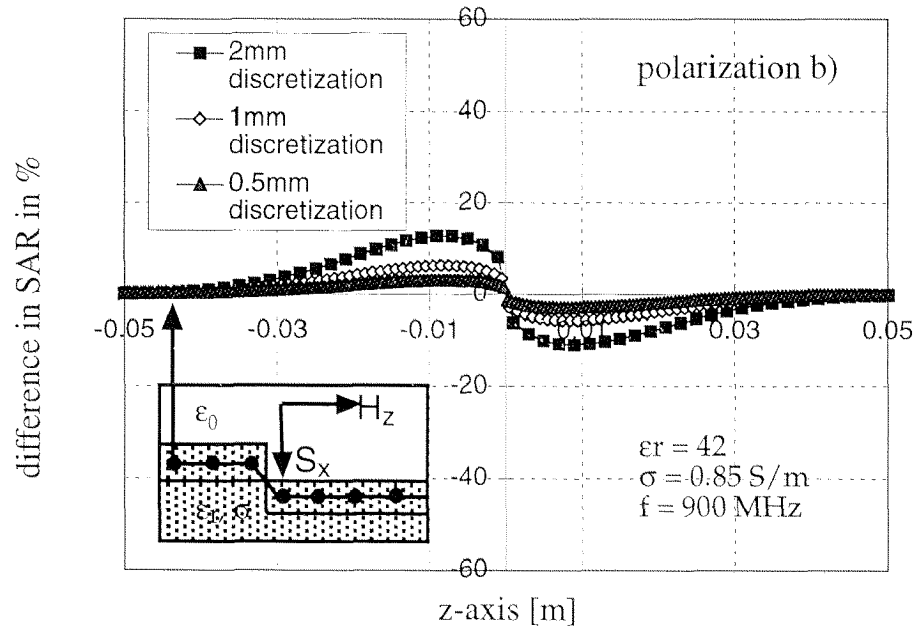


Figure 5.5: Difference in SAR distribution in the first row of voxels relative to a plane tissue layer depending on the discretization. The E-field vector is parallel to the edge of the step.

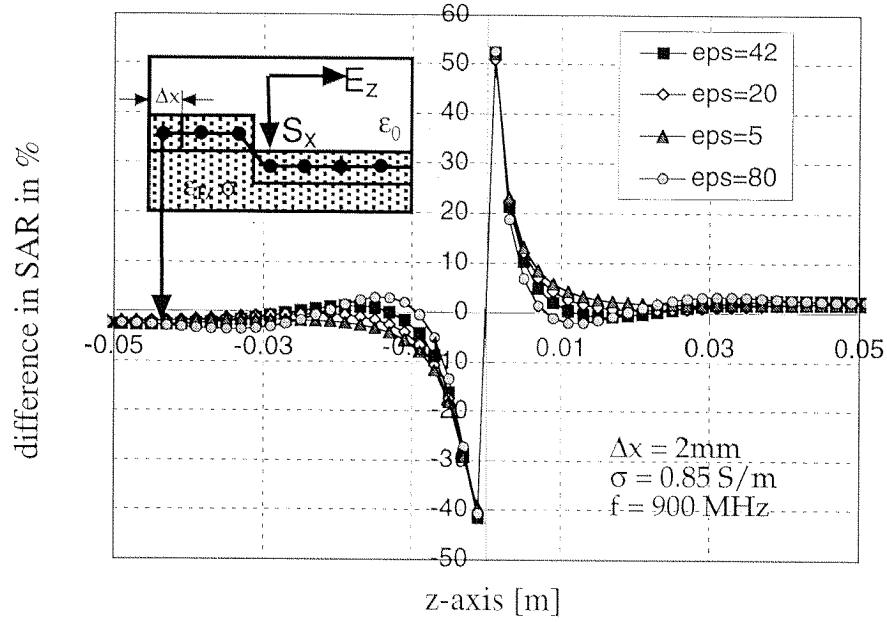


Figure 5.6: Difference in SAR distribution in the first row of voxels relative to a plane tissue layer depending on the permittivity. The E-field vector is perpendicular to the edge of the step.

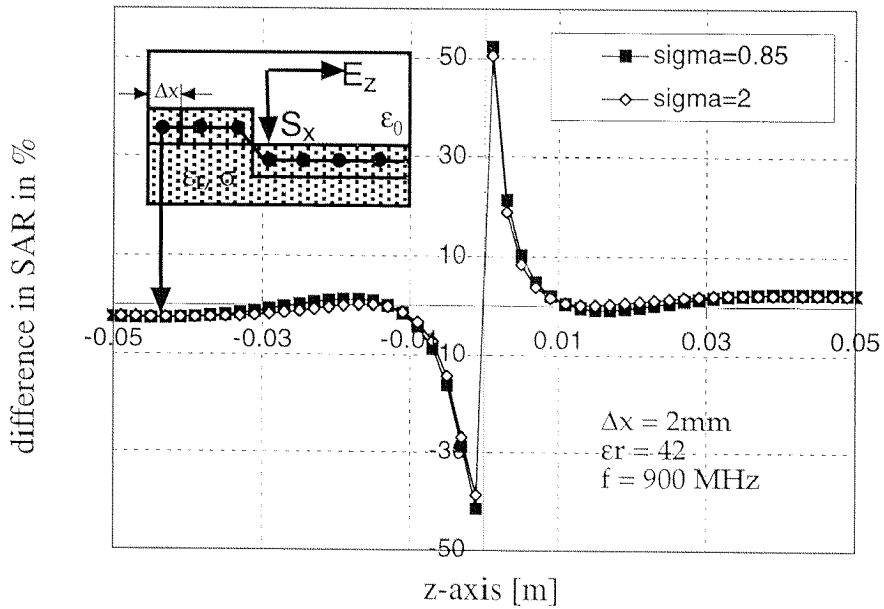


Figure 5.7: Difference in SAR distribution in the first row of voxels relative to a plane tissue layer depending on the conductivity. The E-field vector is perpendicular to the edge of the step.



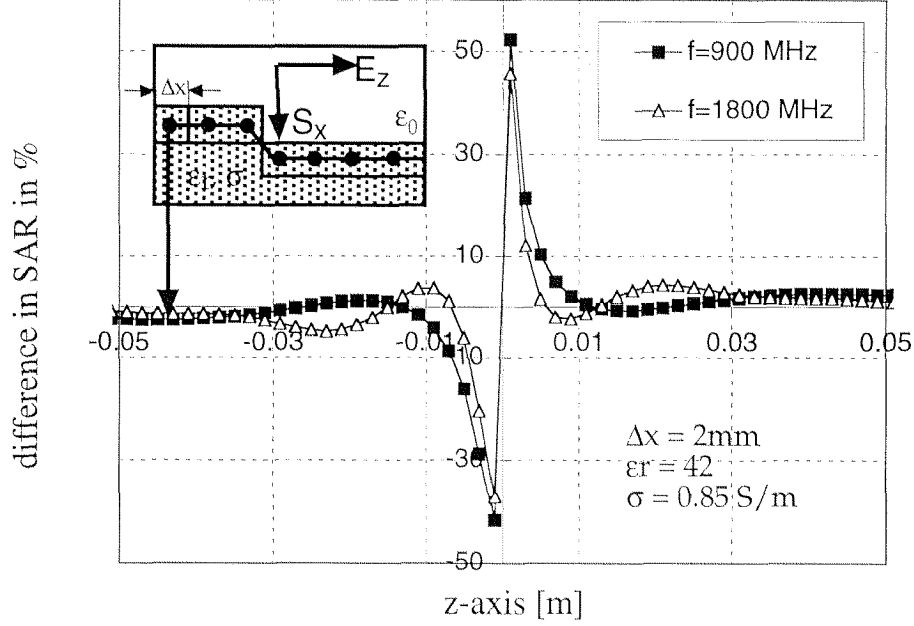


Figure 5.8: Difference in SAR distribution in the first row of voxels relative to a plane tissue layer depending on the frequency. The E-field vector is perpendicular to the edge of the step.

cations and in too thick layers at others. It must also be concluded that modeling of the human ear with 2-5 mm voxels, as used in some of the studies for compliance testing [6]-[14], may result in questionable one-voxel peak SAR values. It is therefore recommended that the voxel size is considerably smaller than half the dimension of the finest structure of the object. Another error induced by stair modeling is that the simulated material boundary might shift by almost half a voxel. This may have significant consequences if the electromagnetic source is located at distances of just a few voxels [52].

## 5.6 Global Errors in Absorption due to Staircasing

### 5.6.1 Model

A simple staircasing effect which produces globally significant errors strongly dependent on the resolution of the discretization was the subject of further investigation. This is demonstrated on the basis of a dielectric sphere (diameter 200 mm,  $\epsilon=42$ ,  $\sigma=0.85$ ) exposed to a plane wave at 900 MHz. The discretizations used vary between 1-4 mm. This setup was chosen because it had multiply served as a benchmark, e.g., in [53], and because a solution of great and known precision can be obtained by GMT.

### 5.6.2 Results

The qualitatively, normalized SAR distribution in the sphere calculated by GMT is represented in Figure 5.9. The error with respect to the GMT reference solution

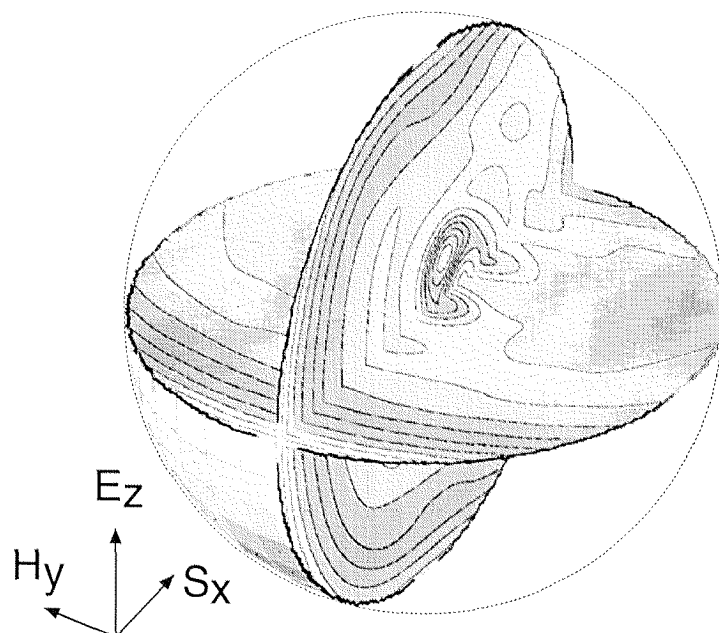


Figure 5.9: Sphere modeled by GMT and exposed to a plane wave excitation. The qualitative SAR distribution in two orthogonal planes is given as well as the location of the evaluation plane used for Figures 5.10- 5.12.

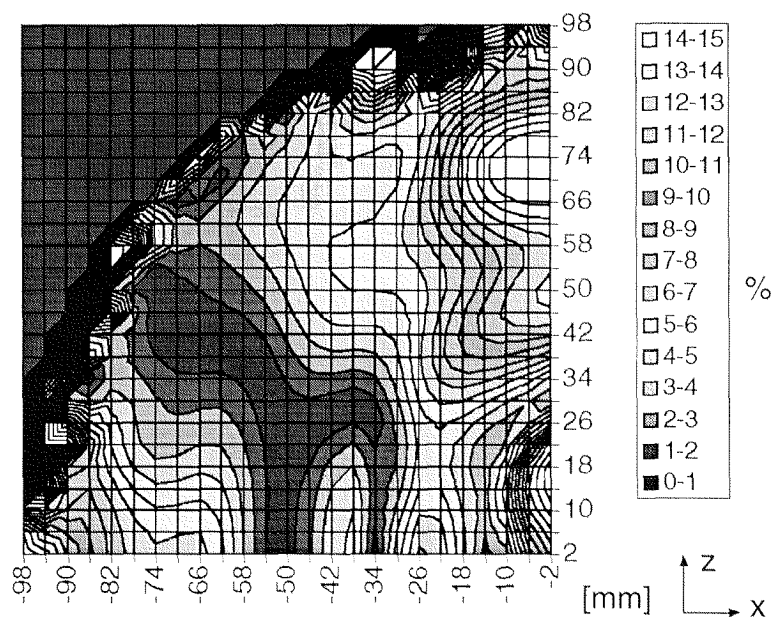


Figure 5.10: The error in SAR relative to the GMT reference solution in % in a plane orthogonal to the H-field vector (4mm discretization).

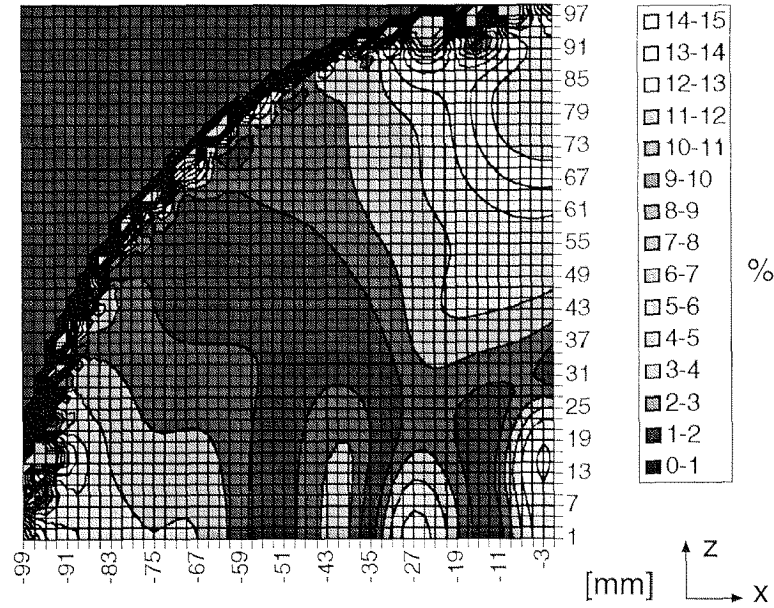


Figure 5.11: The error in SAR relative to the GMT reference solution in % in a plane orthogonal to the H-field vector (2mm discretization).

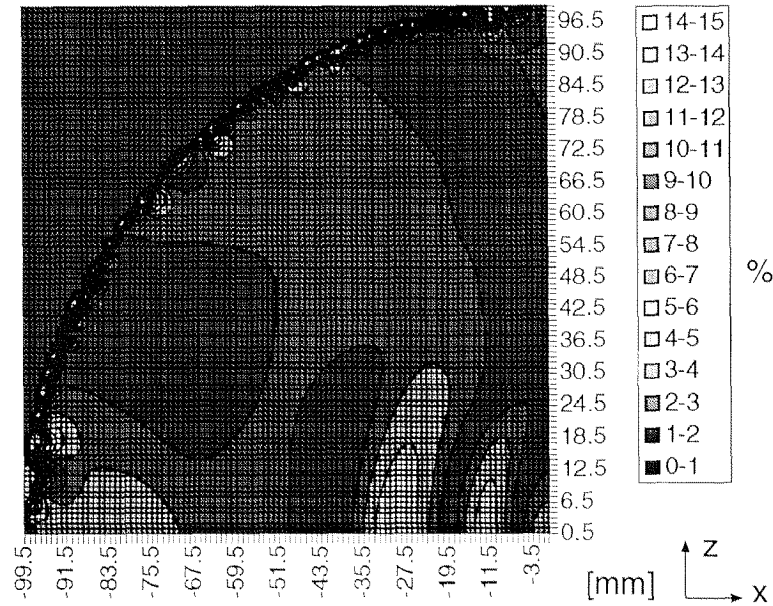


Figure 5.12: The error in SAR relative to the GMT reference solution in % in a plane orthogonal to the H-field vector (1mm discretization).

in a quarter of the sphere for the three different discretizations is given in Figures 5.10-5.12. Figure 5.10 indicates that for the most coarse discretization (4mm), the error is as large as approximately 15% distributed over larger regions, whereby for

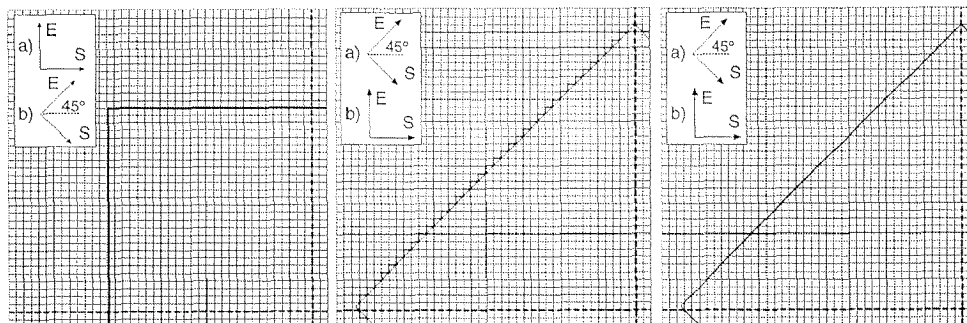


Figure 5.13: The three investigated modeling cases of a cube: conformal model (left), 45 degrees rotated staircase model (middle), 45 degree rotated model with diagonal cells (right).

the 1 mm discretization the error is below 5% (Fig. 5.12). This is mainly due to the different focusing effects depending on differently pronounced staircasing at the sphere surface for the chosen discretizations. Although globally significant errors may occur for certain geometric bodies, they are of minor relevance for actual biological bodies due to their limited geometric regularity.

## 5.7 Performance of Partially Filled Cells to Reduce Staircasing Effects at Dielectric Material Boundaries

### 5.7.1 Model

The performance of partially filled cells to reduce staircasing effects at dielectric material boundaries was studied using a cube ( $\epsilon_r=42$ ,  $\sigma=0.85$  S/m, dimensions:  $(200\text{ mm})^3$ ) exposed to a plane wave of different polarizations at 900 MHz. The six cases studied are represented in Figure 5.13. Basically, they differ in the angle of the incident wave, the geometric location and the modeling of the cube. Either the propagation vector is orthogonal to the surface of the cube or at an oblique angle of 45 degrees. The electric field vector was oriented perpendicular to the edge of the stairs, since section 5.5 has shown that this configuration produces the highest errors in local SAR values. The cube was oriented conformal to the grid or rotated by 45 degrees, whereby either staircasing or diagonally filled cells were regarded. A grid size of approximately 3.8 mm was maintained to optimally fit the rotated and the grid-conformal cube into the grid. A graded mesh with expanding mesh steps was used further away from the cube.

### 5.7.2 Results

The SAR distribution for the different cases was analyzed and compared in the first row of voxels. Figures 5.14 and 5.15 represent the SAR distributions along the outer edge of the cube for the two incident angles. Compared are the models when the cube is modeled conformal to the grid and when the excitation as well as the cube is rotated. The same figures show the differences for staircase modeling and using diagonal cells as discussed in section 5.4. In the case of a 45 degree angle between

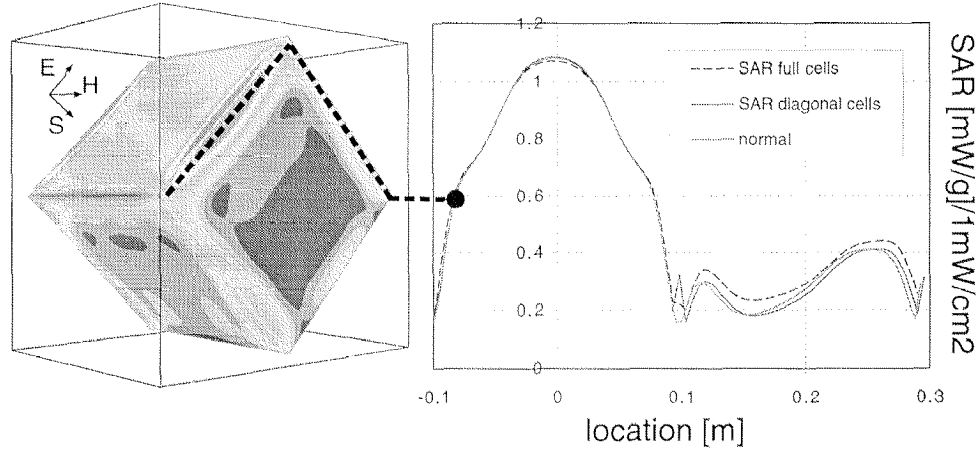


Figure 5.14: Comparison of local SAR values in the first row of voxels for conformal, staircased and diagonal cell conditions (right); Qualitative SAR distribution on the surface of the cube (left) for incident angle a).

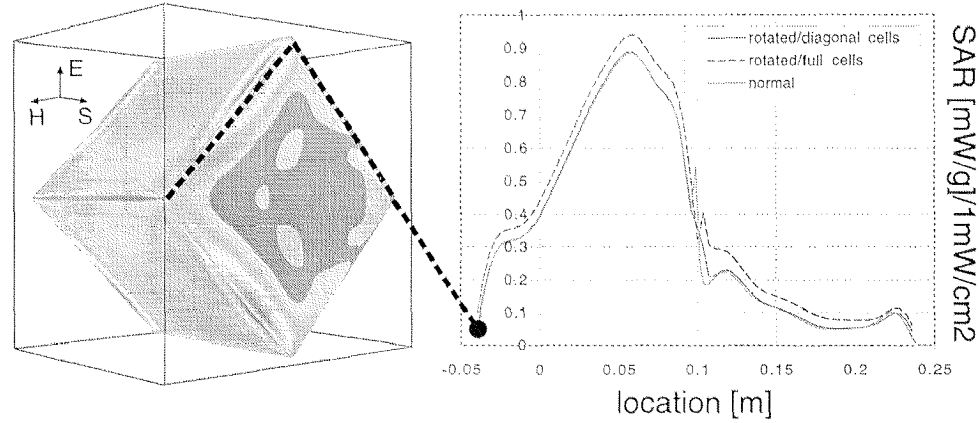


Figure 5.15: Comparison of local SAR values in the first row of voxels for conformal, staircased and diagonal cell conditions (right); Qualitative SAR distribution on the surface of the cube (left) for incident angle b).

the propagation vector and the surface of the cube (Fig. 5.15), differences in SAR of 4-10 % between non-rotated and staircased modeled rotated cube occur. In the case of diagonal cell modeling, the agreement between the conformal and rotated cube models is excellent. If the incident wave is orthogonal to the cube, even the staircased model of the rotated cube is in good agreement with the non-rotated reference cube. This is due to the representation of the staircased material boundary as a regular rough surface which is symmetric with respect to the excitation. For other voxel rows located at the material boundary, the differences are slightly lower but similar. In the case of the E-field vector parallel to the staircasing edge, similar results were achieved.

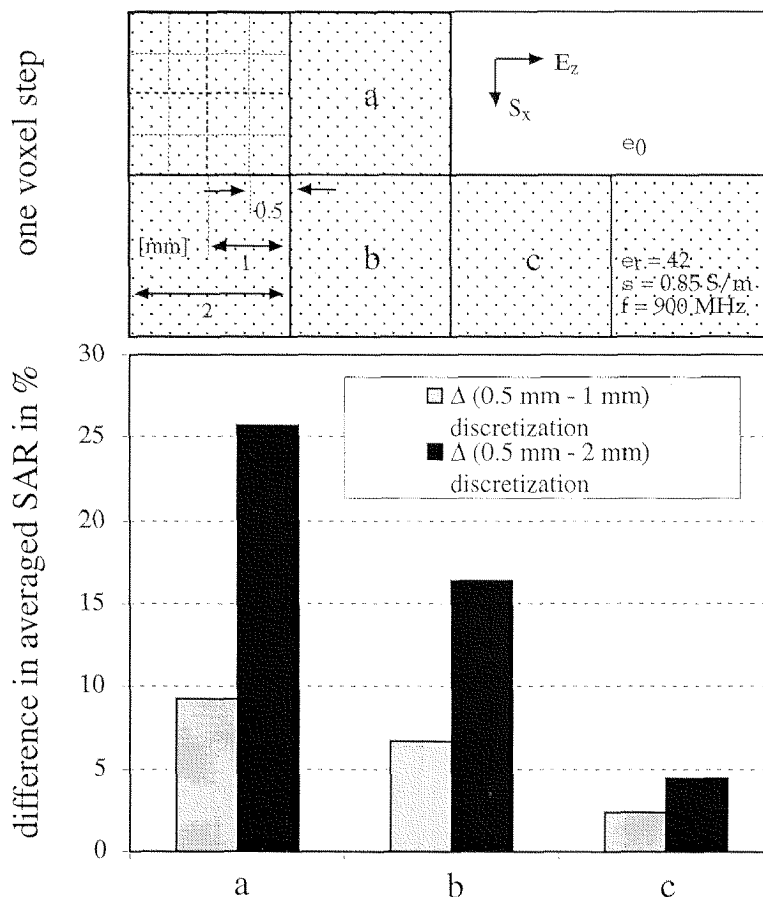


Figure 5.16: Difference for a 1 and 2 mm discretization in spatial SAR values averaged over a plane of  $2\text{ mm}^2$  close to a step. The E-field vector is perpendicular to the edge of the step.

## 5.8 Modeling of a Step

Supposing a step shall be modeled within FDTD at a material boundary since it occurs in the actual physical dielectric object, the accuracy of conventional straight-forward FDTD modeling is of interest. A two-dimensional step of 2 mm dimensions has been investigated for discretizations between 2 and 0.5 mm. Fig. 5.16 shows the difference for a spatial SAR value averaged over a plane of  $2\text{ mm}^2$  for the 1 and 2 mm discretizations compared to a 0.5 mm discretization. For the given polarization (E-field vector perpendicular to the step) the difference between the 0.5 and 2 mm discretizations is as large as 25%. With the H-field vector perpendicular to the step, the differences for all voxels is less than 1.5%.

## 5.9 Conclusion

Uncertainties in the exposure assessment with FDTD due to staircasing effects were studied. Local values, when directly derived from voxels located at material bound-

aries, may involve uncertainties that are greater than 50% in the case of conventional FDTD modeling. However, the precision of spatially averaged values is generally high if the number of values from non-boundary voxels is significantly larger than from voxels at material boundaries. In view of this fact, it is a questionable approach to discretize highly complex structures with voxel-sizes in the range of the smallest dimension of the biological substructures, i.e., the voxel size should be significantly smaller than half of the smallest of those dimensions.

Globally significant uncertainties can occur for specific structures, i.e., structures resulting in pronounced focuses or resonances. However, these uncertainties are generally negligible for actual biological bodies, which in general do not possess such properties.

If high precision is required for local values with a voxel size not much smaller than the finest structure, special considerations and careful interpretation of the results are required when straightforward modeling is used. Significant improvement in precision is possible without additional computational cost by use of the well known contour path modeling approach. Similar improvements can be achieved by deriving effective permittivities from the electric flux field values. These are effective and inexpensive alternatives compared to more sophisticated gridding.

It shall further be noted that this study only dealt with uncertainties due to the modeling of the lossy dielectric object. An additional uncertainty source which has not been evaluated in this study, but which is of eminent relevance for many wireless applications, is the uncertainty of modeling the electromagnetic RF characteristics of actual transmitters when operated in the closest vicinity of the biological body.

## References

- [1] Kane S. Yee, "Numerical solution of initial boundary value problems involving Maxwell's equations in isotropic media", *IEEE Transactions on Antennas and Propagation*, vol. 14, no. 3, pp. 302–307, May 1966.
- [2] Karl S. Kunz and Raymond J. Luebbers, *The finite difference time domain method for electromagnetics*, CRC Press, 1993.
- [3] Allen Taflov, *Computational Electromagnetics: The Finite-Difference Time-Domain Method*, Artech House Publishers, 1995.
- [4] Allen Taflov and Morris E. Brodwin, "Computation of the electromagnetic fields and induced temperatures within a model of the microwave-irradiated human eye", *IEEE Transactions on Microwave Theory and Techniques*, vol. 23, no. 11, pp. 888–896, Nov. 1975.
- [5] R. J. Spiegel, M. B. E. Fatmi, and K. S. Kunz, "Application of a finite-difference technique to the human radiofrequency dosimetry problem", *Journal on Microwave Power*, vol. 20, pp. 241–254, 1985.
- [6] Jorn Toftgard, Sten N. Hornsleth, and Jorgen Bach Andersen, "Effects on portable antennas of the presence of a person", *IEEE Transactions on Antennas and Propagation*, vol. 41, no. 6, pp. 739–746, June 1993.
- [7] Hsing-Yi Chen and Hou-Hwa Wang, "Current and SAR induced in a human head model by the electromagnetic fields irradiated from a cellular phone", *IEEE Transactions on Microwave Theory and Techniques*, vol. 42, no. 12, pp. 2249–2254, Dec. 1994.
- [8] P. J. Dimbylow and S. M. Mann, "SAR calculations in an anatomically realistic model of the head for mobile communication transceivers at 900 MHz and 1.8 GHz", *Physics in Medicine and Biology*, vol. 39, pp. 1537–1553, 1994.
- [9] Michael A. Jensen and Yahya Rahmat-Samii, "EM interaction of handset antennas and a human in personal communications", in *Proceedings of the IEEE*, 1995, vol. 83, pp. 7–17.
- [10] L. Martens, J. De Moerloose, and D. De Zutter, "Calculation of the electromagnetic fields induced in the head of an operator of a cordless telephone", *Radio Science*, vol. 30, no. 1, pp. 283–290, Feb. 1995.
- [11] Om P. Gandhi and Jin Yuan Chen, "Electromagnetic absorption in the human head from experimental 6-GHz handheld transceivers", *IEEE Transactions on Electromagnetic Compatibility*, vol. 37, pp. 547–558, 1995.
- [12] Soichi Watanabe, Masao Taki, Toshio Nojima, and Osamu Fujiwara, "Characteristics of the SAR distributions in a head exposed to electromagnetic fields radiated by hand-held portable radio", *IEEE Transactions on Microwave Theory and Techniques*, vol. 44, no. 10, pp. 1874–1883, Oct. 1996.
- [13] Michal Okoniewski and Maria A. Stuchly, "A study of the handset antennas and human body interaction", *IEEE Transactions on Microwave Theory and Techniques*, vol. 44, no. 10, pp. 1855–1863, Oct. 1996.



- [14] Volker Hombach, Klaus Meier, Michael Burkhardt, Eberhard Kühn, and Niels Kuster, "The dependence of EM energy absorption upon human head modeling at 900 MHz", *IEEE Transactions on Microwave Theory and Techniques*, vol. 44, no. 10, pp. 1855–1863, Oct. 1996.
- [15] Jin-Yuan Chen and Om P. Gandhi, "Electromagnetic deposition in an anatomically based model of man for leakage fields of a parallel-plate dielectric heater", *IEEE Transactions on Microwave Theory and Techniques*, vol. 37, no. 1, pp. 174–180, Jan. 1989.
- [16] Michael Burkhardt, Yuri Spinelli, and Niels Kuster, "Exposure setup to test effects of wireless communications systems on the CNS", *Health Physics*, vol. 73, no. 5, pp. 770–778, 1997.
- [17] J. V. Hese, L. Martens, D. D. Zutter, C. D. Wagter, L. O. G. Malmgren, B. R. R. Persson, and L. G. Salford, "Simulation of the effect of inhomogeneities in TEM transmission cells using the FDTD-method", *IEEE Transactions on Electromagnetic Compatibility*, vol. 34, no. 3, pp. 292–298, Aug. 1992.
- [18] M. Burkhardt, K. Pokovic, M. Gnos, T. Schmid, and N. Kuster, "Numerical and experimental dosimetry of petri dish exposure setups", *Bioelectromagnetics*, vol. 17, pp. 483–493, 1996.
- [19] R. W. M. Lau and R. J. Sheppard, "The modelling of biological systems in three dimensions using the time domain finite-difference method: II. the application and experimental evaluation of the method in hyperthermia applicator design", *Physics in Medicine and Biology*, vol. 31, no. 11, pp. 1257–1266, 1986.
- [20] Dennis Sullivan, "Three-dimensional computer simulation in deep regional hyperthermia using the finite-difference time-domain method", *IEEE Transactions on Microwave Theory and Techniques*, vol. 38, no. 2, pp. 204–211, Feb. 1990.
- [21] Andreas C. Cangellaris and Diana B. Wright, "Analysis of the numerical error caused by the stair-stepped approximation of a conducting boundary in FDTD simulations of electromagnetic phenomena", *IEEE Transactions on Antennas and Propagation*, vol. 39, no. 10, pp. 1518–1525, Oct. 1991.
- [22] L. R. A. X. de Mezenes and W. J. R. Hoefer, "Accuracy of TLM solutions of Maxwell's equations", *IEEE Transactions on Microwave Theory and Techniques*, vol. 44, no. 12, pp. 2512–2517, Dec. 1996.
- [23] John W. Nehrbass, Jovan O. Jevtic, and Robert Lee, "Reducing the phase error for Finite-Difference methods without increasing the order", *IEEE Transactions on Antennas and Propagation*, vol. 46, no. 8, pp. 1194–1201, Aug. 1998.
- [24] M. J. Beaubien and A. Wexler, "An accurate finite-difference method for higher order waveguide modes", *IEEE Transactions on Microwave Theory and Techniques*, vol. 16, no. 12, pp. 1007–1017, Dec. 1968.
- [25] P. H. Harms, J. F. Lee, and R. Mittra, "A study of the nonorthogonal FDTD method versus the conventional FDTD technique for computing resonant frequencies of cylindrical cavities", *IEEE Transactions on Microwave Theory and Techniques*, vol. 40, no. 4, pp. 741–746, Apr. 1992.

- [26] D. S. Katz, M. J. Piket-May, A. Taflove, and K. R. Umashankar, "FDTD analysis of electromagnetic wave radiation from systems containing horn antennas", *IEEE Transactions on Antennas and Propagation*, vol. 39, no. 8, pp. 1203–1212, Aug. 1991.
- [27] K. S. Yee, Jei Shuan Chen, and Albert H. Chang, "Conformal finite-difference time-domain (FDTD) with overlapping grids", *IEEE Transactions on Antennas and Propagation*, vol. 40, no. 9, pp. 1068–1075, Sept. 1992.
- [28] C. Reig, E. A. Navarro, and V. Such, "FDTD analysis of E-sectoral horn antennas for broad-band applications", *IEEE Transactions on Antennas and Propagation*, vol. 45, no. 10, pp. 1484–1487, Oct. 1997.
- [29] Thomas Weiland, "Verlustbehaftete Wellenleiter mit beliebiger Randkontur und Materialbelegung", *Electronics and Communication*, vol. 33, no. 4, pp. 170–174, 1979.
- [30] Thomas Jurgens, Allen Taflove, Korada Umashankar, and Thomas G. Moore, "Finite-difference time-domain modeling of curved surfaces", *IEEE Transactions on Antennas and Propagation*, vol. 40, no. 4, pp. 357–365, Apr. 1992.
- [31] C. J. Railton, "An algorithm for the treatment of curved metallic laminas in the finite difference time domain method", *IEEE Transactions on Microwave Theory and Techniques*, vol. 41, no. 8, pp. 1429–1438, Aug. 1993.
- [32] Chris Railton, Ian J. Craddock, and John B. Schneider, "The analysis of general two-dimensional PEC structures using a modified CPFDTD algorithm", *IEEE Transactions on Microwave Theory and Techniques*, vol. 44, no. 10, pp. 1728–1733, Oct. 1996.
- [33] J. Anderson, M. Okoniewski, and S. S. Stuchly, "Practical 3-D contour/staircase treatment of metals in FDTD", *IEEE Microwave and Guided Wave Letters*, vol. 6, no. 3, pp. 146–148, Mar. 1996.
- [34] Richard Holland, "Finite-difference solution of Maxwell's equations in generalized nonorthogonal coordinates", *IEEE Transactions on Nuclear Science*, vol. 30, no. 6, pp. 4589–4591, Dec. 1983.
- [35] K. K. Mei, A. Cangellaris, and D. J. Angelakos, "Conformal time domain finite difference method", *Radio Science*, vol. 19, no. 5, pp. 1145–1147, Sept. 1984.
- [36] Mario A. Fusco, Mary V. Smith, and Lawrence W. Gordon, "A three-dimensional FDTD algorithm in curvilinear coordinates", *IEEE Transactions on Antennas and Propagation*, vol. 39, no. 10, pp. 1463–1471, Oct. 1991.
- [37] J. F. Lee, R. Palandech, and R. Mittra, "Modeling three-dimensional discontinuities in waveguides using nonorthogonal FDTD algorithm", *IEEE Transactions on Microwave Theory and Techniques*, vol. 40, no. 2, pp. 346–352, Feb. 1992.
- [38] Vijaya Shankar and Alireza H. Mohammadian, "A time-domain, finite-volume treatment for the Maxwell equations", *Electromagnetics*, vol. 10, pp. 127–145, 1990.

- [39] Kane S. Yee and Jei S. Chen, "Conformal hybrid finite difference time domain and finite volume time domain", *IEEE Transactions on Antennas and Propagation*, vol. 42, no. 10, pp. 1450–1458, Oct. 1994.
- [40] S. S. Zivanovic, K. S. Yee, and K. K. Mei, "A subgridding method for the time-domain finite-difference method to solve Maxwell's equations", *IEEE Transactions on Microwave Theory and Techniques*, vol. 39, no. 3, pp. 471–479, Mar. 1991.
- [41] P. Thoma and T. Weiland, "A consistent subgridding scheme for the finite difference time domain method", *International Journal of Numerical Modelling: Electronic Networks, Devices and Fields*, vol. 8, pp. 359–374, 1996.
- [42] M. Mrozowski, M. Okoniewski, M. A. Stuchly, and S. S. Stuchly, "Combining different coordinate systems in the time domain finite difference method", in *Applied Computational Electromagnetic Society*, 1995, vol. 12, pp. 534–541.
- [43] V. Sathiasselean, A. Taflove, M. J. Piket-May, C. Reuter, and B. B. Mittal, "Application of numerical modeling techniques in electromagnetic hyperthermia", *ACES Special Issue on Bioelectromagnetic Computation*, vol. 7, no. 2, pp. 61–71, 1992.
- [44] CST, *The MAFIA collaboration, Mafia Version 3. x, User's Guide*, CST GmbH, Lautenschlägerstr. 38, D-64289 Darmstadt, 1994.
- [45] T. Weiland, "Time domain electromagnetic field computation with finite difference methods", *International Journal of Numerical Modelling: Electronic Networks, Devices and Fields*, vol. 9, pp. 295–319, 1996.
- [46] J. Fang, *Time Domain Finite Difference Computation for Maxwell's Equations*, University of California at Berkeley, 1989.
- [47] Niels Kuster, Michael Burkhardt, and Peter Regli, "A CAD tool for rigorous electromagnetic simulations of microsystems", in *Swiss Physical Society*, University of Bern, Bern, Switzerland, Feb. 1999, p. 73.
- [48] N. Kuster, "Multiple multipole method for simulating EM problems involving biological bodies", *IEEE Transactions on Biomedical Engineering*, vol. 40, no. 7, pp. 611–620, July 1993.
- [49] J. Berenger, "A perfectly matched layer for the absorption of electromagnetic waves", *Journal of Computational Physics*, vol. 114, pp. 185–200, 1994.
- [50] C. Furse, Y. Cui, G. Lazzi, and O. Gandhi, "Use of PML boundary conditions for wireless telephone simulations", *Microwave and Optical Technology letters*, vol. 15, no. 2, pp. 95–98, June 1997.
- [51] N. Kaneda, B. Houshmand, and T. Itoh, "FDTD analysis of dielectric resonators", *IEEE Transactions on Microwave Theory and Techniques*, vol. 45, no. 9, pp. 1645–1649, Sept. 1997.
- [52] N. Kuster and Q. Balzano, "Energy absorption mechanism by biological bodies in the near field of dipole antennas above 300 MHz", *IEEE Transactions on Vehicular Technology*, vol. 41, no. 1, pp. 17–23, Feb. 1992.

- [53] J. Cooper, V. Hombach, and A. Schiavoni, “Comparision of computational electromagnetic codes applied to a sphere canonical problem”, *Antennas and Propagations*, vol. 143, no. 4, pp. 309–316, Aug. 1996.

Seite Leer /  
Blank leaf

## Part III

# Benchmarks and Applications

Seite Leer /  
Blank leaf

## Chapter 6

# Study on the FDTD Performance for Transmitters in Complex Environments

*Abstract* - The objective of this study was to investigate the potential difficulties of simulating transmitters in the closest proximity of lossy scatterers using Finite-Difference Time-Domain techniques. For this purpose, a geometrically and electrically well-defined generic phone was developed. This phone was experimentally characterized in the far and near fields as well as in the closest proximity of a lossy flat phantom. The results were compared to those obtained from FDTD simulations. These simulations predicted all parameters important for antenna design purposes with good to excellent precision, such as the feedpoint impedance, radiation pattern and near field, as well as the field strengths induced in a lossy scatterer in the antennas closest proximity. The impressive robustness of the simulations opens the feasibility of an automated problem discretization, a basic condition of implementing an optimizer.

### 6.1 Introduction

Finite-Difference Time-Domain (FDTD) techniques are increasingly being applied in the area of antenna design [1], [2]. Although the Method of Moments (MoM) approach is still more popular in this topic, FDTD techniques appear to be particularly well suited for the study of antennas in complex environments. The latter is an area in which clear limitations of MoM techniques have become apparent, e.g., for mobile handsets, identification tags, etc. Some research and engineering groups have even begun applying FDTD for the testing of commercial cellular phones for compliance with safety limits [3], [4]. In a recent study [5], the near field of a commercial cellular phone operating at 1800 MHz was independently evaluated by using a FDTD code and a near field scanner. The comparison in the close proximity of various lossy scatterers revealed significant differences in the amplitude and distribution of the high-frequency currents between physical and simulated phones. The differences were attributed to the relative crudeness of the modeling of the phone's casing as a



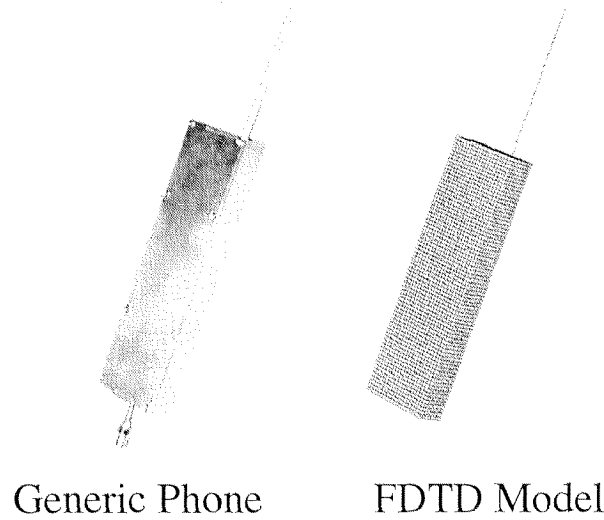


Figure 6.1: The generic phone used for measurements and its computer model for the FDTD simulations.

metallic box. In order to evaluate whether limitations of FDTD for this particular problem contributed to these differences, a follow-up study was performed using a generic phone.

## 6.2 Generic Setup

In order to study possible limitations of FDTD for transmitters in complex environments, a generic phone was built satisfying the following design criterion. 1) All parameters, especially the feedpoint impedance, must be determinable as accurately as possible by means of measurements. 2) It should have a simple geometric structure that is easy to model on a rectangular grid. 3) It should have similar dimensions as common cellular phones.

The generic phone shown in Figure 6.1 consists of a metallic casing of the dimensions  $140 \times 40 \times 16 \text{ mm}^3$ , equipped with a monopole antenna to operate at 900 MHz (thickness=2.5 mm, length=80 mm). Current leakage on the feeding coaxial cable is suppressed by means of a  $\lambda/4$ -yoke, enabling measurement of the feedpoint impedance by a network analyzer.

The near field was evaluated and compared in free space and in the close proximity of a flat lossy medium. This flat phantom consisted of a Plexiglas box ( $\epsilon_r = 2.7$ ) of the dimensions  $0.6 \times 0.8 \times 0.1 \text{ m}^3$  with a base plate thickness of 4 mm (see Figure 6.4). Tissue simulating liquid with a relative permittivity of  $\epsilon_r = 41 \pm 5\%$  and a conductivity  $\sigma = 0.86 \pm 5\% \text{ mho/m}$  was filled into the box to a height of  $\approx 80 \text{ mm}$ . Since actual skin depth is only about 40 mm and the wavelength inside this medium at 900 MHz is about 51 mm, the dimensions of the box are sufficient for a good approximation of the absorption in the vicinity of the phone inside an infinite lossy half space.

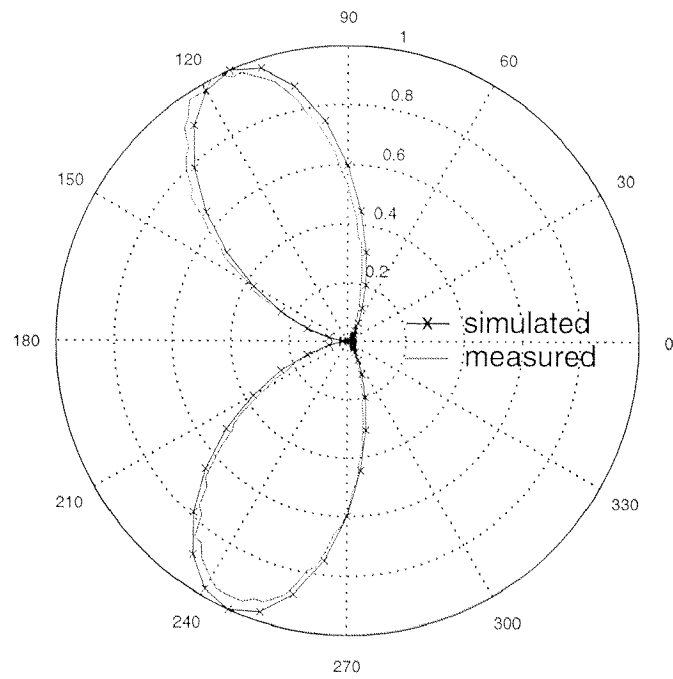


Figure 6.2: Simulated and measured gains in a vertical cut ( $xz$ -plane) of the far field.

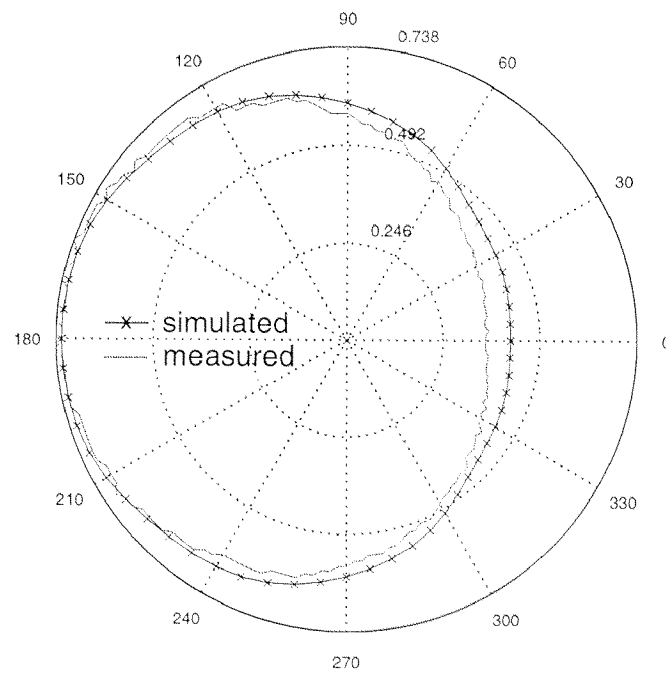


Figure 6.3: Simulated and measured gains in a horizontal cut ( $yz$ -plane) of the far field.

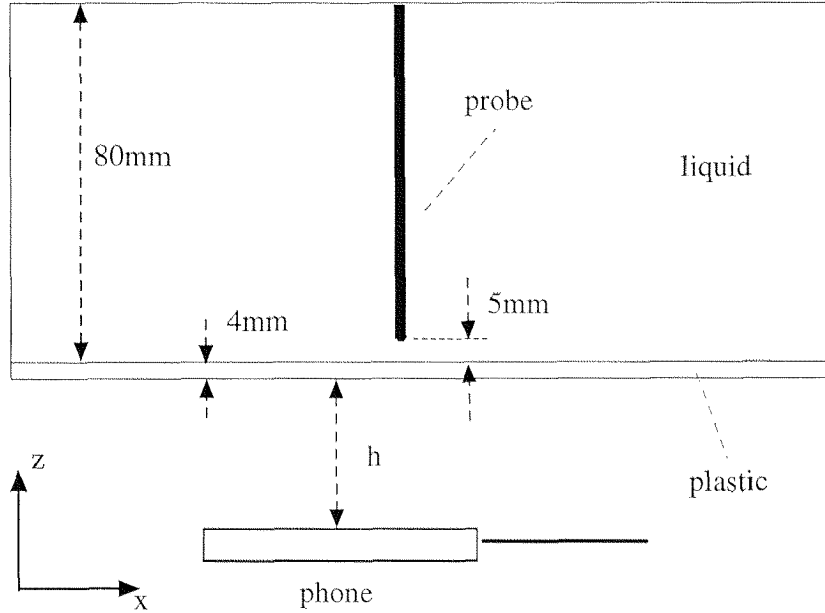


Figure 6.4: Setup for the evaluation of the performance of the generic phone close to the flat phantom filled with absorbing material.

## 6.3 Methods

### 6.3.1 Simulation

The simulations were performed using the Finite-Difference Time-Domain (FDTD) code, which has been recently implemented at ETH, the results of which were cross-checked using the commercially available MAFIA code [6], which is an implementation of the Finite Integration Technique (FIT).

The phone was discretized to a resolution of  $2 \times 2 \times 2 \text{ mm}^3$  voxels. The antenna was simulated by enforcing the tangential E-field components to zero along one grid line. The grid spacing at the location of the antenna and perpendicular to the axis of the antenna was chosen to be approximately equivalent to the diameter of the wire. Non equidistant mesh spacings were used to enlarge the computation domain bounded by second order Mur boundaries. The distance between boundary and phone was approximately  $\lambda$ , whereby the reflections have been shown to affect the feedpoint impedance by a factor of less than 1%. The entire computation domain encompassed approximately 2.3 million voxels. The excitation at the feedpoint was modeled by introducing a dipole moment with a smoothly increasing sinusoidal 900 MHz signal. Steady state was attained after 6-12 periods. The feedpoint impedance was determined by the Fourier transformed E- and H-fields at the driving point.

### 6.3.2 Far Field Measurement

The far field radiation patterns were measured in an anechoic chamber ( $4.9 \times 4.6 \times 16.5 \text{ m}$ ; quiet zone of 1 m radius centered at 2.3 m above the floor level)

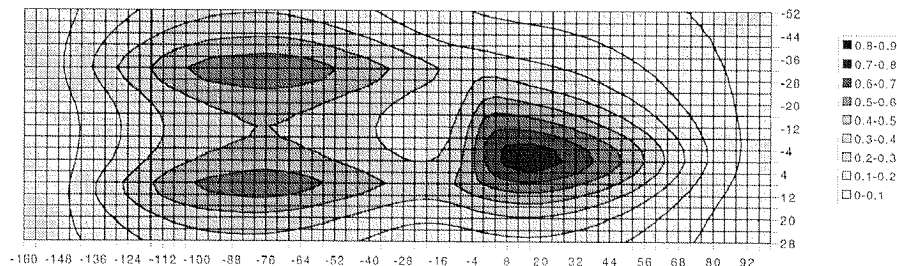


Figure 6.5: Measured H-field in A/m 5mm above the phone, normalized to 1 W antenna input power.

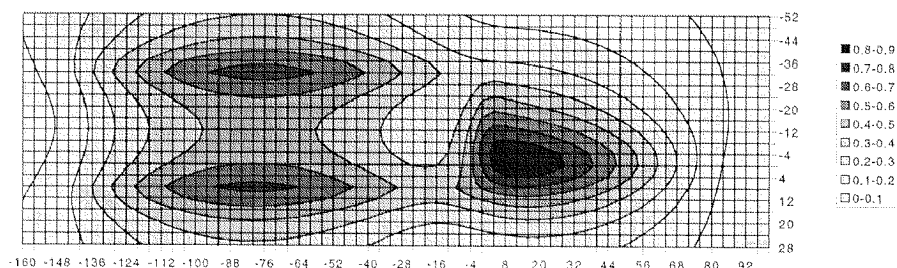


Figure 6.6: Simulated H-field in A/m 5mm above the phone, normalized to 1 W antenna input power.

by the Gain-Comparison method using a log-periodic antenna. The reference was the log-periodic antenna #WJ-48010 SN 203.

### 6.3.3 Near Field Measurement

In the experimental setup, the feedpoint impedances for each configuration were determined by a HP85047A network analyzer which was previously calibrated at the location of the feedpoint.

The 900 MHz input signal was generated by a HP8648C synthesizer combined with a Mini-Circuit ZHL-42W amplifier. The antenna input power was determined by a bi-directional coupler and two HP436A power meters.

The near field measurements were performed with the automated near field scanning system DASY2. This system and the E-field probes are described in detail in [7]. The overall uncertainty of dosimetric measurements with this system had been determined to be better than  $\pm 0.8$  dB [8].

The H-field measurements were performed with a new isotropic probe consisting of three orthogonally and concentrically arranged loops (deviation from isotropy:  $< 0.2$  dB). The 3.8 mm loops with resistively loaded detectors were designed to achieve optimal sensitivity in the desired frequency range of 300 MHz to 2.5 GHz. The calibration was performed with the same setup as described in [9] with a precision of better than  $\pm 0.5$  dB.

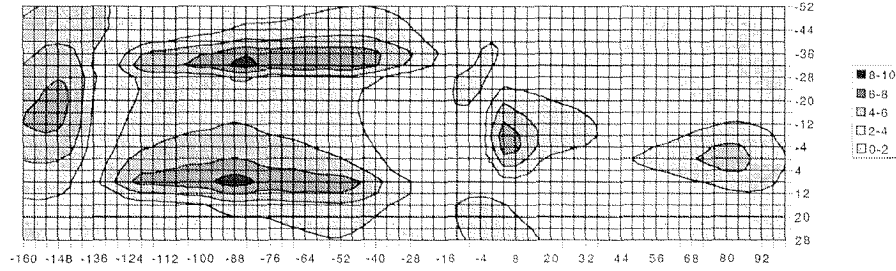


Figure 6.7: Difference between measured and simulated H-fields in percent, normalized to the maximum H-field.

## 6.4 Results

### 6.4.1 Free Space Evaluation

The simulated and measured gain of the far field is represented in a vertical cut (xz-plane) in Figure 6.2 and in a horizontal cut (yz-plane) in Figure 6.3. Simulated and measured far field data were normalized to their maximum values. Excellent agreement was found between simulation and measurement.

The E- and H-field distributions were determined in planes 5 and 19 mm above and parallel to the phone. In Figures 6.5 and 6.6 the simulated and measured H-field distribution at the distance of 5 mm are compared whereby the antenna input power was normalized to 1 W. Since the plots are almost identical, a differential plot reveals more information (Figure 6.7), i.e., indicates that the maximum difference is less than  $\pm 10\%$ , which only slightly exceeds the measurement uncertainty of  $\pm 7\%$ . These differences might also be partly due to the coupling between case and feeding cable. On the other hand, Figure 6.7 shows that these currents are small.

### 6.4.2 Near Field Evaluation with a Flat Absorbing Phantom

The SAR distribution was assessed numerically and experimentally with the phone at different distances  $d$  from the base plate of the flat phantom. The results for the distances  $d = 0$  and 26 mm are discussed here. In Figures 6.8 and 6.9 the results

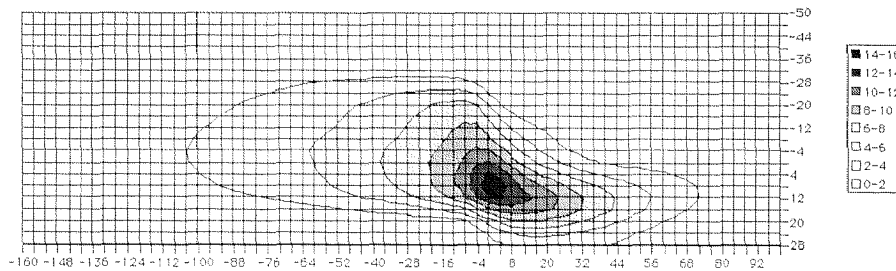


Figure 6.8: The difference between measured and simulated SAR distribution, measured 5 mm above the base plate of the flat phantom, in percent normalized to the maximum SAR. The phone is placed directly below the base plate.

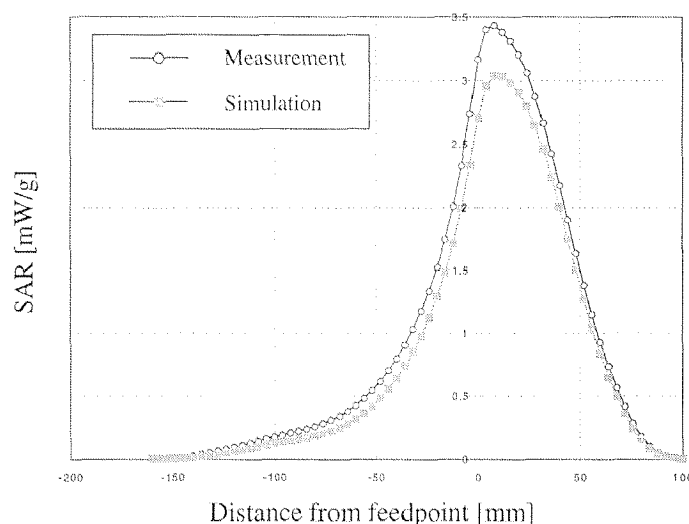


Figure 6.9: SAR distribution along a line parallel to the monopole, 5 mm above the base plate of the flat phantom, normalized to a feedpoint current of 100 mA. The phone is placed directly below the base plate.

are compared for  $d = 0$  mm, and in Figures 6.10 and 6.11 the same comparison is presented for the distance  $d = 26$  mm. In all cases the results had been normalized to a feedpoint current of 100 mA. In Table 6.1 the numerically and experimentally determined feedpoint impedances are shown. In all cases the absolute agreement is better than the absolute worst-case measurement uncertainty of  $\pm 0.8$  dB.

Nevertheless, some of the differences cannot be attributed to the measurement uncertainty alone, since the linearity of the measurement is considerably better (i.e.,  $< \pm 0.2$  dB) than the absolute uncertainty of  $\pm 0.8$  dB. Especially obvious is the relative differences in the distribution for the distance  $d = 26$  mm. A larger sensitivity to small differences in the modeling (e.g., tip of the antenna, edges, etc.) was expected due to the capacitive coupling at larger distances, whereas inductive coupling is dominant in the closest proximity of the scatterer.

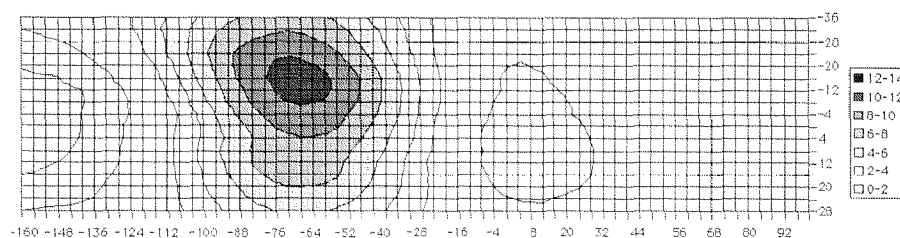


Figure 6.10: The difference between measured and simulated SAR distributions, measured 5 mm above the base plate of the flat phantom, in percent normalized to the maximum SAR. The distance between the phone and the flat phantom is 26 mm.

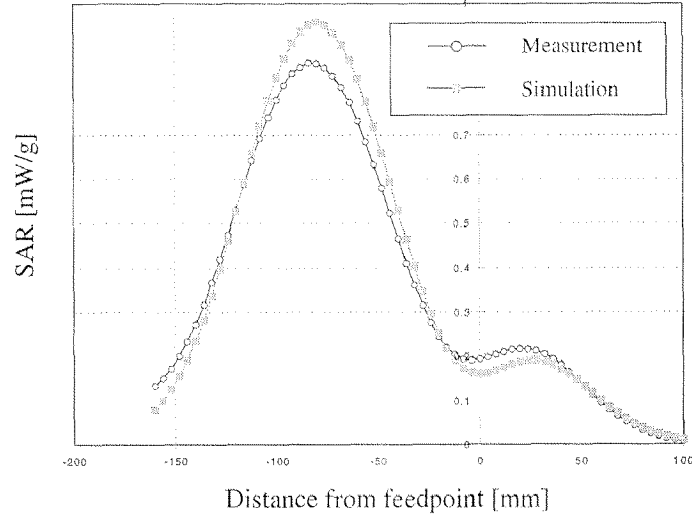


Figure 6.11: SAR distribution along a line parallel to the monopole, 5 mm above the base plate of the flat phantom, normalized to a feedpoint current of 100 mA. The distance between the phone and the flat phantom is 26 mm.

## 6.5 Conclusion

The good to excellent correspondence between measured and simulated antenna parameters reaffirms the suitability of FDTD techniques for simulating antennas in complex environments. For this simple FDTD adapted structure, slight differences were only observed in the intermittent distance from the scatterer, where the current distribution is very sensitive to the capacitive coupling with the environment. Specifically, the robustness of the simulations opens the possibility of automated modeling based on geometrical data, which is a basic condition for implementing an optimizer for antenna design.

However, testing compliance of existing phones with safety limits based on FDTD remains highly questionable, since the results must ensure that the exposure of the physical phone does not exceed the simulated values including the specified uncertainty values. The problem is the observed strong dependence of the current distribution on internal structures (see [5]). Even more difficult is the assessment of possible secondary effects (e.g., RF coupling between internal structures, non-perfect screening) which might become the dominant source of absorption.

d [mm]	Measured $Z$ [ $\Omega$ ]		Simulated $Z$ [ $\Omega$ ]	
	$Re\{Z\}$	$Im\{Z\}$	$Re\{Z\}$	$Im\{Z\}$
0	55	10.7	53	-9.8
26	85	-87	85	-93

Table 6.1: Feedpoint Impedance

## References

- [1] Daniel S. Katz, Melinda J. Piket-May, Allen Taflove, and Korada R. Umashankar, "FDTD analysis of electromagnetic wave radiation from systems containing horn antennas", *IEEE Transactions on Antennas and Propagation*, vol. 39, no. 8, pp. 1203–1212, Aug. 1991.
- [2] Michael A. Jensen and Yahya Rahmat-Samii, "Performance analysis of antennas for hand-held transceivers using FDTD", *IEEE Transactions on Antennas and Propagation*, vol. 42, no. 8, pp. 1106–1113, Aug. 1994.
- [3] Om P. Gandhi, Gianluca Lazzi, and Cynthia Furse, "Electromagnetic absorption in the human head and neck for mobile telephones at 835 and 1900 MHz", *IEEE Transactions on Microwave Theory and Techniques*, vol. 44, no. 10, pp. 1884–1897, Oct. 1996.
- [4] Michael Okoniewski and Maria A. Stuchly, "A study of the handset antenna and human body interaction", *IEEE Transactions on Microwave Theory and Techniques*, vol. 44, no. 10, pp. 1855–1864, Oct. 1996.
- [5] Achim Bahr, Ralf Kästle, Sheng-Gen Pan, Thomas Schmid, Thomas Becks, and Niels Kuster, "Numerical and experimental near-field evaluation of a dcs 1800 mobile telephone", *IEEE Radio Science*, vol. 33, no. 6, pp. 1553–1563, Nov. 1998.
- [6] CST, *The MAFIA collaboration, Mafia Version 3.x, User's Guide*, CST GmbH, Lautenschlägerstr. 38, D-64289 Darmstadt, 1994.
- [7] Thomas Schmid, Oliver Egger, and Niels Kuster, "Automated E-field scanning system for dosimetric assessments", *IEEE Transactions on Microwave Theory and Techniques*, vol. 44, pp. 105–113, Jan. 1996.
- [8] Niels Kuster, Ralph Kästle, and Thomas Schmid, "Dosimetric evaluation of mobile communications equipment with known precision", *IEICE Transactions on Communications*, May 1997, in press.
- [9] Klaus Meier, Michael Burkhardt, Thomas Schmid, and Niels Kuster, "Broadband calibration of E-field probes in lossy media", *IEEE Transactions on Microwave Theory and Techniques*, vol. 44, no. 10, pp. 1954–1962, Oct. 1996.



Seite Leer /  
Blank leaf

## Chapter 7

# Numerical and Experimental Dosimetry of Petri Dish Exposure Setups

*Abstract* - Crawford TEM cells are often used to expose cell cultures or small animals in order to study effects caused by high frequency fields. They are self-contained, easy-to-use setups which provide a rather homogeneous field distribution in a large area around its center, corresponding approximately to far-field conditions. However, a number of conditions must be met if such TEM cells are intended to be used for *in vitro* experiments. For instance, poor interaction with the incident field must be maintained in order to avoid significant field disturbances in the TEM cell. This is best achieved with E-polarization, i.e., when the E-field vector is normal to the investigated cell layer lining the bottom of a synthetic Petri dish. In addition, E-polarization provides the most homogeneous field distribution of all polarizations within the entire layer of cells. In this paper we present a detailed dosimetric assessment for 60 mm and 100 mm Petri dishes, as well as for a 48-well titer plate at 835 MHz. The dosimetry is performed by numerical computations. The modeling and the simplifications are validated by a second numerical technique and by experimental measurements. For thin liquid layers, an approximation formula is given with which the induced field strength for many other experiments conducted in Petri dishes can reliably be assessed.

### 7.1 Introduction

In bioelectromagnetics, *in vitro* biological experiments on cell cultures are often performed in Crawford transverse electromagnetic (TEM) cells [1]. Well-matched TEM cells provide a reasonably homogeneous field distribution in the area around its center. The power density can be easily regulated and monitored with the help of standard equipment. Further advantages are their relative affordability and ease of use, which allows well-controlled sham exposures since the field is guided within the TEM cell.

Nevertheless, TEM cells should only be used with caution for *in vitro* studies. The following must be considered carefully: 1) The TEM cell must be well matched; 2) The dimension of the Petri dish containing the medium with the cell culture should be smaller than the area of the homogeneous field distribution; 3) The field disturbances caused by the Petri dish should be negligible since any scattered field may generate standing waves or higher order nonsymmetric modes [2]; 4) If the Petri dish is placed too close to the walls or the septum of the TEM cell, the absorption may significantly differ from far-field exposure conditions due to additional coupling. If any of these conditions are not met, a well-controlled exposure is difficult to achieve. It would also require that the entire setup, i.e., Petri dish and TEM cell, including small position variations, needs to be considered in the dosimetric analysis.

A feasibility study performed at our laboratory in 1991 [3] has shown that TEM cells are suited for cell culture experiments if the Petri dishes are placed centered and parallel between the septum and the top wall of the TEM cell, whereby the layer of the medium should be kept thin. The reason for the choice of this setup is that the resulting E-polarization provides extremely small field distortions in comparison to H- and S-polarization.

The objective of this study is to verify these results and to perform the specific dosimetric assessment for three different Petri dishes used in a series of *in vitro* biological experiments that were performed at the Jerry L. Pettis Memorial Veterans Administration Medical Center in Loma Linda, California [4], [5], [6]. To ensure a high degree of reliability of the results, a fourfold approach was chosen. The basic assessment was performed using the numerical code MAFIA, based on the Finite Integration Technique (FIT) [7], [8]. The suitability of the modeling was verified by a second independent numerical approach and finally with measurements. In addition, the findings were generalized by an analytical approximation.

## 7.2 Problem Description

The biological experiments [4], [5], [6] were performed using standard Petri dishes. A given volume of isotonic medium was added to the layer of cells lining the bottom of the dish. The dishes were exposed to a narrow band signal at 835 MHz in the center of the standard TEM cell IFI-CC110s (Instruments for Industry Inc., Ronkonkoma, N.Y.) with the dimensions: 18 cm x 18 cm x 18 cm.

Three different standard dishes were used for the study: 60 mm and 100 mm Petri dishes and a 48-well titer plate. Their dimensions are shown in Figures 7.1 and 7.2. For the biological experiments 5 ml and 20 ml of medium were introduced into the 60 mm and 100 mm Petri dishes, respectively. This corresponds to a medium height of 2.4 mm and 3.4 mm. Each of the 48 wells was filled with 0.5 ml of medium, which is equivalent to approximately 4.8 mm of height.

Since the sensitivity of temperature probes for the given power levels is not sufficient to perform the experimental dosimetry in these thin layers of medium, the numerical modeling was validated using the 60 mm Petri dish filled with 20 ml (9.4 mm) of medium.

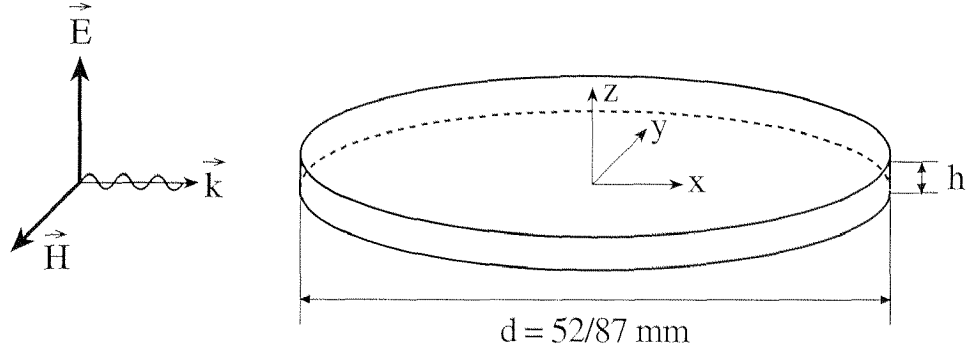


Figure 7.1: Modeling of the 60mm Petri dish filled with 5ml of medium ( $d = 52$  mm,  $h = 2.4$  mm) and the 100mm Petri dish filled with 20 ml of medium ( $d = 87$  mm,  $h = 3.4$  mm) and polarization of the plane wave excitation. The SAR is evaluated along a plane 0.2mm above the bottom.

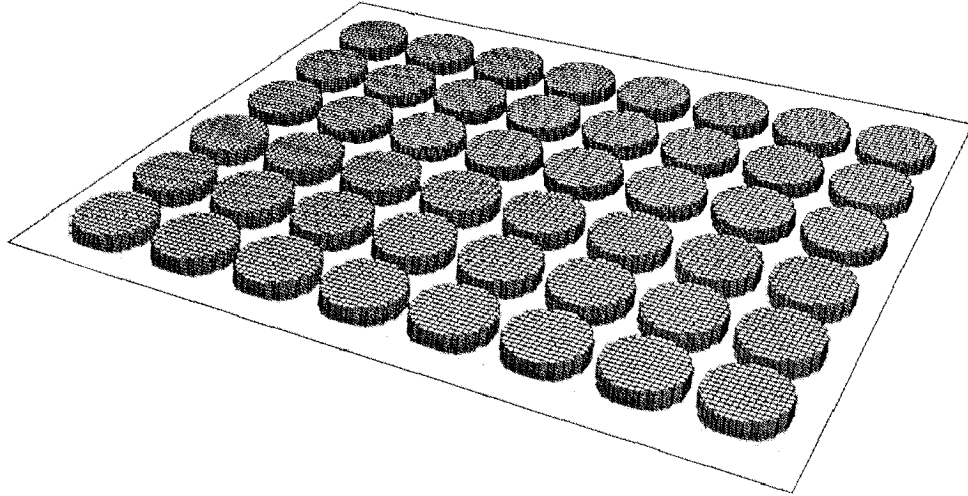


Figure 7.2: Modeling of the 48-well titer plate. The diameter of each well is  $d = 11.5$  mm and the separation is 1.8 mm. Each well is filled with 0.5 ml of medium, which corresponds to a medium height of 4.8 mm. Shown is the actual discretization used for the simulation with MAFIA.

### 7.3 Applied Numerical Techniques

Two electromagnetic simulation tools based on different techniques were used for the numerical dosimetry of the Petri dishes. While the simulation tool MAFIA is based on a Finite Integration Technique (FIT) [7], [8], the 3D MMP (Multiple Multipole) code is based on the semi-analytical Generalized Multipole Technique (GMT) [9], [10].

#### 7.3.1 MAFIA Code

The FI-technique transforms Maxwell's equations in integral form into equivalent Maxwell grid equations, whereby the resulting system of equations is similar to that

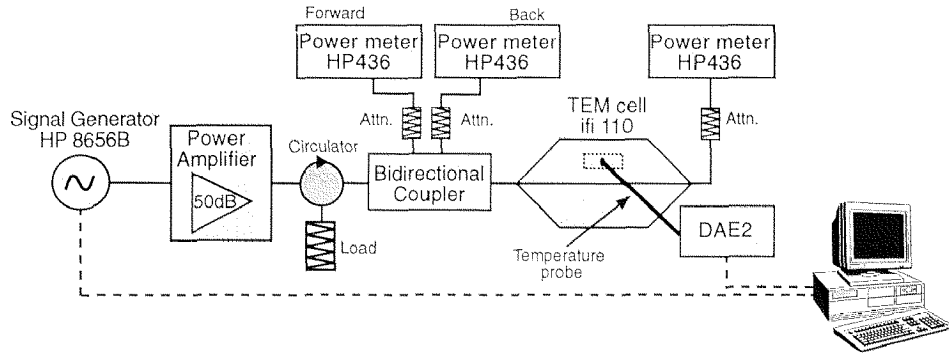


Figure 7.3: Setup used for the experimental dosimetry

of a FDTD approach. The entire computation domain must be discretized, and the scattering problem is solved in the time domain by the “leapfrog” algorithm.

In the first step only the medium exposed to a plane wave with E-polarization was studied (Figure 7.1), i.e., the Petri dish container and the coupling with the TEM cell walls were neglected. In the second step these simplifications were validated by simulating the Polystyrol container in addition to the medium, as well as the coupling between septum or walls and the Petri dish.

The Petri dishes and the well plate were discretized using a mesh with equidistant mesh steps. Due to the symmetries inherent in the structure, it was only necessary to model a quarter of the simplified problem. This was achieved by enforcing the tangentially electric respective magnetic field components at the symmetry planes to zero. If the septum was included in the model, half of the structure needed to be modeled. In order to avoid reflected waves from the open boundaries, first order Mur-absorbing boundary conditions were applied. The number of mesh cells was varied between 200,000 and 500,000 for the whole computation domain and between 40,000 and 80,000 for the simulated medium. This is equivalent to a voxel size of about  $0.6 \times 0.6 \times 0.2 \text{ mm}^3$  to  $0.6 \times 0.6 \times 0.4 \text{ mm}^3$  for the medium. The dimensions of the computation domain were  $160 \times 80 \times 60 \text{ mm}^3$ . The largest allowable simulation time-step was determined by MAFIA applying the Courant-Friedrichs-Levy-Criterion [11] for finite difference methods. The calculation was performed for 8-12 periods to ensure that a steady state had been reached. The 48-well titer plate was simulated in the same manner as the Petri dishes. Due to the larger dimensions of the plate, the computation domain had to be enlarged. It consisted of about 750,000 mesh cells and about 80,000 cells for the plate itself. The plate, as modeled with MAFIA, is represented in Figure 7.2.

### 7.3.2 3D MMP Code

The 3D MMP code based on GMT has proven to be well suited for 2D and 3D scattering problems which may consist of a moderate number of piecewise linear, homogeneous and isotropic domains. The technique approximates the unknown field in each domain by several sets of functions which are analytical solutions of Maxwell’s equations. The implemented functions are finite series of spherical multipoles, line multipoles, ring multipoles, normal expansions, plane waves, waveguide modes, etc.

and may be placed at different origins. The unknown amplitudes of these functions are numerically evaluated by enforcing the boundary conditions on discrete points at the boundaries, whereby 3 to 10 times more points than unknowns are used. The concept of weighting the matrix lines is derived from the energy concept. This results in an efficient tool for solution validation within the code. The code has been successfully applied in several dosimetric studies [12], [13].

Only the 60 mm Petri dish filled with 10 ml and 20 ml was simulated, due to the difficulties of this code in handling extremely thin dishes. Multipoles and line multipoles, as well as ring multipoles were used. The dishes were discretized with about 700 matching points.

## 7.4 Experimental Setup

The setup used for the experimental dosimetry was essentially the same as that used for the biological experiments, as illustrated in Figure 7.3. However, the TEM cell IFI-CC110 (dimensions: 18 cm x 18 cm x 12 cm) which is smaller than the IFI-CC110s but provides a considerably better field homogeneity was used. The maximum power applicable at the input of the TEM cell was 48.2 dBm (i.e., 66 W), resulting in a power density in the center of the TEM cell of approximately 240 mW/cm<sup>2</sup>. The reflections were less than -25 dB both with and without the presence of the dish inside the TEM cell. In addition, the electric and magnetic field distribution in the TEM cell, in an area larger than the Petri dish, was measured using the electromagnetic scanner described in [14]. The homogeneity was found to be better than  $\pm 0.2$  dB.

### 7.4.1 Temperature Probes

Temperature or E-field probes are only suited for this assessment if they meet the following requirements: 1) high spatial resolution; 2) high sensitivity and 3) operational ability in a strong field environment. Although E-field probes are generally more sensitive than temperature probes, they are not suitable for this assessment mainly due to their spatial dimensions, which are greater than 0.1 cm<sup>3</sup>. The only temperature probe available which sufficiently met all of the above mentioned requirements (Table 7.1) was a prototype developed by Schmid & Partner Engineering AG (SPEAG, Zurich, Switzerland) which is based on the Bowman probe [15]. Its high sensitivity is achieved by specialized electrometer grade amplifiers and sophisticated software for filtering and data evaluation. The probe was calibrated prior to the measurements in water baths at 10 different temperatures in the range from 10° to 60° C. The response is linearized by a polynomial function. The software further enables the evaluation of the temperature increase by linear regression. The noise level and short term drifts over two-minute periods with a sampling rate of 10 samples per sec were determined to be within  $\pm 0.005^\circ\text{C}$  and the sensitivity for 10 s of exposure to be 0.15 mK/s. By exposing the first 6 cm of the resistive lines from the tip of the probe to an incident field of 950 V/m inside the TEM cell, the sensitivity to RF exposure at 835 MHz was assessed to be less than 0.5 mK/s for the line parallel to the E-field vector and less than 0.1 mK/s for the line normal to the E-field vector.

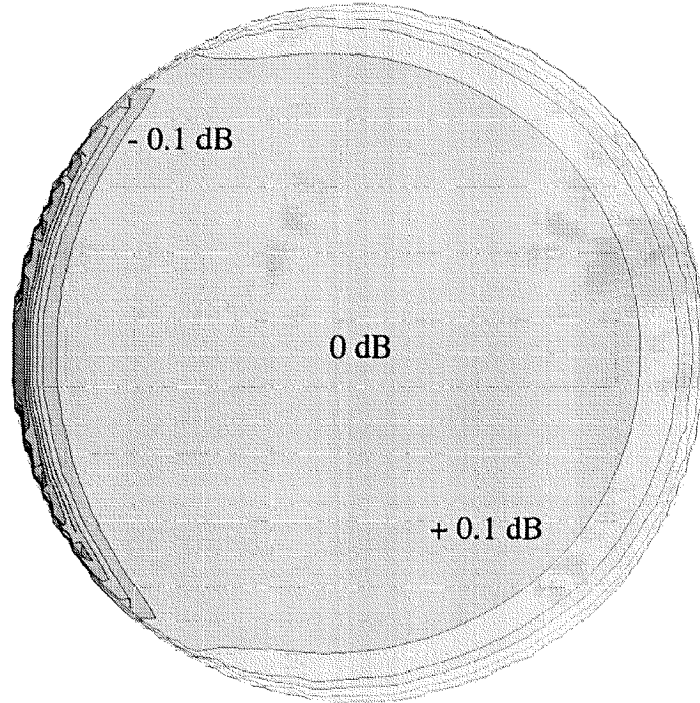


Figure 7.4: SAR distribution in a horizontal layer located 0.2 mm from the bottom of the 60 mm Petri dish. The dish contains 5 ml of medium. The SAR value in the center of the dish is 3.6 mW/kg.

## 7.5 Results

Samples of the media used in the biological experiments [4], [5], [6] were made available and used for the experimental dosimetry. The electrical parameters of the different media were measured by the HP 85070A dielectric probe kit in the temperature range of 20° - 40° C. They were determined to be  $\epsilon_r = 76 \pm 5$  and  $\sigma = 1.8 \pm 0.3$  S/m. The dosimetric assessments were performed with the MAFIA code for three different kinds of Petri dishes: 1) the 60 mm Petri dish filled with 5/10/20 ml of medium, 2) the 100 mm Petri dish filled with 20 ml of medium and 3) the 48-well titer plate, with each well filled with 0.5 ml. In the first step only the simplified model was studied, i.e., only the medium exposed to far-field conditions with E-polarization. The specific mass density of the medium was chosen to be 1 g/cm<sup>3</sup>. All SAR values were normalized to a power density of 1 mW/cm<sup>2</sup>.

The results were evaluated in a layer parallel to and at a distance of 0.2 mm from the bottom of the Petri dish. The average SAR values and the standard deviations in these planes are given in Table 7.2, and the SAR distributions for the different kinds of Petri dishes are represented in Figures 7.4, 7.5 and 7.6. As expected, enhanced values for the thin layers are found close to the edges along the curved outer surface of the dish (where the E-field is parallel to the surface). Local SAR disturbances

	Model 755 LUXTRON Mountain View, CA	Model 1400 PHOTONETICS Woodinville, WA	Prototype SPEAG Zurich, CH
Noise level/Short term drifts over 2 min periods	$\pm 0.1^\circ\text{C}$ (1 sample/sec)	$\pm 0.1^\circ\text{C}$	$\pm 0.005^\circ\text{C}$ (10 samples/sec)
Sensitivity (10s of exposure)	$\pm 15\text{mK/s}$	$\pm 10\text{mK/s}$	$\pm 0.15\text{mK/s}$
Sensitivity to RF exposure (835 MHz)			
- resistive lines parallel to E-field	not sensitive	not sensitive	$< 0.5 \text{ mK/s}^a$
- resistive lines normal to E-field	not sensitive	not sensitive	$< 0.1 \text{ mK/s}^a$

Table 7.1: Comparison of available temperature probes. <sup>a</sup>Measured by exposing the first 6 cm of the line from the tip to an incident field of 950 V/m.

Cell Dish	average SAR per 1mW/cm <sup>2</sup>	Standard deviation
60mm Petri dish (5 ml)	2.6 mW/kg	8% (0.2 mW/kg)
100mm Petri dish (20 ml)	6.6 mW/kg	10% (0.7 mW/kg)
48-Well titer plate (0.5 ml)	9.5 mW/kg	30% (2.9 mW/kg)

Table 7.2: Average SAR Values in the plane  $z = 0.2 \text{ mm}$ , calculated using MAFIA. The outer ring of 2 mm thickness is not considered in this evaluation. Note: The given deviation is a measure of the nonhomogeneity of the exposure and does not reflect any uncertainties inherent in the modeling or simulations.

might also be caused due to the adhesion effects in the closest vicinity of the side wall. In case of the well plate these border effects are of greater importance, due to the small diameter of a single well. Therefore the cells located within 2 mm of the side wall of the dish should not be evaluated. This outer ring was also not evaluated for the standard deviation analysis in Table 7.2.

## 7.6 Validation

Since most numerical techniques do not provide a reliable assessment of modeling and simulation errors and since the possible sources of errors are numerous, the correct modeling of any particular problem must be validated. Furthermore, it must be demonstrated that the simplifications made do not misrepresent the actual exposure conditions.



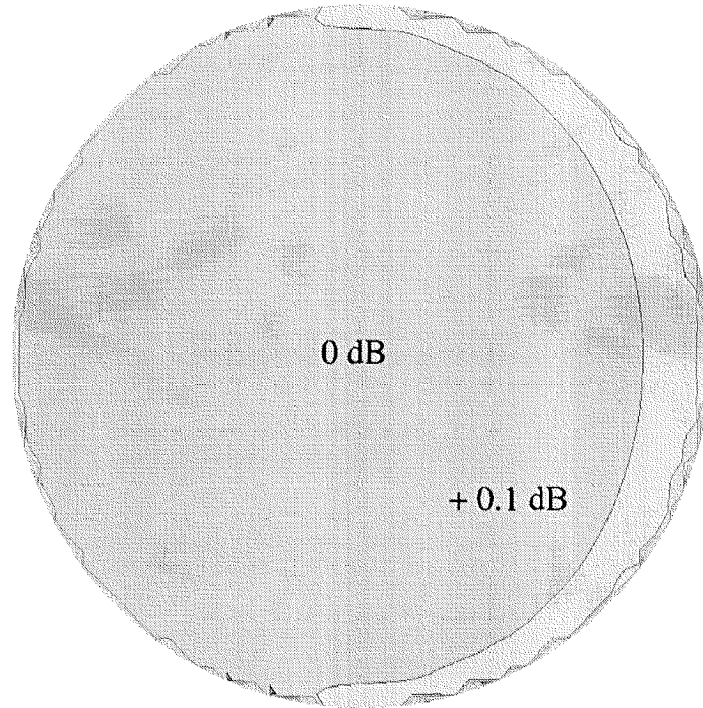


Figure 7.5: SAR distribution in a horizontal layer located 0.2 mm from the bottom of the 100 mm Petri dish. The dish contains 20 ml of medium. The SAR value in the center of the dish is 6.7 mW/kg.

### 7.6.1 Validation of modeling

The numerical results showed that the validation cannot be directly performed by experimental means. The reasons are that only a small temperature increase of about 0.15 mK/s can be expected at the maximum available input power of 48 dBm and that the enhanced noise and short term drifts occur close to such large surfaces (cooling by air fluctuations, evaporation, etc.). In addition, the induced E-field values are strongly non-uniform with respect to the z-axis.

A better signal-to-noise ratio could be expected with a quadrupling of the medium height, since the induced SAR levels at the surface of the dish are approximately proportional to the square of the thickness. However, such a setup would still have about the same characteristics as the original setup, i.e., slight disturbance of the field in the TEM cell and minimal thickness compared to the x-y dimensions. Thus, the experimental validation of the MAFIA modeling was performed using the 60 mm Petri-dish filled with 20 ml of medium.

The setup used for the experimental validation is represented in Figure 7.3. The Petri dish was placed in the center between the septum and the top wall of the TEM cell using spacers. Optical probes would have been ideal since the measurements needed to be performed in a high field strength environment ( $E_{\text{external}}^2/E_{\text{internal}}^2 >$

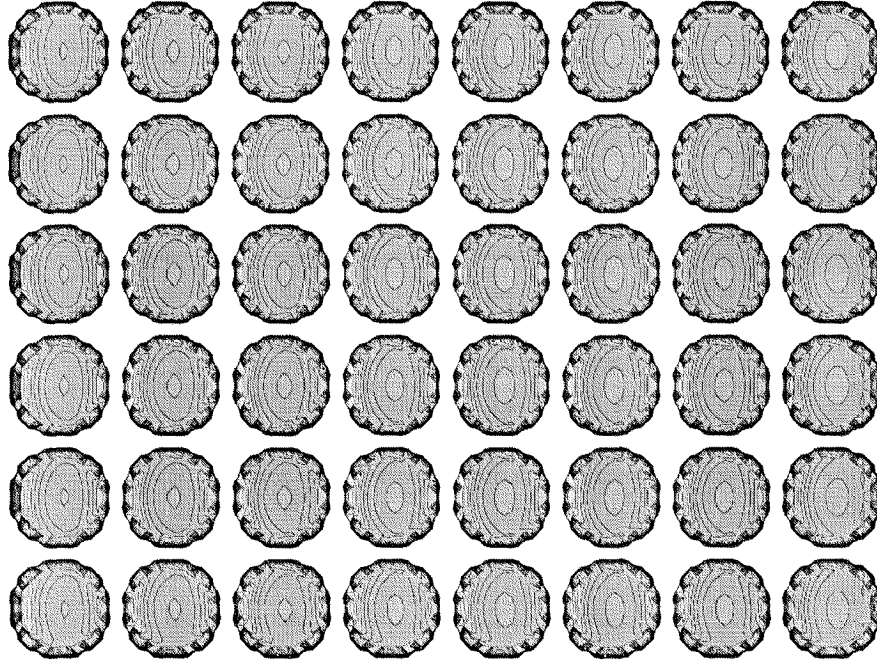


Figure 7.6: SAR distribution in a horizontal layer 0.2 mm from the bottom of the 48-Well titer plate. Each of the 48 wells contains 0.5 ml of medium. The SAR value in the center of the middle wells is 11.6 mW/kg. Each isoline represents a decay of -0.5 dB.

100). However, only the SPEAG probe provides the required sensitivity of less than 1 mK/s. In order to minimize the coupling of the lines with the external E-field, the probe was introduced through a hole in the sidewall of the dish. For the short distance from the dish to the door opening of the TEM cell, the resistive lines of the probe were protected and thermally stabilized by a thin metal tube. Since the tube was perpendicular to both the E-field and the S-vector, the field disturbances were slight. The tip of the probe was placed in the center of the dish and the vertical distance was varied using spacers. Since the medium basically consisted of water and salt, a specific heat capacity of 4.2 J/g/K was assumed.

The same dish was simulated by MAFIA and 3D MMP. The results are compared in Figure 7.7 to 7.11. The agreement between the two numerical techniques is good, although in the case of the 3D MMP simulation, the edges had to be rounded because of problems with sharp edges inherent in the simulation technique. The measured

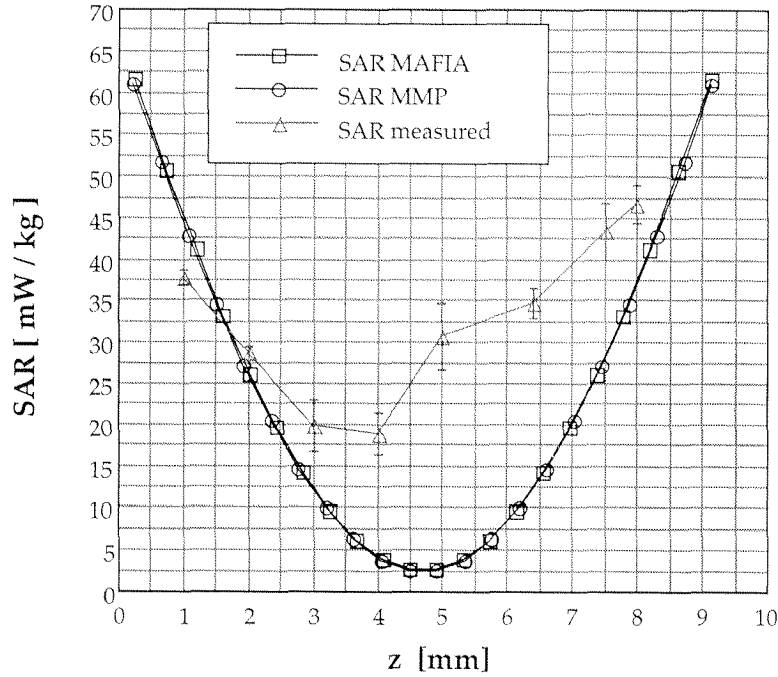


Figure 7.7: SAR distribution in the center of the 60 mm Petri dish filled with 20 ml of medium. Compared are the results obtained using the MAFIA and 3D MMP codes and from the experimental approach. The error bars of the experimental data only represent the standard deviation of a number of measurement samples, i.e., they are an indication of the noise level and do not include systematical errors.

values deviate from those values, although the general quantitative agreement is satisfactory (Figure 7.7). These deviations can be explained by the experimental difficulties: 1) induced temperature increase in the range of the thermal noise inherent in the system; 2) extremely nonhomogeneous spatial SAR distribution; 3) medium with high conduction and convection effects.

In Table 7.3, the MAFIA and 3D MMP results are compared in points 0.2 mm above the surface. In Figures 7.8 and 7.9, the cross-sectional SAR distributions are compared. In Figures 7.10 and 7.11, those of the vertical plane 0.2 mm from the bottom of the Petri dish are given. The SAR enhancements on the sidewalls of the Petri dish (Figure 7.9) can also be seen in the plane of the cell layer for smaller medium heights (Figures 7.4, 7.5), because the evaluated plane is closer to the middle of the Petri dish. In addition, border effects become more important for small medium heights (Figures 7.4, 7.5). The good agreement between the results obtained by MAFIA and 3D MMP and the good quantitative agreement with the measured results show the suitability of the MAFIA code and of the chosen discretization for this problem.

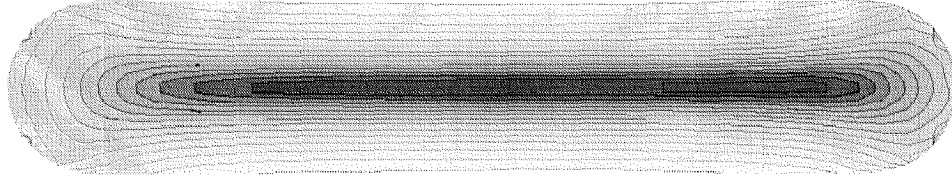


Figure 7.8: 3D MMP result: SAR distribution in the cross section ( $y=0$ ) of the 60 mm Petri dish containing 20 ml of the medium. Each isoline represents a decay of -1 dB; the SAR value in the middle of the surface is 61.7 mW/kg.

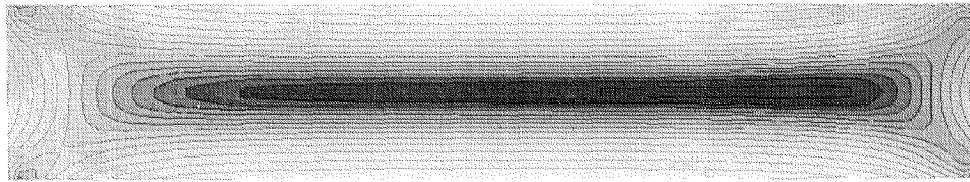


Figure 7.9: MAFIA results: SAR distribution in the cross section ( $y=0$ ) of the 60 mm Petri dish containing 20 ml of the medium. Each isoline represents a decay of -1 dB; the SAR value in the middle of the surface is 61.6 mW/kg.

### 7.6.2 Validation of Simplifications

The totally absorbed power of the 60 mm Petri dish filled with 20 mm of medium is less than 1%. Since the absorbed power drops drastically with the layer thickness  $h$  ( $\approx h^{-3}$ ) and the cross section is proportional to  $1/h$ , the Petri dish does not cause any significant distortion of the field in the TEM cell. This has also been verified by comparison of the reflected power with and without the dish. Hence, plane wave excitation is a valid simplification, if the Petri dish is placed in the middle between septum and top/bottom wall of the TEM cell.

The minimum distance of the Petri dish from the septum at which the coupling can be neglected was assessed by simulating various distances of the dish from a perfectly conductive plane. At a distance of 10 mm from the septum, using a 60 mm Petri dish filled with 5 ml of medium, the change of the SAR values was found to be less than 2% for the cells lining the bottom. Therefore, the coupling with TEM cell walls can be neglected for all studied cell cultures if the dishes are placed in the middle between septum and top/bottom wall of the TEM cell. When the Petri dish is not placed in the center but directly on the septum or bottom wall of the TEM cell, the problem is – at first approximation – equivalent to the same dish but with the double thickness, i.e., the induced field is strongly reduced to approximately the capacitive part at the bottom and increased up to about the fourfold at the top. In addition, the enhancement at the side walls of the dish is more pronounced for the bottom layer. The 60 mm Petri dish filled with 5 ml and 20 ml of medium, including a Polystyrol container ( $\epsilon_r = 2.6$ ,  $\sigma = 0$  S/m), was simulated to check if the container itself alters the absorption. The effect has been assessed to be less than 10% for small medium heights and smaller for increasing medium heights for the cells lining the bottom of the Petri dish ( $< 10\%$  for 5 ml,  $< 1\%$  for 20 ml). Thus the effect can be neglected for the experimental dosimetry, but becomes more important for

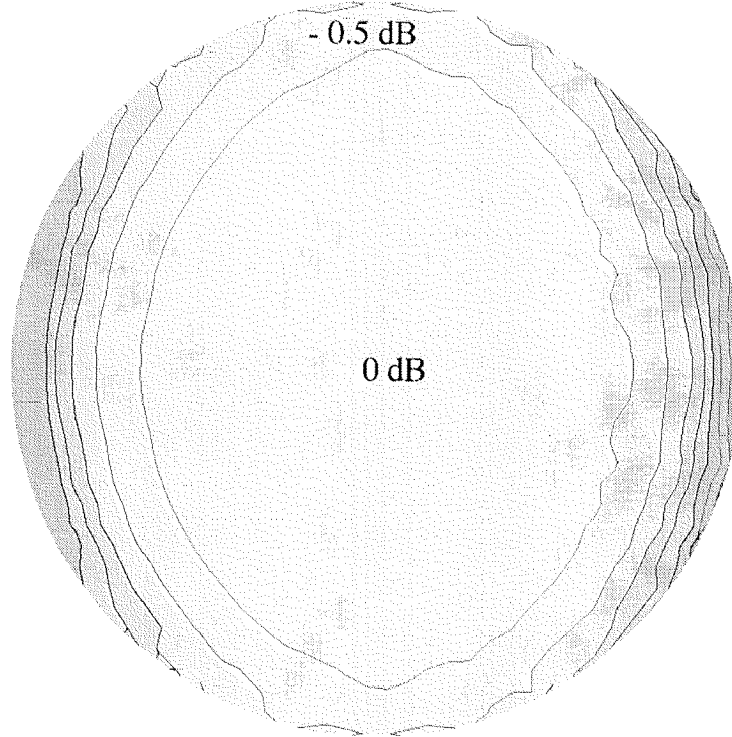


Figure 7.10: 3D MMP result: SAR distribution in the layer  $z = 0.2$  mm from the bottom of the Petri dish, filled with 20 ml of medium. The SAR value in the center of the dish is 61.7 mW/kg. Each isoline represents a decay of -0.5 dB.

Point	3D MMP	MAFIA
(24,0, $z_0$ )	–	23.0 mW/kg
(12,0, $z_0$ )	59.4 mW/kg	59.8 mW/kg
(0,0, $z_0$ )	61.7 mW/kg	61.6 mW/kg
(-12,0, $z_0$ )	58.9 mW/kg	58.8 mW/kg
(-24,0, $z_0$ )	–	15.4 mW/kg
(0,12, $z_0$ )	60.3 mW/kg	60.4 mW/kg
(0,24, $z_0$ )	–	50.7 mW/kg
(12,12, $z_0$ )	55.7 mW/kg	56.2 mW/kg
(-12,12, $z_0$ )	54.3 mW/kg	54.8 mW/kg

Table 7.3: MAFIA results versus 3D MMP results of the 60 mm Petri dish containing 20 ml of medium. Note:  $z_0$  is 0.2 mm from the bottom.

extremely small medium heights.

### 7.6.3 Analytical Approximation

An attempt was made to derive an approximation formula of the SAR distribution in the middle of the Petri dish along the  $z$ -axis (Figure 7.1), since the coupling

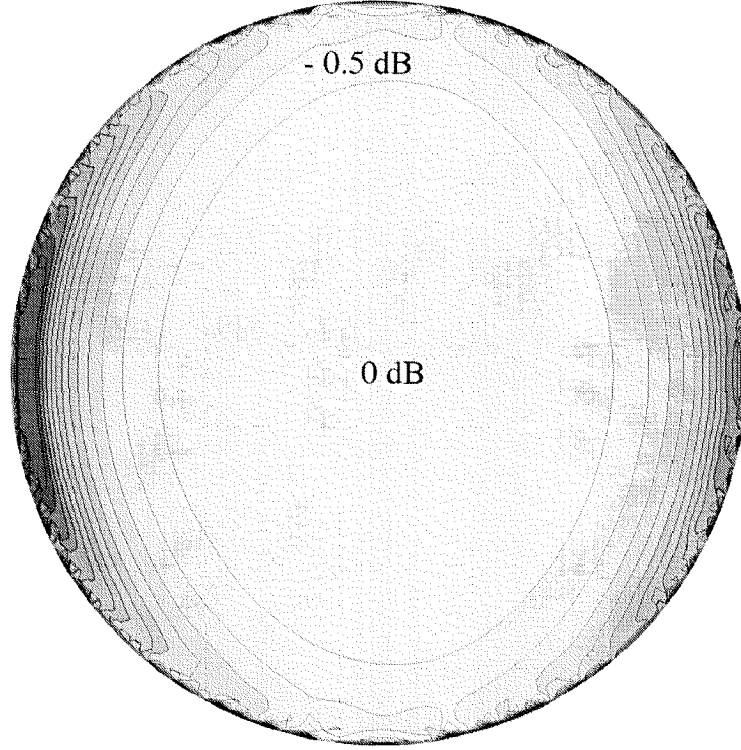


Figure 7.11: MAFIA result: SAR distribution in the layer  $z = 0.2$  mm from the bottom of the Petri dish, filled with 20 ml of medium. The SAR value in the center of the dish is 61.6 mW/kg. Each isoline represents a decay of -0.5 dB.

of the scatterer with the field is poor and the numerical results suggest a quasi-static approach, i.e., separation between “capacitive” and “inductive” coupling. The geometry can be simplified to that of a thin conductive sheet, since the height of the medium in the Petri dish is small compared to the  $x$  and  $y$  dimensions. The capacitively induced part of the  $E$ -field is normal and the inductively induced part parallel to the surface of the Petri dish.

Let us assume the center of the bottom of the Petri dish to be at the origin of our cartesian coordinate system as indicated in Figure 7.1. The absolute value of eddy currents caused by an incident time-dependent magnetic field can be described within a thin conductive sheet by [16]:

$$|J| = A \sqrt{\cosh(2kz') - \cos(2kz')} \quad (7.1)$$

where  $k$  is the wave number inside the medium,  $z' = z - h/2$  and  $A$  a constant. Assuming further that  $kh \ll 1$  we can approximate equation (7.1) and arrive at an expression for the dependency of the electric field caused by inductive coupling along the  $z$ -axis:

$$|E_{ind}| = \frac{A}{\sigma} (2kz') \quad (7.2)$$

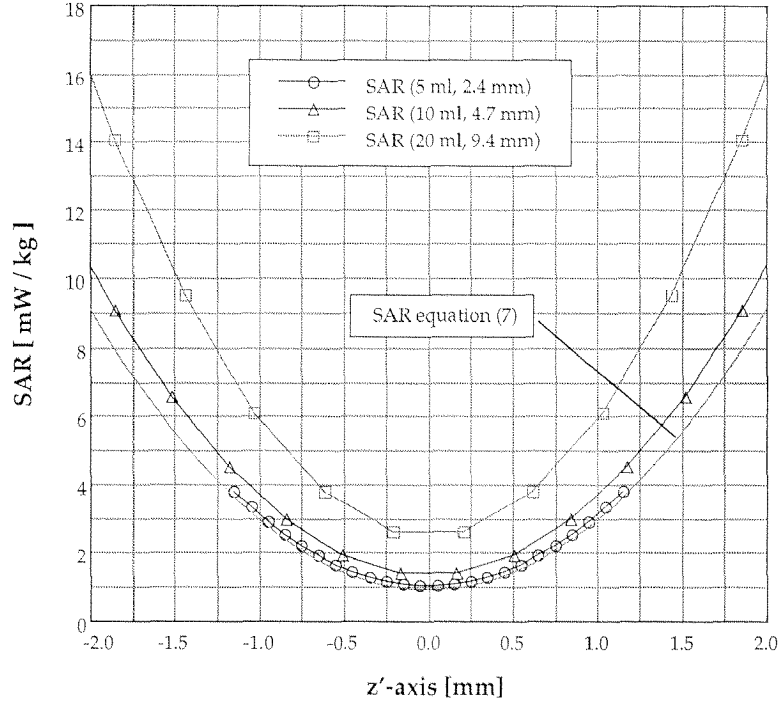


Figure 7.12: SAR distribution along the  $z'$ -axis of the simulations and of the analytical expression (7).

The maximum absolute value of this electric field will occur on the surface of the sheet and can be derived from Faraday's equation in integral form.

$$\oint_{\partial S} \vec{E}(\vec{r}, t) d\vec{s} = \frac{d}{dt} \iint_S \mu \vec{H}(\vec{r}, t) d\vec{S} \quad (7.3)$$

In a first approximation, the integral parts for the  $E_{ind}$ -field along the  $z$  direction are neglected, and if  $kh \ll 1$  the  $H$ -field throughout the dish can be approximated as being equal to the incident  $H_{inc}$ -field. With these assumptions, the inductively induced  $E_{ind}$ -field at the location  $z' = h/2$  can be approximated as:

$$|E_{ind}(z')|_{z'=\frac{h}{2}} = \frac{\mu\omega h}{2} |H_{inc}| \quad (7.4)$$

Introducing equation (7.4) into equation (7.2) results in:

$$|E_{ind}| = \mu\omega z' |H_{inc}|. \quad (7.5)$$

The capacitively induced electric field  $E_{cap}$  can be simply described by:

$$|E_{cap}| = \frac{|E_{inc}|}{|\epsilon_k|} \quad (7.6)$$

with  $\epsilon_k = \epsilon_r - j\sigma/(\epsilon_0\omega)$ . Hence, the SAR induced throughout the Petri dish can be estimated as:

$$\begin{aligned} SAR(z') &= \frac{\sigma}{\rho} \left( |E_{ind}|^2 + |E_{cap}|^2 \right) \\ &= \frac{\sigma}{\rho} |E_{inc}|^2 \left( \left( \frac{\mu\omega z'}{Z_0} \right)^2 + \frac{1}{|\epsilon_k|^2} \right) \end{aligned} \quad (7.7)$$

where  $Z_0 = 377\Omega$ . In Figure 7.12, the approximation (7.7) is compared with the simulated SAR distribution of the Petri dishes for different heights of the medium (f=835 MHz). Expression (7.7) describes very closely the SAR distribution in the Petri dish for small heights. To verify the approximation for different media and different frequencies, the 60 mm Petri dish was simulated with 5 ml of medium ( $\epsilon_r = 40$  and  $\sigma = 0.8$  S/m) at a frequency of 600 MHz. Again, a good agreement was found.

## 7.7 Conclusions

The suitability of using Crawford TEM cells for *in vitro* experiments has been analyzed and discussed. The SAR distributions and the average SAR values for three different Petri dishes have been determined by numerical simulations. These dishes had been used for different experiments as reported in [4], [5], [6]. The modeling and simplifications have been validated. In addition, a simple approximation has been given, allowing the assessment of the induced field levels for a wide range of experiments conducted in Petri dishes exposed to E-polarization.

To perform well-controlled biological experiments, only well-matched TEM cells should be used, i.e., return loss  $> 20$  dB. The size of the Petri dish should not be larger than the area of homogeneous field distribution and the dish must be placed in the center of the TEM cell, i.e., between the septum and the top wall. The amount of medium added to the cell layer must be determined with great precision due to the high dependence of the induced fields in the cell layer to the medium height. A large height to diameter ratio causes higher SAR values in the plane of the cell layer, but also much higher variation of the SAR in this plane. In case of the well plate, the SAR distribution in the plane of the cell layer is less homogeneous, due to the small diameter. Furthermore, the cells close to the curved dish border should not be considered because of higher induced fields due to border effects. It should also be noted that the incident H-field is scarcely altered throughout the dish.



## References

- [1] Myron Crawford, "Generation of standard EM fields using TEM transmission cells", *IEEE Transactions on EMC*, vol. 16, no. 4, pp. 189–195, Nov. 1974.
- [2] Luc Martens, J. Van Hese, D. De Zutter, C. De Wagter, L. Malmgren, B.R.R. Persson, and L.G. Salford, "Electromagnetic field calculations used for exposure experiments on small animals in TEM-cells", *Bioelectrochemistry and Bioenergetics*, vol. 30, pp. 73–81, 1993.
- [3] Niels Kuster, "Dosimetric assessment for the cell dish experiment", Tech. Rep. Immediate report No.3, Laboratory of EMF and Microwave Electronics, ETH-Zurich, 1991.
- [4] W.R. Adey, R.B. Stagg, and W.J. Thomas, "DNA synthesis and cell proliferation in C6 glioma and primary glial cells exposed to a 837 MHz modulated radiofrequency field", *Journal of the Bioelectromagnetics Society*, 1996, submitted.
- [5] W.R. Adey, C.D. Cain, and D.L. Thomas, "Cellular radiofrequency fields and in vitro tumor promotion", *Journal of the Bioelectromagnetics Society*, 1996, submitted.
- [6] J.L. Phillips, O.I. Ivaschuk, and W.R. Adey, "Exposure of nerve growth factor-treated PC12 rat pheochromocytoma cells to a modulated radiofrequency field at 836.55 MHz: Effects on c-jun and c-fos expression", *Journal of the Bioelectromagnetics Society*, 1996, submitted.
- [7] T. Weiland, "Maxwell's grid equations", *Frequenz*, vol. 44, no. 1, pp. 9–16, 1990.
- [8] CST, *The MAFIA collaboration, Mafia Version 3.x, User's Guide*, CST GmbH, Lautenschlägerstr. 38, D-64289 Darmstadt, 1994.
- [9] Ch. Hafner and Lars H. Bomholt, *The 3D Electrodynamic Wave Simulator*, New York: John Wiley & Sons Inc., 1993.
- [10] Niels Kuster, "Multiple multipole method for simulating EM problems involving biological bodies", *IEEE Transactions on Biomedical Engineering*, vol. 40, no. 7, pp. 611–620, July 1993.
- [11] A.Taflove and K.Umashankar, "Numerical solution of steady-state electromagnetic scattering problems using the time-dependent maxwell's equations", *IEEE Transactions on Microwave Theory and Techniques*, vol. 23, no. 8, pp. 1248–1257, Aug. 1987.
- [12] Niels Kuster and Quirino Balzano, "Energy absorption mechanism by biological bodies in the near field of dipole antennas above 300 MHz", *IEEE Transactions on Vehicular Technology*, vol. 41, no. 1, pp. 17–23, Feb. 1992.
- [13] Niels Kuster, "Multiple multipole method applied to an exposure safety study", in *ACES Special Issue on Bioelectromagnetic Computations*, A.H.J. Fleming and K.H.Joyner, Eds., vol. 7, pp. 43–60. Applied Computational Electromagnetics Society, No. 2, 1992.

- [14] Thomas Schmid, Oliver Egger, and Niels Kuster, "Automated E-field scanning system for dosimetric assessments", *IEEE Transactions on Microwave Theory and Techniques*, vol. 44, pp. 105–113, Jan. 1996.
- [15] Ronald R. Bowman, "A probe for measuring temperature in radio-frequency-heated material", *IEEE Transactions on Microwave Theory and Techniques*, vol. 24, no. 1, pp. 43–45, 1976.
- [16] K. Simonyi, *Theoretische Elektrotechnik*, VEB Deutscher Verlag der Wissenschaften, 1989.

Seite Leer /  
Blank leaf

## Chapter 8

# Exposure Setup to Test CNS Effects of Wireless Communications Systems

*Abstract* - In this chapter an *in vivo* exposure system is presented and analyzed which was designed to test the possible CNS effects of wireless communications systems operating at the frequency band of 900 MHz. It allows the simultaneous exposure of ten rats. They are restrained in tubes that are placed radially around a dipole antenna, with the heads directed toward the antenna. The dosimetric analysis of the setup was performed by numerical and experimental means for rats weighting 250 - 300 g. The results document the suitability of the setup for CNS studies. It enables the induction of well defined field strengths in the brain tissue, whereby variations of the brain average SAR due to movement and different animal sizes are less than  $\pm 16\%$ . The SAR distribution in the brain is nonuniform but comparable to that induced in the brain of a human using a handheld wireless phone. The efficiency is about  $0.20 \pm 0.05$  mW/cm<sup>3</sup> (brain average) per 100 mA feedpoint current. As desirable, the whole-body average SAR is considerably lower, i.e., about half of that of the brain averaged value. In addition, the setup has proven to be practical in use and the induced stress levels from restraint of the animal in the setup is considered to be minor by neurologists and veterinary scientists.

### 8.1 Introduction

The phenomenal worldwide growth in wireless communications and accompanying proliferation and sharp increase of radio frequency (RF) exposure of their users has attracted the attention of the public, media and health agencies, regarding the possible adverse health effects of this technology. Since previous experiments have provided some indication of the sensitivity of the central nervous system (CNS) to specific RF exposure [1], the initial emphasis was put on studying the possible adverse health effects of wireless communications systems on the brain.

In this paper an *in vivo* exposure setup for testing the hypothesis of possible

CNS effects which might occur during use of handheld mobile telecommunications equipment (MTE) operating at the 900 MHz band is presented and analyzed. The basic demands on such an exposure system are: (1) similar signal characteristics, (2) similar field strengths and (3) similar SAR distribution in the brain tissue of the animal as is actually induced in the human brain during daily life use of handheld MTE; (4) low exposure in the rest of the body and (5) low stress levels caused by the exposure setup. For example, if the latter two points are poorly satisfied, the CNS effects might be masked by other effects, such as whole-body heating or stress caused by restraint of animal movement. Furthermore, the exposure setup must be practical to use and of reasonable cost.

In 1992 a project group of engineers, neurologists and veterinary scientists suggested the setup described below to expose rats in the near field of a dipole antenna. It was predicted, on the basis of the absorption mechanism in the near field of sources [2], that the induced absorption in the brain is considerably larger than the whole-body average absorption. Since these assumptions were confirmed by a preliminary dosimetric assessment [3] and initial tests also showed that the setup is suitable with regard to animal stress and practicability, several experiments were carried out using basically identical setups; Among them life long brain tumor promotion studies (e.g., [4]) and studies on acute CNS effects (e.g., [5]).

The purpose of this study is to obtain a detailed dosimetric analysis of the setup. This includes the determination of the ratio of induced field strengths to the antenna input power, the distribution of the absorption in the brain and trunk of the animal as well as an uncertainty analysis with respect to modeling, anatomy, position, movement and weight of the animals. The study was conducted both numerically and experimentally.

## 8.2 Exposure Setup

Figure 8.1 shows the near-field exposure setup used to test acute CNS effects of GSM exposure [4]. GSM is a worldwide digital cellular telecommunications standard (multiple access: time-domain multiple access (TDMA); RF carrier frequency: 900 MHz, repetition frequency: 217 Hz, duty cycle: 1:8). Ten male Wistar rats of 4 month of age and weighting 250 - 300 g were positioned around a symmetrical, sleeved dipole optimized for the carrier frequency of 900 MHz. Since the induced field distribution and strength strongly depend on the distance and orientation with respect to the antenna, the animals had to be restrained in tubes. To prevent them from moving backwards, they were kept in place by radially shiftable pins. The PVC tubes are mounted on an acrylic carrousel to allow for easy access. They can be detached and adjusted to the animal so that they just prevent each animal to turn around, yet are not so tight as to cause the animal distress. The whole setup is placed on a wooden platform in a RF chamber that is lined with absorbers. This was necessary to prevent interferences with local cellular communication services.

In the center of the carrousel, i.e., at the location of the antenna, fresh air was blown to cool the area closest to the antenna and to ventilate the chamber. The air flow was estimated to be between 50 and 150 m<sup>3</sup>/h. This had the positive effect of further stabilizing the position of the head during the experiment, since the animals all tended to stick their snouts as far as possible into the air stream. The distance of the snouts from the antenna feedpoint was estimated to be 35±5 mm.

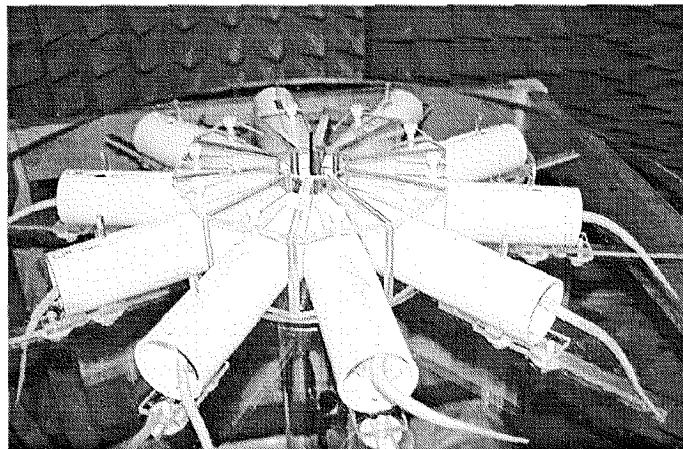


Figure 8.1: Near field exposure setup used to study possible acute effects on the CNS at the MTE frequency band of 900 MHz. Ten adult rats were grouped around a symmetrical dipole. The distance between feedpoint and snout was kept constant to approximately 35 mm by restraining the animals in the tubes.

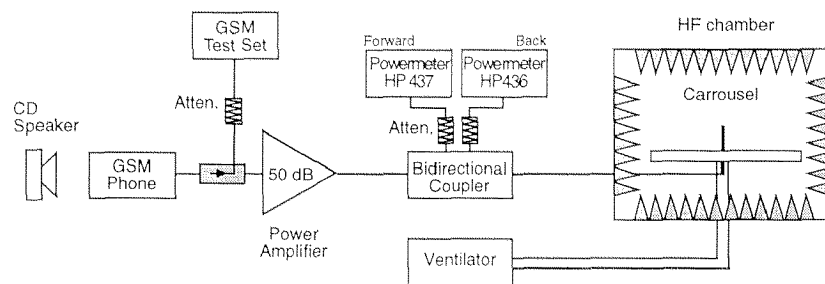


Figure 8.2: Scheme of the entire exposure setup. A GSM signal was applied during biological experiments. The GSM phone was replaced in the experimental dosimetry by a HP 8656B signal generator, providing a CW signal of 900 MHz.

The technical setup is schematically illustrated in Figure 8.2. The GSM signal simulating actual life exposure conditions was generated using a commercial portable GSM phone, Motorola International 2000, controlled by the GSM RF Test Set HP8922A. The discontinuous transmission mode (DTX) of GSM was chosen, because its signal has a larger proportion of low frequency amplitude-modulated components. A telephone conversation was simulated by repeatedly playing the first half of Heinrich von Kleist's comedy "Der zerbrochene Krug". This piece consists of all the pauses and changes in tone and volume of voice that can be found in an average telephone conversation. The average power was greater than 80% of that produced by the non DTX mode. The uplink signal was amplified using the adjustable 100 W Kalmus 717FC amplifier, and the antenna input power was monitored using two HP437 power meters.

### 8.3 Experimental Dosimetry

The primary objective of the experimental dosimetry was to obtain instant data about the antenna input power required to achieve the desired specific absorption rate (SAR) in the brain tissue of the animal. In addition, the experimental results could be well used to validate the detailed numerical findings.

However, the exact experimental determination of the SAR distribution is fraught with difficulties. 1) An extremely high spatial resolution is required because of the large field gradients which are expected to be induced by eddy currents. 2) Because of the rather poor coupling with the incident fields, high sensitivity is also necessary at antenna input power levels of 100 W. 3) The different tissues are thermally well isolated. 4) The thermal constant of the various tissues is not known and must be approximated.

The SAR can be determined either with thermal or E-field probes using

$$SAR = \frac{\sigma}{\rho} \mathbf{E}^2 = c \frac{dT}{dt} \quad (8.1)$$

whereby  $c$  is the specific heat capacity,  $\sigma$  the conductivity and  $\rho$  the mass density of the tissue and  $\mathbf{E}$  the Hermitan magnitude of the induced electric field vector.

Because of the large field gradients it is necessary to use thermal probes, although the achievable sensitivity is poor compared to that of E-field probes.

#### 8.3.1 Setup

The dosimetry was performed using the same exposure setup as used during the *in vivo* experiments in order to avoid additional error sources which might be introduced using a modified setup. Only the tube was slightly modified to enable the positioning of the temperature probes inside a rat cadaver. A Photonetics 1450 HS Fiberoptical Multisensor System (Woodinville, WA) was used with sensors whose active area is less than  $1 \text{ mm}^2$  and have been shown to perform better than the LUXTRON 755 device (Mountain View, CA) [6].

For the first set of measurements three thermoprobes were precisely positioned within the brain of the animal by standard stereotaxic means. One of the probes was placed directly in the center of the dorsal *Hippocampus*. The other two at the positions 0 mm and 7 mm with respect to the *Bregma* (Figure 8.4). Shortly after implantation, sagittal MR-images were taken to determine the initial positions of the probes. The probe holders were constructed so as to allow vertical shifts in the position of the probes to an accuracy of better than  $\pm 0.25 \text{ mm}$ . A second set of measurements was taken in 6 insertion points in the trunk of the animal with a total of 38 different measurement points (Figure 8.5).

The tube was positioned so that the snout of the animal was at the shortest distance from the feedpoint of the antenna that was encountered in the biological experiments, i.e., 30 mm. The two neighboring rats were simulated by rat-like containers filled with tissue simulating liquid. The remaining seven rats were not simulated at all. The dosimetric measurements were performed at the maximum available antenna input power at 900 MHz of 49.1 dBm, i.e., 82 W.

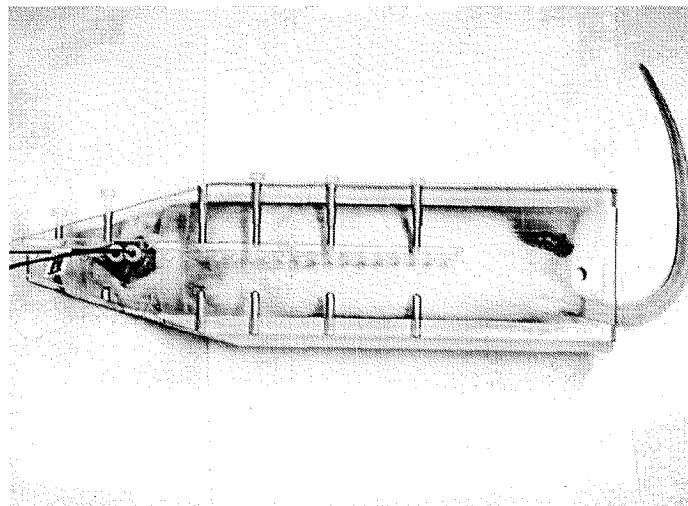


Figure 8.3: Modified tube for the experimental dosimetry

### 8.3.2 Discussion of Uncertainties

Since the maximum induced SAR levels were close to the sensitivity of the temperature system, it was necessary to perform several preliminary tests to ensure the suitability of the adopted approach and to provide a good estimation of the uncertainty of the measurement.

- *Nonthermal detection:* To be able to exclude systematic errors due to non-thermal or direct detection of the microwave exposure, measurements were performed with probes placed near the antenna in E-, H-, and S-polarization. No evidence of direct microwave effects on the probes could be detected.
- *Short term drifts and noise:* Short term drifts and noise were checked in a waterbath and were found to be within  $0.5 \text{ mK/s}$ . This value represents the lower limit of noise in the dosimetric assessments. In the tissue larger noise levels had been observed that were in the range of  $1 \text{ mK/s}$  for a measurement period of 1 minute.
- *Tissue temperature:* Since a thermal equilibrium previous to each exposure was necessary, the assessment had to be conducted at room temperature, i.e., the average tissue temperature was  $22 \pm 3^\circ \text{C}$ . According to [7] the conductivity of the various non-living tissues is reduced by 24-36% compared to living tissue, whereby the change in permittivity with respect to living tissue is negligible (1%). Simulations showed that this effects the brain average SAR by approximately -15% to -20% and the whole-body average SAR by approximately 5%.
- *Tissue aging:* Further uncertainties also arise from changes of the dielectric parameters of the biological tissue caused by aging (mainly due to drying out). For this reason the rat cadaver was used immediately after the death of the animal and a sugar-salt solution was added regularly into the holes for the probes. Nevertheless, this effect has been monitored and found to be less than 6% of the SAR in the first hour and much less in the following time.



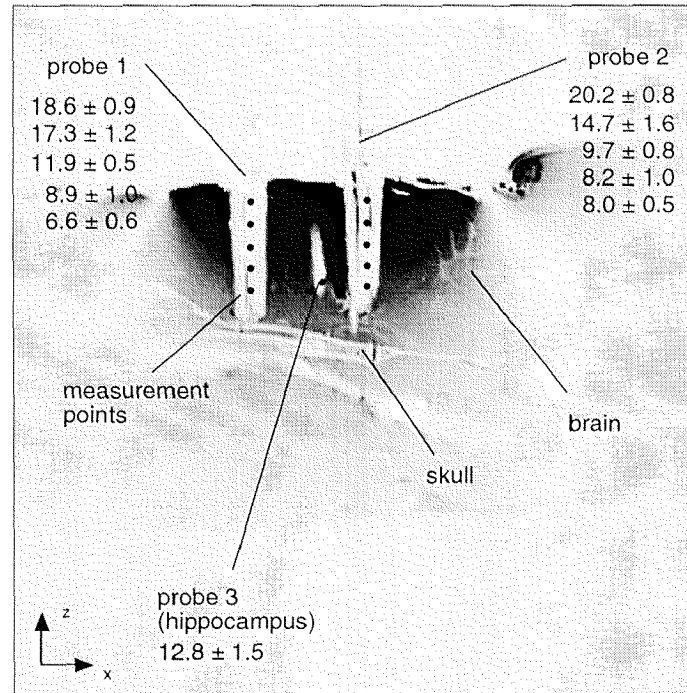


Figure 8.4: Temperature rise ( $dT/dt$  [mK/s]) and location of the measurement points inside the brain region. The variation gives the standard deviation of all measurements at that location and is not a measure of the uncertainties of the experimental dosimetry

- *Thermal conduction rate:* An exposure time of 1 minute was needed to reach the required sensitivity. Although the experiments had shown that the local accumulations of heat disperse slowly by conduction to the neighboring regions of the body, the errors for the local value might be considerable in areas of such large absorption gradients as is found in the brain tissue (see discussion in the next Section).

### 8.3.3 Results

For each discrete measurement point the rat was exposed for 1 minute, followed by a period of 14 minutes to determine the temperature rise. It would have been desirable to have had longer pauses between temperature measurements in order to reach thermal equilibrium, the constraint was to perform the measurements as soon as possible after the death of the animal. The time derivative of the temperature was recorded upto 3 minutes before the exposure to verify if the steady state had been reached or otherwise to determine the appropriate correction factor.

The results of the temperature measurements for a single rat are summarized in Figures 8.4 and 8.5. The average value of the four measurements is provided, as well as their standard deviation. Since the *Hippocampus* served as a reference point, a larger number of measurements was taken and averaged at this location. The large deviation for this set of measurements is explained by the aging effects, since these measurements spanned over several hours.

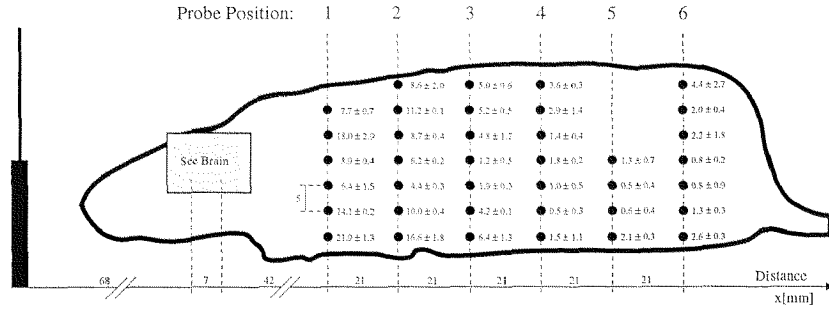


Figure 8.5: Temperature rise ( $dT/dt$  [mK/s]) and location of the measurement points in the whole body. The variation gives the standard deviation of all measurements at that location and is not a measure of the uncertainties of the experimental dosimetry

The effects due to positional changes of the head with respect to the antenna were also assessed and are reported in Section 8.5.

## 8.4 Numerical Dosimetry

### 8.4.1 Method

The electromagnetic simulation tool MAFIA was used for the numerical dosimetry [8]. This tool is based on the Finite-Integration-Technique (FIT), which transforms the Maxwell equations in integral form into the equivalent Maxwell grid equations, whereby the resulting system of equations is similar to that of a FDTD approach [9]. First-order Mur-absorbing boundary conditions [10] were applied on the lattice truncation to calculate the electromagnetic field.

Applying the FI-method to a scattering problem in the time domain, the electric and magnetic field vectors are calculated at discrete timesteps following the well-known “leapfrog”-algorithm [11]. MAFIA has proven to be very suitable for absorption studies in bioelectromagnetics [6], [12].

### 8.4.2 Modeling

The antenna was simulated as a simple filament dipole on a meshline having the same length ( $\lambda/2$ ) as the sleeved dipole used. The excitation was introduced as an electric dipole in the feedpoint of the antenna. Since the induced absorption is expected to be proportional to the square of the antenna current and not to the antenna input power [2] the computational results were compared with the experimental values for a feedpoint current of 100 mA. The ratio between antenna input power and feedpoint current was assessed to have been  $65 \text{ W/A}^2 \pm 10\%$  and the symmetry of the dipole by the near field scanner described in [13] and [14].

The rat phantom was derived from 74 magnetic resonance images (MRI) taken from a rat of the same breed and age as used in the experiments. 13 different tissue types were distinguished (Table 8.1). To determine the effect of the exposure setup made of acrylic glass ( $\epsilon_r=5$ ,  $\sigma=0 \text{ mho/m}$ ), the closer setup was also discretized, as shown in Figure 8.6.

The geometry of the different tissues was first outlined with an image-processing program for each of the 74 MRI scans. In the second step the different tissues were discretized by fitting them into the computational grid. The discretized model of the rat contained approximately 230.000 voxels with the dimensions 1.5 mm x 1 mm x 1 mm. The voxel thickness in the direction of the longest axis of the rat represents one half of the separation between the different MRI scans. The whole computation domain consisted of about 1.7 million voxels. To reduce reflections on the open boundaries, non-equidistant meshsteps were used to enlarge the computational domain.

Steady state was reached after approximately 8 to 12 periods. All simulations were performed on a SparcStation 20, each of which took about 9 hours of computational time. Depending on how much data had to be stored for the further postprocessing, file sizes reached up to 160 MByte.

Biological tissue	$\epsilon_r$	$\sigma$ [mho/m]	Reference
brain	55	1	[15]
bone	5	0.15	[16]
muscle	50	1.4	[16]
fat	2.5	0.02	[17]
skin	43	0.76	extrapolated
heart	50	1.18	extrapolated
lungs	35	0.93	[15], extrapolated
digesting system	40	0.9	extrapolated
liver	48.2	0.93	[18]
kidneys	52.6	1.03	[18]
testicles	40	0.8	extrapolated
eyes	70	1.7	[15], extrapolated
nose-region	5	0.15	extrapolated

Table 8.1: Separated biological tissues of the rat and their dielectric parameters as used for the simulations.

The dielectric values of the biological tissues were taken from [15]- [18]. Since there is not much data published for all different tissues of rats, some values had to be estimated on the basis of the water/fat content or by comparing them to human tissue. The parameters used are listed in Table 8.1. To illustrate the resolution of the model, the bone structure of the rat is represented in Figure 8.7. As can be seen, very fine structures, such as the ribs could not be simulated with the chosen resolution.

#### 8.4.3 Dependence of the SAR Distribution on the Rat Modeling

It is evident that the local SAR value strongly depends on the electrical parameters at this location. The achievable accuracy in dosimetry is largely impaired by the uncertainty of the dielectric parameters. On the other hand, it is not expected that small differences at a fair distance away from the location of interest would have a

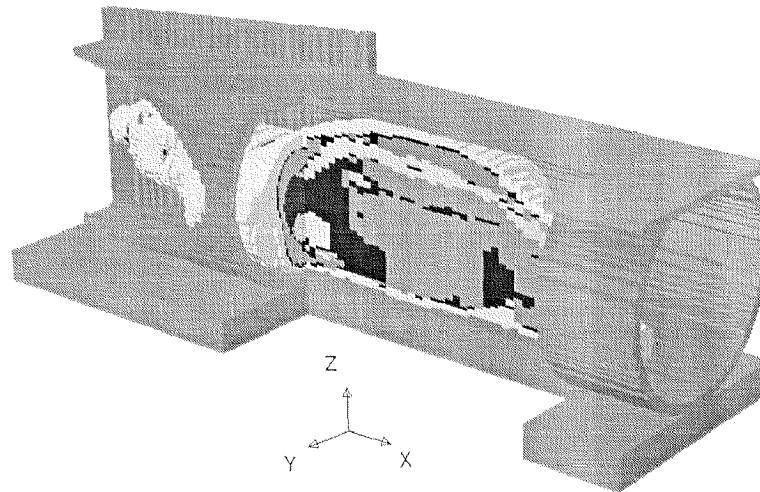


Figure 8.6: Discretized rat phantom and exposure setup

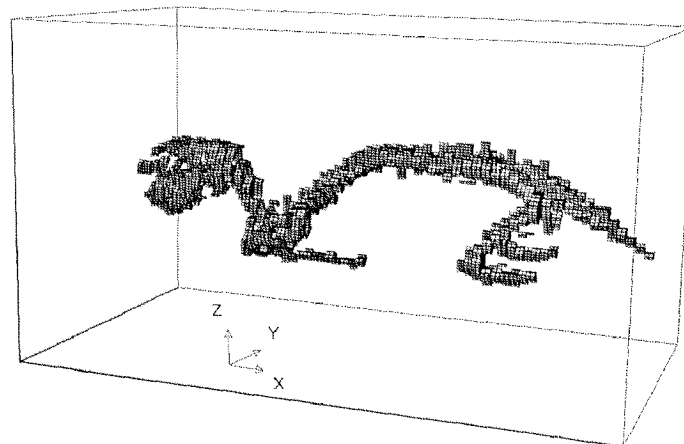


Figure 8.7: Discretized bone structure of the rat

significant influence on the SAR. To assess the sensitivity of these uncertainties on the SAR levels, different sets of dielectric parameters were assigned to the 13 different tissues. The absorption in the following six phantoms was compared:

- Phantom 1: modeling of all 13 different tissues according to Table 8.1 (13-tissue phantom).
- Phantom 2 and 3: modeling of all 13 tissues with the parameters of averaged tissue or muscle tissue, except bone/skull tissue (simplified phantom).
- Phantom 4 and 5: modeling of all 13 tissues including bone/skull with the parameters of averaged tissue or muscle tissue (homogeneous phantom).
- Phantom 6: modeling of the head and neck region identical to Phantom 1 but

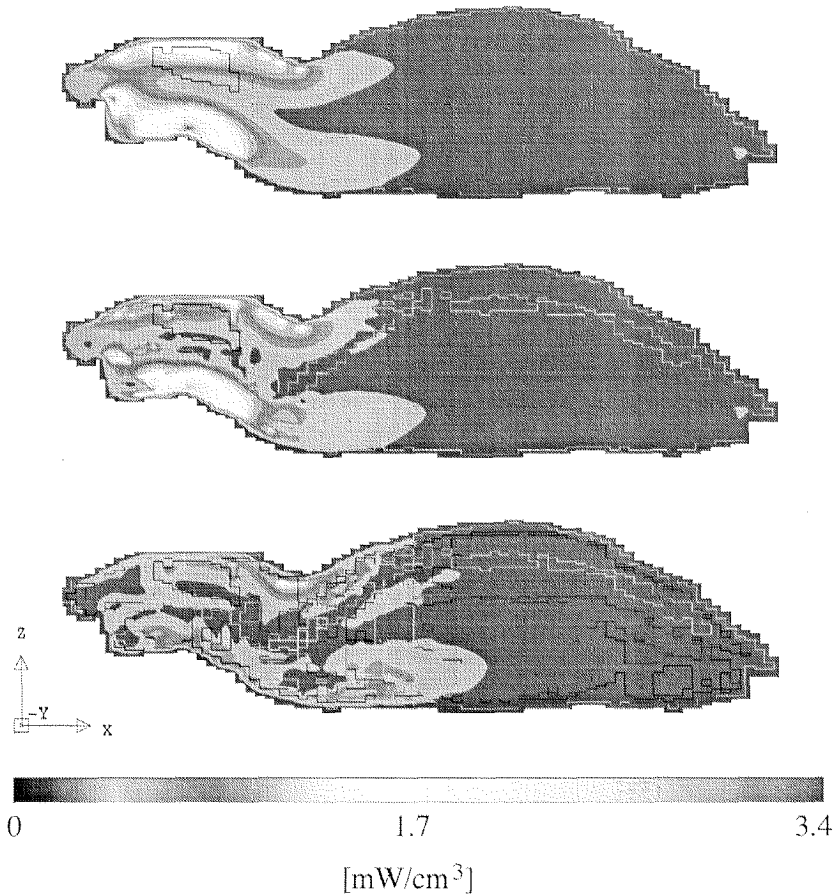


Figure 8.8: SAR distribution in a sagittal plane through the middle of the rat. Models from top to bottom: Homogeneous phantom with averaged dielectric parameters, Simplified phantom with averaged dielectric parameters and 13-tissue phantom. All SAR values are normalized to 100 mA antenna feedpoint current.

replacing all tissues further than 95 mm away from the snout with averaged tissue or muscle tissue parameters (head model).

Comparing the SAR distributions in Figure 8.8, it becomes obvious that the dominant interaction mechanisms can be described by means of eddy currents induced by the magnetic field, as predicted from study [2]. Quasi-static considerations would suggest a significant dependence of the induced E-field strength from the local tissue distribution and a less pronounced dependence on the whole-body average SAR values.

Figures 8.9 and 8.10, which summarize all different simulations, basically confirm this dependence of the SAR on the modeling. The whole-body average SAR value is inherent to the modeling, whereas the brain average seems to be sensitive not only to the accurate skull and brain modeling but also to the closer vicinity of the head area. It has been found to be critical that the modeled skull completely surrounds the brain tissue. Since the modelling of this area is rather coarse (Figure 8.7), a much

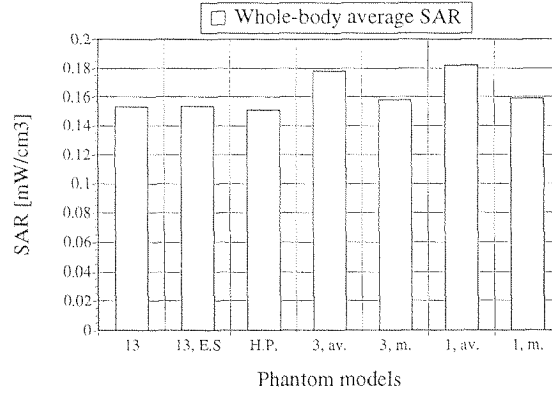


Figure 8.9: Whole-body-average-SAR for the different simulated phantoms. All values are normalized to 100 mA antenna feedpoint current. The number gives the number of tissues used for the 13-tissue, simplified or homogeneous model, followed by (m.) for simulating muscle tissue, (av.) for averaged dielectric parameters, (E.S.) for taking the exposure setup into account and H.P. for the head phantom.

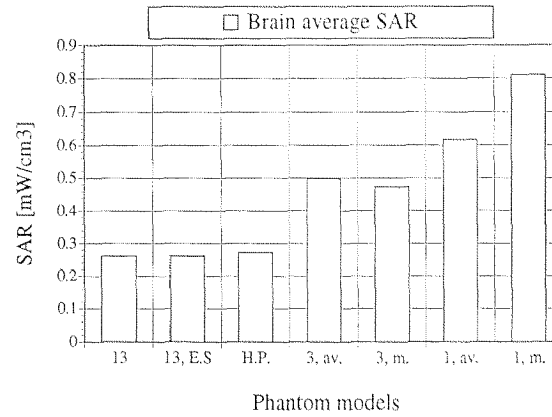


Figure 8.10: Brain-average-SAR for the different simulated phantoms. All values are normalized to 100 mA antenna feedpoint current. The number gives the number of tissues used for the 13-tissue, simplified or homogeneous model, followed by (m.) for simulating muscle tissue, (av.) for averaged dielectric parameters, (E.S.) for taking the exposure setup into account and H.P. for the head phantom.

finer discretization would be necessary to reduce significantly the discretization error in this area. To assess the uncertainty of the brain average SAR value due to the uncertainty of the dielectric parameters for brain and bone tissue, simulations with different sets of parameters were performed. Assigning  $\epsilon_r=41$ ,  $\sigma=0.77$  mho/m instead of  $\epsilon_r=55$ ,  $\sigma=1$  mho/m (Table 8.1) to brain tissue, the whole-body average SAR differs by approximately 1%, the brain average SAR by 6%. Exchanging the parameters of the skull/bone structure ( $\epsilon_r=5$ ,  $\sigma=0.15$  mho/m) with  $\epsilon_r=10$ ,  $\sigma=0.25$  mho/m, the whole-body absorption is increased by approximately 2% and the brain average SAR considerably by 20%.

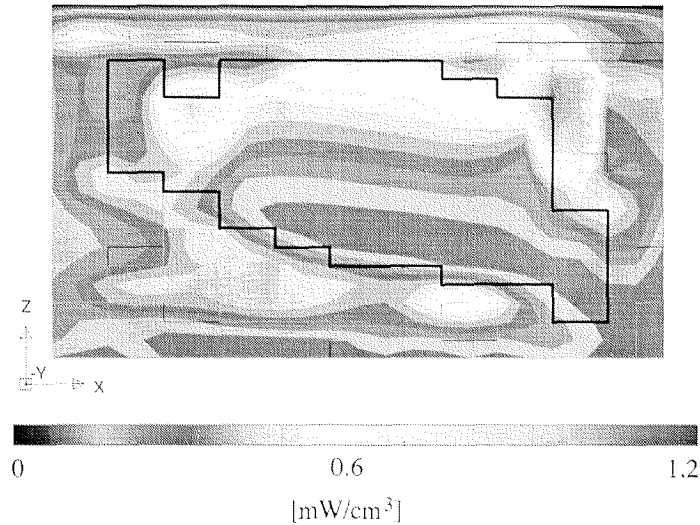


Figure 8.11: SAR distribution in a sagittal plane in the brain region of the 13-tissue rat phantom. The SAR values are normalized to 100 mA antenna feedpoint current.

The effect of a possible different shape of the rat during the experimental dosimetry than during MRI-scanning and thus in the numerical model was investigated by rearranging the discretized MR-images in a slightly different, but still anatomically realistic way. The whole-body average SAR was hereby affected by less than 1%, the brain average SAR was altered by more than 10%, since a change of the material distribution in an area of high field gradients has a stronger impact on a local SAR distribution.

The effects of the surrounding acrylic material on the absorption is negligible, as expected on the basis of the dominant interaction mechanism (Figures 8.9 and 8.10).

#### 8.4.4 Results

Figure 8.11, which is a close-up of the SAR distribution of the 13-tissue phantom in Figure 8.8, shows more clearly the SAR distribution in the brain area. In Figures 8.12 and 8.13 the measured and simulated SAR values in the brain area are compared for the locations of probes 1 and 2 respectively, whereby a specific heat of  $c=3.7$  J/kg/K for the brain tissue was assumed. A lower gradient of absorption was expected for the experiment due to heat conduction effects over the relatively long exposure periode of 1 minute.

In Figures 8.14 and 8.15 the measured and simulated SAR-values inside the trunk of the rat are compared. The comparison is difficult since it could not be determined in which tissue the probe was actually located, i.e., MRI data was not available. The error bars in Figures 8.12-8.15 of the experimental data only represent the standard deviation of a number of measurement samples, i.e., they are an indication of the noise level and do not include systematical errors.

Nevertheless, the general agreement is considerably better than the discussed uncertainties of the numerical and experimental analysis would suggest.

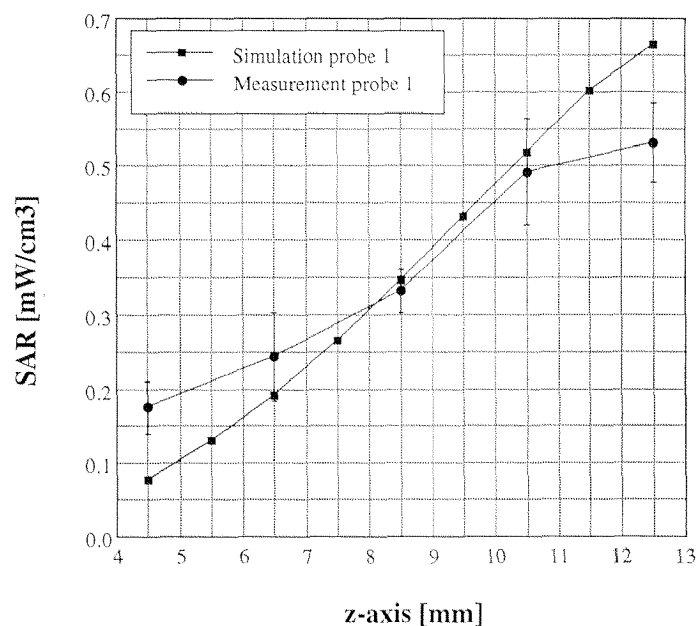


Figure 8.12: Comparison between measured and simulated SAR values for probe 1 inside the brain region. All values are normalized to 100 mA antenna feedpoint current. For brain tissue,  $1\text{g}/\text{cm}^3$  was assigned to the density.

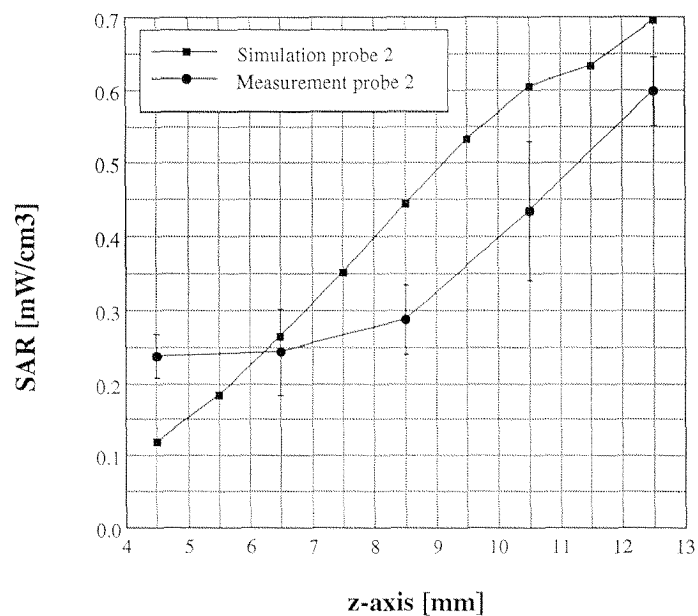


Figure 8.13: Comparison between measured and simulated SAR values for probe 2 inside the brain region. All values are normalized to 100 mA antenna feedpoint current. For brain tissue,  $1\text{g}/\text{cm}^3$  was assigned to the density.



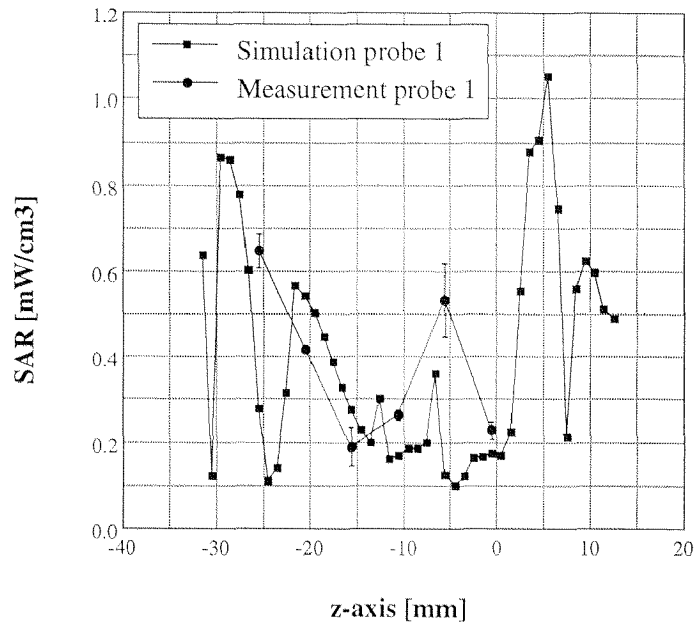


Figure 8.14: Comparison between measured and simulated SAR-values for probe 1 inside the body region. All values are normalized to 100 mA antenna feedpoint current. For all tissues,  $1\text{g}/\text{cm}^3$  was assigned to the density.

## 8.5 Effects of Movements and Different Sizes

### 8.5.1 Effects of Movements

The influence of the animal's position with respect to the antenna was studied by changing the distance of the rat from the antenna feedpoint in the radial and vertical direction. The dependence of the induced fields in the brain tissue (probe position 3) for shifts in the radial direction was  $1.3\text{ dB}/\text{cm}$  when assessed by the experimental approach, compared to  $1.2\text{ dB}/\text{cm}$  obtained by numerical simulations. This agrees well with the  $1/r$  dependence of the H-field, which is about  $1.2\text{ dB}/\text{cm}$  at the location of the brain. Since the H-field hardly changes in the vertical direction, the dependence for vertical shifts is smaller than  $0.7\text{ dB}/\text{cm}$ .

### 8.5.2 Sensitivity to Size

The influence of the size of the rat (250-300 g) was investigated by rescaling the 13-tissue rat model. The variation due to different sizes of the rat is  $\pm 8\%$  for the whole-body average SAR and  $\pm 5\%$  for the brain average SAR. Larger rats result in lower whole-body average SAR values due to the dominant  $1/r^2$  dependency of this value for longer rat phantoms. At the same time the brain average SAR value increases because of higher inductively induced E-fields, due to the larger cross section of the rat.

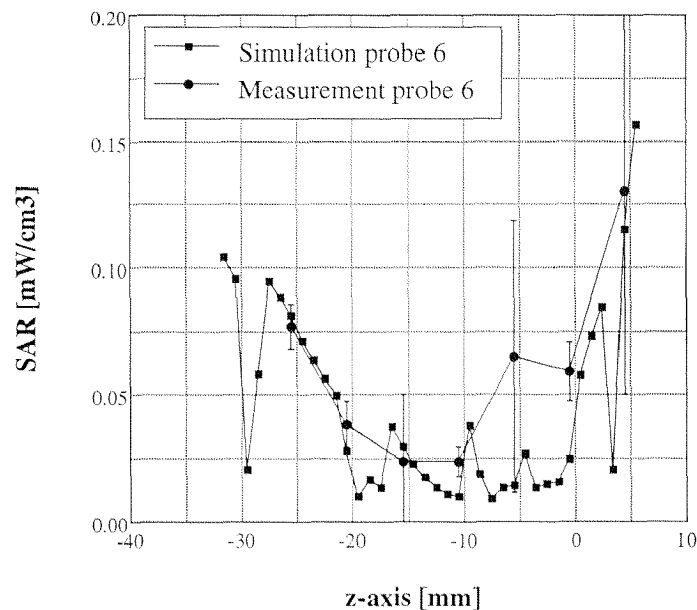


Figure 8.15: Comparison between measured and simulated SAR-values for probe 6 inside the body region. All values are normalized to 100 mA antenna feedpoint current.  $1\text{g}/\text{cm}^3$  was assumed for all tissues for the mass density. For all tissues,  $1\text{g}/\text{cm}^3$  was assigned to the density.

## 8.6 Exposure Efficiency

The exposure efficiency for a single rat placed in the exposure setup at a distance of 30 mm from the snout to the antenna feedpoint is  $0.26 \pm 0.07 \text{ mW}/\text{cm}^3$  per 100 mA antenna feedpoint current for the brain average SAR and about  $0.15 \pm 0.04 \text{ mW}/\text{cm}^3$  per 100 mA for the whole-body average value. These values are based on the numerical results whereby all uncertainties have been considered as statistically independent error sources.

To be able to extrapolate these findings to the actual exposure situation when all ten rats are exposed, the effect of coupling between the animals had to be assessed. This was necessary, since simulating the entire setup by a volume technique would increase the computational volume beyond the computational power available.

This effect was experimentally assessed by comparing the results with and without the two rat phantoms next to the rat cadaver. The decrease of the fields induced in the brain tissue was found to be about 20%. Since this is a critical assessment for this study and larger than initially expected, this finding was validated by numerical simulations, applying the volume method Generalized Multipole Technique (GMT) [19]. This technique allows the simulation of ten bodies grouped around a dipole antenna, as in the experiment, but only with strongly simplified rat phantoms. Simulations with different modeling were conducted, and the SAR values were compared with those of simulating a single rat and found to be scarcely dependent on the modeling. The SAR was reduced by  $20 \pm 3\%$  for the brain average and by  $25 \pm 2\%$  for the whole-body average SAR values. The efficiency for the entire setup

per 100 mA feedpoint current at the average distance of 35 mm would therefore be SAR  $0.20 \pm 0.05$  mW/cm<sup>3</sup> per 100 mA for the brain average and  $0.11 \pm 0.02$  mW/cm<sup>3</sup> per 100 mA for the whole-body average.

## 8.7 Whole Body Temperature rise

To ensure that the chosen exposure levels during the biological experiments did not cause a significant rise of the whole-body temperature, the temperature rise for exposure levels which corresponded to the range of 0.4 W/kg to 20 W/kg for the average brain absorption was measured using anesthetized rats.

The test was made by inserting a rectal probe and measuring the temperature every minute for 30 minutes using a Quick Novo device. It was found that exposure levels up to 6 W/kg for the whole-body SAR do not cause a detectable increase of the rat's rectal temperature. These findings are in good agreement with the results for 250 - 300g rats described in [20], where a rise of the whole-body temperature was found for a whole-body average SAR higher than 8 W/kg.

## 8.8 Conclusion

The dosimetric analysis performed demonstrates the suitability of the presented setup to test CNS effects at the mobile communications frequency band at 900 MHz.

The SAR averaged over the brain has been assessed to be  $0.20 \pm 0.05$  mW/cm<sup>3</sup> for a feedpoint current of 100 mA, if a distance of 35 mm between feedpoint and snout is assumed to be the mean position of the head during exposure.

The variations of induced brain-averaged SAR values due to movement ( $\pm 5$  mm) of the head and variation of the size of the animal (250 - 300 g) are estimated for the presented setup to be less than  $\pm 16\%$ .

The SAR distribution in the brain is largely nonuniform, i.e., larger values closer to the surface and smaller values at the bottom of the brain. This represents well the exposure of human using a handheld MTE.

The whole-body average SAR is about half (55%) of the brain averaged values which is not as low as desired but still reasonably low, especially since it is only about 10% of the peak SAR (averaged over 0.1 g) induced in the brain.

In addition the setup has proven to be practical in use, and the induced stress levels caused by restraining the animals in the setup have been declared to be minimal by neurologists and veterinary scientists.

Overall the described exposure setup meets the requirements defined in Section 8.1 very well.

## References

- [1] N. Kuster, Q. Balzano, and J. C. Lin, Eds., *Mobile Communications Safety*, Chapman & Hall, London, 1997.
- [2] Niels Kuster and Quirino Balzano, "Energy absorption mechanism by biological bodies in the near field of dipole antennas above 300 MHz", *IEEE Transactions on Vehicular Technology*, vol. 41, no. 1, pp. 17–23, Feb. 1992.
- [3] Niels Kuster, "Immediate report no. 4: Dosimetric assessment for the near field exposure system", Tech. Rep., Institut für Feldtheorie und Höchstfrequenztechnik, 1992.
- [4] W.R. Adey, C.V. Byus, W. Haggren C.D. Cain, R.J. Higgins, R.J. Jones, C.J. Kean, N. Kuster, A. MacMurray, J.L. Phillips, R.B. Stagg, and G. Zimmerman, "Brain tumor incidence in rats chronically exposed to digital cellular telephone fields in an initiation-promotion model", in *Proceedings of the 18th Annual Meeting of the Bioelectromagnetics Society*, Victoria, Canada, June 9–14, 1996, p. 27.
- [5] Christoph Wiessner, K. Fritze, B. Schmitz, Niels Kuster, and K.A. Hossman, "Acute effects of GSM signals on the rat CNS, (invited)", in *25th General Assembly of the International Union of Radio Science (URSI)*, Lille, France, Aug. 1996, p. 565.
- [6] Michael Burkhardt, Katja Poković, Marcel Gnos, Thomas Schmid, and Niels Kuster, "Numerical and experimental dosimetry of petri dish exposure setups", *Journal of the Bioelectromagnetic Society*, vol. 17, no. 6, pp. 483–493, 1996.
- [7] K. R. Foster and H. P. Schwan, *Handbook of Biological Effects of Electromagnetic Fields, Dielectric properties of tissues*, 2nd ed., CRC Press, Boca Raton, Fla, 1994.
- [8] CST, *The MAFIA collaboration, Mafia Version 3.x, User's Guide*, CST GmbH, Lautenschlägerstr. 38, D-64289 Darmstadt, 1994.
- [9] T. Weiland, "Maxwell's grid equations", *Frequenz*, vol. 44, no. 1, pp. 9–16, 1990.
- [10] G. Mur, "Absorbing boundary conditions for the finite-difference approximation of the time-domain electromagnetic field equations", *IEEE Transactions on Electromagnetic Compatibility*, vol. 23, pp. 377–382, 1981.
- [11] K. S. Yee, "Numerical solution of initial boundary value problems involving Maxwell's equations in isotropic media", *IEEE Transactions on Antennas and Propagation*, vol. 14, pp. 585–589, 1966.
- [12] Volker Hombach, Klaus Meier, Michael Burkhardt, Eberhard Kühn, and Niels Kuster, "The dependence of EM energy absorption upon human head modeling at 900 MHz", *IEEE Transactions on Microwave Theory and Techniques*, vol. 44, no. 10, pp. 1865–1873, Oct. 1996.

- [13] Thomas Schmid, Oliver Egger, and Niels Kuster, "Automated E-field scanning system for dosimetric assessments", *IEEE Transactions on Microwave Theory and Techniques*, vol. 44, pp. 105–113, Jan. 1996.
- [14] Thomas Schmid and Niels Kuster, "Novel field probes for close near field scanning", *submitted*, 1996.
- [15] S.S. Stuchly M.A. Stuchly, "Dielectric properties of biological substances - tabulated", *Journal of Microwave Power*, vol. 15, no. 1, pp. 19–26, 1980.
- [16] Carl H. Durney, M. F. Iskander, H. Massoudi, S. J. Allen, and J. C. Mitchell, "Radiofrequency radiation dosimetry handbook", Tech. Rep., 3rd ed., USAF School of Aerospace Medicine, Aerospace Medical Division (AFSC), Brooks Air Force Base, 1980.
- [17] S.O. Nelson W.R. Tinga, "Dielectric properties of materials for microwave processing-tabulated", *Journal of Microwave Power*, vol. 8, no. 1, pp. 23–65, 1973.
- [18] A. Kraszewski, M.A. Stuchly, and S.S. Stuchly, "In vivo and in vitro dielectric properties of animal tissues at radio frequencies", *Journal of the Bioelectromagnetics Society*, vol. 3, pp. 421–433, 1982.
- [19] Niels Kuster, "Multiple multipole method for simulating EM problems involving biological bodies", *IEEE Transactions on Biomedical Engineering*, vol. 40, no. 7, pp. 611–620, July 1993.
- [20] Christopher Gordon, Merrit D. Long, Kimi S. Fehlner, and Andrew G. Stead, "Body Temperature in the Mouse, Hamster, and Rat Exposed to Radiofrequency Radiation: an Interspecies Comparison", *Journal of thermal biology*, vol. 11, no. 1, pp. 59–65, 1986.

## Chapter 9

# Appropriate Modeling of the Ear for Compliance Testing of Handheld MTE with SAR Safety Limits at 900/1800 MHz

*Abstract* - A variety of phantoms simulating the human head have been used to test compliance of mobile telecommunications equipment with safety standards. Whereas numerical compliance procedures have mostly been performed using complex anatomical phantoms based on magnetic resonance imaging data, experimental procedures have mainly relied on homogeneous phantoms, the ears of which have often been modeled as lossless spacers. Previous studies had indeed demonstrated that the absorption in the head tissue except the outer ear can be well represented by a homogeneous head of appropriate shape and material. The objectives of this study were to fill the gap of the remaining open issues, namely, (1) to evaluate the exposure in the ear region with respect to the spatial peak specific absorption rate and (2) to evaluate the most appropriate modeling of the ear for experimental evaluations such that it represents the maximum exposure of a reasonable cross-section of cellular phone users. This study is based on a detailed numerical phantom produced using high resolution magnetic resonance imaging scans. During scanning, the ear was naturally collapsed as it occurs when using a cellular phone. The results of this study lead to the conclusion that the spatial peak absorption occurring in the inner and outer ear can be reliably modeled either by a lossless spacer of not thicker than 3 - 4 mm or by partially filling the simulated pinna with head tissue simulating media whereas the minimal distance between the device and liquid should not be larger than 3 mm.

### 9.1 Introduction

Regulatory bodies in the US [1], Europe [2] and Japan [3] require compliance testing of handheld mobile communications equipment prior to market introduction. For example [2] requires that demonstration of compliance must be shown for a rea-

sonable cross-section of mobile telecommunications equipment (MTE) users in four different operational conditions and for all device configurations, whereby the uncertainty must be added to the results. Devices with antenna input powers of less than 20 mW are excluded. Many compliance tests of handheld devices have been performed experimentally using measurement systems similar to the one described in [4]. Although multi-tissue phantoms have been developed [5], demonstration of compliance can only be performed based on homogeneous head phantoms since the entire volume must be accessible by the probe. In most cases the ear was replaced by a lossless spacer [4, 124, 125]. The suitability of homogeneous phantoms for exposure evaluations had been demonstrated based on the results of a series of studies [8, 49, 50, 94] systematically investigating the dependence of the absorption on the internal anatomy. The objective of another study [7] was to experimentally evaluate the head shape in the vicinity of the ear as well as the thickness of the collapsed ear. The study was performed with 52 male and female volunteers. Based on this data, a phantom was proposed for compliance testing, the shape of which corresponds to the 90%-percentile of greatest absorption for the evaluated group. Following the same approach it was suggested that the ear should be modeled by a lossless spacer of 4 mm, corresponding to the 10%-percentile. Although it was noted that there is absorption in the pinna, it was argued that the losses in the outer ear would be compensated by the replacement of the low-loss structure of the inner ear (bony structure with air cavities) by the lossy tissue simulating material. However, this argument was rather based on rational reasoning than on hard scientific facts. Providing similar arguments, some groups have used the same phantom but increased the distance to 6 mm, which approximately represents the average thickness of the collapsed ear.

The lossless spacer has always been criticized since it does not account for the losses in the pinna, which might be quite large due to the close proximity of this tissue to parts of the phone, potentially conducting significant radio frequency (RF) currents. This criticism was supported by data obtained from numerical studies based on inhomogeneous head phantoms derived from magnetic resonance images (MRI) which showed greatly enhanced specific absorption rate (SAR) values in the external ear [12], [13], [14]. However, all these studies were performed based on phantoms with non-collapsed ears, which obviously overestimates the ratio between energy absorbed in the ear and the rest of the head. In addition, the maximum voxel sizes were rather large (up to 15 mm<sup>3</sup>) which may result in significant overestimation of the exposure due to numerical artifacts [15].

Nevertheless, there was a clear need to thoroughly address the question regarding the appropriate modeling of the ear for compliance testing. The objective of this study was to evaluate the exposure in the ear region based on a high resolution phantom having an accurate model of a collapsed ear and to investigate possibilities for appropriate modeling of the ear in experimental setups which does not greatly overestimate nor underestimate the actual user exposure.

## 9.2 Head Modeling and Transmitter Representation

The magnetic resonance imaging (MRI) data sets from which our previous phantoms were derived were taken without collapsing the ear, nor did they provide the necessary resolution for accurate modeling of the ear region. For the purpose of this study, a high-resolution MRI data set of the complete head of a healthy female volunteer

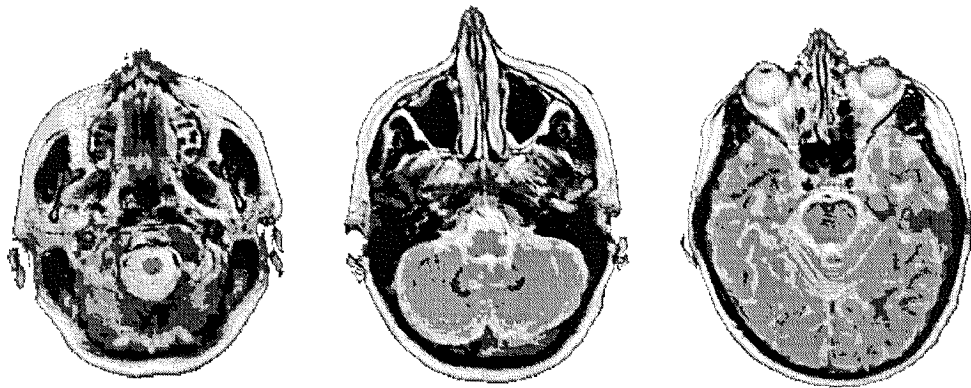


Figure 9.1: MRI slices at three different locations in the ear region. The ears had been gently pressed towards the head as it would occur in a real world MTE user situation.

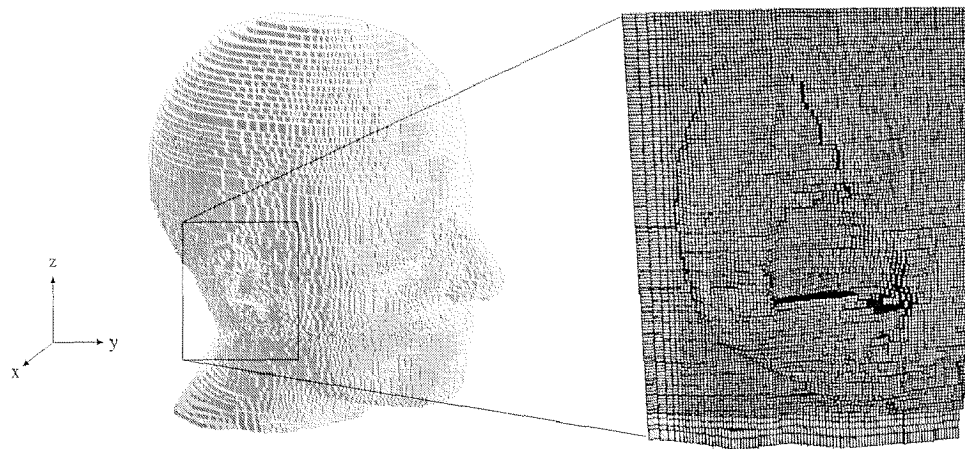


Figure 9.2: Voxel model of the head (left) and a closeup view of the high resolution ear region (right).

(age 40) was obtained from the University Hospital of Zurich. The ears were gently pressed to the head surface in order to obtain the appropriate ear shape for a realistic MTE user situation (Figure 9.1). The MRI slices were separated by 1 mm in the ear region and 3 mm in the upper and lower head regions. From this data a CAD model was constructed consisting of 121 slices, which were separated into 12 different tissue types. Two different numerical phantoms were created: (1) a high resolution model with  $0.125 \text{ mm}^3$  voxels in the ear region and expanding meshsteps in the upper and lower head regions and (2) a model with  $1 \text{ mm}^3$  voxels in the ear region and  $9 \text{ mm}^3$  voxels in the upper and lower head regions for fast parametric studies. A detailed view of the high resolution ear region is given in Fig. 9.2. The model with the highest resolution required a computational domain of approximately 14 million voxels and 1.2 GBytes of memory and took approximately 60 hours for 10 periods on a SunUltra 2 (300 MHz) computer.

Additionally, a homogeneous phantom was created by cutting the ear away in all MRI slices and smoothing the head surface in the ear region. The air containing



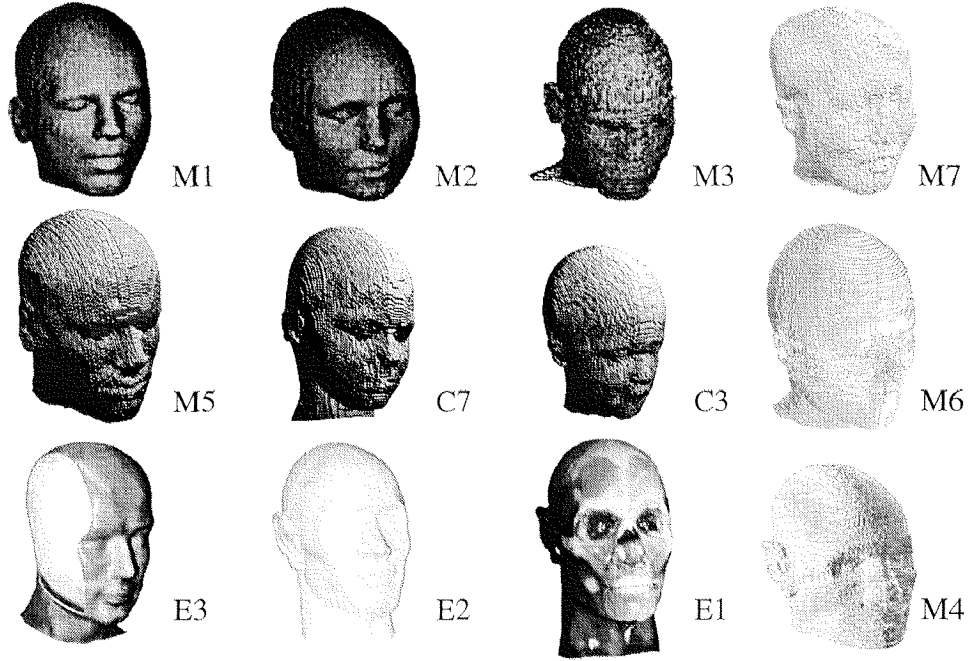


Figure 9.3: Head phantom database used in previous studies. Numerical head phantoms based on MRI data: Male head phantoms evaluated in [9], [10] and [11] (M1,M2,M3,M5), asian male head (M7) which has not yet been studied, 7-year (C7) and 3-year (C3) old children evaluated in [11], new female head with collapsed ears (M6). Experimental head phantoms: Shell phantom for compliance testing described in [9] (E3), shell phantom (E2) with the same head shape as E1, a 5 tissue phantom described in [5]. M4 is the numerical model of E1, based on CT scans.

auditory canal was filled with tissue. All tissues were simulated with the same dielectric parameter sets of HTSL1 and HTSL2 as given in Table 9.2. HTSL1 corresponds to the values used in our previous studies [9], [10], [11] and HTSL2 was initially proposed by the FCC and approximately corresponds to the arithmetic average of grey and white matter.

In order to comprehensively study the exposure of the ear region, two different generic transmitters were used: (1) a  $0.45\lambda$  dipole and (2) a generic phone (Figure 9.10). The basic study was performed using the dipole. In order to validate the generality of the findings for other transmitters, additional simulations were performed with a generic phone in various positions.

### 9.3 Methods

The study was performed by employing the Finite-Difference Time-Domain (FDTD) technique, applying a 3D in-house kernel developed within the framework of a Swiss priority research program. For the numerical model an inhomogeneous grid with expanding meshsteps was used to minimize memory costs and computation time. The time step was chosen according to the Courant limit [16]. 2nd order Mur absorbing boundary conditions (ABC) were used for these calculations to truncate the compu-

tational domain despite the availability of other ABC in the current implementation including Higdon operator up to 4th order and Perfectly Matched Layer (PML). This enables some computational expenses to be saved, since scattering at non-perfectly absorbing boundaries is of negligible significance for close near-field studies due to the strong dependence of the absorption on the distance [8]. The head models for validation purposes have been simulated with the FDTD-similar Finite-Integration (FI) implementation applying the commercially available software package MAFIA [17]. Details on the FDTD technique can be found in [16] and on FI in [18].

A CAD tool (SEMCAD, Schmid & Partner Engineering AG, Zurich) was used for the import of CAD data derived from the MRI images, for the rotation of the CAD data and the subsequent automatic discretization. The rotation of the CAD data prior to discretization is necessary to obtain reliable tilted head models as used in this study.

The excitation of the dipole and generic phone exposure was chosen to be an added source [19] in order to directly normalize all values to the feedpoint current. This approach is advantageous, since the SAR is predominantly induced by the  $H$ -field, which is directly proportional to the feedpoint current [8]. SAR values were calculated in the center of the voxels by interpolating all 12 electric field values of the surrounding edges.

The 1 g/10 g spatial peak SAR values were calculated by expanding a cube at each grid point until the desired mass was reached. The cube was always aligned parallel to the grid coordinates and each outermost layer of the cube consisted of at least one voxel of tissue, i.e., the cube not only contained tissue but also air voxels. This evaluation approach is in good agreement with the latest definition for the “cube” described in the various standards.

The experimental data used for validation purposes was obtained using DASY3 (Schmid & Partner Engineering AG, Zurich), which is the successor of the dosimetric assessment scanner described in [4] and provides enhanced precision and flexibility.

## 9.4 Validation of the New Head Model

In the first step, the performance of the new phantom was compared with those of the previous phantoms (Fig. 9.3). A comprehensive data set is available for the excitation of a  $0.45 \lambda$  dipole source at 900 MHz. The orientation of the dipole is vertical and the position of the feedpoint is 5 mm above the pinna and at a distance of 15 mm between the feedpoint and the surface of the head. The same dielectric parameter set as in the previous studies was chosen, which corresponds to the Dielectric Database from Microwave Consultants [20]. The SAR distribution and spatial peak SAR values were computed for the inhomogeneous phantom as well as for the homogeneous phantom in which the dielectric parameters of all tissues were replaced by the parameters of the head tissue simulating liquid (HTSL1).

The SAR distributions along a line perpendicular to the dipole axis directly behind the feedpoint are compared in Figures 9.4 and 9.5. In Fig. 9.5 the experimental data for the three different head phantoms E1/E2/E3 (see Fig. 9.3) have been added. In Fig. 9.6 the 1 g and 10 g spatial peak SAR values are compared.

The obtained SAR data for the new head model is well within the given range of the other head models (Figures 9.4, 9.5), verifying the previous conclusions that local absorption is strongly dependent on differences of the internal anatomy, whereas the

Table 9.1: Dielectric parameters at 900 MHz and 1800 MHz [21] and tissue densities [14].

tissue	Spec. gravity $\rho[g/cm^3]$	900 MHz		1800 MHz	
		$\epsilon_r$	$\sigma[mho/m]$	$\epsilon_r$	$\sigma[mho/m]$
bone	1.81	20.8	0.34	19.3	0.59
skin	1.01	43.7	0.86	41.4	1.21
fat	0.92	11.3	0.11	11.0	0.19
muscle	1.04	56.0	0.97	54.4	1.39
brain	1.04	45.8	0.77	43.5	1.15
CSF	1.01	68.6	2.41	67.2	2.92
blood	1.06	61.4	1.54	59.4	2.04
cartilage	1.10	42.7	0.78	40.2	1.29
eye:					
vitreous humour	1.01	68.9	1.64	68.6	2.03
lens	1.10	46.6	0.79	45.4	1.15
sclera	1.17	55.3	1.17	53.6	1.60
air	0.00	1.0	0.00	1.0	0.00

Table 9.2: Dielectric parameter sets of the Head Tissue Simulating Liquids (HTSL) used for the homogeneous head modeling

tissue	Spec. gravity $\rho[g/cm^3]$	900 MHz		1800 MHz	
		$\epsilon_r$	$\sigma[mho/m]$	$\epsilon_r$	$\sigma[mho/m]$
HTSL1:					
Head Tissue Simul. Media	1.00	43.5	0.90	41.0	1.69
HTSL2:					
Average Brain (FCC)	1.00	45.8	0.77	43.5	1.15

spatial peak SAR values vary only within a small range (Figure 9.6). In other words, the spatial peak SAR - at least for the area above the ear - can be well assessed using a homogeneous phantom having the appropriate dielectric parameters.

## 9.5 Results at 900 MHz

### 9.5.1 Dipole Configurations

The position of the dipole in the above mentioned absorption studies [9, 50, 94] was chosen because it results in the largest absorption. The brain was also considered to be the most relevant tissue with respect to health risk considerations. Another reason for choosing the position was its rather simple and well defined tissue distribution, i.e., small shifts parallel to the surface of the skin do not result in significant changes of the absorption pattern. Much larger variation must be expected for the ear region, which is composed of a complex 3-dimensional tissue distribution including air cavities and

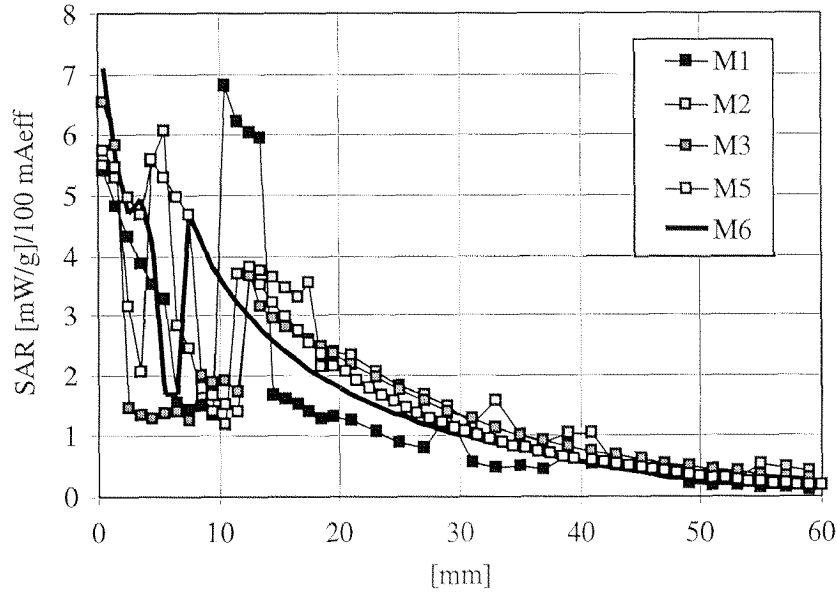


Figure 9.4: SAR distribution along a line perpendicular to the axis of a  $0.45 \lambda$  (900 MHz) dipole directly behind the feedpoint for 5 inhomogeneous MRI-based head phantoms. The dipole is located with its feedpoint 5 mm above the pinna, at a distance of 15 mm to the surface of the head.

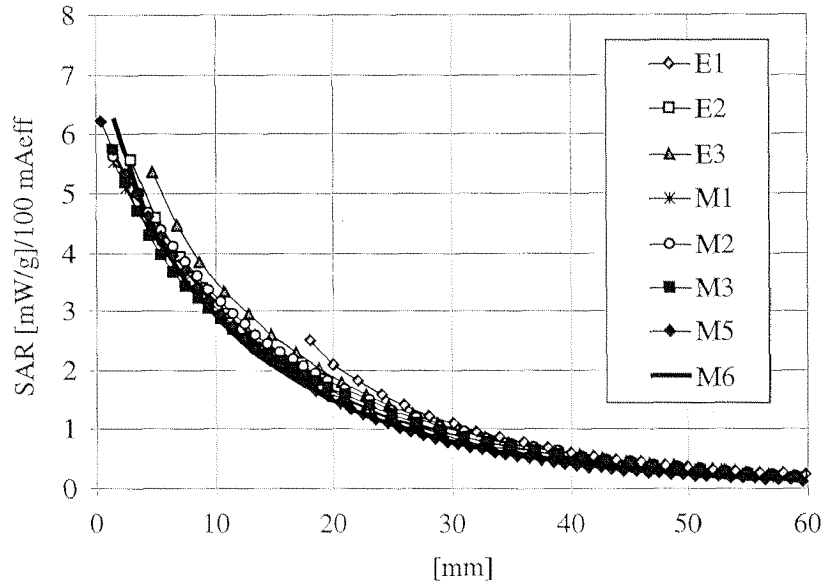


Figure 9.5: Comparison of the SAR distribution for the same excitation and phantoms (M1 ... M6) than in the previous Figure but for which the dielectric parameters of all tissues were replaced by  $\epsilon_{r1} = 43.5$ ,  $\sigma_1 = 0.9 \text{ mho/m}$  and  $\rho = 1 \text{ g/cm}^3$ . In addition, the experimental values for three experimental head phantoms (E1, E2 and E3) are given.

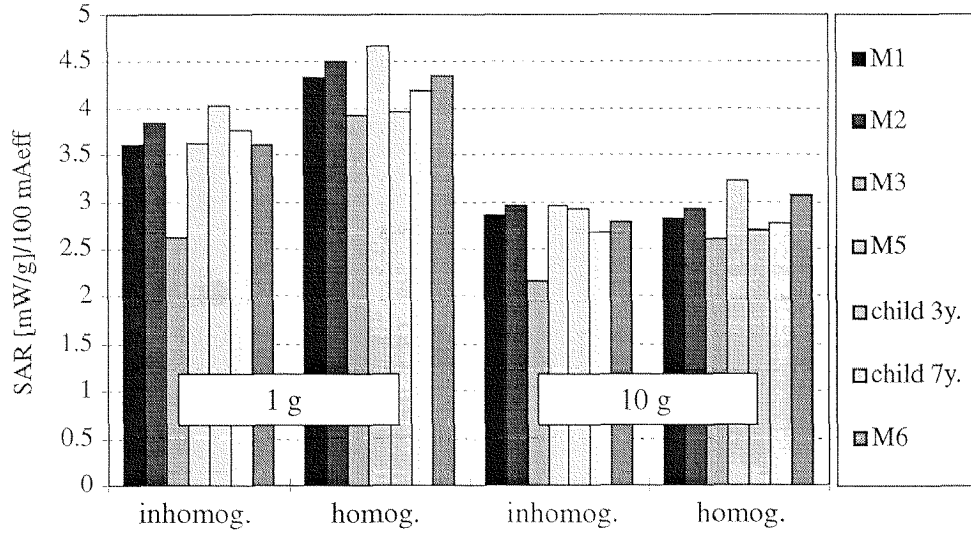


Figure 9.6: Comparison of the spatial peak SAR values averaged over 1 and 10 g for the five phantoms M1 ... M6 and the two children phantoms C7 and C3.

low-loss bone structures, as well as various wet tissues.

The basic investigation on the absorption in the ear region was also performed using the dipole, since it has a well defined current distribution which does not strongly depend on the load, i.e., on the scattered field. The effect on the impedance, which would significantly distort the evaluation of the absorption in the ear as a function of the modeling, can be avoided by normalizing all values to a constant feedpoint current of 100 mA. The vertical dipole was shifted on a matrix parallel to the head surface, with a distance to the closest tissue voxel of 2 mm for the inhomogeneous phantom. The separation of the  $3 \times 3$  matrix was 20 mm in the  $z$ - and 15 mm in the  $y$ -direction. The values were compared to those of the homogeneous phantom (HTSL1:  $\epsilon_{r1}=43.5$ ,  $\sigma_1 = 0.9 \text{ mho/m}$ ) with a 4 mm lossless spacing. The dielectric parameters were chosen from [21] (Table 9.1), which are more recent than the dielectric parameters used in the previous studies.

The results of a representative position directly behind the opening of the auditory canal is shown in Figure 9.7, in which the two additional distances of 5 and 10 mm were also evaluated in order to verify whether the findings have a strong distance dependence.

At this particular position, the earlier assumption holds that filling the low-loss structure of the inner ear with lossy liquid compensates for the losses in the pinna (Figure 9.8). However, the volume containing the spatial peak SAR value shifts away from the feedpoint to areas of greater wet tissue content. This is represented in Figure 9.11, showing a shift in position of the averaging volume to outside the complex shaped, air containing ear region for inhomogeneous modeling. Since the homogeneous phantom shall be designed to well represent the spatial peak SAR values, the homogeneous head without the ear will not well represent the local peak SAR which occurs in the pinna (Figure 9.7). It must also be noted, that these local values strongly depend on the shape of the ear. On the other hand such single voxels

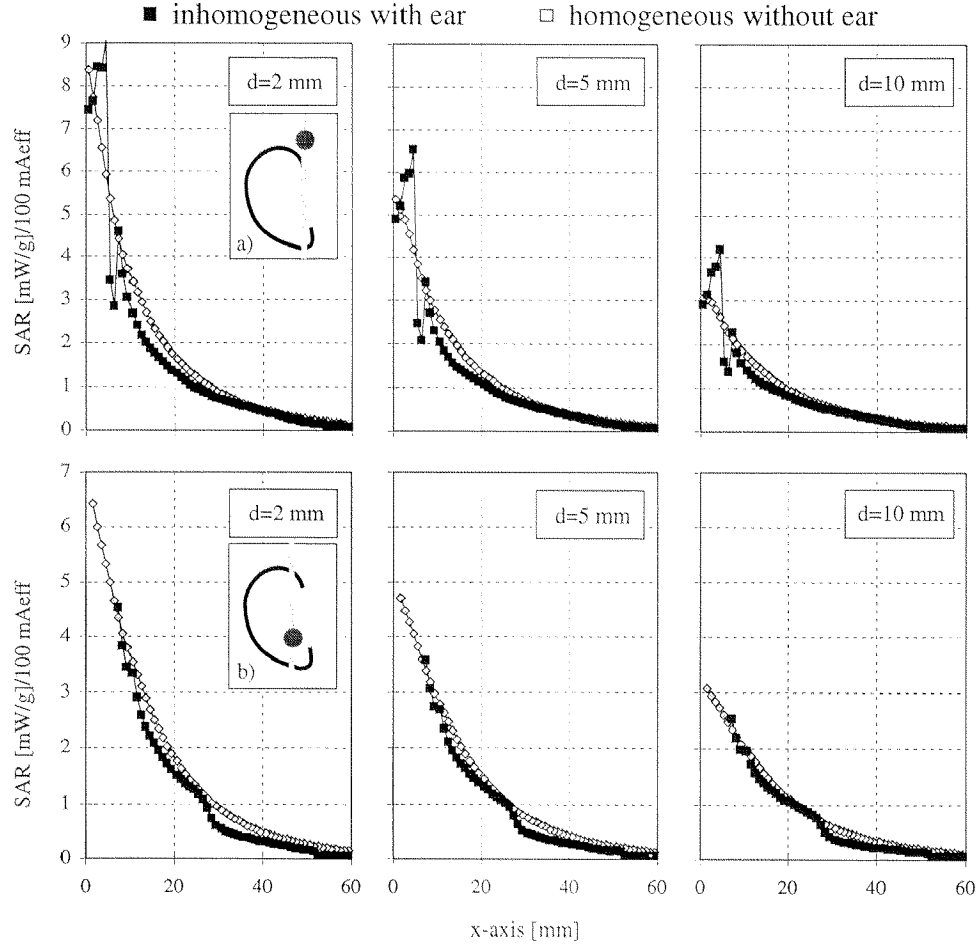


Figure 9.7: SAR distribution along a line perpendicular to the  $0.45\lambda$  (900 MHz) dipole axis a) 5 mm above the pinna (top) and b) directly behind the feedpoint (bottom). The dipole was positioned with its feedpoint directly behind the opening of the auditory canal at three distances (2/5/10 mm) to the outermost voxel of the pinna. The dot in sketches a) and b) corresponds to the position of the axis where the SAR was evaluated. In each diagram, anatomically correct modeling including the complicated shaped ear region is compared to homogeneous modeling (HTSL1:  $\epsilon_{r1}=43.5$ ,  $\sigma_1 = 0.9 \text{ mho/m}$ ) without ear and a simplified ear region.

based values incorporate large uncertainties due to numerical artifacts, which can easily exceed 100% [15].

Based on these results, considerably larger spatial peak SAR values had to be expected when the feedpoint of the dipole is shifted to locations where the tissue volume of the pinna in the proximity of the feedpoint is considerably larger. To study this dependence, the dipole's position was shifted on a plane parallel to the ear on a  $3 \times 3$  matrix, the results of which are plotted in (Figure 9.9). The largest spatial peak SAR (1 g-averaged) was approximately 3 dB above the value found at the center position. The reason is the larger volume of the pinna and that the bone

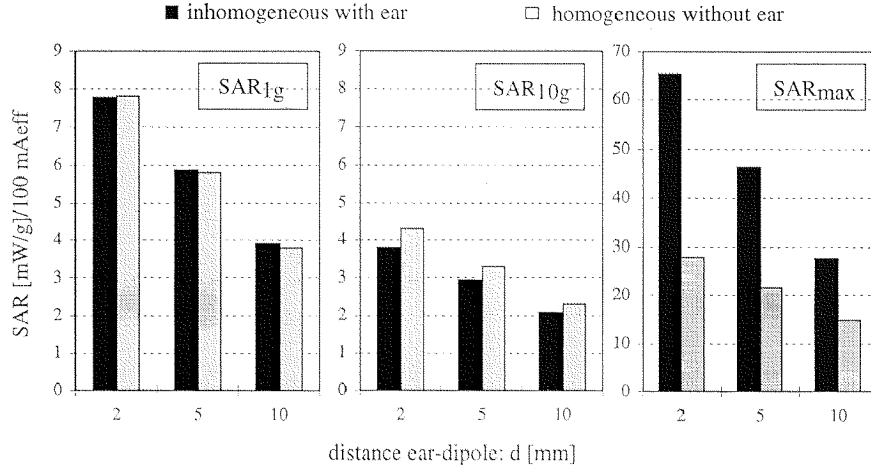


Figure 9.8: Spatial peak SAR values averaged over 1 and 10 g and the maximum one-voxel SAR for the  $0.45\lambda$  dipole (900 MHz) located with its feedpoint at the opening of the auditory canal for the inhomogeneous phantom including the ear as well as for the homogeneous phantom (HTSL1:  $\epsilon_{r1}=43.5$ ,  $\sigma_1 = 0.9$  mho/m) without ear but with a 4 mm spacer.

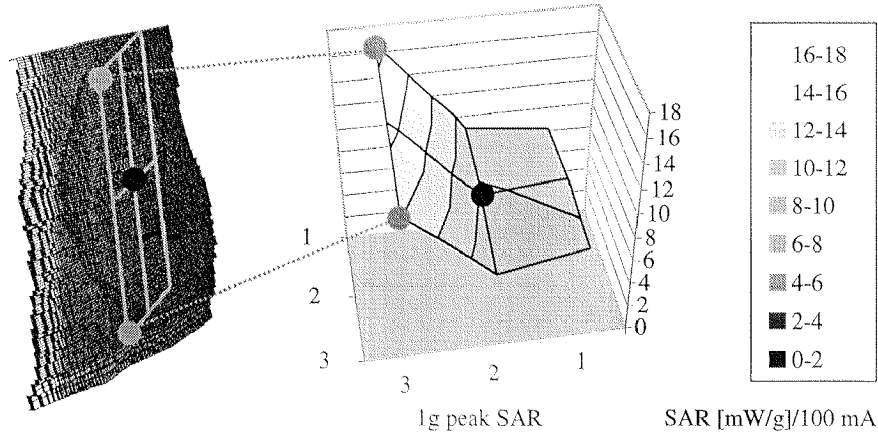


Figure 9.9: Spatial peak SAR values (right) averaged over 1 g for the  $0.45\lambda$  dipole (900 MHz) located with its feedpoint at 9 different locations on a plane parallel to the ear (left). The middle position (black dot) corresponds to the position described in Fig. 8 and 7.

structure of the inner ear does not entirely extend to this ear region. However, this dipole simulates a concentrated source within only 2 mm from the tissue which is unlikely to occur in daily situations.

### 9.5.2 Generic Phone Configuration in Simplified Positions

In order to better represent the actual exposure having a more distributed source in the area of the ear, a generic phone with dimensions as represented in Figure 9.10 has been used in the following studies. It consists of a simple box with a monopole antenna of realistic dimensions. In order to compare our results with the

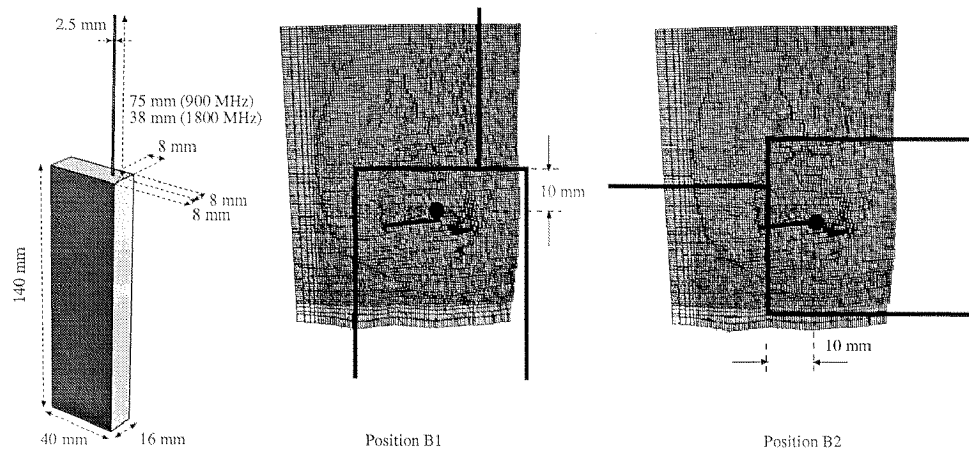


Figure 9.10: Dimensions of the metal case of the generic phone (left) and vertical (B1) and horizontal (B2) phone position (right). The metallic box is at a distance of 2 mm from the outermost voxel of the pinna, corresponding to a 2 mm plastic layer covering the metal case. The dot corresponds to the location of the opening of the auditory canal.

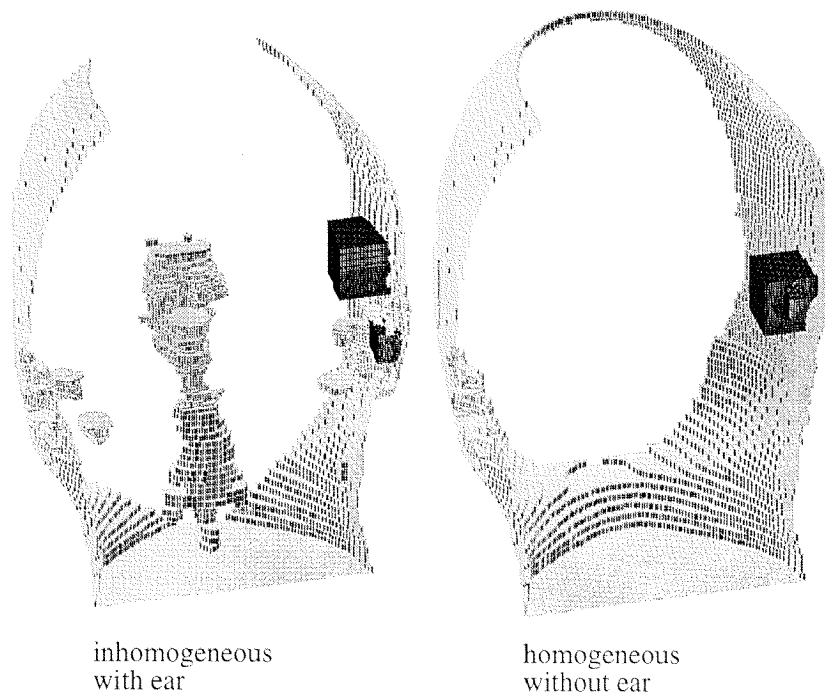


Figure 9.11: The location of the 1g and 10g averaging volume in the human head model is shown for inhomogeneous modeling (left) and homogeneous modeling (right) for a  $0.45\lambda$  dipole. The feedpoint is located directly behind the auditory canal, the distance between the dipole and the closest voxel is 2 mm. For homogeneous modeling, the 1g cube is located inside the 10g cube.



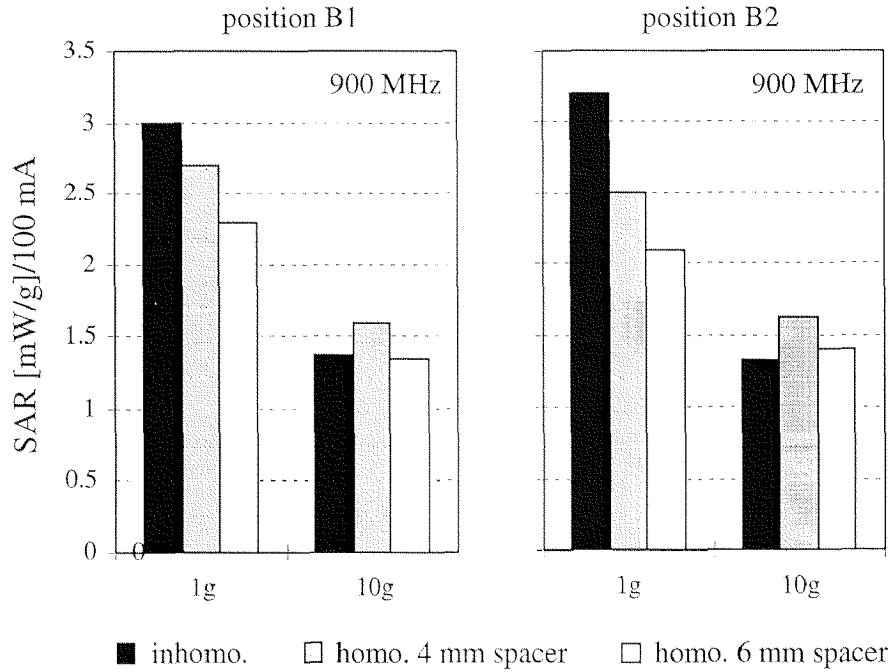


Figure 9.12: Spatial peak SAR values averaged over 1 g and 10 g for vertical B1 (left) and horizontal B2 (right) phone positions for the inhomogeneous phantom including the ear, as well as for the homogeneous phantom (HTSL1:  $\epsilon_{r1}=43.5$ ,  $\sigma_1 = 0.9$  mho/m) without ear but with a 4/6 mm spacer at 900 MHz.

findings of previous studies, the phone was first positioned vertically (position B1) and horizontally (position B2) next to the ear ( $90^\circ$  with respect to the line connecting both auditory canals). The reason that this rather uncommon position was favored by most studies was the shortcoming of most numerical tools in the support of tilting head models without significantly impairing modeling accuracy.

The distance to the closest voxel of the pinna was in both positions 2 mm in order to account for the thickness of the synthetic material around the device body. The location of the imaginary loudspeaker was directly behind the opening of the auditory canal as represented in Figure 9.10. For the homogeneous phantom (HTSL1:  $\epsilon_{r1}=43.5$ ,  $\sigma_1 = 0.9$  mho/m) a lossless spacer of 4 mm (i.e., 6 mm between the surface of the phantom's skin and the metallic box) and 6 mm (respectively 8 mm) was chosen. The results for the 1 g and 10 g values for positions B1 and B2 are summarized in Figure 9.12. It becomes obvious that a spacer of 3 - 4 mm much better represents the maximum exposure of the inhomogeneous phantom than a spacer of 6 mm. As expected, the spatial peak SAR values averaged over a cube of 10 g are much less sensitive to the location of the phone and modeling of the ear.

### 9.5.3 Intended Use Position

To verify these findings for more realistic positions with respect to the head, the dipole and phone were evaluated in a position which corresponds to the intended use position defined by [2]. In the first step, the CAD data of the head was rotated

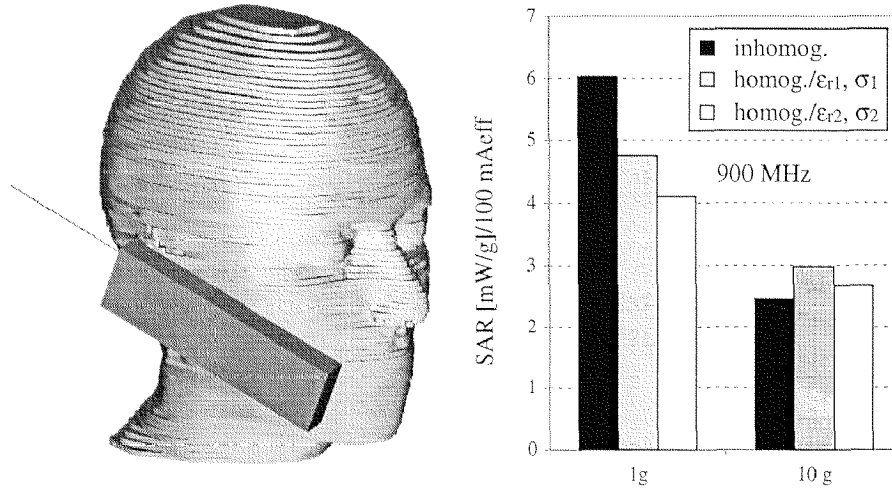


Figure 9.13: Rotated head (left) and spatial peak SAR values averaged over 1g and 10g for an intended use position of the generic phone (position B3) for homogeneous (HTSL1:  $\epsilon_{r1}=43.5$ ,  $\sigma_1 = 0.9$  mho/m and HTSL2:  $\epsilon_{r2}=45.8$ ,  $\sigma_2 = 0.77$  mho/m) and inhomogeneous modeling at 900 MHz.

by  $23^\circ$  around its x-axis and  $-7^\circ$  around its z-axis (Figure 9.2), which represents the intended use position (position B3). The CAD model of the dipole or phone was added and a new graded mesh aligned to the coordinate system of the source was then generated (Figure 9.13). This procedure results in a discretization which neither adds uncertainties to the phone modeling nor changes the accuracy of the head modeling compared to the previous positions.

The spatial peak SAR values averaged over 1g and 10g are represented in Figure 9.14 for the dipole and in Figure 9.13 for the generic phone for a 4 mm lossless spacer. As for the previous position, the maximum underestimation exposure for the investigated source with homogeneous modeling without ear, using a spacing of 4 mm and dielectric parameter set of HTSL1 was 20% for the 1g spatially averaged SAR. Using the dielectric parameter set of HTSL2, the underestimation was more pronounced (30%).

## 9.6 Results at 1800 MHz

Additional studies were necessary at 1800 MHz, since it is not *per se* obvious that the findings are also valid at higher frequencies due to the significantly reduced skin depth. It is expected that a larger amount of the total energy loss is absorbed in the external ear and skin. For comparison, the homogeneous phantom was simulated with both dielectric parameter sets HTSL1 and 2.

The results are summarized in Figures 9.14 and 9.15, from which similar conclusions as at 900 MHz can be drawn under the condition that the homogeneous phantom is modeled with the dielectric parameter set of HTSL1. Employing the dielectric parameter set of HTSL2, the underestimation is quite significant suggesting that the thickness of the spacer must either be reduced or the ear must be modeled by a lossy cartilage-like material.

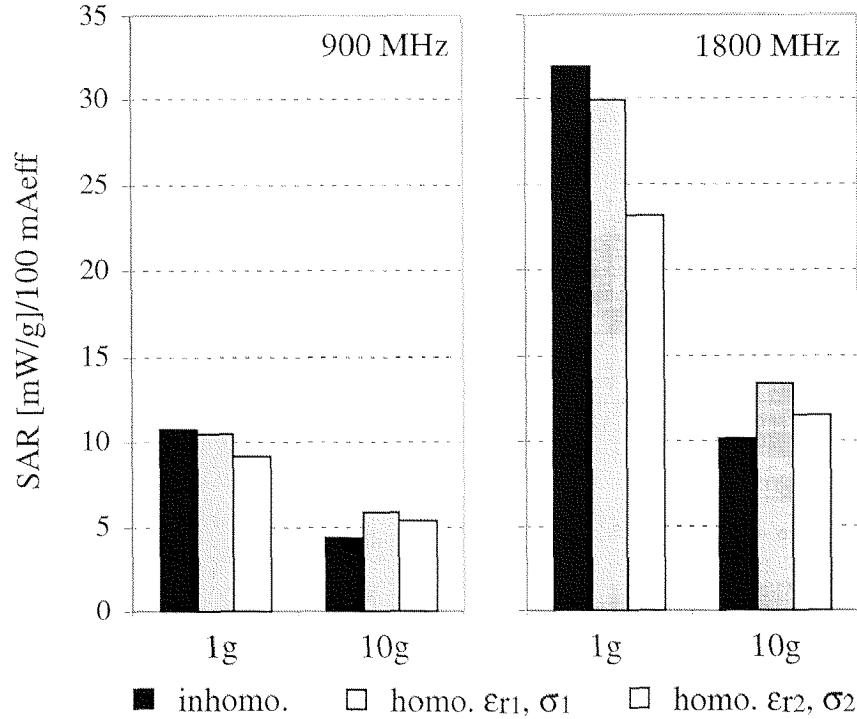


Figure 9.14: Dipole configuration with a rotated head in position B3 and spatial peak SAR values averaged over 1g and 10g for a  $0.45\lambda$  dipole at 900 MHz (left) and 1800 MHz (right). The closest distance between dipole and head is 4mm. The dielectric parameters for the homogeneous phantoms are HTSL1:  $\epsilon_{r1}=43.5$ ,  $\sigma_1 = 0.9\text{mho/m}$  and HTSL2:  $\epsilon_{r2}=45.8$ ,  $\sigma_2 = 0.77\text{mho/m}$  at 900 MHz, HTSL1:  $\epsilon_{r1}=41$ ,  $\sigma_1 = 1.69\text{mho/m}$  and HTSL2:  $\epsilon_{r2}=43.5$ ,  $\sigma_2 = 1.15\text{mho/m}$  at 1800 MHz

## 9.7 Discussion and Conclusions

This study on the exposure of the ear was based on one particular phantom only, i.e., it does not provide information about the variations of different ears. In addition, the exposure was only investigated for two generic transmitters. Nevertheless, the study enables conclusions to be made which are generally valid within reasonable limits.

The basic requirement for a sound procedure shall enable demonstration of compliance for a reasonable cross-section of users. This ultimately requires simplifications, since the absorption significantly depends on the internal and external anatomy of the user. The simplification is driven by the requirement to define a single phantom which satisfies the following criteria: The exposure assessed with this phantom for a given MTE and position shall not underestimate the actual maximum exposure occurring in a reasonable cross-section of users. Based on the previous studies, it was shown that this is possible with a homogeneous head of appropriate shape and dielectric parameters despite the considerable anatomical variations. This had been validated with the exception of the ear region. The ear region is of special complexity with respect to absorption because of the complex structure of the inner ear and the

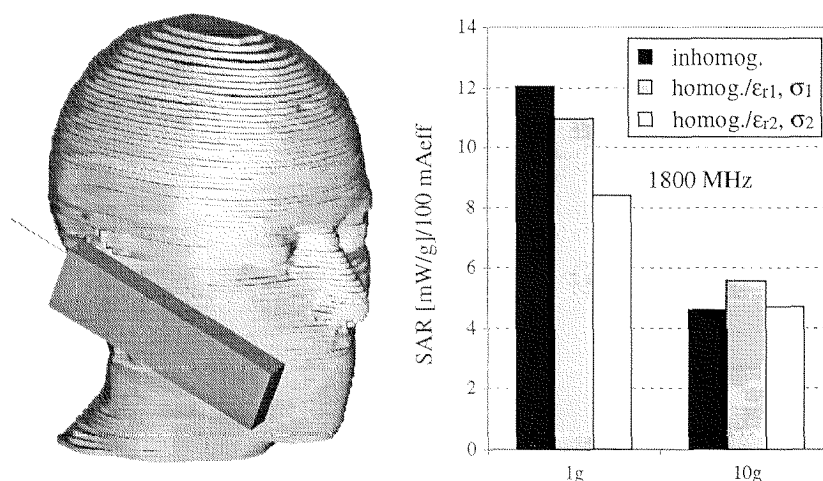


Figure 9.15: Rotated head (left) and spatial peak SAR values averaged over 1g and 10g for an intended use position of the generic phone (position B3) for homogeneous (HTSL1:  $\epsilon_{r1}=41$ ,  $\sigma_1 = 1.69$  mho/m and HTSL2:  $\epsilon_{r2}=43.5$ ,  $\sigma_2 = 1.15$  mho/m) and inhomogeneous modeling at 1800 MHz.

considerable anatomical variations in shape, size and thickness of the external ear. In addition, the external ear is always in direct contact with the device. On the other hand, the external ear has proven to be quite resistant to all kinds of chemical and physical agents as well as environmental stress. However, current safety guidelines do not define different safety limits for the external ear.

The results of this study suggest that for this particular person the spatial peak exposure in the ear region can be appropriately modeled by simulating the head homogeneously by selecting the dielectric parameter set of HTSL1 and simulating the ear pinna by a lossless spacer of 3 - 4 mm thickness. Using a 4 mm spacer, the maximum underestimation of the spatially 1g-averaged peak SAR using a generic phone as a source was below 20%. The 10g-averaged spatial peak SAR, however, was never underestimated. In case of a worst-case exposure source, the underestimation of the 1g-averaged value could be as high as 3 db.

To obtain a more comprehensive data base valid for a reasonable cross-section of the user group, a larger number of human head models including realistically modeled ears would have to be analyzed in a similarly detailed approach as presented. This would clearly exceed the resources of our laboratory. Nevertheless, since the head phantom used has no obvious significant deviation from a normal head, it is unlikely that using other head phantoms will change the basic findings of this study significantly. Consequently, this study allows the general conclusion that a lossless spacer of  $>4$  mm would result in significant underestimation of some exposures. On the other hand, a very thin spacer would overestimate the exposure in the area above the ear. Consequently, a rigorous approach fully complying with the results of this study would be to model the extension of the outer ear sufficiently large (e.g., 90% percentile) and the thickness of the compressed ear correspondingly thin (e.g., 10% percentile) whereby the ear should be partially filled with tissue simulating liquid by providing a minimal distance between the device and liquid of not larger than 3 mm.

## References

- [1] FCC, "Evaluating compliance with FCC guidelines for human exposure to radiofrequency electromagnetic fields", Tech. Rep. OET Bulletin 65, Federal Communications Commission, Washington, D.C. 20554, 1997.
- [2] CENELEC, *prES 59005, CLC/TC211 (SEC) 17, Considerations for evaluation of human exposure to Electromagnetic Fields (EMFs) from Mobile Telecommunication Equipment (MTE) in the frequency range 30 MHz - 6 GHz*, Brussels, Mar. 1998.
- [3] ARIB, *STD-T56, Specific Absorption Rate (SAR) Estimation for Cellular Phone*, Jan. 1998.
- [4] T. Schmid, O. Egger, and N. Kuster, "Automated E-field scanning system for dosimetric assessments", *IEEE Transactions on Microwave Theory and Techniques*, vol. 44, no. 1, pp. 105–113, Jan. 1996.
- [5] Camelia Gabriel, "Phantom models for antenna design and exposure assessment", in *IEE Colloquium on Design of Mobile Antennas for Optimal Performance in the Presence of Biological Tissue*, Jan. 1997.
- [6] Quirino Balzano, Oscar Garay, and Thomas J. Manning, "Electromagnetic energy exposure of simulated users of portable cellular telephones", *IEEE Transactions on Vehicular Technology*, vol. 44, no. 3, pp. 390–403, Aug. 1995.
- [7] N. Kuster, R. Kästle, and T. Schmid, "Dosimetric evaluation of handheld mobile communications equipment with known precision", *IEICE Transactions on Communications*, vol. 80, no. 5, pp. 645–652, May 1997.
- [8] N. Kuster and Q. Balzano, "Energy absorption mechanism by biological bodies in the near field of dipole antennas above 300 MHz", *IEEE Transactions on Vehicular Technology*, vol. 41, no. 1, pp. 17–23, Feb. 1992.
- [9] Volker Hombach, Klaus Meier, Michael Burkhardt, Eberhard Kühn, and Niels Kuster, "The dependence of EM energy absorption upon human head modeling at 900 MHz", *IEEE Transactions on Microwave Theory and Techniques*, vol. 44, no. 10, pp. 1855–1863, Oct. 1996.
- [10] K. Meier, V. Hombach, R. Kästle, R. Y-S. Tay, and N. Kuster, "The dependence of electromagnetic energy absorption upon human-head modeling at 1800 MHz", *IEEE Transactions on Microwave Theory and Techniques*, vol. 45, no. 11, pp. 2058–2062, Nov. 1997.
- [11] F. Schoenborn, M. Burkhardt, and N. Kuster, "Differences in energy absorption between heads of adults and children in the near field of sources", *Health Physics*, vol. 74, no. 2, pp. 160–168, 1998.
- [12] P. J. Dimbylow and S. M. Mann, "SAR calculations in an anatomically realistic model of the head for mobile communication transceivers at 900 MHz and 1.8 GHz", *Physics in Medicine and Biology*, vol. 39, pp. 1537–1553, 1994.

- [13] T. Hamada, Soichi Watanabe, and Masao Taki, "Effect of pinna on the local sars in a human head exposed to microwave", in *Twentieth Annual Meeting of the Bioelectromagnetics Society*, St. Pete Beach, Florida, USA, June 1998, p. 99.
- [14] Om P. Gandhi, Gianluca Lazzi, and Cynthia M. Furse, "Electromagnetic absorption in the human head and neck for mobile telephones at 835 and 1900 MHz", *IEEE Transactions on Microwave Theory and Techniques*, vol. 44, no. 10, pp. 1884–1897, Oct. 1996.
- [15] M. Burkhardt and N. Kuster, "Artifacts at material boundaries of lossy dielectric bodies in FDTD simulations", in *IEEE Antennas and Propagation Symposium*, Atlanta, USA, June 1998, p. 72.
- [16] Allen Taflove, *Computational Electromagnetics: The Finite-Difference Time-Domain Method*, Artech House, Inc., Boston and London, 1995.
- [17] CST, *The MAFIA collaboration, Mafia Version 3. x, User's Guide*, CST GmbH, Lautenschlägerstr. 38, D-64289 Darmstadt, 1994.
- [18] T. Weiland, "Maxwell's grid equations", *Frequenz*, vol. 44, no. 1, pp. 9–16, 1990.
- [19] Dale N. Buechler, Daniel H. Roper, Carl H. Durney, and Douglas A. Christensen, "Modeling sources in the FDTD formulation and their use in quantifying source and boundary condition errors", *IEEE Transactions on Microwave Theory and Techniques*, vol. 43, no. 4, pp. 810–813, Apr. 1995.
- [20] C. Gabriel, *Dielectric database*, Microwave Consultants Ltd, London, 1994.
- [21] Camelia Gabriel, "Compilation of the Dielectric Properties of Body Tissues at RF and Microwave Frequencies", in *Technical Report AL/OE-TR-1996-0037*, Brooks Air Force Base, 1996.

Seite Leer /  
Blank leaf

# Epilogue

In summary, the objectives described in the introduction have been achieved. An extensive literature survey of numerical and experimental techniques used for electromagnetic field prediction of antennas embedded in complex dielectric environments was presented. Within the MINAST project EMSIM, a FDTD kernel was developed and benchmarked focusing on near-field antenna configurations. Error sources for FDTD simulations were analyzed and modeling uncertainties when using rectilinear grids were investigated in detail. Finally the FDTD technique was applied to a wide range of applications, ranging from the dosimetric analysis of *in vitro* and optimization of *in vivo* exposure setups onto human electromagnetic absorption studies. However, knowing the accuracy of the obtained results is essential not only for the described class of problems but also for all electromagnetic field assessments. Results must include a comprehensive uncertainty assessment in order to be of any value for scientific and engineering purposes.

In contrast to the previously assessed effects of staircasing on the scattered field of metallic scatterers and artificial reflections from boundaries which have been discussed extensively in the literature, this thesis addressed the relevance of material boundary representation of complex dielectric bodies for simulation with FDTD.

The error sources have been systematically investigated, and techniques for improved dielectric material boundary representation of complex dielectric bodies within FDTD have been characterized with respect to uncertainty and are currently being implemented.

However, the issue of source modeling was only briefly discussed. This plays a minor role for well defined and simple antennas (e.g., dipole antennas) or sources which are sufficiently far from any scatterers. This is the case for dosimetric analysis of *in vitro* and *in vivo* exposure setups but not for realistic mobile telecommunications equipment operated in the closest vicinity of the body. In the latter case, the near-field radiation characteristics of a MTE will not only depend on the modeling of the antenna, but also on the matching network and casing. It may even significantly depend on the exact modeling of the internal details of the radio, e.g., PCB, wiring, battery, etc. In addition, appropriate modeling of the feedpoint is a challenging problem for any technique. Also the modeling of more complex antenna structures with respect to the FDTD grid, e.g., helices, is already a challenge of its own.

These problems would clearly be beyond the scope of a single thesis and are consequently being addressed by my colleagues. Nicolas Chavannes is currently working on modeling of grid nonconformal antenna structures and general implementation of subgrids. The issues of optimized meshes automatically generated on the basis of complex CAD data and minimization of the dispersion in strongly graded meshes as well as the modeling of the feedpoint are currently part of the PhD topic of my colleague Andreas Christ.

In the future it might also be worth looking again at the issue of hybrid approaches, i.e., combining FDTD with other techniques.



Seite Leer /  
Blank leaf

## Curriculum Vitae

### Education

Dipl. El-Ing. TH (Certified Electrical Engineer), degree 1995  
Technical University of Darmstadt, Germany.  
Major: Numerical Electromagnetics.

Semester Work October 1994 - May 1995  
Institute National Polytechnique de Grenoble,  
Laboratoire d'Electromagnetisme, Micro-  
Ondes et Optoelectronique, Grenoble, France.

Abitur Überwaldgymnasium Wald-Michelbach, degree 1989  
Wald-Michelbach, Germany.

High School Diploma, degree 1986  
Senior High School, Grand Island, Nebraska, USA.

Primary School 1975 - 1979  
Grundschule, Mörlenbach, Germany.

### Professional Experience

Graduate Research Assistant 5/95 - present  
Laboratory for Field Theory and Microwave Electronics,  
Swiss Federal Institute of Technology, Zurich, Switzerland.

Trainee July - August 1993  
Broadcast Television Systems GmbH (BTS),  
Darmstadt, Germany.

Trainee February - April 1992  
Siemens AG, Munich, Germany.

Trainee July - September 1989  
Carl Freudenberg, Weinheim, Germany.

### Awards

Student Award of the Bioelectromagnetics Society June 1998

### Personal data

Birth : 31 March 1969 in Ludwigshafen, Germany  
Citizenship : German  
Parents : Friedericke & Gottfried Burkhardt